

Dye Sensitized Solar Cells – An Investigation of p-type DSSCs

Inauguraldissertation

zur

Erlangung der Würde eines Doktors der Philosophie

vorgelegt der

Philosophisch-Naturwissenschaftlichen Fakultät

der Universität Basel

von

Nathalie Marinakis

Tramelan (BE)

2020

Originaldokument gespeichert auf dem Dokumentenserver der Universität
Basel <https://edoc.unibas.ch>



This work is licensed under a [Creative Commons Attribution-NonCommercial 4.0
International License](https://creativecommons.org/licenses/by-nc/4.0/).

Genehmigt von der Philosophisch-Naturwissenschaftlichen Fakultät

auf Antrag von

Prof. Dr. Catherine Housecroft und Prof. Dr. Anders Hagfeldt

A handwritten signature in black ink, appearing to read 'CHousecroft', with a large, sweeping flourish extending from the end of the name.

Basel, den 19.02.2019

Prof. Dr. Martin Spiess
The Dean of Faculty

Acknowledgments

Firstly, I would like to express my sincere gratitude to my advisors Prof. Dr. Catherine Housecroft and Prof Dr. Ed Constable. Your guidance through my PhD was more than precious. Your immense patience for all our little questions and your endless curiosity about our new (sometimes crazy) ideas will always amaze me. I believe that you are both wonderful teachers because you created for us the opportunity to conquer the knowledge, and this knowledge is the one that will always stay. Your group leading skills kept our group solid to each other and working towards our goal providing us a healthy and very pleasant working environment. For that I have a great respect towards you and I would like express my gratitude.

Many thanks to Prof. Dr. Anders Hagfeldt, for accepting the invitation as a co-examiner, and spending your precious time reading and commenting my thesis.

During the time of my Phd I had the privilege to make some very good friends. Special thanks to Dr. Sara Keler for the amazing time that we had in our office in Spitalstrasse but also during the trips that we make together, you are a true friend. Dr. Max Klein, I admire your skill in learning Greek words, thank you for the endless fun that we had in the lab and in the trips that we did together. Dr. Angelo Lanzilotto, being around you is like being closer to my other home, thank you for all the nice memories. Dr. Alex Prescimone, thank you for the nice time during our coffee breaks (even when it was cold) and for the wonderful time in Greece were I finally learned what a carbonara taste like. Dr. Alex Wiesler, you are the definition of a positive person, thank you for the very nice time that we had in Japan and for the numerous information that I gain concerning horses. Fabien Brunner, I would like to thank you for our very interesting discussions and for the amazing time that we had in all our trips. Dr. Fredi Malzner, thank you for all the nice chats that we had concerning our work and the fun while tasting beers in Halifax. A big thanks also to Luc Driencourt for all our discussions concerning the physics of the DSSCs and for all the nice time that we had. Dr. Annika Büttner I would like to thank you for the very nice collaboration that we had making tandem cells, I truly enjoy working with you. I would like to say a special thanks to Cedric Wobill for synthesizing the WOC53 dye and for producing the electrolyte for the tandem cells but also for being a very nice person to talk to and give joy to the group. A big thank to Dr. Markus Willgert for the fruitful collaboration that we had. A sincere thanks to Jens Top for the warm welcome at his lab in EMPA and the very nice collaboration that we had with the APS measurements. I would like to give special thanks to Dr. Sara Freund for the excellent collaboration that we had, it was a pleasure working with you and learning to speak physics. A warm thank to Dr. Thilo Glatzel, for all the discussion and the meetings that we had concerning the physics of DSSCs.

I would also like to say a special thanks to Myrto Kyropoulou my Greek friend with whom we started from the same university in Thessaloniki and we end up doing our PhD in the same university with a brief stop in Geneva for our Master's degree. You are a dear friend and it was wonderful sharing with you this parkour.

Bea Erisman thank you for all your administration work and for making all things work smoothly. Moreover, I would like to thank all the members of the workshop for their dedication and their hard work. A special thanks to the staff of the Nano Imaging Lab and specially to Daniel Mathys for helping me and teaching me microscopy techniques and for all their patience and commitment at their work.

I would like to acknowledge the Swiss National Science Foundation for the finance support of my PhD

A big thank to Amalia, Elena, Monica, Sevi, you made my life so much funnier and colourful, you are a great support system and true friends.

Furthermore, I would like to thank the CFF for safely and comfortably transporting me from Neuchâtel to Basel every day. The ICE train have been my office during my PhD years and I have to say that in for years of PhD and early group meetings, I was late only once due to train delays and that is an excellent score.

Last but not least I would like to thank my beloved family, my parents for believing in me and being my louder supporters thought out my life. I would not have achieved any of this without you and for that I would be forever grateful. My brother, for always being my reference point and always be there for me and Dimitris for cheering me during the writing of this thesis with nothing but his look.

I would like to say the biggest thank to my husband Toni. You were always there before and during my PhD, you bring balance in my life and I can always count on you. Thank you for making my life easier by being the sweetest person and having the patience to listen to all my little and big problems.

Part of this work in this thesis have been published as follow:

F. Brunner, N. Marinakis, C. Wobill, M. Willgert, C. D. Ertl, T. Kosmalski, M. Neuburger, B. Bozic-Weber, T. Glatzel, E. C. Constable, C. E. Housecroft, *Modular synthesis of simple cycloruthenated complexes with state-of-the-art performance in p-type DSCs*, *J. Mater. Chem. C*, 2016, **4**, 9823.

N. Marinakis, M. Willgert, E. C. Constable, C. E. Housecroft, *Optimization of performance and long-term stability of p-type dye-sensitized solar cells with a cycloruthenated dye through electrolyte solvent tuning*, *Sustainable Energy Fuels*, 2017, **1**, 626

N. Marinakis, C. Wobill, E. C. Constable, C. E. Housecroft, *Refining the anchor: Optimizing the performance of cyclometallated ruthenium(II) dyes in p-type dye sensitized solar cells*, *Polyhedron*, 2018, **140**, 122

Y. M. Klein, N. Marinakis, E. C. Constable, C. E. Housecroft, *Phosphonic acid anchoring analogue of the dye P1 for p-type dye-sensitized solar cells*, *Crystals*, 2018, **8**, 389.

Abbreviations

AcCN	Acetonitrile
AN	Acetonitrile
APS	Ambient pressure photoemission spectroscopy
ALP1	((6,6'-dimethyl-[2,2'-bipyridine]-4,4'-diyl)bis(4,1-phenylene)) bis(phosphonic acid)
AM	Air mass
bpy	2,2'-bipyridine
CO ₂	Carbon dioxide
C _μ	chemical capacitance
DMSO	Dimethyl sulfoxide
eq.	Equivalent
E _F	Fermi level
E _g	Energy gap
eV	Electron volt
E _{vac}	Vacuum level
EQE	External quantum efficiency
ESI	Electrospray ionisation
Et	Ethyl
Et ₂ O	Diethyl ether
EtOH	Ethanol
F	Farad
FF	Fill factor
FIB	Focus ion beam
FTO	Fluorine doped tin oxide
HCl	Chloric acid
HOMO	Highest occupied molecular orbital
Hz	Hertz
I	Current
I ⁻	Iodide
I ₃ ⁻	Triiodide
IPCE	Incident photon to electrical conversion efficiency
IQE	Internal quantum efficiency
I _{sc}	Short-circuit current

IV	Current voltage
J_{MPP} point	Current density measured at maximum power
J_{SC}	Current density measured at short-circuit
JV	Current density versus potential
KP	Kelvin probe
L_d	Diffusion length
LiI	Lithium iodide
LiPF ₆	Lithium hexafluorophosphate
LUMO	Lowest unoccupied molecular orbital
M	Mol L ⁻¹
mA	Milliampere
Me	Methyl
MeOH	Methanol
mg	Milligram
MHz	Megahertz
min	Minute
MLCT	Metal to ligand charge transfer
mm	Milli meter
mM	Milli molar
mmol	Millimole
mol	Mole
MPP	Maximum power point
MS	Mass spectrometry
mV	Millivolt
mW	Milliwatt
N ^N	Diimine
N3	[Ru(4,4'-(dicarboxylicacid)-2,2'-bipyridine)2(NCS)2]
N719	[Ru(4,4'-(dicarboxylicacid)-2,2'-bipyridine)2(NCS)2][TBA]2
NaOH	Sodium hydroxide
NHE	Normal hydrogen electrode
NiO	Nickel oxide
Ni(acac) ₂	Nickel(II) acetylacetonate
Ni(OAc) ₂	Nickel(II) acetate
nm	Nanometre
P1	4-(bis-{4-[5-(2,2-dicyano-vinyl)-thiophene-2-yl]-phenyl} amino)-benzoic acid
PCE	Photon to power conversion efficiency
PF ₆	Hexafluoridophosphate

pH	Potential of hydrogen
Ph	Phenyl
P_{in}	Power input
$PO(OH)_2$	Phosphonic acid group
ppm	Parts per million
Pt	Platinum
PV	Photovoltaic
Q	pre-factor term of the constant phase element
R_{CE}	Resistance of the counter electrode
R_{rec}	Charge recombination resistance
R_{tr}	Charge transport resistance
Ru	Ruthenium
S	Ground state of the dye
S*	Excited state of the dye
SnO_2 tin(IV)	Tin oxide
TBP	4- <i>tert</i> -butylpyridine
THF	Tetrahydrofuran
$TiCl_4$	Titanium tetrachloride
TiO_2	Titanium dioxide
UV- O_3	Ultraviolet-ozone
UV-Vis	Ultraviolet-visible
V	Potential
V_{MPP}	Voltage at maximum power point
V_{OC}	Open-circuit voltage
W	Watt
W_s	Warburg resistance
W_sT	Warburg capacitance
ϵ	Molar absorption coefficient
ϵ_{max}	Maximum molar absorption coefficient
η	Overall conversion efficiency from solar to electrical energy for a
λ_{max}	Maximum absorption
μm	Micrometre
τ_n	Charge lifetime
τ_{tr}	Charge transport time
Φ	Work function
Φ_{fb}	Flat band potential
Φ_{VB}	Valence band potential

Abstract

Two of the major problems that our world is facing is the energy crisis and the rising of the global temperature. Scientists are called to investigate and assess the problem and the results are very alarming. The fossil fuels used until now for the majority of our energy demands would face a shortage in the foreseeable future. In addition, the use of fossil fuels has a major contribution to the rising of the global warming. The solution may be hidden in the sky during a cloudy day, the sun. The sun can produce in 1.5 hours the energy needed to power the global activities for a year. Among the renewable energies, solar energy is the most abundant, and the technology to harvest this energy already exists in the form of solar cells. There are many types of solar cells, and their assessment is done when taking under consideration their cost of production and the efficiency with which they can produce electricity. Dye sensitized solar cells (DSSCs), fulfil the requirements concerning low cost fabrication and green disposal but on the other hand their efficiency lies below the commonly used silicon solar cells, even though their theoretical efficiency could overcome the efficiency of the silicon cells used today. Moreover, dye sensitized solar cells have a good performance in indoor application under low light intensities, in contrast to the silicon solar cells. All facts considered DSSCs are excellent candidates for research since they answer the environmental problems of our society. In this thesis p-type DSSCs were investigated. These could replace the platinum electrode in n-type DSSCs used today a produce tandem DSSCs.

Chapter 1 Introduction to the energy crisis that the world is facing and solutions through the use of the solar energy, motivations for this thesis researcher

Chapter 2 Description of the methods used during this thesis to investigate DSSCs

Chapter 3 Introduction to the working electrodes used in p-type DSSCs. Fabrication and characterization of the working electrodes created during this thesis

Chapter 4 Introduction to the dyes used in the p-type DSSCs. Synthesis of the dyes used in this thesis, characterization of the DSSCs performance

Chapter 5 Introduction to the electrolyte used in p-type DSSCs. Investigation of different electrolytes.

Chapter 6 Introduction to the tandem DSSCs. Investigation of a tandem cell.

Chapter 7 General conclusion of the thesis and future ideas.

Table of contents

Chapter 1 Introduction.....	1
1.1 Energy crisis.....	1
1.2 Global warming.....	2
1.3 Actions to take.....	3
1.3.1 Solar energy.....	4
1.3.2 Dye sensitized solar cells.....	6
Chapter 2 Methods	10
2.1 Sun simulation measurements	10
2.2 EQE measurements	13
2.3 EIS measurements	16
Chapter 3 Surfaces.....	20
3.1 Introduction	20
3.2 Pre-treatment	22
3.2.1 Introduction	22
3.2.2 Pre-treatment of electrode surface.....	23
3.3 Fabrication of the FTO/NiO electrodes.....	25
3.3.1 Background	25
3.3.2 Screen printing	27
3.3.3 Doctor blading.....	27
3.3.4 Sintering	28
3.3.5 Different layers of NiO.....	33
3.3.6 Screen printed NiO with different drop casting pre-layer treatment at different sintering temperatures	34
3.3.7 Screen printed NiO with different spin coating pre-layer treatment and post-treatment after screen printing.	38
3.3.8 Conclusion.....	42

3.4 Li ⁺ doping of the NiO.....	42
3.4.1 Background	42
3.4.2 Effects of Li ⁺ doping on DSSC performance	43
3.5 Characterisation of the semiconductor by cyclic voltammetry	47
3.6 Effect of introducing graphene into NiO.....	49
3.6.1 Introduction	49
3.6.2 Studies of NiO with graphene added.....	50
3.7 Ambient pressure photoemission spectroscopy (APS) measurements.....	53
3.7.1 Introduction	53
3.7.2 APS measurements of FTO/NiO with and without dyes.....	57
3.8 Tauc plot.....	65
3.9 Mott-Schottky analysis.....	66
3.10 Dyenamo electrodes	73
3.10.1 FIB images	76
3.10.2 Energy-dispersive X-ray spectroscopy (EDX) measurements	79
3.11 Materials and Methods	81
3.11.1 Materials for the pre-treatment.....	81
3.11.2 Materials for screen printing	81
3.11.3 Materials for doctor blading.....	81
3.11.4 DSSCs assembly.....	81
3.11.5 Experimental Li ⁺ doping	82
3.11.6 Cyclic voltammetry	82
3.11.7 Experimental doping with graphene oxide.....	82
3.11.8 Mott-Schottky.....	82
Chapter 4 Dyes	83
4.1 Introduction	83
4.2 Organic dyes for p-type DSSCs	85
4.2.1 Effect of organic dyes in p-type DSSCs.....	89
4.3 Inorganic dyes for p-type DSSCs.....	101
4.3.1 Effects of using cyclometallated ruthenium(II) dyes in p-type DSSCs.....	107

4.3.2 Effect of different anchoring ligands on the performance of p-type DSSCs with cyclometallated ruthenium(II) dyes.....	112
4.4 Materials and Methods	122
4.4.1 Solar cells measurements	122
4.4.2 External quantum efficiency (EQE) measurements	122
4.4.3 Electrochemical impedance (EIS), open circuit voltage and intensity modulated photocurrent spectroscopy (IMPS) measurements	122
4.4.4 Electrodes preparation	122
4.4.5 Assembly of DSSCs	123
4.4.6 Synthesis of dyes	124
Chapter 5 Electrolytes	125
5.1 Introduction	125
5.1.1 Liquid electrolytes	125
5.1.2 Ionic liquids and quasi-solid-state electrolytes.....	127
5.1.3 Solid state electrolytes.....	128
5.2 Electrolytes used in p-type cells	129
5.2.1 Introduction: Redox couple	129
5.2.2 Effect of different iodine concentrations	132
5.2.3 Varying the concentration of iodine/triiodide ions in Stnd I electrolyte	134
5.2.4 Varying the concentration of iodine/triiodide ions in Stnd IV electrolyte	135
5.3 Background of varying the cation size in the electrolyte	138
5.3.1 Effect of varying the cation size in the electrolyte	139
5.4 Introduction: Organic solvents	140
5.4.1 Effect of different organic solvent.....	141
5.5 Additives background.....	154
5.5.1 Effect of different concentrations of additives in p-type DSSCs	155
5.5.2 Dyes as additives in the electrolyte, background	160
5.5.3 Effect of dyes as additives in the electrolyte	161
5.6 Co-adsorbants background.....	177
5.7 Effect of the addition of a co-adsorbant on the semiconductor surface	177

5.8 Materials and Methods	185
5.8.1 DSSCs assembly.....	185
5.8.2 Sun simulation measurements	185
5.8.3 Electrochemical impedance spectroscopy (EIS)	185
Chapter 6 Tandem DSSCs.....	186
6.1 Introduction	186
6.2 Preliminary results of tandem DSSCs	190
6.2.1 Synthesis of dyes and redox couple for the electrolyte	191
6.2.2 Cyclic voltammetry and solid-state UV-Vis. spectroscopy.....	194
6.2.3 Sun simulation and External quantum efficiency (EQE) measurements.....	194
6.2.4 Electrochemical impedance spectroscopy (EIS) measurements.....	198
6.2.5 Intensity modulated photocurrent spectroscopy measurements (IMPS)	204
6.2.6 Short circuit charge extraction measurements.....	206
6.2.7 Intensity modulated photovoltage measurements (IMVS).....	208
6.2.8 Open circuit voltage decay measurements (OCVD)	209
6.2.9 Conclusion.....	211
6.3 Materials and Methods	212
6.3.1 Fabrication of TiO ₂ electrodes	212
6.3.2 Synthesis of dyes and electrolyte	212
6.3.3 Fabrication of NiO electrodes	212
6.3.4 DSSCs assembly.....	213
6.3.5 Sun simulation measurements	213
6.3.6 Electrochemical impedance spectroscopy (EIS)	213
6.3.7 Intensity modulated photocurrent spectroscopy measurements (IMPS) / Intensity modulated photovoltage measurements (IMVS), Open circuit voltage decay measurements (OCVD) and charge extraction measurements.....	213
Chapter 7 Conclusion and Outlook	214
Chapter 8 References.....	216

Chapter 1 Introduction

Sentences such as “energy crisis” and “global warming” are becoming very frequent in our everyday speech. What do these sentences mean though? And what is the immediate impact on our life? And most importantly, what can we do to change some of their dramatic outcomes, are some questions that will be addressed during this chapter.

1.1 Energy crisis

The energy crisis is the lack of supplied energy in order to keep the global operation running. The main source of power nowadays is fossil fuels (Fig. 1.1) (e.g. petroleum-based products, coal, natural gas). These energy sources will run out in the foreseeable future ¹, more specifically scientific reports predict the shortage of the earth’s oil stock in 30 years and the shortage of the natural gas stock in 40 years from now. The coal reserve will last for another 200 years. Thus, we have to take into consideration that these predictions have been made based on today consumption of these goods, without taking into consideration the rapid increasing of earth’s population which is predicted to achieve 10 billion by 2050 ².

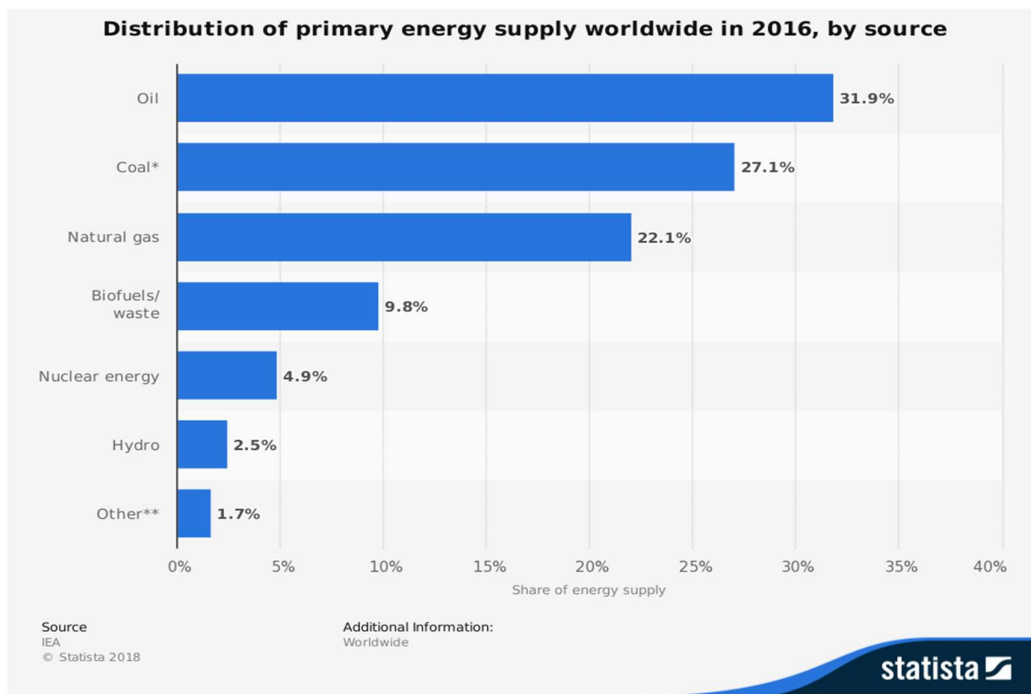
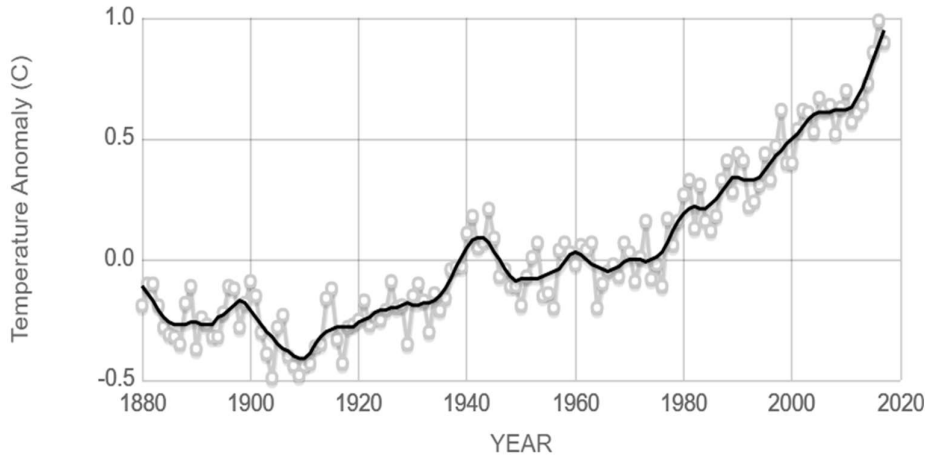


Fig. 1.1: Distribution of primary energy supply worldwide in 2016, by source. Data source: IEA statista 2018®.

1.2 Global warming

The consumption of fossil fuels is exclusively done by combustion which leads to emission of greenhouse gases (GHG) and contributes to the greenhouse effect which in turn contributes to the increase of the global warming (Fig. 1.2) ³ which is calculated as the average temperature of the earth's atmosphere. From the report of the Intergovernmental Panel on Climate Change (IPCC) ⁴, it is deduced



Source: climate.nasa.gov

Fig. 1.2: Global land-ocean temperature index. Data source: NASA's Goddard institute for space Studies (GISS).

that if the global warming exceeds the 1.5 °C barrier, to attenuate a 2 °C of increase in global temperature “the adaptation is expected to be more challenging for ecosystems, food and health systems” ⁴ as it can be seen from Fig. 1.3 ⁵. Among others, some of the direct consequences of exceeding the barrier of 1.5 °C of increase of the global temperature, will be more extreme weather (such as hurricanes, heavy precipitations, heat wave, droughts), rising of sea levels, uncontrollable wildfires, increase in air pollution, more intense allergy seasons, drop of groundwater supply, changing seasons, destruction of coral reefs, food insecurity, increase poverty and social inequalities ^{4, 5, 6}.



Fig. 1.3: Differential climate impact limits to global warming in the case of 1.5 °C and 2 °C. Data source: IPCC ⁴ and ref 5.

1.3 Actions to take

As proposed from the IPCC the best action to take in the effort to limit global warming and the energy crisis, is sustainable development ⁴. Sustainable development includes actions to eradicate poverty, and hunger, ensure health, promote sustained economic growth, reduce social inequalities, protect ecosystems, conserve the oceans and ensure access to affordable, reliable sustainable and modern energy. The latter action involves the development of renewables energy. The different types of renewable energy are the 1. solar energy, 2. wind energy, 3. geothermal energy, 4. hydropower energy. During this thesis we will concentrate on solar energy.

1.3.1 Solar energy

Solar energy is the energy produced by the sun's light and it is renewable and inexhaustible. It can produce photovoltaic energy by harvesting sunlight using solar panels, or thermal energy that can be harvested by mirrors. The sun supply in energy is by far greater in Terawatt/year (TW/yr) than any other source of energy as seen in Fig.1.4 ⁷. The annual global consumption in energy was calculated to be 16 TW/yr in 2009 and it is estimated to reach 27 TW/yr in 2050, from Fig. 1.4 it is seen that the annual

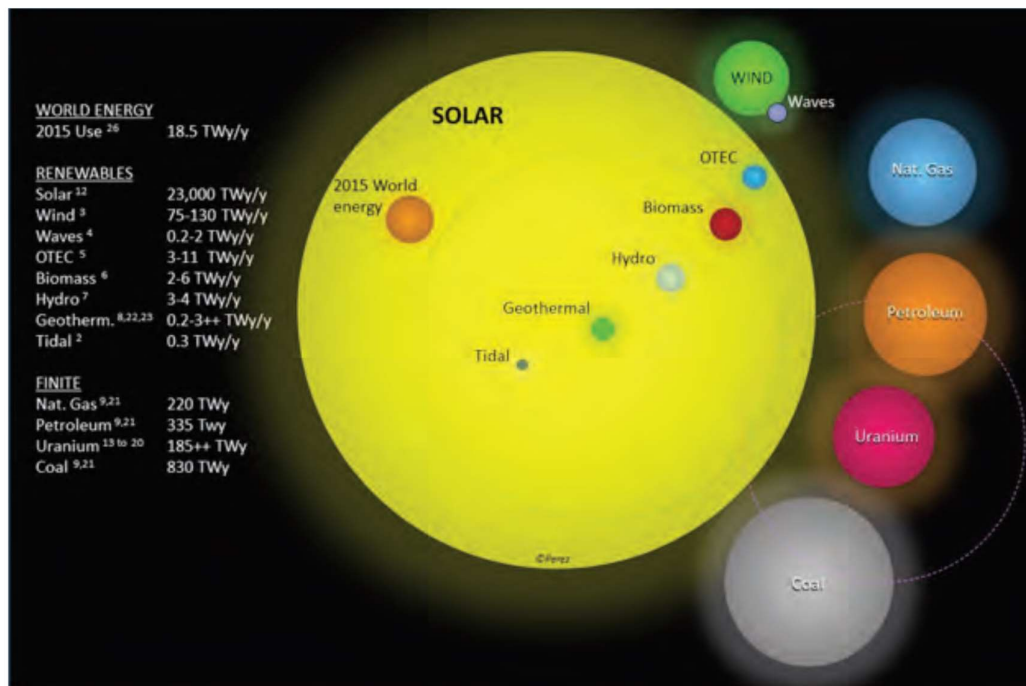


Fig. 1.4: Estimated finite and renewable global energy reserves in terawatt/year. Total recoverable reserves are shown for the finite resources. Yearly potential is shown for the renewable's resources. Figure reprinted from ref. 7

solar energy supply per year can reach 23.000TW/yr which by far exceeds the global annual consumption in energy. Thus, solar energy is the most abundant among the renewable energies. Towards the direction of harvesting the solar energy, a great number of countries have installed solar cells for the production of photovoltaic energy. In fact, it is predicted that there will be an increase in the solar energy market as seen in Fig.1.5.

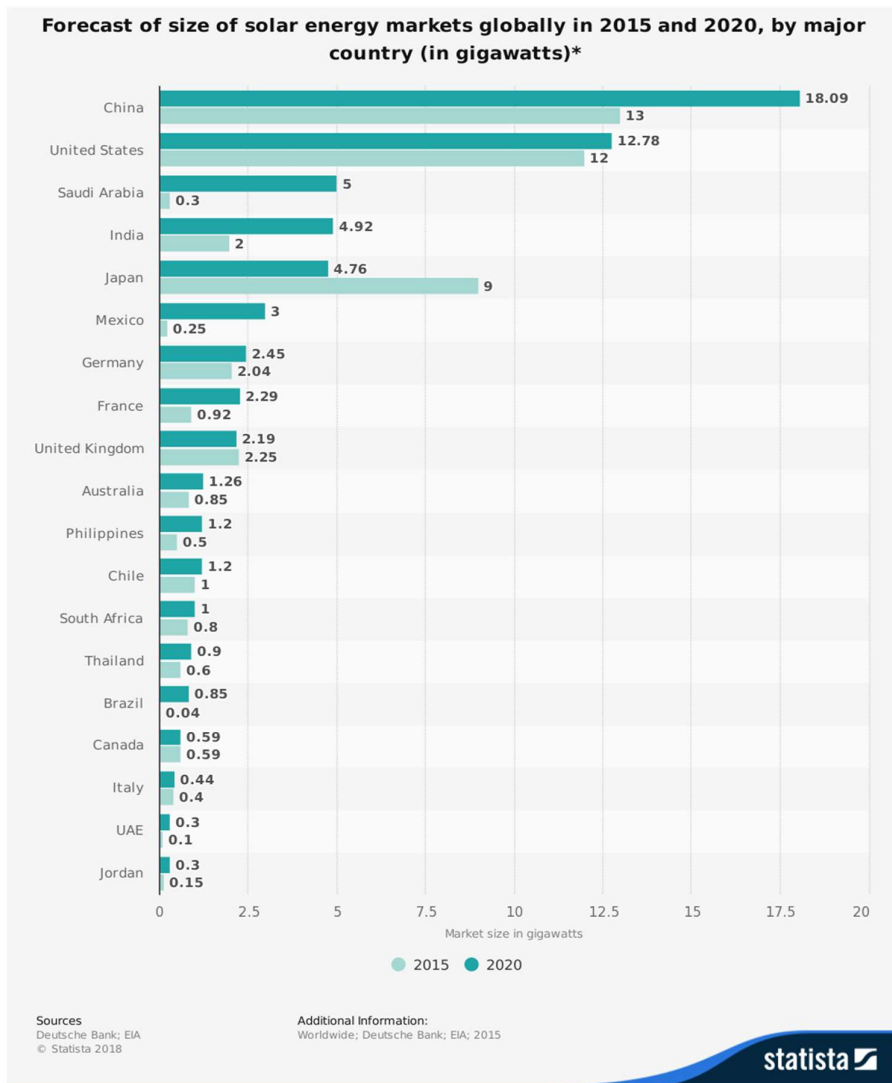


Fig. 1.5: Forecast of size of solar energy market globally in 2015 and 2020 in gigawatts. Data source: IEA statista 2018 ®.

There are a multitude of solar cells developed to harvest solar energy. The most common are silicon cells (e.g. monocrystalline or polycrystalline silicon solar cells) with a photon to current efficiency (PCE) between 20 - 27% (Fig. 1.6). but the disadvantage of these cells is the high manufacturing cost due to the high purity of the silicon which is obtained through expensive high temperature and high vacuum processes ⁸. Other examples of solar cells with greater efficiencies are the multijunction solar cells (Fig. 1.6, PCE \approx 44%) with a production cost even greater than the silicon cells ⁹.

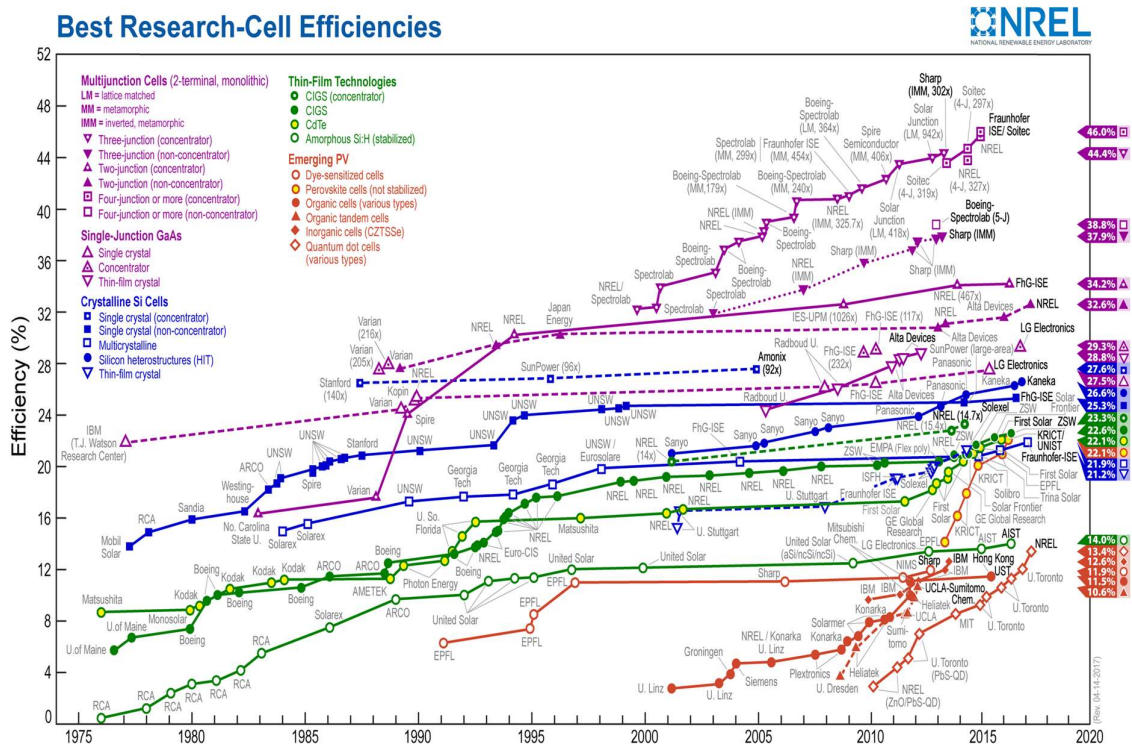


Fig. 1.6: Best research solar cell efficiency. Data source: national renewable energy laboratory (NREL)

1.3.2 Dye sensitized solar cells

Dye sensitized solar cells have attracted considerable attention since the first introduction in 1991 in the paper of *O'Regan and Grätzel*¹⁰. They consist of a working electrode fabricated with a wide band gap semiconductor (e.g. TiO_2)¹¹ sensitized by a dye on a substrate of a transparent conductive oxide (TCO), an electrolyte comprising a redox couple as a charge transport medium and a counter electrode (e.g. platinum electrode)¹¹. The working principal¹² of an n-type DSSCs can be described in Fig. 1.7. Upon photoexcitation the dye anchored on the TiO_2 injects an electron in the conductive band of the semiconductor and the dye is regenerated by intercepting an electron from the redox couple of the electrolyte. The electron injected to the semiconductor is delivered to the external circuit and then to the counter electrode and will be used to regenerate the redox couple of the electrolyte. Dye sensitized solar cells, have a low PCE compared with other solar cells (Fig. 1.6) but have certain advantages over the conventional solar cells such as silicon solar cells. They have a good price to performance ratio¹³, even that the PCE of n-type DSSCs (PCE $\leq 14\%$) is lower compared to the silicon cells, the ratio of price to performance is higher than other better performing solar cells. The DSSCs have a low manufacturing cost due to the inexpensive technics, such as screen and inject-printing or doctor

blading that are used to manufacture the working electrode out of a semiconductor material ^{14, 15}. Non-toxic and environmentally friendly materials are used for their fabrication of DSSCs ¹². They can work with a non-direct or diffuse light irradiation compared to silicon cells ¹⁰ that work almost exclusively with direct irradiation. This is due to the high recombination occurring in a silicon cell which can be translated into loss of charge and

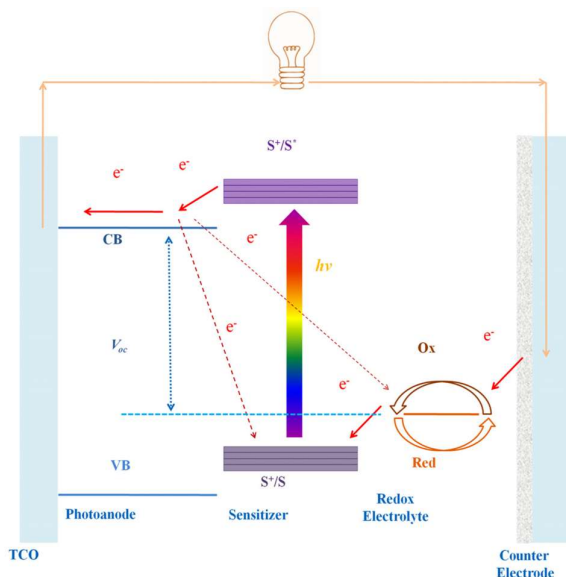


Fig. 1.7: Working principal of an n-type DSSC. Figure taken and reprinted of with the permission *Lin and co-workers* ¹². Copyright © 2014 Elsevier.

ultimately drop of efficiency. Thus, a high flux of light (direct irradiation) is required for silicon cell in order decrease the impact of recombination processes in the efficiency of the cell. In DSSCs this recombination process is much lower and as a consequence DSSCs can perform well in lower light flux so ultimately with flux from diffuse irradiation. Thus, DSSCs are a suitable photovoltaic for outdoor but also for indoor applications. Moreover, DSSCs have a good lifetime ¹⁶, manufacturers guaranty a longevity of the cell up to 3 years ¹⁷. Furthermore, DSSCs, perform better in high temperatures compared to the traditional silicon cells ^{18, 19}. Last, the substrate of the DSSCs can be modified to a flexible substrate ²⁰, textiles ²¹ or paper ²², reducing even more the cost of the cells and increasing the range of applications. Dye sensitized solar cells market value was estimate to be 49.6 million USD in 2104 and is estimated to grow over 12% from 2015 to 2022 ²³. Taking all the facts under consideration, DSSCs have a great potential for the production of green and cheap energy thus, making DSSCs a hot topic for research.

The DSSCs can be classify in two categories, the n-type DSSCs and the p-type DSSCs. The n-type DSSCs are the most investigated category. The p-type DSSCs is the second category and were first

introduced by *Lindquist and co-workers*²⁴ in contrast to n-type DSSCs, the p-type consist of a p-type semiconductor such as NiO or CuO²⁵ for the fabrication of the working electrode. The p-type DSSCs exhibit a lower efficiency compare to the n-type DSSCs (PCE = 2.5% vs. 13.4% for p- type and n-type DSSCs respectively)²⁵. The charge mobility pathway of a p-type DSSC is the inverse process compare to that of an n-type DSSC and can be described as follow: The dye anchored on the NiO gets excited from the solar irradiation. A hole is injected from the sensitizer to the valence band of the semiconductor. The redox shuttle of the electrolyte intercepts an electron from the reduced sensitizer. The injected hole diffuses in the semiconductor and then through the external circuit to reach the counter electrode where the electrolyte is regenerated by oxidation (Fig. 1.8).²⁶

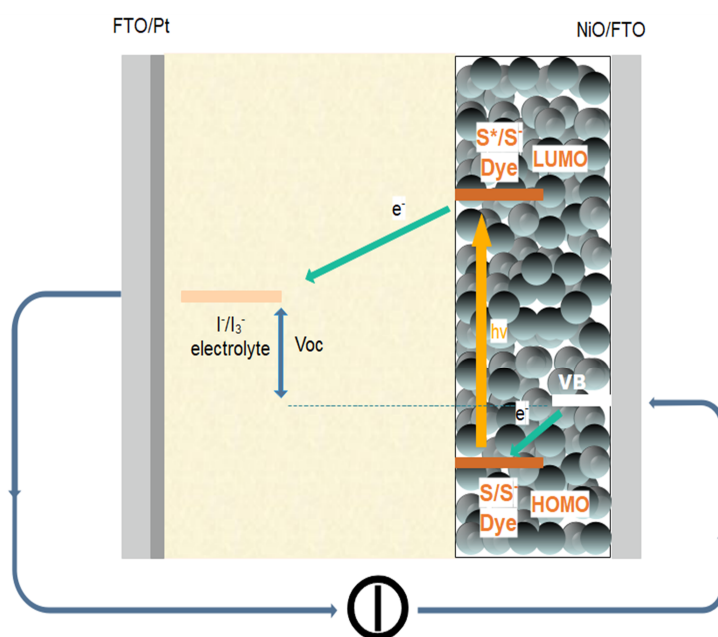


Fig. 1.8: Working principal of a p-type DSSC.

During this thesis p-type DSSCs will be investigated. Initially the fabrication of their working electrode will be explored and different microscopic techniques such as focus ion beam microscopy (FIB) will be used for measuring the thickness and asses the porosity of the NiO electrode. JV curves, electrochemical techniques (e.g. cyclic voltammetry) and spectroscopic techniques (ambient pressure photoemission spectroscopy) will be used for the analysis of the surface and/or the fabricated DSSC. in the next chapter the dyes used for the sensitization of the working electrode will be explored, and the fabricated DSSCs will be investigated with JV curves and electrochemical techniques such as electrochemical impedance spectroscopy. In the following chapter the liquid electrolyte used as a

charge transport medium will be examined. The redox reactions of the redox couple comprised in the electrolyte will be explored and different composition of electrolytes comprising of a redox couple and different additives in different organic solvents will be tested in a working DSSCs. In the last chapter a tandem DSSC with a p-type side in the cathode of the cell and an n-type electrode in the anode of the tandem DSSC will be fabricated and analysed with JV curves and electrochemical impedance spectroscopy.

Chapter 2 Methods

2.1 Sun simulation measurements

The efficiency of converting photons to electrons in a DSSC, (or photon to power conversion efficiency PCE) is the first characteristic that defines a DSSC. This measurement is produced under a sun simulator by irradiating a specific area of a DSSC with a light intensity of 1 sun (1 sun = 100 mW cm⁻²) under standard AM 1.5 conditions. Furthermore, the cell is electrically connected to a potentiostat which can be controlled to sweep the voltage at a predefined voltage range and at a specific rate while the current (I) is monitored. The fraction between the output power (P_{out}) and the input power (P_{in}) defines the efficiency of the DSSC (eq. 2.1) ²⁷.

$$\eta = \frac{P_{out}}{P_{in}} = \frac{P_{\max(mW\ cm^{-2})}}{100} \quad (2.1)$$

where η is the photon to power conversion efficiency of the cell.

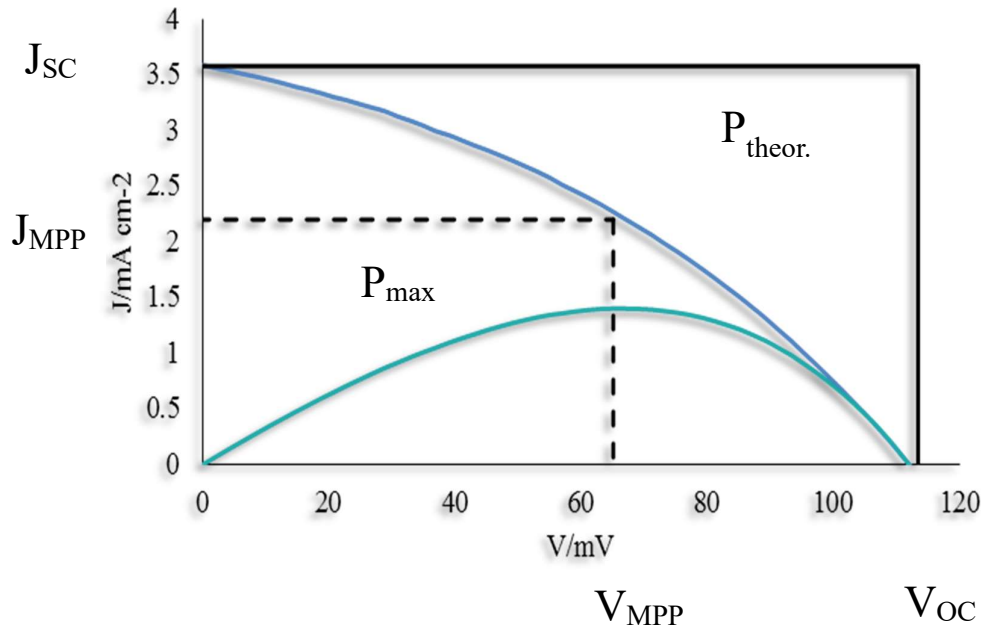


Fig. 2.1: JV and power curve for a p-type DSSC.

The theoretical power ($P_{\text{theor.}}$) that a DSSC can produce under optimal conditions and with no losses occurring is dictated by the short circuit current density (J_{SC} , where $V = 0$) and the open circuit voltage (V_{OC} , where $J = 0$) as illustrated in Fig. 2.1. The maximum power point (P_{max}) is defined at the maximum product of the current density (J_{MPP}) and the voltage (V_{MPP}) of the cell (Fig. 2.1). The rectangle defines by the J_{MPP} and V_{MPP} is the fill factor (FF) of the cell in percentage and indicates the

$$FF = \frac{P_{\text{max}}}{V_{\text{OC}} J_{\text{SC}}} = \frac{\eta}{V_{\text{OC}} J_{\text{SC}} 100} \quad (2.2)$$

satisfactory (or not) performance of the DSSC. It can be calculated from eq. 2.2.

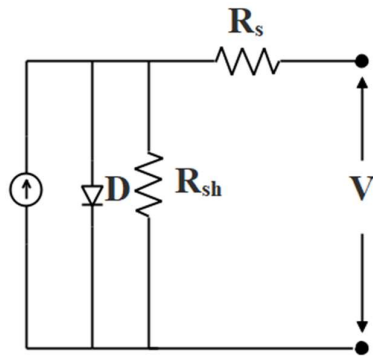


Fig. 2.2: A basic electrical model for solar cell

In a p-type DSSC, the FF of the cell is low compared to an n-type DSSC (30-40% for p-type vs. 60-80% for n-type DSSCs)²⁸. This can be observed by the flatness of the JV curves compared to the

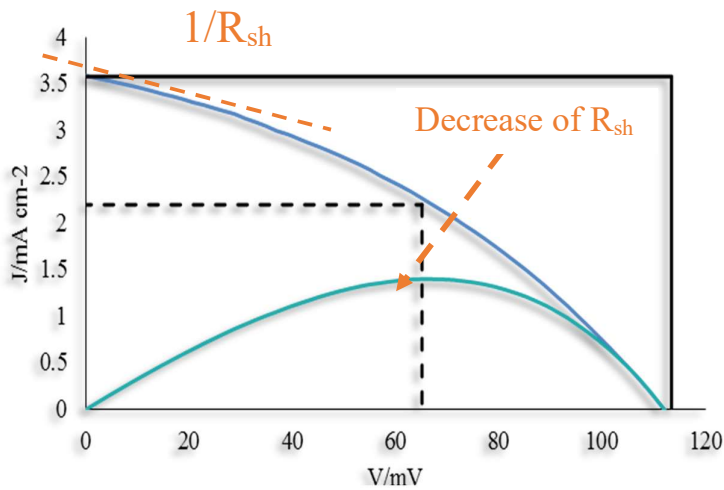


Fig. 2.3: Effect of R_{sh} on JV curves of DSSCs.

squarer shape at n-type DSSCs. A DSSC can be represented as an electrical model (Fig. 2.2) with a

diode (D), a shunt resistance (R_{sh}) and a series resistance (R_s). Ideally the shunt resistance should be infinite and

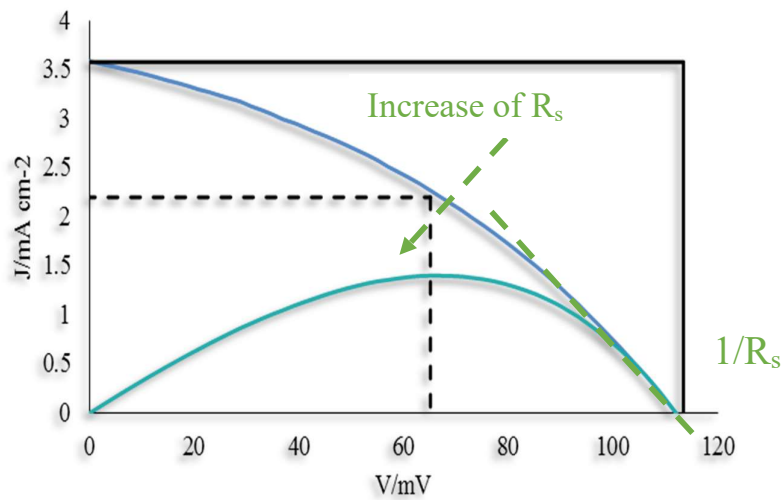


Fig. 2.4: Effect of R_s on JV curves of DSSCs.

the series resistance zero. The R_{sh} resistance is caused due to leakage current through the cell through recombination losses to both the dye and the electrolyte. The R_s is caused by metal contact or bulk substrate (FTO). The R_{sh} is responsible for the flatness of the JV curve and the R_s for the verticality of the JV curve as illustrated in Fig. 2.3 and 2.4.

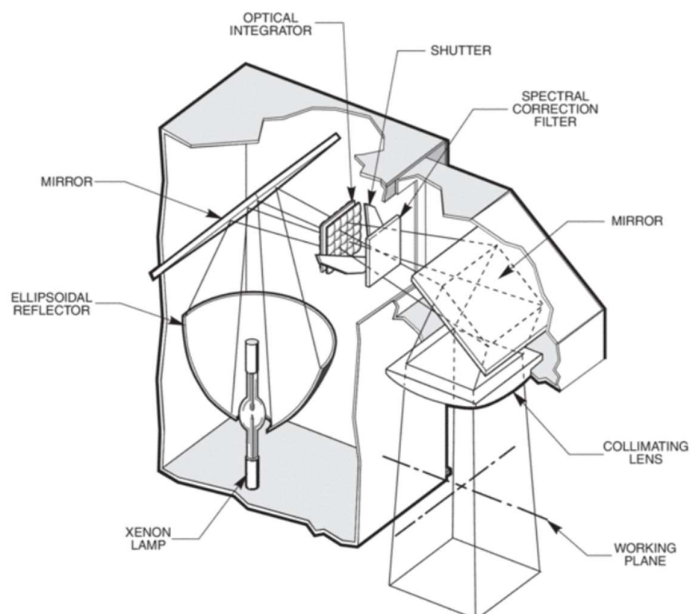


Fig. 2.5: Cut-away view of sun simulator. Retrieved of www.newport.com/n/simulation-of-solar-irradiation.

In Fig. 2.5 a schematic representation of a sun simulation is shown. Before every measurement the light intensity was measured and calibrate to 1 sun intensity with the help of a reference silicon solar cell. For the sun simulation measurements, a xenon arc lamp was used (LOT, LSB 545U), in Fig. 2.6 the good overlapping of the xenon lamp photon flux against the solar spectrum can be observed ²⁹.

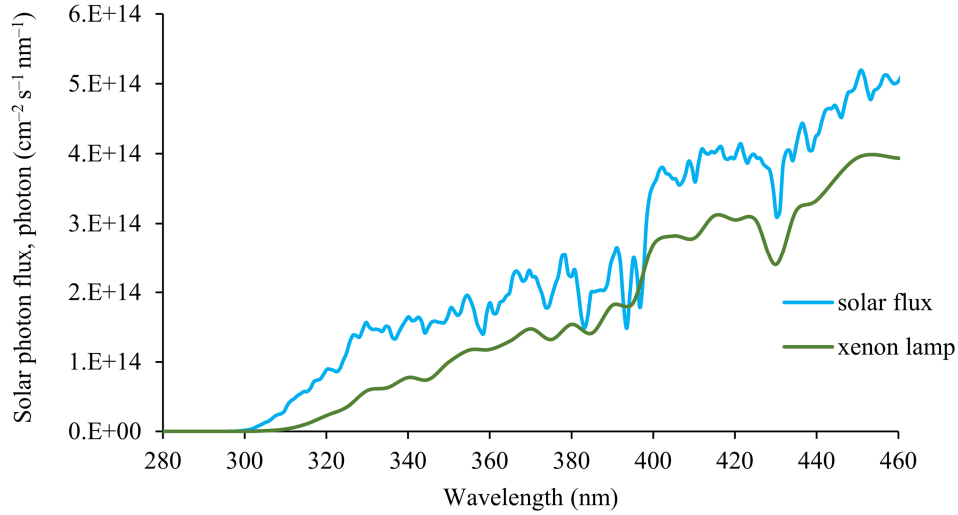


Fig. 2.6: Comparison of the xenon arc lamp light spectra with the solar actinic spectra over the visible part of the spectra ²⁹.

2.2 EQE measurements

The external quantum efficiency (EQE) measurements or incident photon-to-current conversion efficiency (IPCE) is a measurement during which the solar cell is irradiated with light of a predefined range of wavelengths and the current is measured (Fig. 2.7). Thus, the capability of a DSSC to convert photons to current can be calculated following eq. 2.3 ²⁷.

$$IPCE = \frac{\text{number of collected electrons}}{\text{number of incident photons}} \quad (2.3)$$

$$\text{number of collected electrons} = \frac{I_{SC}(\lambda)}{e^-} \quad (2.4) \quad \text{number of incident photons} = \frac{P_{in}(\lambda)}{h\nu} = \frac{P_{in}(\lambda)\lambda}{hc} \quad (2.5)$$

where:

and if we combine eq. 2.4 and 2.5:

where $I_{sc}(\lambda)$ is the monochromatic short circuit, $P_{in}(\lambda)$ is the monochromatic light flux, h is the Planck

$$IPCE = \frac{hc I_{sc}(\lambda)}{e^- P_{in}(\lambda)\lambda} = 1240 \frac{I_{sc}(\lambda)}{P_{in}(\lambda)\lambda} \quad (2.6)$$

constant, c is the speed of light, and e^- is the elementary charge.

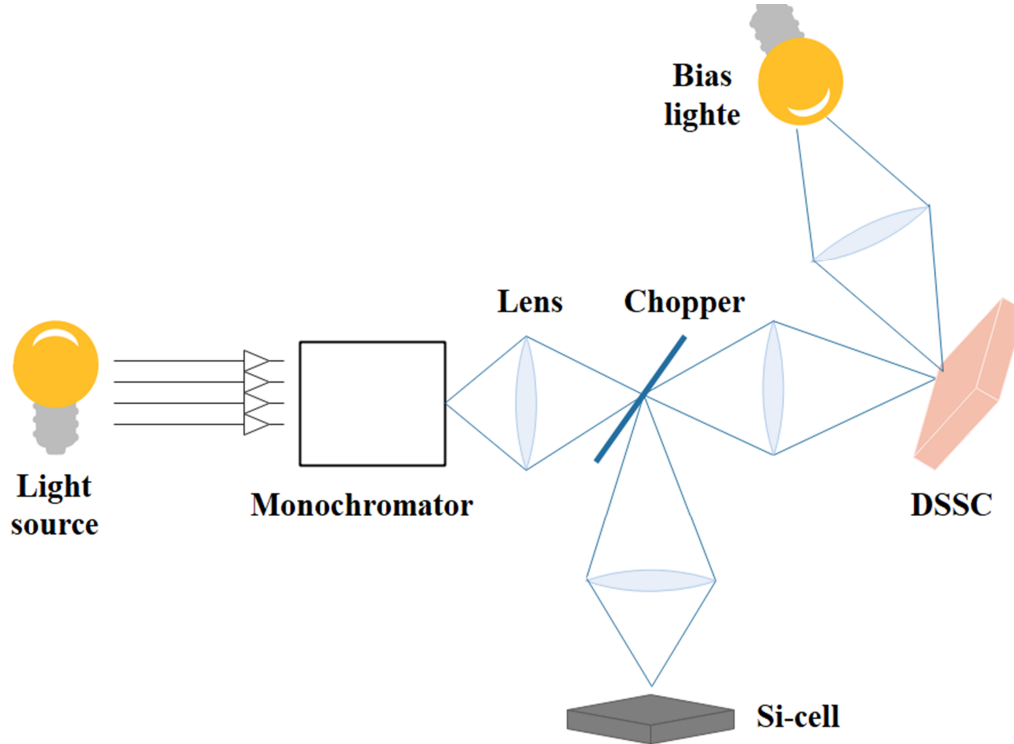


Fig. 2.7: Schematic representation of an IPCE instrument.

IPCE can also be expressed in terms of light harvesting efficiency (LHE), charge injection efficiency (Φ_{inj}) and charge collection efficiency (Φ_{col}) (eq. 2.7)

$$IPCE = LHE \Phi_{inj} \Phi_{col} \quad (2.7)$$

In an ideal system Φ_{inj} and Φ_{col} will be 100% and the IPCE would be equal to the LHE. But after the photoexcitation of the dye and before the injection of the charge to the semiconductor, radiative or non-radiative processes can take place such as recombination of the generated charge with the dye and the electrolyte. Thus, the Φ_{inj} will be lower than 100%. The Φ_{inj} can be defined by eq. 2.8 ³⁰

$$\Phi_{inj} = \frac{k_{inj}}{k_{inj} + k_{rad} + k_{nrad}} \quad (2.8)$$

The Φ_{inj} would be 100% when the radiative (k_{rad}) and non-radiative processes (k_{nrad}) are much smaller than the injection rate (k_{inj})^{31, 32}. In order to calculate conversion rate of the absorbed photons to current, the absorbed photons to current conversion (APCE) or internal quantum efficiency (IQE) should be calculated by eq. 2.9

$$APCE = \frac{IPCE}{1 - R - T} = \frac{IPCE}{LHE} = \Phi_{inj} \Phi_{col} \quad (2.9)$$

where R is the reflection spectra and T the transmission spectra of the cell.

If the incident light in an IPCE experiment is calibrate to produce 1 sun irradiation, by integrating the IPCE output current the short circuit current of the cell can be calculated according to equation 2.10²⁷.

$$J_{IPCE} = \sum_{near\ UV}^{near\ IR} J_{measured}(\lambda) = \int_{near\ UV}^{near\ IR} IPCE(\lambda) e P_{in}(\lambda) d\lambda \quad (2.10)$$

Nevertheless, during the work of *Zou and co-workers*³³ it was showed that when calculating the J_{SC} using equation 2.10, an error is produced due to the dependence of the J_{SC} on the frequency of the chopper (Fig. 2.7). It was found that DSSCs deviate from the normal behaviour observed in Si-cells and two capacitances should be considered for describing the electrical circuit of a DSSC, a shunt capacitance (C_{sh}) and a series capacitance (C_s) (Fig. 2.8). The results showed that when the frequency of the chopper changed it was the capacitance characteristics that lead to the variation of the IPCE output. That was justified by experimental results that proved that when the chopper cuts the incident light to a Si-cell the current drops to zero which was not the case for DSSCs.

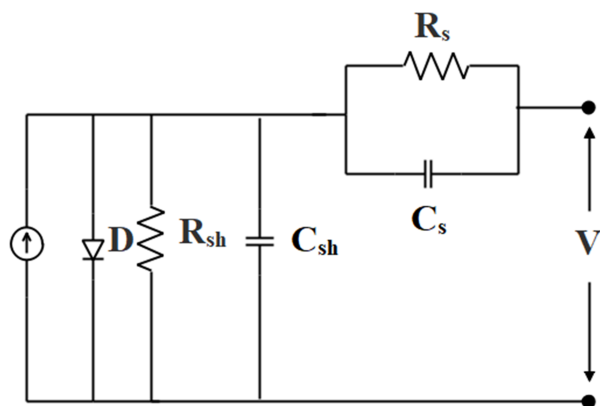


Fig. 2.8: Electrical model for DSSCs suggested by *Zou and co-workers*³³

2.3 EIS measurements

During electrochemical impedance spectroscopy (EIS) measurements, the DSSC is kept under steady state operational conditions. A small amplitude harmonic AC voltage modulation $V_{AC}(\omega, t)$ is superimposed on the DC voltage of the cell and the resulting AC current $i_{AC}(\omega, t)$ response is measured while scanning the frequency over a defined range with respect to both amplitude and phase shift (Fig. 2.9). The impedance spectra of the cell $Z(\omega)$ can be calculated from equation 2.11³⁴.

$$Z(\omega) = \frac{V_{AC}(\omega, t)}{i_{AC}(\omega, t)} \quad (2.11)$$

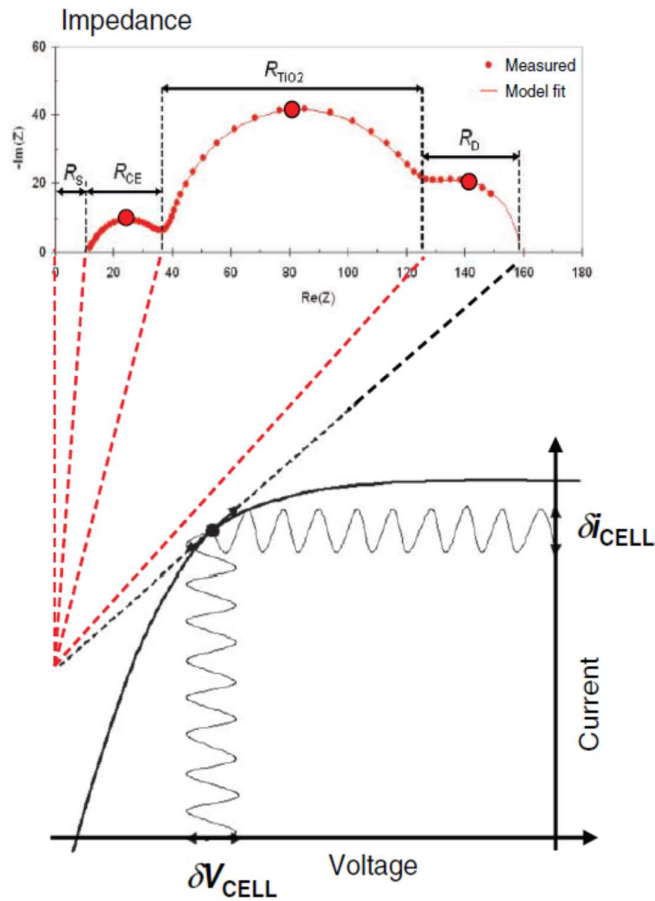


Fig. 2.9: Schematic representation of the relation between the IV curve of a DSSC and its different internal resistance measured by EIS. Reprinted with permission of *Lund and co-workers*³⁴ John Wiley and Sons Copyright © 2010.

EIS is a frequency dependent measurement. Thus, the individual charge transfer process and capacitance of the cell can be monitored and calculated. The EIS results are usually plotted on Nyquist plots and Bode plots. The Nyquist plots are described by the real part of the impedance (Z') on their x-axis and the imaginary part (Z'') on their y-axis. The real part of the impedance contains information regarding the resistances of the DSSC and the imaginary part contains information regarding the capacitances of the cell²⁷. On a Bode plot the logarithm of the frequency is on the x-axis of the graph and the phase shift or the absolute impedance on the y-axis. All these plots describe the same system using different variants as shown in Fig. 2.10.

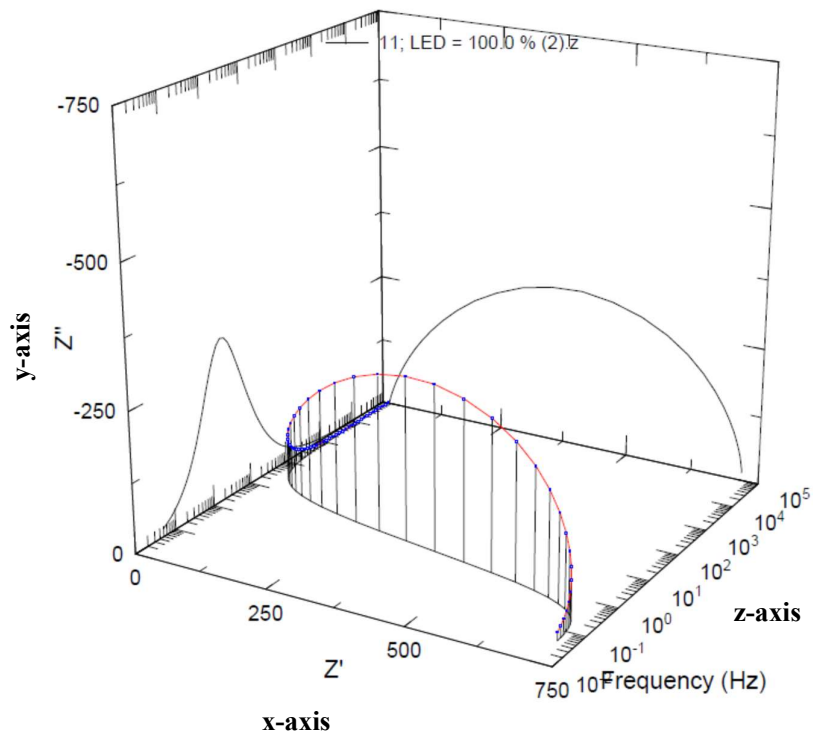


Fig. 2.10: 3-D plots of EIS measurements including Nyquist and Bode plots.

The angle between the two vectors ($V_{AC}(\omega, t)$, $i_{AC}(\omega, t)$) in Fig. 2.11, represents the phase shift that is plotted against the frequency in a logarithmic scale in a Bode plot. $V_{AC}(\omega, t)$ represents the small amplitude AC voltage applied to the system to obtain the perturbation and $i_{AC}(\omega, t)$ the output current monitored. Since the EIS is a frequency dependent measurement the, $V_{AC}(\omega, t)$ and $i_{AC}(\omega, t)$ can be represented as a vector rotating at an angular frequency of $\omega = 2\pi f$ as illustrated in Fig. 2.11, or in a Cartesian system as a Bode plot (Fig 2.10).

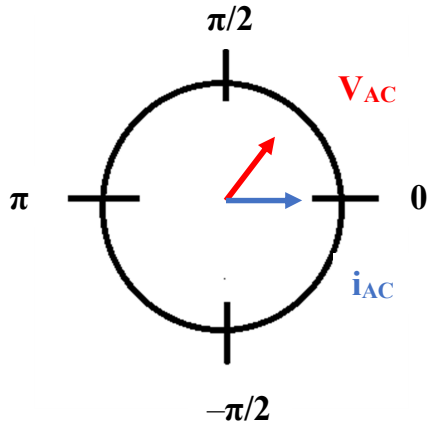


Fig. 2.11: Phase shift in EIS measurements

The EIS measurements can be recorded under different illumination conditions or under different bias. The DSSCs measured are represented as an electrical circuit or equivalent circuit such as the one illustrated in Fig. 2.12. After fitting the different plots, information concerning the series resistance, the recombination resistance, the transport resistance, the Warburg resistance and the capacitance of the cells can be obtained. These components can be numerically defined on an EIS spectra due to their characteristic time constant. Thus, the series resistance is seen in the Nyquist plot on the abscissa from zero to the start of the first semicircle, the transport and recombination resistances and capacitances at the second semicircle of the Nyquist plot and the Warburg resistance and capacitance at the last semicircle at higher frequencies. In p-type DSSC is common to observe only the two first semicircles (Fig. 2.10), this may be due to the overlapping of the time constant of the process taking place at the second and the third semicircles.

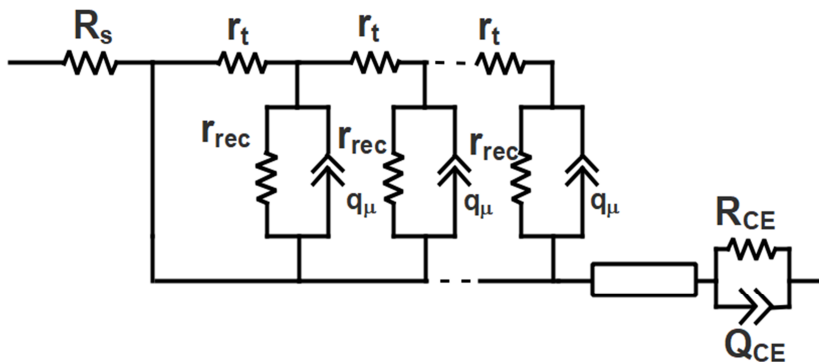


Fig. 2.12: Equivalent circuit used to fit the EIS data.

Chapter 3 Surfaces

3.1 Introduction

The working electrode of a p-type dye sensitized solar cell is made out of a p-type semiconductor. A p-type semiconductor has to satisfy some conditions in order to be used as a functional cathode. A wide band semiconductor is needed for the following reasons. The orbital characteristics of the dye which is absorbed onto the surface of the semiconductor are important. When the dye is excited, an electron from the HOMO is transferred to the LUMO, leaving a vacancy in the original HOMO. This procedure is described in Fig. 3.1.

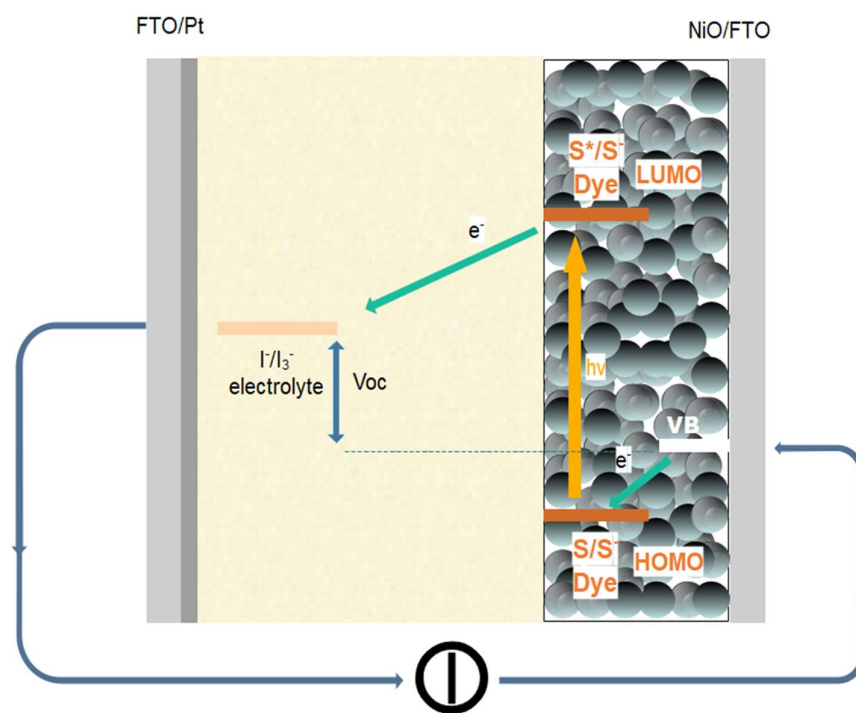


Fig. 3.1: Function of a p-type DSSC.

The energy of the HOMO of the sensitizer should be lower than the valence band of the semiconductor in order to have efficient electron injection from the semiconductor to the dye. At the same time, the valence band should be low enough in order for the difference between the redox energy of the liquid mediator (yellow area in Fig. 3.1) used and the valence band energy to yield a satisfactory open circuit voltage. On the other hand, the conduction band of the semiconductor should be high enough to avoid electron injection from the excited dye. With this in mind, it can be concluded that a wide band gap

semiconductor should be used. Moreover, the structural characteristics of the semiconductor should be closely examined. The semiconductor should present binding sites on the surface for the sensitizer to anchor. The porosity of the semiconductor is another important characteristic because it increases the surface area of the material³⁵. Flat surfaces, with lower surface areas produce much less photocurrent due to poor dye loading. During the past few years, several p-type semiconductors have been used in order to fulfil the aforementioned criteria, and these include, CuI, CuSCN, CuSnI₃,³⁵ and delafossites such as CuAlO₂³⁶, CuSrO₂³⁷, CuGaO₂³⁸. Nevertheless, the most investigated semiconductor for the p-type dye sensitized solar cells is NiO. NiO has a band gap of 3.6 eV and has the valence band at 0.54 eV vs. NHE at pH = 7, and is therefore a strong candidate. In order to meet this goal, research has been done in the development of the NiO surface. *Bach and co-workers*³⁹, report that hierarchical and highly crystalline NiO microballs boost the current density up to 7 mA cm⁻² and achieve an IPCE value of 74%. Towards the same goal, *Suzuki and co-workers*⁴⁰ have been reported, using polyethyleneoxide-polypropyleneoxide-polyethyleneoxide (PEO-PPO-PEO) triblock co-polymers as a template, for the preparation of nanoporous NiO, this increased the surface area of the electrode and consequently, the dye loading with a consequential increase in the current density of the device.

On the other hand, after the work of *Hosono and co-workers*³⁶, it became clear that, since the upper edge of the valence band in the metal oxide is strongly localized on the oxides ions, the holes created on the valence band of the NiO cannot easily be transported through the semiconductor. Compared to TiO₂ which is used in n-type DSSCs, which has a charge mobility of 20 cm² V⁻¹ s⁻¹, NiO has only a small charge mobility of 0.30-0.35 cm² V⁻¹ s⁻¹⁴¹. As a consequence, the photocurrent of the p-type cell will be inferior compared to the one produced from an n-type cell. In order to improve the poor transport properties of NiO, research has focused on doping the NiO semiconductor. A good p-type dopant should introduce more electron deficiencies in the valence band of the semiconductor. Examples are Li⁺^{42, 43}, Co²⁺/Co³⁺⁴⁴, Mg²⁺^{45, 46} cations that will create holes in the lower energy valence band. Indeed, during work by *Wu and co-workers*⁴⁴, it was proved that the valence band of the NiO, could be tuned towards more positive potentials by increasing the amount of Co²⁺ doping cations (from 2-10% with respect to the NiO nanoparticles). But the efficiency of the dye sensitized solar cell, decrease when 10% of doping was used, compared with a cell made with an un-doped electrode. This finding, coupled with the results of *Boschloo and co-workers*⁴⁷, in which it was shown that the transport and lifetime of the hole in the NiO semiconductor is independent of the light intensity, give rise to another explanation about the charge transport mechanism. Until recently, the dominant explanation about charge transport in the semiconductor was based on research made on n-type cells, with TiO₂ as semiconductor. The transport mechanism in TiO₂ is described as trapping and de-trapping of electrons. This mechanism was suggested by *Peter*⁴⁸, according to which, after photoexcitation of the dye, electrons are injected into the conduction band of the semiconductor or more specifically in the trap states. The higher the light intensity, the higher the density of states, which will result in an increase in electron transport and ultimately in an increase in current density of

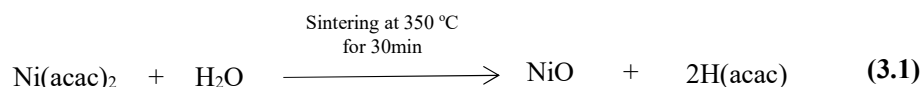
the solar cell. So, based on this fact, the light intensity has little to do with the transport time of the hole in a p-type NiO electrode. In addition to the fact that the performance of the cell did not increase as predicted after the doping of the semiconductor, lead to the conclusion that the transport mechanism of holes in NiO electrodes is done through charge hopping at the NiO/electrolyte interface. During this transport, the hole is hopping between surface states (Ni^{3+})⁴⁷. Thus, the transport mechanism depends on the mobility of the charge rather than the concentration of carriers, so the polaron hopping mechanism is more probable to happen than the band-like charge transport. Regarding the doping of the semiconductor, it can be deduced from the results described earlier, that an initial doping is favourable as it increases the number of charge carriers but furthermore could be detrimental for the cell performance since it creates scattering points for the electrons or the holes in the semiconductor lattice, thereby reducing the probability of polaron hopping and ultimately leads to a decrease in the mobility of the charge⁴². Moreover, a hopping transport mechanism could lead to an enhancement of charge recombination processes with the electrolyte, since the transport mechanism of the charge is localized on surface states of the NiO. In order to decrease the recombination of charge, the surface of the NiO should be doped with more Ni^{3+} . After XPS measurements, *Abe and co-workers*⁴⁹ demonstrated that more Ni^{3+} sites are formed when the NiO paste is sintered under ambient condition rather than in vacuum.

After considering the points discussed above, it is clear that the composition and preparation of the p-type electrode has a major impact on the overall performance of the dye sensitized solar cell. In this chapter, different compositions of semiconductor material and different preparation methods of the working electrodes are explored in order to optimize the properties of the p-type electrodes.

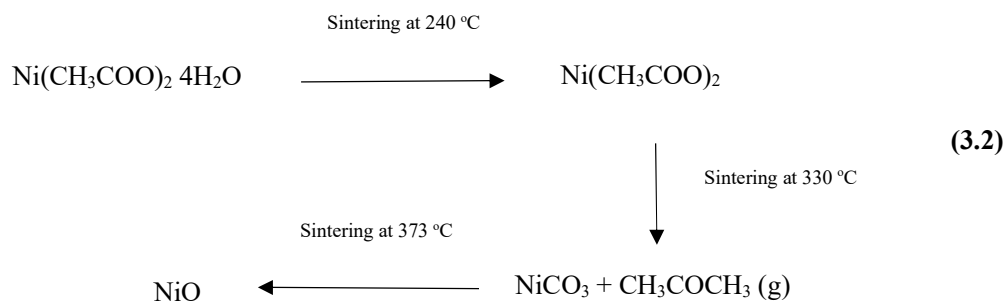
3.2 Pre-treatment

3.2.1 Introduction

The treatment of the FTO (fluorine-doped tin oxide) glass involves addition of a pre-layer. The FTO is a few μm thin layer on a glass substrate and is included in the general category of transparent conductive layers (TCL). In the case of the NiO electrodes the FTO layer prevents the recombination of the electrons. Moreover, the FTO contributes by decreasing the high resistivity of the p-type semiconductor ($\rho_{\text{NiO}} = 10^{10} \Omega \text{ cm}$)⁵⁰. For the pre-treatment, the FTO was covered by a nickel-containing precursor which after the sintering of the electrode was transformed into NiO which will consist the pre-layer of the electrode⁵¹. The most common nickel-containing precursors that have been reported in literature are, nickel (II) acetylacetonate and nickel (II) acetate tetrahydrate. As reported, both are transformed into NiO after being sintered at a temperature of 300 °C to 450 °C. Nickel(II) acetylacetonate has a green colour, and becomes black after the sintering process. This procedure was broadly investigated by *Niinistö and co-workers*⁵², and is described in eq. 3.1.



Nickel(II) acetate was also investigated as a good pre-layer candidate. *Kim and co-workers*⁵³ reported that the transformation to NiO happened in three steps. First, at a temperature below 240 °C, the dehydration occurred that lead to anhydrous nickel(II) acetate. Then, the anhydrous nickel(II) acetate was transformed into nickel(II) carbonate at 330 °C and acetone was released into the gas phase. At the last step, the nickel(II) carbonate was transformed to NiO at a temperature of 373 °C eq. 3.2.



3.2.2 Pre-treatment of electrode surface

There are different methods to apply the pre-treatment layer on the FTO glass. A good technique is qualified according to its ability to produce a well adhered layer on the FTO glass and to give homogeneous spreading of the layers on the entire surface on the FTO glass. In order to grasp a better understanding of the function and application of the pre-layer, during this research two different precursors and two different techniques of application were used. Spin-coating with two different rounds per minute speeds and dip coating, which consists of fully immersing the glass into an AcCN solution of the precursors, removing the excess and then allowing it to dry on a flat surface. This last procedure was repeated multiple times to give a good surface coverage. The different techniques and the different precursors used were compared in order to choose the best among them. Microscope images were taken in order to determine which components are better as a pre-treatment.

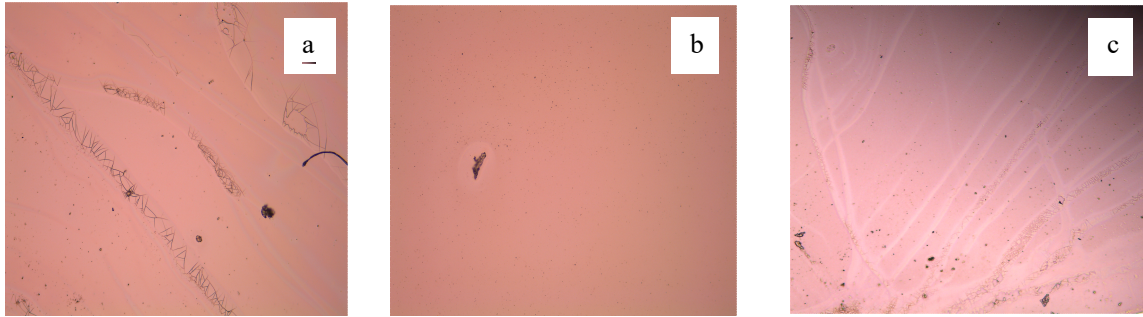


Fig. 3.2 **a:** Microscope image of FTO glass dip coated in an AcCN solution of nickel(II) acetate **b:** spin coated at 2000 rpm and **c:** spin coated at 3000 rpm

From Fig. 3.2a it was detected that the layer of $\text{Ni}(\text{OAc})_2$ after dip coating is far from being homogeneous; cracks were observed through all the surface. Moreover, crystals were detected, which will prevent the adhesion of the NiO paste on the pre-treatment layer prior to sintering. In Fig. 3.2b a homogeneous application of the $\text{Ni}(\text{OAc})_2$ solution was observed and in Fig. 3.2c the application was not homogeneous, due to the high speed of the spin coater.

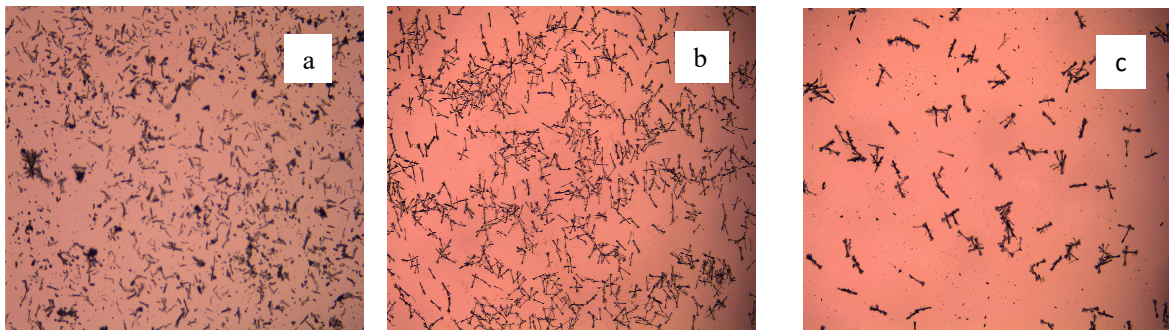


Fig. 3.3 **a:** Microscope image of FTO glass dip coated in an AcCN solution of nickel(II) acetylacetonate. **b:** spin coated at 2000 rpm and **c:** spin coated at 3000 rpm

Fig. 3.3a shows the results of the dip coating technique with a $\text{Ni}(\text{acac})_2$ solution. As one can see, evenly spread aggregates were formed. The microscope image for a spin coated solution (Fig. 3.3b, c) does not change dramatically as the spin coater speed increases at Fig. 3.3c, the aggregates are more dispersed, due to the higher speed applied. From both images, (Fig. 3.2 and 3.3) it was concluded that for $\text{Ni}(\text{OAc})_2$ solution, the best application method is spin-coating at 2000 rpm whereas for $\text{Ni}(\text{acac})_2$ solution, the dip-coating technique is preferred.

In Fig. 3.4 microscope pictures of spin coated FTO plate with $\text{Ni}(\text{OAc})_2$ solution and ethanolamine, can be observed. This procedure was first introduced by *Odobel and co-workers*⁵⁴. In this study, an undisclosed quantity of the solution was spin coated at 3000 rpm for 30 s. In order to optimize the process, different tests were made concerning the time of spin coating and the quantity of applied

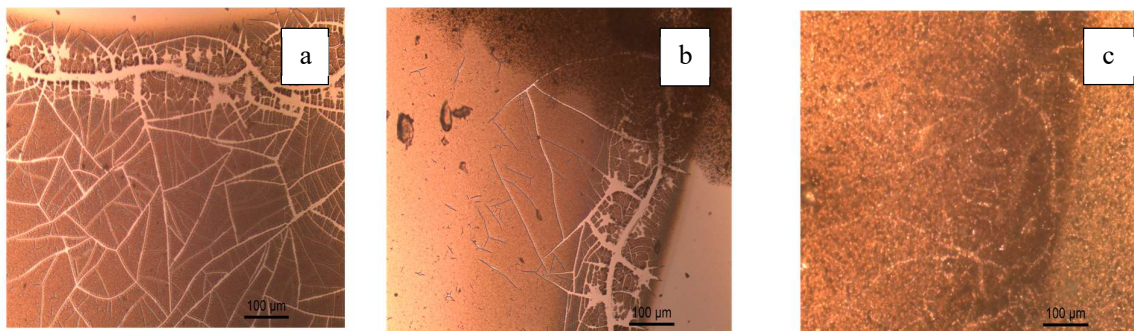


Fig. 3.4 a: Microscope image of FTO glass spin coated at 3000 rpm in a methoxyethanol solution of 20 µL of nickel(II) acetate and ethanolamine for 30 s. **b:** spin coated at 3000 rpm in a methoxy ethanol solution of 20 µL of nickel(II) acetate and ethanolamine for 1min. **c:** Microscope image of FTO glass spin at 3000 rpm coated in a methoxyethanol solution of 100 µL of nickel(II) acetate and ethanolamine for 1 min

solution. When applying 20 µL of solution for a spin coating time of 30 s, cracks are observed in all the surface of the FTO, as seen in Fig. 3.4a, when spin coating for double the time (Fig. 3.4b), less cracks are observed. Additionally, an inhomogeneous coverage of the whole FTO surface was observed which lead to the increase of applied $\text{Ni}(\text{OAc})_2$ solution (100 µL) and as it can be seen in Fig. 3.4c, a homogeneous coverage is observed without cracks.

3.3 Fabrication of the FTO/NiO electrodes

3.3.1 Background

The NiO layer is the final layer applied to the electrode before sintering. There are different techniques in order to apply the NiO paste to the pre-treated FTO glass. Since NiO was initially used as a photocathode in p-type DSSCs, a multitude of techniques, for the application of the NiO paste, have been investigated. One of the first methods of fabrication of NiO electrodes was demonstrated by *Lindquist and co-workers*⁵⁵ after preparing electrodes by spreading an $\text{Ni}(\text{OH})_2$ slurry using a doctor blading technique onto an FTO plate and sintering in ambient conditions. The sintering temperature used during that work was 500 °C, but temperatures between 300 °C^{47, 56, 57} and 450 °C,⁵⁸ have also been used. The film thickness during these studies varied between 0.5-1.4 µm. *Odobel and co-workers*⁵⁹ increased the thickness of the NiO electrode to 3.5 µm, after annealing of nickel acetate

films obtained by recrystallization under hydrothermal conditions in the presence of hexamethylenetetramine. During the annealing process, the temperature was raised to 450 °C in order to fully convert the $\text{Ni}(\text{OAc})_2 \cdot 4\text{H}_2\text{O}$ to NiO. Additional work, done by *Qu and co-workers*⁶⁰ reports annealing temperatures of 400 °C, the efficiency of the p-type DSSCs ($\eta = 0.09\%$) was better than the one reported by *Odobel* ($\eta = 0.032\%$)⁵⁴ above, but the surface area and the porosity of the NiO layer as well as the stability of the film decreased as the temperature increased, but crystallinity increased. Another revolutionary method for the application of the NiO, was first presented by *Suzuki and co-workers*⁶¹. In this methodology, a template based on triblock co-polymer containing polyethyleneoxide (PEO) - polypropyleneoxide (PPO) - polyethyleneoxide (PEO) polymers was used for the preparation of mesoporous NiO. The triblock co-polymer template and a solution containing NiCl_2 was spin coated onto an FTO substrate and sintered at 450 °C. *Suzuki and co-workers*⁴⁰ prepared templates based on triblock co-polymers with different ratios of PEO and PPO. Moreover, the deposition on the FTO substrate was done by doctor blading technique. The sintering temperature used for these methods using polymers are higher (400 - 450 °C) compared to the polymer-free precursor for which only the organic compound contained need to be removed. *Dini and co-workers*⁶² demonstrated that reproducible results could be achieved after spraying a 2-propanol solution of pre-formed NiO nanoparticles onto ITO (indium tin oxide)-coated glass. The advantage of this method is the fact that unlike the paste containing organic compounds which need to be sintered at a high temperature (300 - 450 °C), the alcoholic solution of the precursor used during this work, can be annealed at a much lower temperature (60 - 70 °C). For the sintering process of the electrode, the most common way is in a furnace. Aside from this, other techniques were evolved for the same purpose, for example, rapid discharged sintering (RDS)^{63, 64}. Other techniques, that have been used for the application of NiO are electrospun⁶⁴ chemical deposition⁶⁵, electrochemical deposition⁶⁶, pulse laser deposition⁶⁷, plasma-enhanced chemical deposition⁶⁸. Nevertheless, the method that has been most broadly used for the application of the NiO precursor onto the FTO substrate, is screen printing⁶⁹. With this method, the thickness of the semiconductor can be easily tuned by adjusting the numbers of screen-printed layers. A good porosity of the NiO layer was achieved after sintering at temperatures between 300-450 °C. *Cheng and co-workers*⁷⁰ reported a record Jsc of 5.11 mA cm⁻² and a V_{OC} of 294 mV after using a screen-printing technique with a paste made of NiO nanoparticles, mixed with organic solvents. The sintering temperature used was 550 °C in order to improve the nanoscale crystallinity and the thickness of the NiO layer obtained was approximately 2.7 μm , which is the optimal thickness for the NiO electrode according to the review of *Gibson and co-workers*⁷¹ since it led to the best efficiency cells. The methods used during this thesis were screen printing and doctor blading⁷². The choice was made based on the literature⁷³ and also due to previous experience in our laboratory of these techniques for n-type DSSCs⁷⁴.

3.3.2 Screen printing

In the screen-printing technique, an aluminium frame (90-48Y PET mesh from Serilith AG) and two sliders with different tilting angles were used. A resin covered the entire frame, except from the designated dots (in our case, dots with 0.237 cm^2 surface area) that the nanoparticle paste was able to penetrate in order to form the semiconductor in dot form. At first, the NiO (Ni-Nanoxide N/SP, Solaronix) paste was homogeneously applied onto a frame. In order to do this, a slider with a tilting angle of 45° was used (Fig. 3.5). Then the NiO dots were created. For that, an FTO glass with the pre-treated $\text{Ni}(\text{acac})_2$ or $\text{Ni}(\text{OAc})_2$ layer was placed under the frame and with the use of the second slider, which has a tilting angle of $70^\circ - 80^\circ$ (Fig. 3.5), an even force was applied across all the width of the frame. Once the first layer of NiO was printed, the plate is kept in an EtOH chamber for 3 min to reduce surface irregularities of the printed layer and was dried for 6 min at 125°C on a heating plate, evaporating the ethanol and other volatile solvents from the paste. After the heating procedure, the printing procedure was repeated as many times as the required numbers of NiO layers. This technique has proved more reproducible than other procedures such as doctor blading. Moreover, it gives the opportunity to tune the thickness of the NiO layer with a good precision.

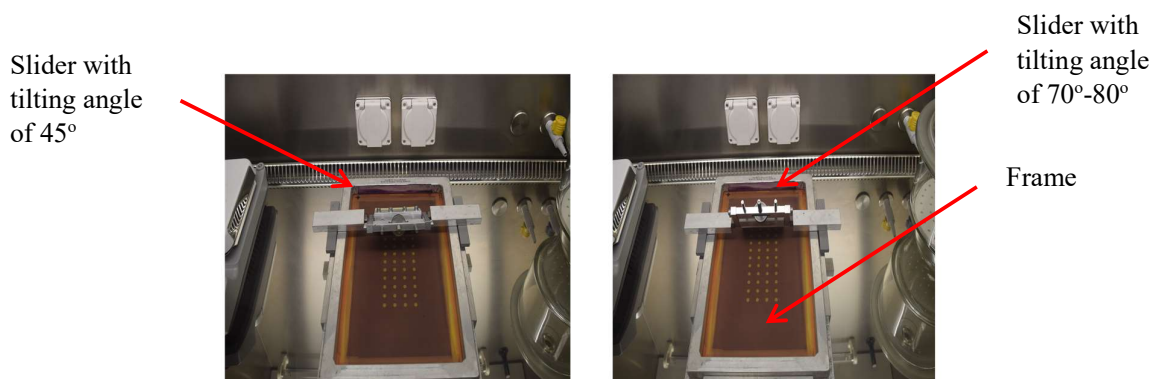


Fig. 3.5: Screen printing equipment.

3.3.3 Doctor blading

Doctor blading is another technique to create working electrodes and was trialed in the initial phase of our work. It was broadly used in the past, mostly in the case of TiO_2 electrodes. A hole of the desired electrode diameter was made on adhesive tape. The adhesive tape was put on top of an FTO plate which has been pre-treated with $\text{Ni}(\text{acac})_2$ or $\text{Ni}(\text{OAc})_2$. Then, a strip of NiO paste was placed it on the top of the formed hole (Fig. 3.6) and with the help of a glass rod it was spread, in one move and homogeneously on the hole of the adhesive tape. Then the adhesive tape was removed leaving the

formed electrode. The FTO was placed in an ethanol chamber for 3min and then on a heating plate for 6min. This on cycle counted, for one layer of NiO. In order to tune the thickness of the NiO electrode single or multiple layers of adhesive tape were used. This technique was less reproducible than the screen printing previously explained.

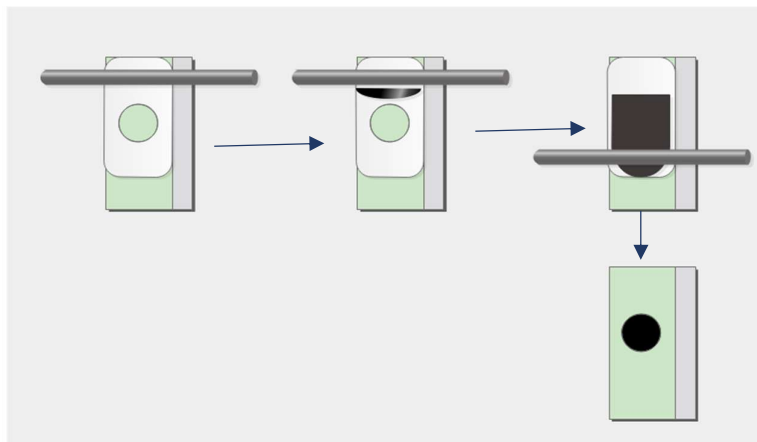


Fig. 3.6: Doctor Blading procedure, showing FTO glass with Ni(acac)₂ or Ni(OAc)₂ pre-layer (green), tape with hole (white) and paste (black) applied with glass rod

3.3.4 Sintering

The sintering process is the final step during the fabrication of the electrodes. Literature ⁵² agrees that a temperature of 300 °C or higher should be applied to the NiO electrodes in order to decompose the organic ingredients of the paste (e.g.: ethylene cellulose, terpineol, ethanol), to boost the adhesion of the NiO nanoparticles with each other and with the FTO glass. The choice of the right temperature is related with the final porosity that the nanoparticulate layers on the electrode gains. During the work of *Cahoon and co-workers* ⁵⁸ extensive research was done regarding the sintering process of the NiO electrodes. The NiO paste used during this experiment was composed of Ni(OH)₂ mixed with α -terpineol and ethylene cellulose which share the same characteristics with the commercially available (Ni-Nanoxide N/SP, Solaronix) paste used in our lab. Their investigation concerns the influence of the sintering temperatures between 100-600 °C on the morphology of the NiO paste which was examined by powder XRD measurements. They found that by increasing the sintering temperature there was an increase in the crystallite size of the nanoparticles from 9-15 nm at 140 to 250 °C and from 18 - 25nm from 500 to 600 °C. Moreover, during those temperature variations, a colour change was observed from bright green for Ni(OH)₂ to black and then to light grey. Between the temperatures of 350 to 450 °C, a decrease in surface area was observed, as the temperature was increased which was coupled with a 4-fold decrease in dye loading. At a temperature of 550 °C the stability of the NiO become

worse and sintering above 600 °C lead to a loss of porosity. The best performing electrodes were the ones sintered at 400 and 450 °C.

During this present study, different sintering temperatures based on the literature values, were used in order to monitor and optimize the fabrication of the NiO electrode. In Fig. 3.7 unsintered NiO

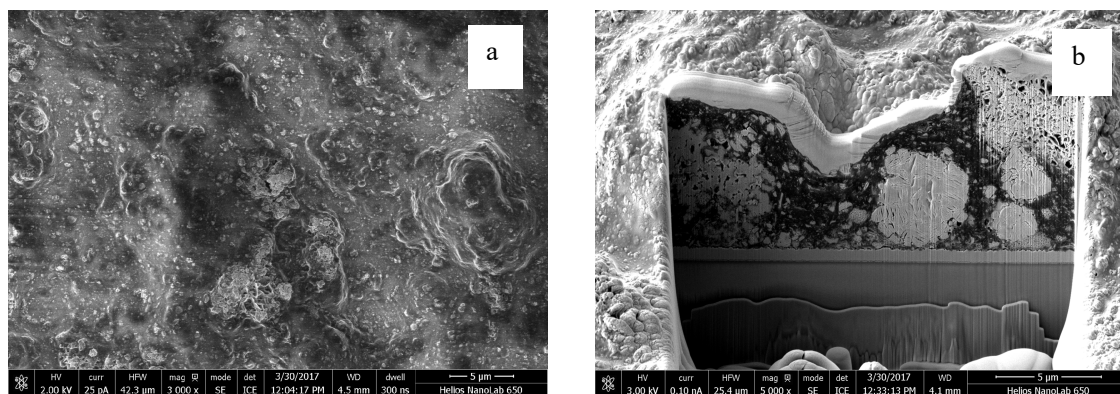


Fig. 3.7: FIB images of unsintered three screen printed NiO layers and Ni(acac)₂ solution in AcCN was used as a pre-layer a platinum layer was sputtered on top of the electrode which functions as a protective layer against the ion beam. **a:** surface image of the electrode. **b:** cross section of the NiO electrode.

electrodes were studied with FIB imaging. The NiO precursor has not been transformed to the desired NiO layer. Moreover, the porosity of the surface is poor which will lead to a poor dye loading. Previous experiments done in our lab, suggested that the optimal sintering temperature for the NiO electrodes, is 300 °C. But a bench marking paper⁷⁵ has shown that the optimal temperature is 350 °C. During the experiments described here, 300, 350 and 450 °C sintering temperatures were used and the results were compared.

FIB images of the surface and of the cross section of the sample were recorded. With this method, we were able to characterize the homogeneity and the porosity of the surface; moreover, the thickness of the semiconductor layer on the electrode was measured. These characteristics are of a great importance for the good performance of the DSSC. Ideally the electrode should be porous in order to achieve a good dye loading and of an optimum thickness of 2 to 4 μm, in order to provide a good capacitance but a low electron resistance and ultimately short charge diffusion. If the semiconductor layer is too thin, this will worsen the short circuit current of the cell, due to a lack in dye loading. Moreover, the recombination of the electrons with the FTO layer is more probable to happen. If the semiconductor layer is too thick, the short circuit current of the cell will be once more negatively affected, this time, because the transport resistance of the working electrode will increase to such extent that the holes injected from the dye to the semiconductor will not be able to reach the back electrode.

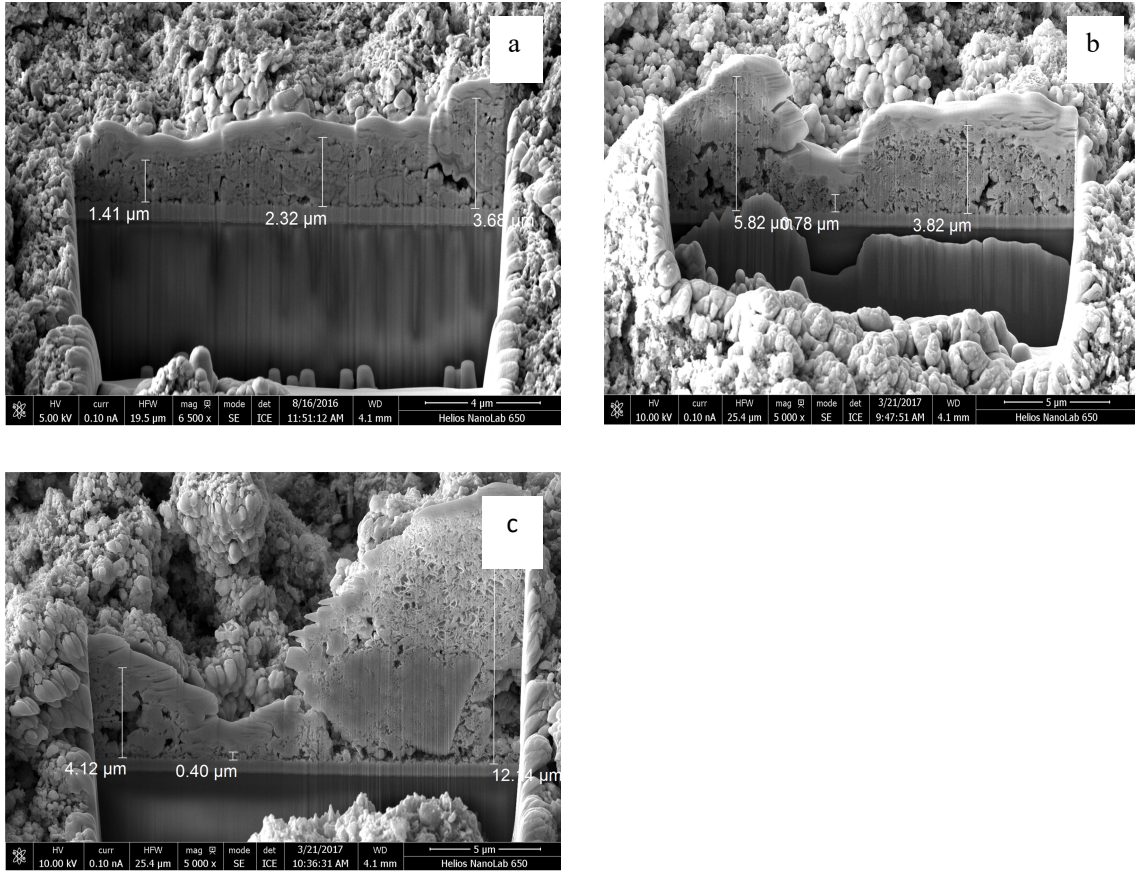


Fig. 3.8: FIB images of two layers screen printed NiO layer and Ni(acac)₂ solution in AcCN was used as a pre-layer a platinum layer was sputtered on top of the electrode which functions as a protective layer against the ion beam. **a:** sintered at 300 °C. **b:** sintered at 350 °C **c:** sintered at 450 °C.

Name	NMA-176	NMA-180	NMA-537
Sintering Temperature of NiO electrode	300 °C	350 °C	450 °C
Pre-layer	Ni(acac) ₂ as pre-layer 5 x dip-coating and air drying		
Electrolyte	0.1 M iodine I ₂ and 1 M lithium iodide LiI in acetonitrile (Stnd III)		
Dye time in the dye solution	P1 (1,2) ^a	P1 (1,2) 16h	P1 (1,2)
Sun Simulator settings	5.3 mV step, reverse scan rate of V, 1 mA range, inverted configuration, settling time of 360 ms		

Table 3.1: Description of experiments NMA-176, NMA-180 and NMA-537. The NiO electrodes were fabricated by screen printed two layers of NiO past at different sintering temperatures.

^a Where P1 (Fig. 3.9) is the sensitizer used and 1,2 signifies the pairs (cell 1 or cell 2) fabricated DSSCs.

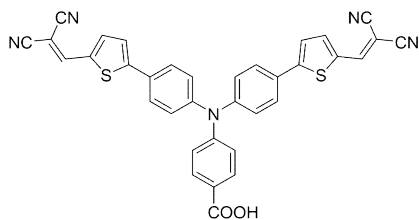


Fig. 3.9: Chemical structure of commercially available organic P1 dye.

Experiment Name	T/ °C	Jsc/ mA cm ⁻²	Voc/mV	FF/%	η/%
NMA-176_1	300	0.53	93	24	0.012
NMA-176_2	300	0.13	104	25	0.003
NMA-180_1	350	1.84	88	35	0.057
NMA-180_2	350	1.96	82	32	0.051
NMA-537_7	450	1.80	109	32	0.063
NMA-536_1	450	1.83	112	32	0.065

Table 3.2: Parameters for the performance of duplicate DSSCs sensitized with P1 dye and with electrolyte comprising of 0.1 M iodine and 1 M lithium iodide in acetonitrile (Stnd III) and surface area of 0.237 cm².

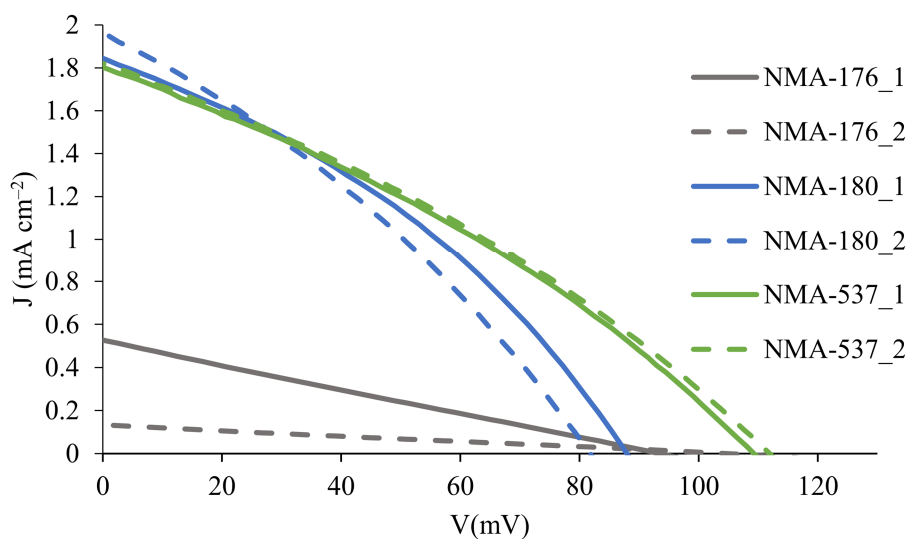


Fig. 3.10: JV curves for duplicate DSSCs with NiO working electrode sintered at different temperatures and electrolyte comprising of 0.1 M iodine and 1 M lithium iodide in acetonitrile (Stnd III) and surface area of 0.237 cm².

From Table 3.2 and Fig. 3.10, it is observed that the best performing DSSCs are the ones with the NiO working electrode sintered at 450 °C. The electrode sintered at 350 °C (NMA-180_1, 2) had a small

increase of J_{SC} compared with the one at 450 °C (NMA-536_1, 2) but a worse V_{OC} which in total worsen their efficiency. The worst performing cells of this series were the ones sintered at the lower temperature of 300 °C (NMA-176_1,2). This can be explained by the lack of porosity of the electrodes sintered at 300 °C as seen in Fig. 3.8a. Instead, electrodes sintered at 350 °C are shown to be more porous and similarly for electrodes sintered at 450 °C which are thicker ($\leq 12.14\mu\text{m}$ at the highest point, Fig. 3.8c). The J_{SC} observed for NMA-536_1 cell, is due to a higher dye loading but the higher thickness of this NiO electrode will lead to a higher diffusion length for the charge, which will ultimately result in lower charge collection. On the other hand, electrodes sintered at 350 °C, have a thickness of $\leq 5.82\mu\text{m}$ at their higher point and exhibit a higher J_{sc} which suggest a better balancing between a good dye loading and the moderate charge diffusion length.

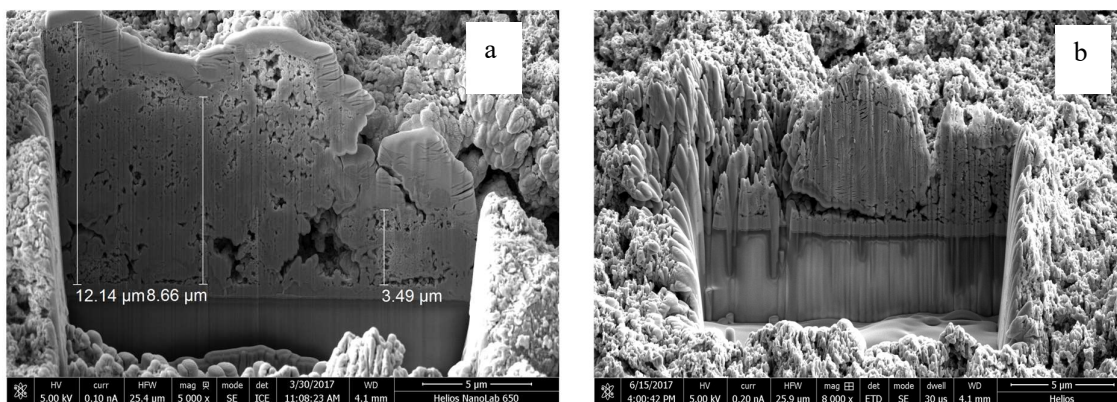


Fig. 3.11: FIB images of three screen printed NiO layers and Ni(acac)₂ solution in AcCN was used as a pre-layer a platinum layer was sputtered on top of the electrode which functions as a protective layer against the ion beam. **a:** sintered at 350 °C. **b:** sintered at 450 °C.

As seen from Fig. 3.11, three screen printed layers of NiO sintered at 350 °C and 450 °C temperature were also fabricated. The porosity of the layers was worse than the electrodes with two layers. The electrode sintered at 350 °C appeared to be more homogeneous, but with a thicker continuous NiO layer that exceed the optimum thickness of 2 to 4 μm .

3.3.5 Different layers of NiO

As it was mentioned earlier, the thickness of the NiO layer plays an important role in the performance of the DSSC. In order to assess the different number of screen printing NiO layers on the performance of the DSSC, one and two screen printing layers of NiO electrodes were fabricated, using different sintering temperatures, FIB images were taken and the solar cells were fabricated out of those working electrodes and measured under the sun simulator to report their efficiency.

3.3.6 Screen printed NiO with different drop casting pre-layer treatment at different sintering temperatures

From Fig. 3.12 it is clear that the thickness of the NiO increased by increasing the screen-printing layers. All surfaces (Fig. 3.12a, b, c) appeared to be porous; moreover, the NiO formed a continuous layer without cracks. This is important in order to prevent electron recombination in a working cell. The thickness of the electrode for one-layer screen printed NiO at a sintering temperature of 300 °C was 1.77 μm at the maximum measured point (Fig. 3.12a), and 6.43 μm for the electrode sintered at 350 °C (Fig. 3.12b) but as seen in the FIB images the thickness varies across the cross section.

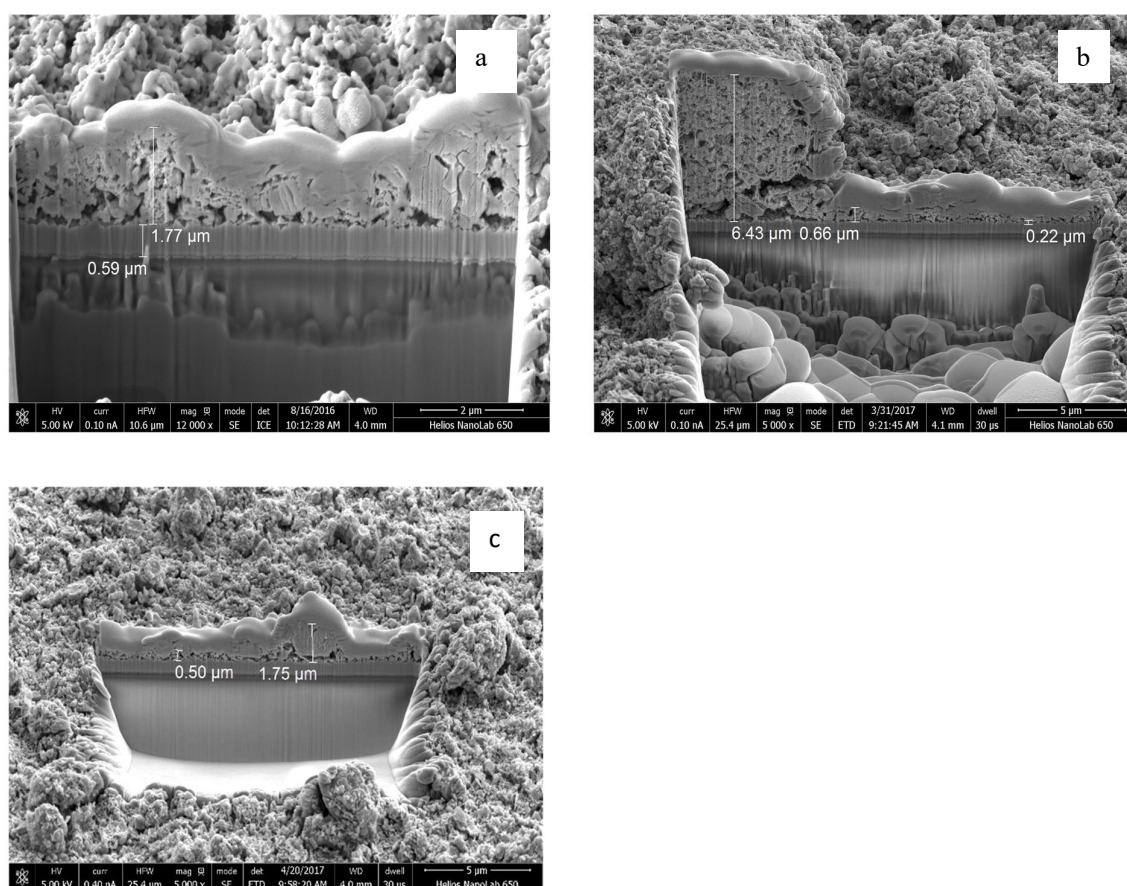


Fig. 3.12: FIB images of one-layer screen printed NiO paste and Ni(acac)₂ solution in AcCN was used as a pre-layer a platinum layer was sputtered on top of the electrode which functions as a protective layer against the ion beam. **a:** sintered at 300 °C. **b:** sintered at 350 °C. **c:** sintered at 450 °C.

For two layers screen printed NiO paste, the thickness of the NiO electrodes for 300 and 350 °C sintering temperature were 3.66 and 5.66 μm respectively, (Fig. 3.8a, b) which according to the

literature ⁷¹ is the optimum thickness. In the FIB images, the pre-layer was not observed, because after the sintering of the electrode, the Ni(acac)₂ was thermally transformed into NiO. The compact layer that was detected under the NiO layer, with a thickness of 0.59 μm (Fig. 3.12a) is the FTO substrate.

In order to better assess the difference between one or two screen printed layers of NiO paste, DSSC were fabricated with one screen printing layer of NiO at two different sintering temperature, 300 °C and 350 °C and their efficiencies were compared with DSSCs using two screen printed layers of NiO.

Name	NMA-174	NMA-178	CM ^a
Sintering Temperature of NiO electrode	300 °C	350 °C	450 °C
Pre-layer	Ni(acac) ₂ as pre-layer 5xdip-coating and air drying		
Electrolyte	0.1 M iodine I ₂ and 1 M lithium iodide LiI in acetonitrile (Std III)		
Dye	P1 (1,2)	P1 (1,2)	P1 (1,2)
time in the dye solution	16h		
Sun Simulator settings	5.3 mV step, reverse scan rate of V, 1 mA range, inverted configuration, settling time of 360 ms		

Table 3.3: description of experiments NMA-174, NMA-178 and CM1 (P1 dye see Fig. 3.9). The NiO electrodes were fabricated by screen printed one layer of NiO past at different sintering temperatures.

^a The DSSC CM_1,2 were fabricated by Camilla Vael-Garn during her Masters internship.

Experiment Name	J _{sc} /mA cm ⁻²	V _{oc} /mV	FF/%	η/%
NMA-174_1	1.55	99	32	0.049
NMA-174_2	1.35	98	33	0.044
NMA-178_1	1.54	91	35	0.049
NMA-178_2	1.26	95	35	0.042
CM_1	1.45	107	33	0.051
CM_2	1.47	100	32	0.047

Table 3.4: Parameters for the performance of duplicate DSSCs sensitized with P1 dye and with electrolyte comprising of 0.1 M iodide and 1 M lithium iodide in acetonitrile (Std III) and surface area of 0.237 cm².

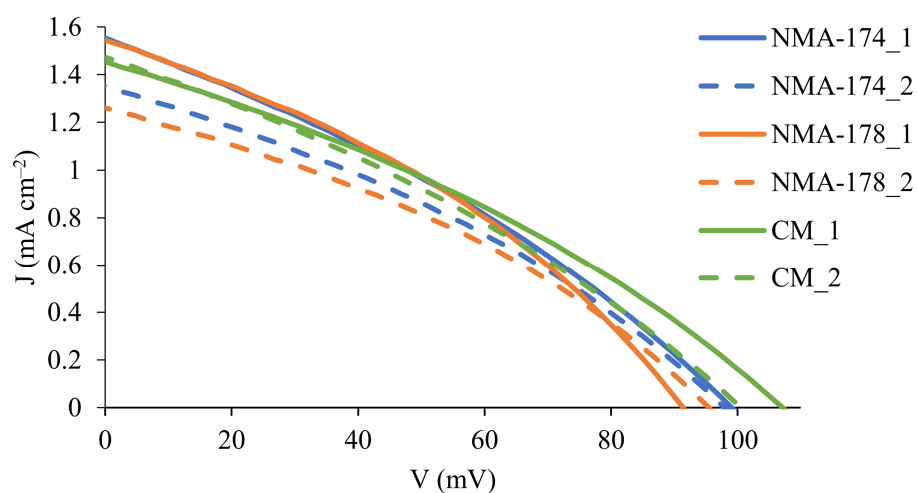


Fig. 3.13: JV curves for duplicate DSSCs with NiO working electrode sintered at different temperatures and electrolyte comprising of 0.1 M iodide and 1 M lithium iodide in acetonitrile (Std III) and surface area of 0.237 cm²

The DSSC sintered at 300 °C with one screen printed NiO layer exhibit a higher efficiency due to a higher J_{sc} compared with the one with two screen-printed NiO layers (NMA-176_1,2, Table 3.2 and 3.3, Fig. 3.10 and 3.13). Is not the case for the cell NMA-180 with two screen printed NiO layer and

the cell NMA-178 with one screen printed layer (sintered both at 350 °C) for which the thicker electrode has a higher efficiency of $\eta = 0.057\%$ compared to 0.049% due to a higher J_{SC} of 1.96 mA cm^{-2} compared with 1.54 mA cm^{-2} . For the solar cells CM_1,2 sintered at 450 °C it is observed that the thicker electrodes performs better ($\eta = 0.065\%$ compare to 0.051% for NMA-536_1 and CM_1 respectively) due to an increase of the J_{SC} , (1.83 compare to 1.45 mA cm^{-2}). The difference between the efficiency of the solar cells with one layer of NiO at three different sintering temperatures is small, there is only a small increase at the porosity of the electrodes sintered at higher temperature as seen in Fig. 3.12.

After comparing Fig. 3.8a and b, it was observed that when the electrode was sintered at 450 °C, the porosity of the NiO increased. But, the Ni(OAc)_2 solution in AcCN, used as a pre-layer in the electrodes shown in Fig. 3.12, lead to poor electrodes. Due, to the crystals of Ni(OAc)_2 formed (observed in Fig. 3.2a) the NiO could not adhere properly to the substrate, and as a consequence the NiO peeled off. After taking those facts under consideration, Ni(acac)_2 was chosen to be the optimum pre-layer and was used for the experiments to come.

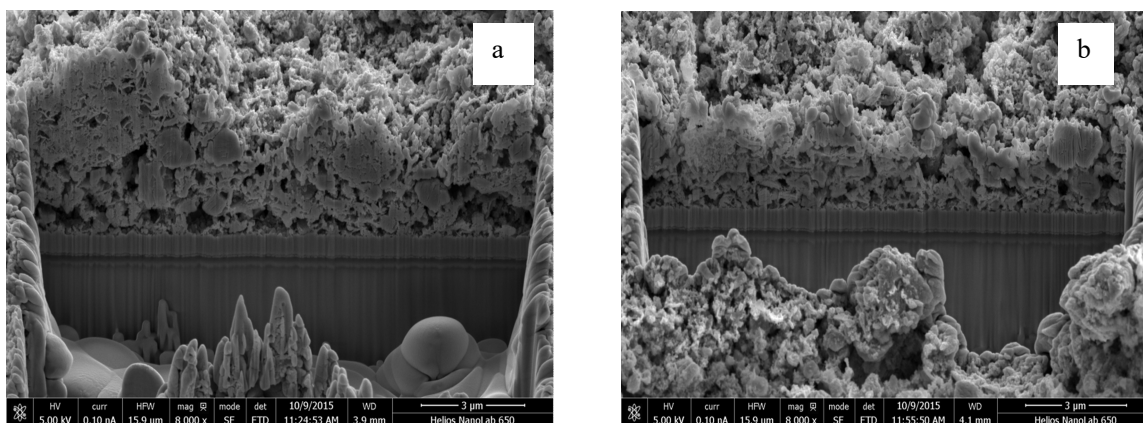


Fig. 3.14 a: FIB image of one layer of NiO, applied with doctor-blading technique, Ni(acac)_2 solution in AcCN as a pre-layer and sintered at 300 °C. **b:** FIB image of two layers of NiO, applied with doctor-blading technique, Ni(acac)_2 solution in AcCN as a pre-layer and sintered at 300 °C.

In Fig. 3.14 FIB images of NiO applied with a doctor blading technique are presented. As expected, the electrode with two doctor blading layers was thicker than the one, with one layer applied. That led to the conclusion, that tuning the thickness of the NiO with the doctor blading technique was more challenging. Overall, screen printing was chosen as the best technique for the fabrication of the NiO electrodes. The DSSCs which have a two-layer screen printed NiO electrode, performed better and the sintering temperature that was chosen as the most optimum was 450 °C.

3.3.7 Screen printed NiO with different spin coating pre-layer treatment and post-treatment after screen printing.

A recent study by *Odobel and co-workers*⁵⁴, reported an increase in the photocurrent ($J_{SC} = 4.76 \text{ mA cm}^{-2}$) of a DSSC sensitized with a commercial P1 dye, and an I^-/I_3^- redox couple in the electrolyte, and a NiO photocathode with some modifications compared to the above-mentioned preparations. As a pre-layer a nickel (II) acetate solution in methoxy ethanol and ethanolamine was spin coated onto an FTO substrate (Fig. 3.4). Then the sample was sintered at 500 °C for 30 min. A NiO paste was screen printed to produce two layers, as was described in section 3.4 and sintered at 450 °C for another 30 min. A final post treatment of the NiO photocathode was done by soaking the electrodes in a nickel (II) acetate solution in ethanol for 30 min at 60 °C. In order to investigate this new method, the amount of spin coating solution was varied and electrodes with and without pre-treatment were prepared. For each spin coating round, 1 ml of solution was used on a clean (see section 3.11.1) FTO substrate (7.5 x 8 cm), the FTO was then spin coated for 1 min. That was done once or five times as shown in Table 3.5. DSSCs were prepared with the same commercial P1 dye used in the publication of *Odobel*⁵⁴ (Fig. 3.9) and FIB images were taken.

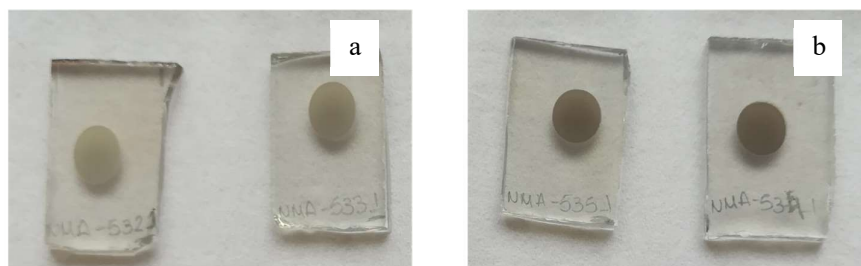


Fig. 3.15: **a:** Electrodes NMA-532 and NMA-533 (from left to right) with post-treatment **b:** electrodes NMA-535 and NMA-534 (from left to right) without post-treatment

Name	NMA-532	NMA-533	NMA-534	MNA-535	NMA-537
Pre-layer	Ni(OAc) ₂ as pre-layer 1xspin coating with post-treatment Ni(OAc) ₂	Ni(OAc) ₂ as pre-layer 5xspin coating with post-treatment of Ni(OAc) ₂	Ni(OAc) ₂ as pre-layer 1xspin coating without post-treatment of Ni(OAc) ₂	Ni(OAc) ₂ as pre-layer 5xspin coating without post-treatment of Ni(OAc) ₂	Ni(acac) ₂ as pre-layer 5xdip-coating and air drying
Electrolyte	0.1M iodine I ₂ and 1M lithium iodide LiI in acetonitrile (Stnd III)				
Dye	P1 (1,2)	P1 (1,2)	P1 (1,2)	P1 (1,2)	P1 (1,2)
time in the dye solution	16h				
Sun Simulator settings	1.5 mV step, reverse scan rate of V, 1 mA range, inverted configuration, settling time of 360 ms				

Table 3.5: Description of experiments NMA-532 to NMA-535 and NMA-537. The NiO electrodes were fabricated by screen printing two layers of NiO paste at a sintering temperature of 450 °C.

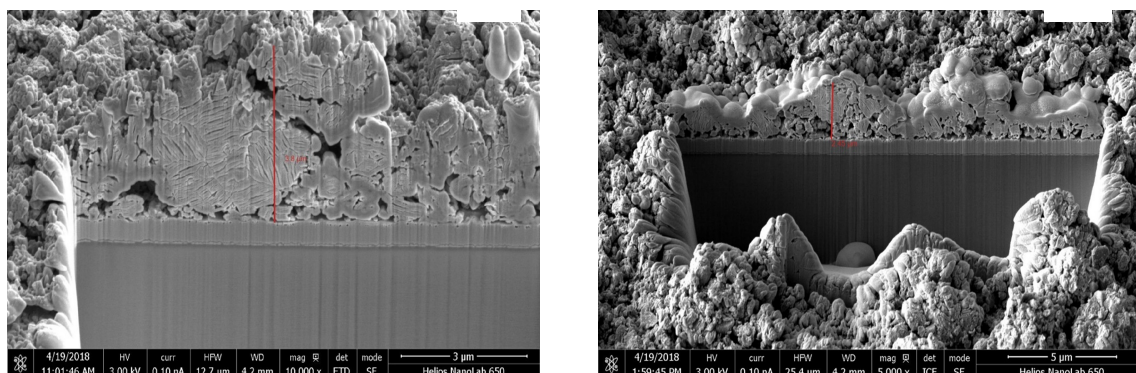


Fig. 3.16: **a**: FIB image of NMA-533 electrode with post-treatment **b**: FIB image of NMA-535 electrode without post-treatment, a platinum layer was sputtered on top of the electrode which functions as a protective layer against the ion beam.

In Fig. 3.15 electrode with and without post-treatment are shown. An obvious optical difference between Fig. 3.15a and b can be detected. From the FIB images in Fig. 3.16 for the electrode with

(NMA-533) and without (NMA-535) post-treatment there is no obvious difference concerning the thickness of the NiO layer (3.8 μm thickness for NMA-533 and 2.45 μm for NMA-535).

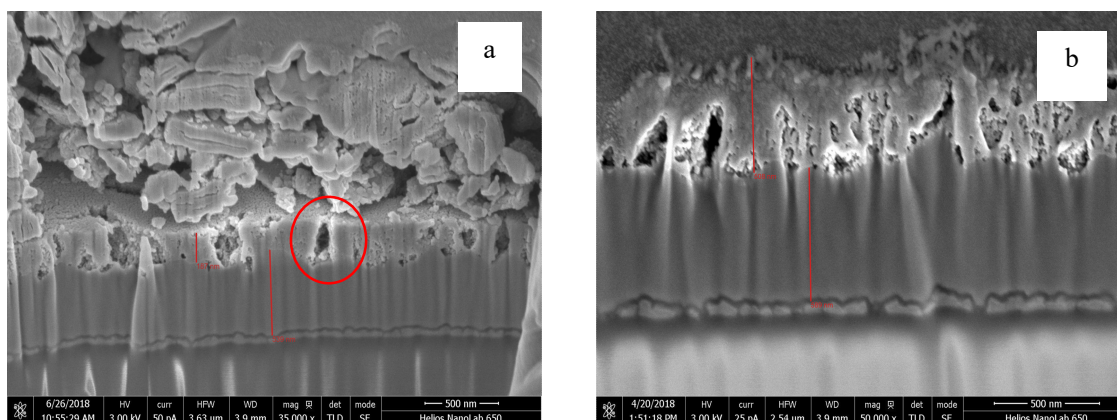


Fig. 3.17: a: FIB image in immersion mode of NMA-532 electrode with 1 x spin coating pre-layer of nickel (II) acetate **b:** FIB image of NMA-533 5 x spin coating pre-layer of nickel (II) acetate.

From Fig. 3.17, the immersion mode FIB images of the pre-layer are shown that the electrode with 5 x spin coating nickel (II) acetate pre-layer has a thickness of 508 nm and the electrode with the 1 x spin coating has a thickness of 187 nm. On the sample with 1x spin coating pre-layer, cracks can be observed until the FTO substrate (red circle in Fig. 3.17a). On the sample with the 5 x spin coating pre-layer, a compact layer of NiO from the pre-layer can be observed, which may prevent the recombination of the electrons with the FTO and consequently improved the performance of the DSSC by increased J_{SC} . That was proven from the performance of the DSSC. For the cell fabricated with the electrode NMA-533 the J_{SC} reached 1.87 mA cm^{-2} (Table 3.6 and Fig. 3.18). The cells fabricated with only one spin coating pre-layer reached a $J_{SC} = 1.21 \text{ mA cm}^{-2}$ which is considerably lower and supports the theory of recombination of the charge with the FTO substrate due to the cracks observed at the NiO pre-layer (Fig. 3.17). The cells fabricate from electrode NMA-534 (with 1 spin coating pre-layer and no post treatment) exhibited a $J_{SC} = 1.79 \text{ mA cm}^{-2}$ which is higher compare with the cells fabricated from the NiO electrode with the same amount of pre-layer but with post-treatment (NMA-532). Same for the cells with NMA-535 electrode that exhibit a $J_{SC} = 2.02 \text{ mA cm}^{-2}$ (compared to NMA-533).

In conclusion the high value of J_{SC} that *Odobel*⁵⁴ reported at his study was not reached but an improvement of the general efficiency of the DSSC by using 5 X spin coating nickel (II) acetate as a pre-layer was obtained. Moreover, the use of a post-treatment on the electrodes lead to a small decree of the J_{SC} of the DSSC.

Experiment Name	Jsc/mA cm ⁻²	Voc/mV	FF/%	η/%
NMA-532_1	1.21	130	32	0.051
NMA-532_2	1.36	122	32	0.053
NMA-533_1	1.80	128	33	0.076
NMA-533-2	1.87	130	32	0.078
NMA-534_1	1.73	117	33	0.066
NMA-534_2	1.79	111	32	0.063
NMA-535_1	2.02	108	32	0.070
NMA-535_2	1.79	111	32	0.063
NMA-537_3	1.90	117	33	0.072

Table 3.6: Parameters for the performance of duplicate DSSCs sensitized with P1 dye and with electrolyte comprising of 0.1M iodine and 1M lithium iodide in acetonitrile (Std III) and surface area of 0.237 cm².

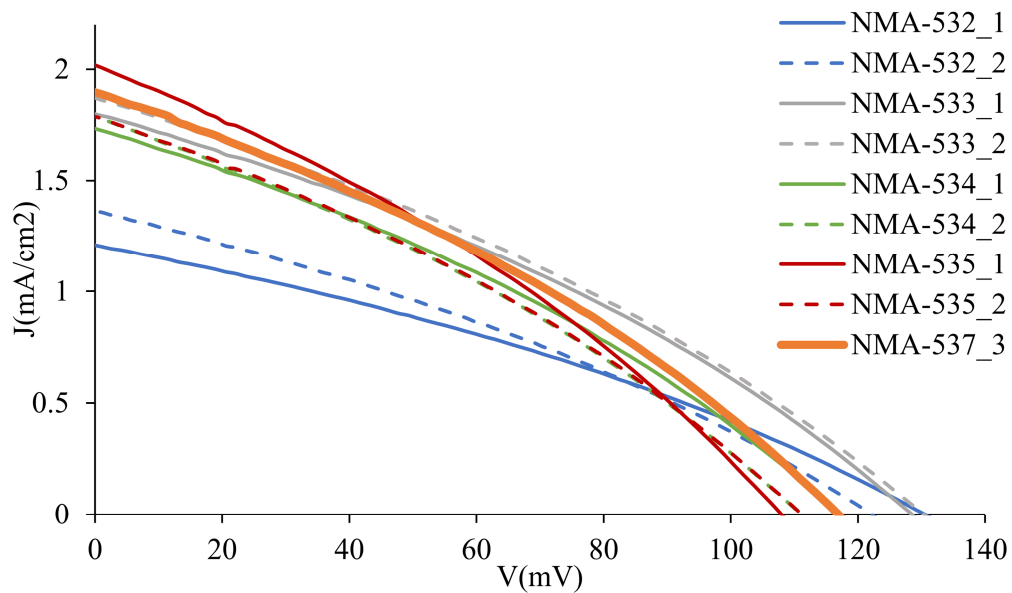


Fig. 3.18: JV curves for the duplicate DSSCs fabricated with the working NiO electrode for table 3.5.

3.3.8 Conclusion

The conclusion of the trials for optimisation of the NiO were as follows, Ni(acac)₂ was chosen as the most optimum pre-treatment with the dip coating method. The homogeneity shown in Fig. 3.2a was good and the NiO paste demonstrated a better adhesion when this pre-treatment was used. The fabrication of NiO electrodes was not a straight forward procedure. The paste was quite viscous, making the reproducibility of the thickness challenging. During the screen-printing technique, the two and three layers of NiO were of a thickness of 2 to 5 μm, which approaches the optimum values in bench marking papers^{71, 53, 76} (2-4 μm). This thickness provides an optimum diffusion length of the injected hole which ultimately will minimize recombination and consequently. On the other hand, when using a doctor blading technique, tuning the thickness of the NiO layers was more challenging, and this method was therefore not used beyond preliminary trials. Additionally, it was concluded that the best sintering temperature was 450 °C, led to a better porosity. However as seen in section 3.6.2, we also used sintering temperature of 350° C in early work. The method suggested by *Odobel*⁵⁴, gave good results in terms of DSSC efficiency and was used for some experiments.

3.4 Li⁺ doping of the NiO

3.4.1 Background

During the initial investigation of optimizing the semiconductor layers, we also investigate the doping of the NiO bulk layer. As was previously mentioned, an important characteristic of the p-type semiconductor is the valence band level (Fig. 3.1) because the difference in energy between the valence band and the redox potential of the redox species in the electrolyte gives the open circuit voltage. By doping the NiO, one can shift the valence band towards more positive potential (vs. NHE) and this will increase the open circuit voltage and, as a consequence, the efficiency of the device. In the introduction part of this chapter, the low mobility of charge in the NiO was already discussed. To overcome this problem, a dopant can be used. This should have a closed shell whose energy is almost comparable to those of the 2p levels of oxide anions³⁶. A good p-dopant will generate an electron deficit, by contributing fewer electrons to the valence band so in consequence creating holes. Lithium cations fulfil these requirements, by creating electron vacancies at the O2p closed orbital, and ultimately shifting the valence band of the semiconductor toward more positive values. *Li and co-workers*⁴³ have shown that by doping the NiO bulk semiconductor with Li⁺, a higher charge carrier density, a shift of the valence band to more positive energy and a narrowing of the trap energy distribution is observed. *Hammarström and co-workers*⁴² confirmed the narrowing trap energy distribution using cyclic voltammetry and electrochemical impedance spectroscopy (EIS) measurements. Moreover, during their work they investigated the difference between the contribution of the Li⁺ in the bulk material of the electrode and the Li⁺ present as a counter ion in the electrolyte,

and concluded that the beneficial effect of the Li^+ doping, mentioned above, comes from the cation inside the bulk material of the semiconductor.

3.4.2 Effects of Li^+ doping on DSSC performance

As discussed earlier, the concentration of the dopant should be optimized in order to gain the beneficial effect of the doping material but avoid the scattering points created in the lattice, which will perturb the hopping mechanism of the holes. Thus, two different concentrations of Li^+ were tested (0.1 and 1% of Li^+ see section 3.11.5).

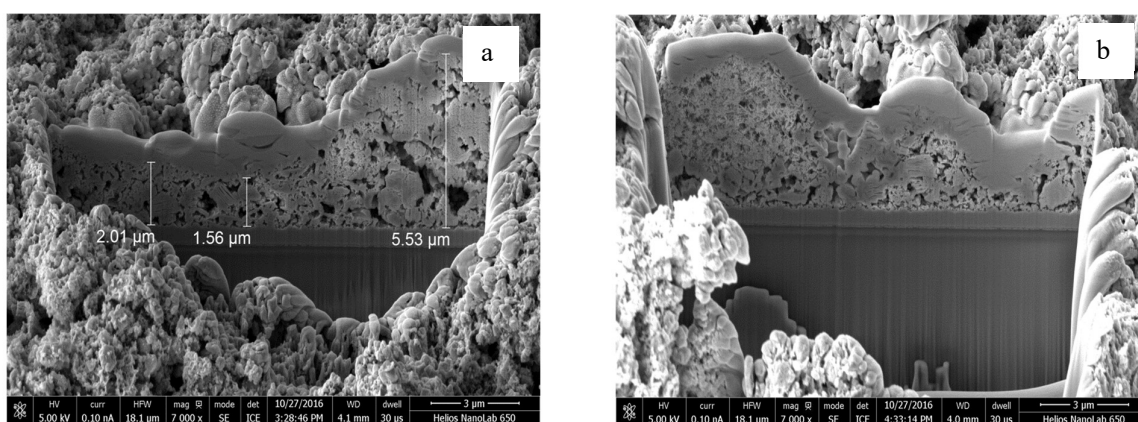


Fig. 3.19: FIB images of screen printed NiO layer. A platinum layer was sputtered on top of the electrode which functions as a protective layer against the ion beam. **a:** layers with 0.1% Li doped screen printed NiO electrode, $\text{Ni}(\text{acac})_2$ solution in AcCN was used as a pre-layer and it was sintered at 350 °C **b:** three layers with 0.1% Li doped screen printed NiO electrode, $\text{Ni}(\text{acac})_2$ solution in AcCN was used as a pre-layer and it was sintered at 450 °C

As can be seen in Fig. 3.19a, the NiO layer has a good porosity and the thickness of the layer is 2-5 μm, which agrees with the previous results. Moreover, a different coloration was observed which is assumed to be due to the Li^+ doping. After comparing the electrodes sintered at 350 °C and 450 °C, a small enhancement of the porosity when sintered at 450 °C was observed.

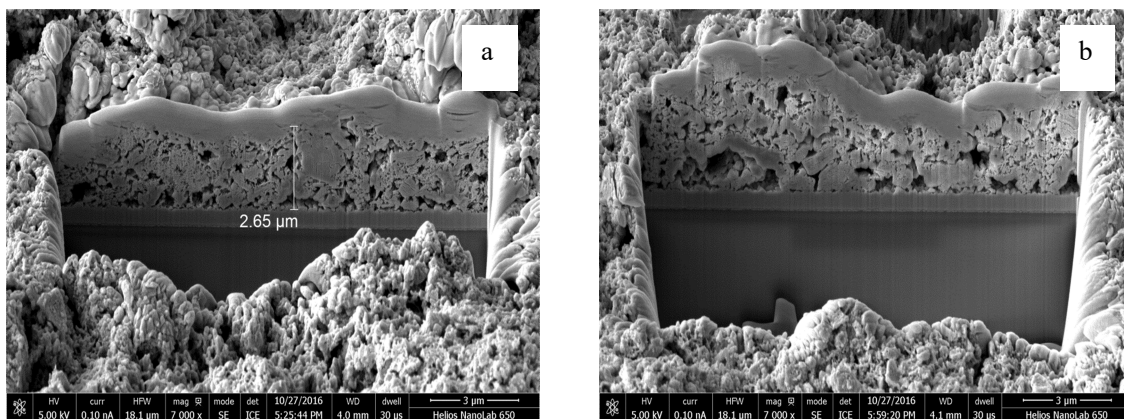


Fig. 3.20: FIB images of screen printed NiO layer, a platinum layer was sputtered on top of the electrode which functions as a protective layer against the ion beam. **a:** three layers with 1% Li doped screen printed NiO electrode, Ni(acac)₂ solution in AcCN was used as a pre-layer and it was sintered at 350 °C **b:** three layers with 1% Li doped screen printed NiO electrode, Ni(acac)₂ solution in AcCN was used as a pre-layer and it was sintered at 450 °C.

In Fig. 3.20, FIB images of the 1% Li⁺ doped NiO is presented. Once more a different coloration was observed which indicates the presence of Li⁺ doping and the porosity is more pronounced in the sample sintered at 450 °C as mentioned above.

In order to gain an understanding about the effect of the Li⁺ doping in the performance of the cell, sun simulation measurements were made. The DSSCs fabricated are described in Table 3.7. The dye used as a sensitizer of the NiO electrode is a ruthenium(II) cyclometallated dye (Fig. 3.21) and the synthesis of this dye is described in section 4.3.1.

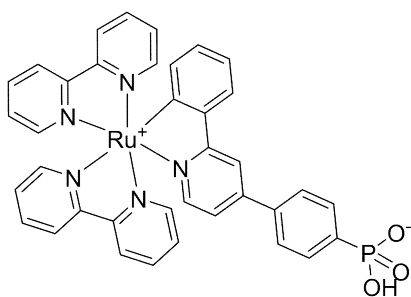


Fig. 3.21: Chemical structure of dye WOC53. The synthesis of WOC53 is described in section 4.3.1.

Name	NMA-215	NMA-217	NMA-385
Sintering time	450 °C	450 °C	450 °C
% of Li ⁺ Doping	1% mol	0.1% mol	0
Electrolyte	0.03M iodine I ₂ , 0.6M tetrabutylammonium iodide (TBAI), 0.1M guanidinium thiocyanate (GuSCN) and 0.5M 4-tert-butylpyridine (4-TBP) in acetonitrile (Stnd IV)		
Dye	WOC53 (1,2)	WOC53 (1,2)	WOC53 (1,2)
time in the dye solution	16h		
Sum Simulator settings	5.3 mV step, reverse scan rate of V, 1 mA range, inverted configuration, settling time of 360 ms		

Table 3.7: Description of experiments NMA-214 to NMA-217 and NMA-385. The NiO electrodes were fabricated by screen printing two layers of NiO at a sintering temperature of 450 °C.

Experiment Name	J_{sc}/mA cm⁻²	V_{oc}/mV	FF/%	η/%
NMA-215_1	1.14	111	30	0.038
NMA-215_2	0.77	103	29	0.023
NMA-217_1	1.79	108	32	0.062
NMA-217_2	2.46	104	33	0.083
NMA-385_1	0.78	128	34	0.034
NMA-385_2	0.63	119	36	0.027

Table 3.8: Parameters for the performance of duplicate DSSCs sensitized with WOC53 dye and with electrolyte comprising of 0.03 M iodine, 0.6M tetrabutylammonium iodide, 0.1M guanidinium thiocyanate and 0.5M 4-tert-butylpyridine in AcCN (Stnd IV) and surface area of 0.237 cm².

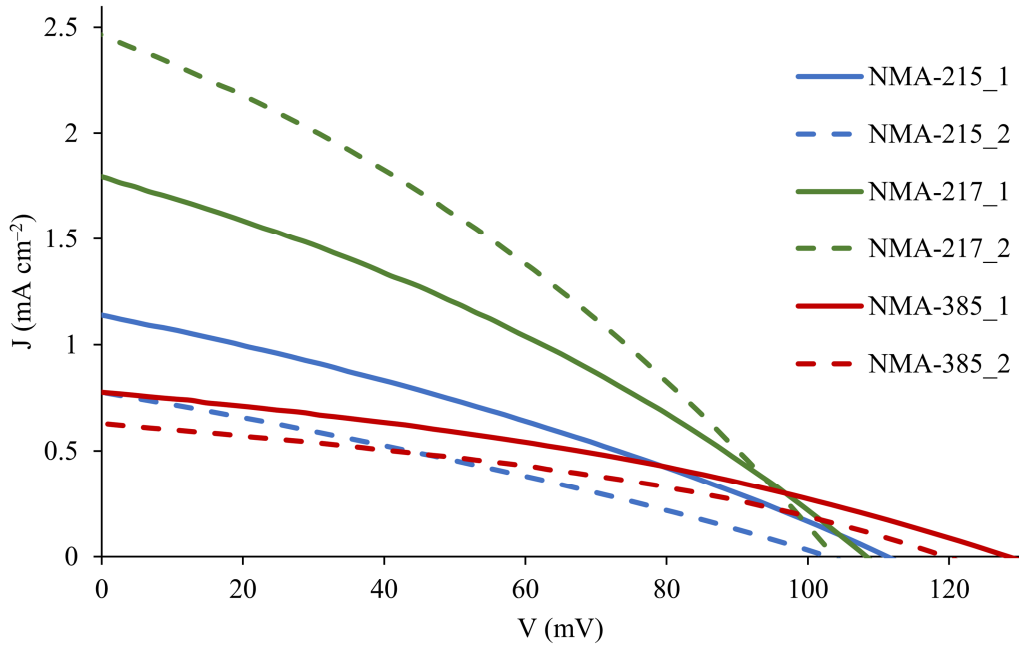


Fig. 3.22: JV curves for the duplicate DSSCs fabricated with the working NiO electrode from Table 3.7

From Table 3.8 and Fig. 3.22, it is observed that the cells fabricated with NiO electrode doped with 0.1% Li^+ were the best performed in terms of efficiency. The short circuit of the best performing DSSC among the two duplicate cells of NMA-217_1 exhibit a remarkable value of 2.46 mA cm^{-2} , the J_{SC} of NMA-217_2 cell is also high with a value of 1.79 mA cm^{-2} compare to the DSSC with no doping NMA-385_1 ($J_{\text{SC}} = 0.78 \text{ mA cm}^{-2}$) which suggests a better charge transport on the semiconductor which as a consequence will result in a higher charge carrier density. This could result from either a positive movement of the valence band of the doped semiconductor or due to the narrowing of the trap energy distribution^{8,9}. Since the open circuit voltage between the DSSCs with and without doping (NMA-215 and NMA-385) remains fairly comparable (104 and 128 mV) it could be assumed that the increase in the J_{SC} of the doped NiO it is due to the narrowing of the trap energy distribution.

3.5 Characterisation of the semiconductor by cyclic voltammetry

Cyclic voltammetry (CV) studies, ^{77, 78} made on the NiO electrodes, show the redox process that the Ni^{x+} ions undergo. Also, changes in the colour of the bulk electrode were observed during the CV sweep; the different colour was attributed to the different oxidation state of Ni during the voltage sweep. In NiO, nickel is in oxidation state +2, but higher oxidation states are available to nickel. The first oxidation process seen in the cyclic voltammogram in Fig. 3.23 is assigned to $\text{Ni}^{2+}/\text{Ni}^{3+}$ and the electrode turned from light grey to a darker shade of grey. The second process is further oxidation to Ni^{4+} , ⁷⁹ at 0.7V vs Ag and, the colour of the electrode turned black. Those processes were reversible during reduction over which the electrode gained its initial colour. When electrochemical studies are performed in aqueous solution the first oxidation peak occur at 0.5V vs. Ag and is described in the following equations.

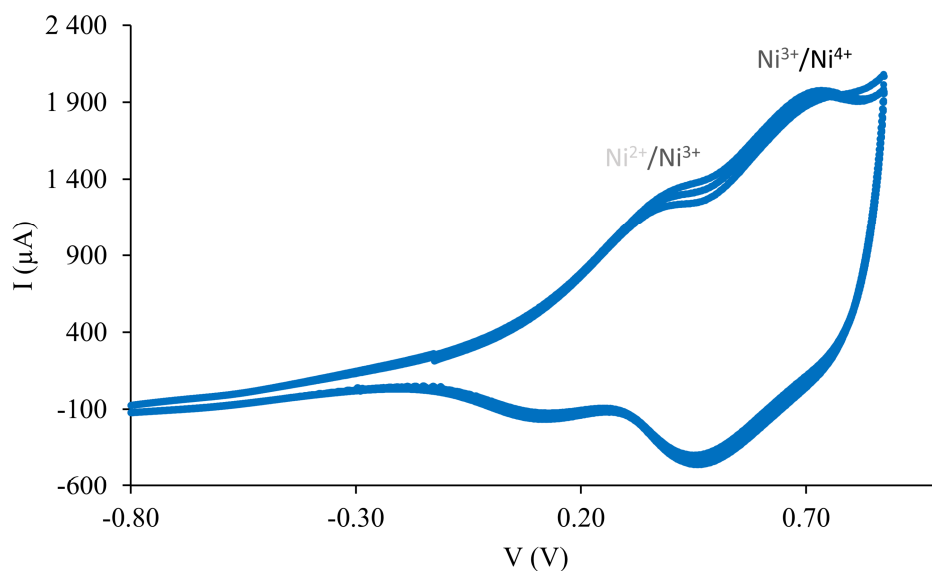
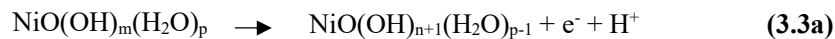
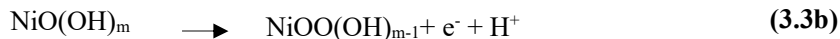


Fig. 3.23: Cyclic voltammetry of three-layer screen printed NiO electrodes, $\text{Ni}(\text{acac})_2$ solution in AcCN as pre-layer sintered at 300 °C, in aqueous solution of 0.2M sodium dihydrogen phosphate mixed with 0.2 M sodium hydrogen phosphate, with 1 M sodium chloride as the supporting electrolyte. The pH was adjusted to 7.

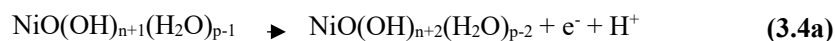
The procedure described in equations 3.3a, b and 3.4a, b takes place to different extents, depending on the hydration of the oxide ⁶².



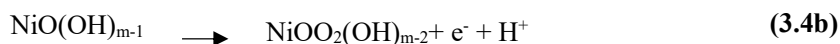
or



The second anodic peak, occurring at 0.7 V vs. Ag can be described as follows;



or



When the electrochemistry studies are performed, in an organic medium in the presence of salts of tetra-tert-butyl ammonium (TBA^+) ion, the redox reactions are as follows ⁷³ for the first oxidation peak:



And for the second oxidation:



In aqueous medium the two-oxidation peaks are carrying higher current than in organic medium.

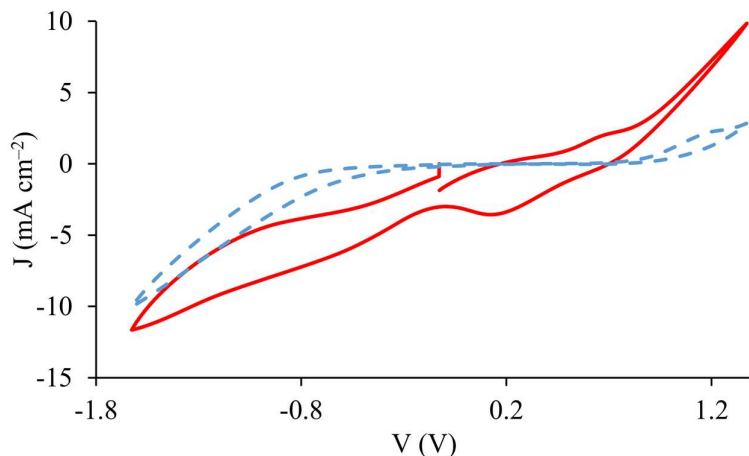


Fig. 3.24: **Solid line:** cyclic voltammetry of three-layer screen printed NiO electrodes, Ni(acac)₂ solution in AcCN as pre-layer sintered at 350 °C in I/I₃⁻ 10 mM 1:1 with TBA as counterion in AvCN. **Dotted line:** FTO coated glass as a control.

As it was observed, from Fig. 3.24 the two oxidations peaks, previously observed in aqueous medium (Fig. 3.23) remained at the same position but in lower intensity.

3.6 Effect of introducing graphene into NiO

3.6.1 Introduction

Graphene is an allotrope of carbon consisted of a single sheet of one atom thickness, when these single sheets of graphene are stacked one on top of the other, they form graphite⁸⁰. Graphene has remarkable properties such as large specific surface area, high transparency and high electrical conductivity^{81, 82, 83}. There have been numerous reports using graphene as a doping material in order to boost the efficiency of a semiconductor by decreasing the transport resistance. *Li and co-workers*⁸⁴ reported the use of a NiO/graphene sheet composite to reduce the transport resistance of the NiO electrode. In fact, by optimizing the concentration of graphene in the precursor solution, they achieved a three-fold increase of the solar cell efficiency due to an increase of the current density as well as of the open circuit voltage. *Zhao and co-workers*⁸⁵ in the n-type DSSC world this time, used TiO₂ and reduced graphene oxide (rGO) as a precursor mixture for the fabrication of TiO₂ electrodes. In order to reduce the graphene to reduced graphene oxide vitamin C was used, which is far less toxic than other reducing agents such as hydrazine or its derivatives. They obtained a 30% increase on the efficiency of the solar cell, due to an increase in the short circuit current and open circuit voltage, which was reflected in the EIS measurements by a decrease of the transport resistance and increase of the capacitance of the semiconductor.

3.6.2 Studies of NiO with graphene added

During this altered research, graphene flakes were used as a doping agent for the NiO semiconductor and concentration was fluctuated (3 and 8% of graphene flakes with respect to the Ni nanoparticles) in order to be optimized. FIB images were taken, in order to detect the presence of the graphene in the paste.

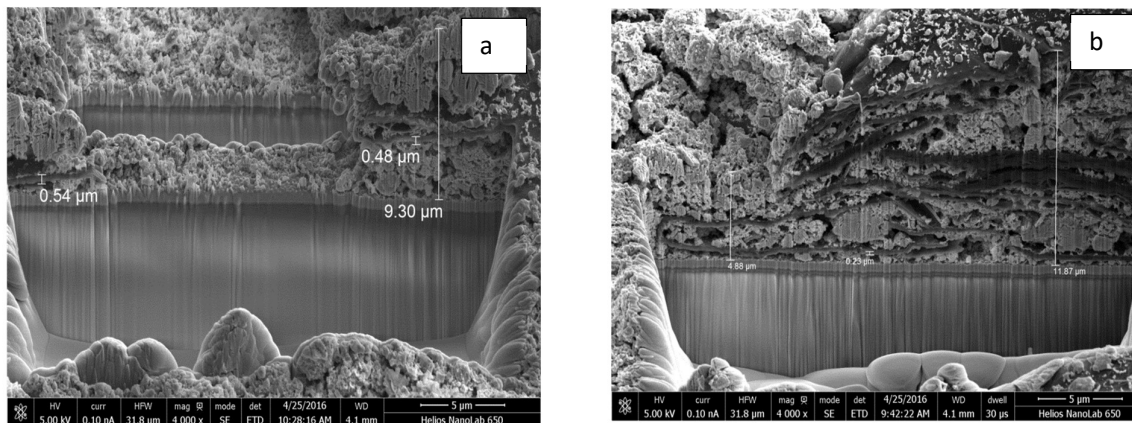


Fig. 3.25 a: FIB image of NiO electrode doped with 3% of graphene **b:** FIB image of NiO electrode doped with 8% of graphene

Fig. 3.25 shows that the graphene present in the NiO paste that forms discrete layered domains. The procedure used for the doping of the NiO is described in section 3.11.7. DSSCs were fabricated in order to evaluate the performance of the electrode. The dye used as a sensitizer of the NiO electrode is commercially available organic dye, P1 (Fig. 3.9).

Name	NMA-86	NMA-95	NMA-96
Graphene doping	No	3%	8%
Electrolyte	0.3M iodine I ₂ , 0.6M 1-butyl-3-methylimidazoliumiodine (BMIMI), 0.1M guanidinium thiocyanate (GuSCN) and 0.5M 4-tert-butylpyridine (4-TBP) in acetonitrile (Stnd I)		
Dye	P1 (1,2)	P1(1,2)	P1 (1,2)
time in the dye solution	16h		
Sum Simulator settings	5.3 mV step, reverse scan rate of V, 1 mA range, inverted configuration, settling time of 360ms		

Table 3.9: Description of experiments NMA-86 to NMA-95 and NMA-96. The NiO electrodes were fabricated by screen printing two layers of NiO past at a sintering temperature of 350 °C.

Experiment Name	Jsc / mA cm⁻²	Voc / mV	FF / %	η / %
NMA-86_1	0.51	91	35	0.017
NMA-86_2	0.59	87	36	0.019
NMA-96_1	0.26	61	35	0.006
NMA-96_2	0.24	59	34	0.005
NMA-95_1	0.26	52	32	0.004
NMA-95_2	0.25	55	32	0.004

Table 3.10: Parameters for the performance of duplicate DSSCs sensitized with P1 dye and with electrolyte comprising of 0.3 M iodine, 0.6 M 1-butyl-3-methylimidazoliumiodine, 0.1 M guanidinium thiocyanate and 0.5 M 4-tert-butylpyridine in acetonitrile (Stnd I) and a masked surface area of 0.06018 cm².

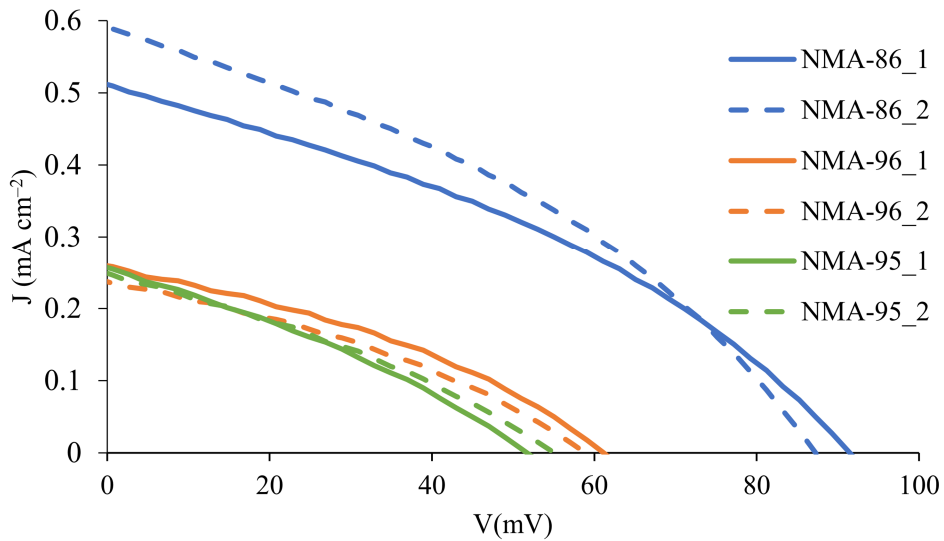


Fig. 3.26: JV curves for the duplicate DSSCs fabricated with the working NiO electrode form Table 3.9

As it can be observed for table 3.10 and Fig. 3.26, the DSSCs fabricated with NiO electrode doped with graphene performed worse ($\eta = 0.006\%$) than the DSSCs with no graphene doping on the NiO electrode ($\eta = 0.019\%$). This is due to both lower J_{sc} and V_{oc} of the NiO electrodes doped with graphene. Between the different amount of graphene doping the DSSC fabricated with the electrode with the higher graphene doping (NMA-96) perform to a small degree better than the one (NMA-95) with a lower graphene doping, due to a higher J_{sc} . In conclusion, the doping with graphene did not bring the expected results, from the performance of the DSSCs described above and from the FIB images (Fig. 3.25) it can be assumed that the domains observed in the images is not graphene but graphite, which in turn will not increase the conductivity but rather deteriorated. Thus, this procedure was abandoned for the following experiments.

3.7 Ambient pressure photoemission spectroscopy (APS) measurements

3.7.1 Introduction

The ambient pressure photoemission spectroscopy (APS) is a method designed for the measurement of the absolute work function (Φ) of a metal sample or the ionization potential of a semiconductor by photoemission in air. The work function is the energy required to free an electron from a metal to vacuum as a free particle. For metals the work function is equal to the ionization energy. In the case of semiconductor material, initially the Fermi level should be localized since it holds, that the Fermi level of a semiconductor is the energy at which the probability of an electronic state being occupied is 0.5 at 0 K and the work function will then be the energy required to subtract an electron from that level to vacuum. For a non-degenerate semiconductor, the Fermi level is located within the band gap as seen in Fig. 3.27 and for a degenerate semiconductor the Fermi level will be located at the edge of the valence band. The ionization energy of a semiconductor is the minimum energy to remove an electron from the HOMO or valence band of the semiconductor to the vacuum level ⁸⁶ (Fig. 3.27). The APS system works in a dual mode coupled with a Kelvin probe. The photoemission in air, is the phenomenon during which an electron is freed from the surface of a material upon an incident light with sufficient energy. This is described as “Photoelectric effect”. In the case of our measurement a UV lamp was used (Fig. 3.29). In order to find the ionization energy, the intensity of the incoming light is modulated ⁸⁷ during this experiment the modulation range was between 3.4 – 7 eV.

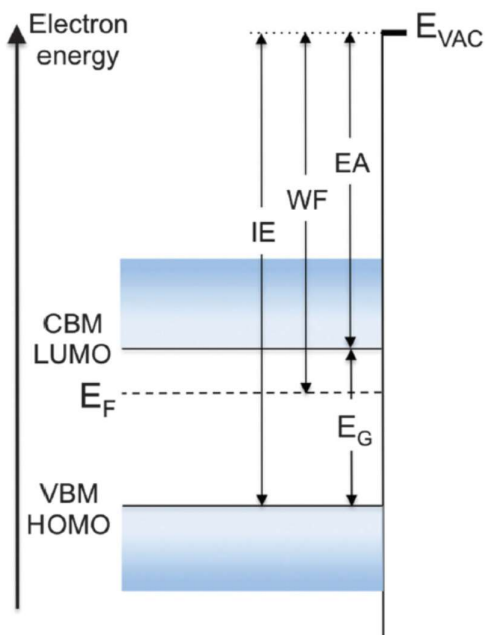


Fig. 3.27: Energy diagram of semiconductor. Band edges conductive band (CBM)/LUMO and valence band (VBM)/HOMO, vacuum level E_{VAC} , work function level WF , energy gap E_G , ionization energy IE and electron affinity EA . Reprinted with permission of *A. Kahn* ⁸⁶, copyright royal society of chemistry, 2016.

The Kelvin Probe (KP) is a non-destructive method that allows the measurement of the work function relative to the probe of a conductor or semiconductor. The setup is made out of a small gold tip (probe) placed on top of the sample and connected to it externally. When a bias is applied to the connector the Fermi level of the tip (E_{fKP}) and the one of the sample (E_{fM}) equalize due to a transfer of electrons from the lower work function conductor resulting in a potential gradient V_{cpd} (contact potential difference) as described in Fig. 3.28. By vibrating the probe, a varying capacitance is produced which causes a current to flow back and forth between the tip and the sample. If an external bias V_b is applied between the sample and the probe, at the unique point when $V_b = -V_{cpd}$ the surface charge is cancelled and null field exists between the probe and the sample. The work function between the probe ($e\Phi_{KP}$) and the one of the sample ($e\Phi_M$) is equal and opposite to the bias V_b , $eV_{cpd} = (E_{fKP} - E_{fM})$ ^{87, 88}.

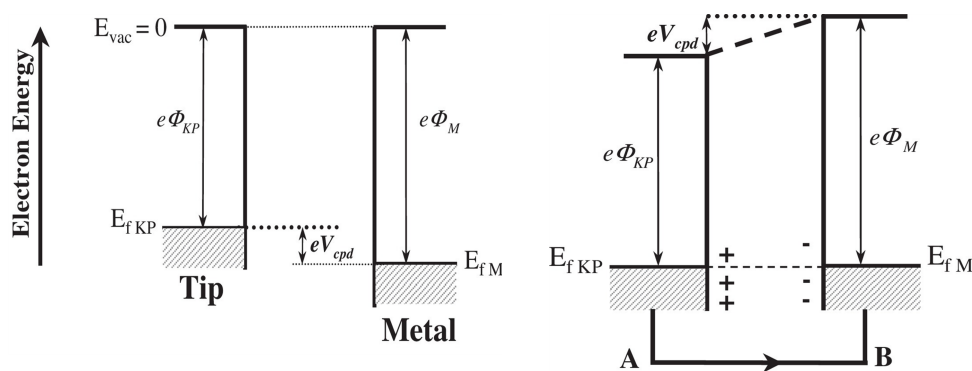


Fig. 3.28: **a:** Electron energy diagram for a metallic Kelvin prob tip, E_{vac} represent the vacuum level. **b:** the equalization of the Fermi level of the tip and the sample upon electrical contact. Reprinted with permission of *I. D. Baikie et al*⁸⁷, copyright royal society of chemistry, 2014.

The combination of both techniques, APS and Kelvin probe, is beneficial since the measurement can be done under ambient condition with the Kelvin probe as a detector. Both measurements can be done quasi-simultaneous and the valence band can be found from APS measurements. From the KP measurement the work function and the contact potential difference (V_{cpd}) can be calculated.

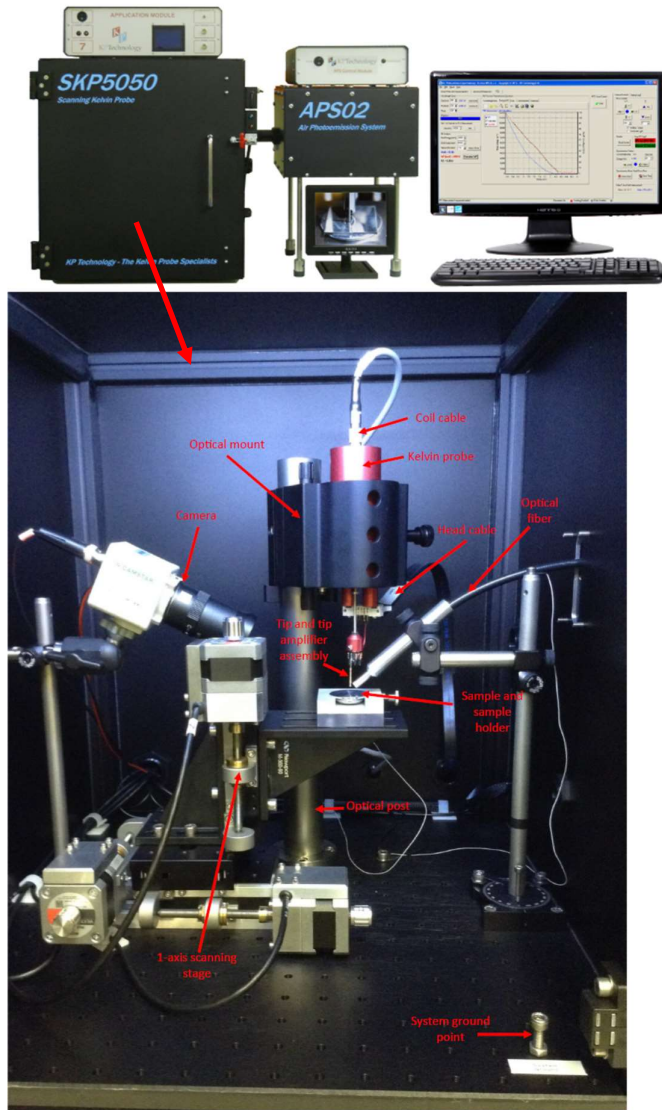


Fig. 3.29: APS and Kelvin Probe instrument from the company KPTechnology Ltd. used for this experiment at the lab of High-Performance Ceramics at Dübendorf EMPA.

As mentioned before, the Fermi level (E_f) of a semiconductor is the energy at which the probability of an electronic state being occupied is 0.5 at 0 K. The flat band potential (ϕ_{fb}) is the potential at which there is no band bending at the semiconductor-electrolyte interface and in ideal cases $\phi_{fb} = -E_f/e$ ^{89, 90}. Thus, if the Fermi level of the semiconductor is known, the valence band can be calculated, but one should assume that the majority carrier concentration is high enough in order to provoke a degeneration of the semiconductor, for that $N_a/N_V \geq 0.05$ where N_V is the density of state at the top of

the valence band. When this assumption is fulfilled, the Fermi level is $3kT$ into the band gap from the valence band edge. The N_V can be calculated from eq. 3.6⁹¹.

$$N_V = 2 \left(\frac{2\pi m_h kT}{h^2} \right)^{3/2} \quad (3.6)$$

where h is the Planck constant, k is the Boltzmann constant and m_h is the density of states effective mass of the valence band of the semiconductor and for NiO is $0.9m_0$ ⁹² and m_0 is the mass of the electron; N_V can be calculated and is $1.2 \times 10^{19} \text{ cm}^{-3}$. When the semiconductor is not degenerated the valence band potential can be calculated from equation 3.7⁸⁸:

$$\varphi_{VB} = \varphi_{fb} + \frac{kT}{e} \ln \left(\frac{N_V}{N_a} \right) \quad (3.7)$$

where N_a is the hole concentration for p-type semiconductors. When the semiconductor is degenerated the valence band potential can be found from equation 3.8⁸⁸:

$$\varphi_{VB} = \varphi_{fb} - \frac{kT}{e} \left[\ln \left(\frac{N_a}{N_{VB}} \right) + 2^{-3/2} \left(\frac{N_a}{N_{VB}} \right) \right] \quad (3.8)$$

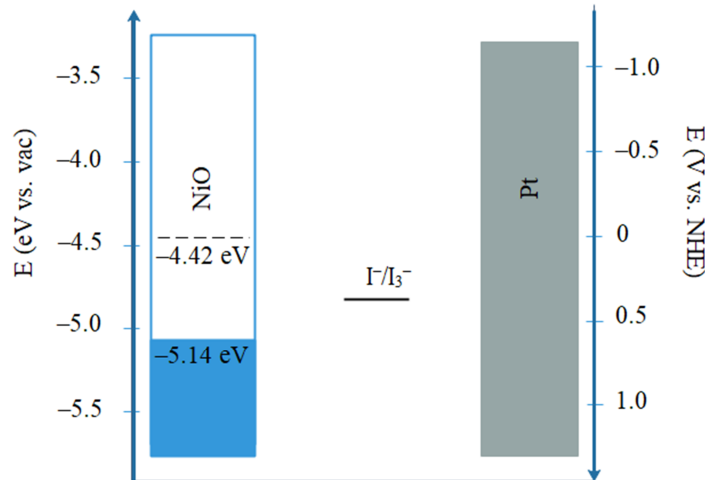


Fig. 3.30: Energy diagram of NiO. Where the energy of the conduction band $E_{CB} = 1.8 \text{ eV}$, the energy of the Fermi level $E_f = -4.42 \text{ eV}$ and the energy of the valence band $E_{VB} = -5.14 \text{ eV}$ ^{44, 95}.

3.7.2 APS measurements of FTO/NiO with and without dyes

This experiment took place at the lab of High-Performance Ceramics at Dübendorf EMPA. The collaborator from EMPA was the PhD candidate Jens Top who was responsible for the APS and KP measurements. During this experiment a blank NiO electrodes and two dye sensitized NiO electrode were measured. The theory above was applied to NiO electrodes fabricated with the method described in section 3.3.7 and sensitized with P1 and WOC53 (Fig. 3.9 and 3.21 accordingly). Moreover, the experiment was conducted under both dark and illumination conditions. The Kelvin probe was used as a stability test before and after the UV irradiation experiments, under both dark and illumination conditions so to make sure that the contact potential difference (CPD) would remain the same after irradiation and the surface would not be damaged by the UV irradiation.

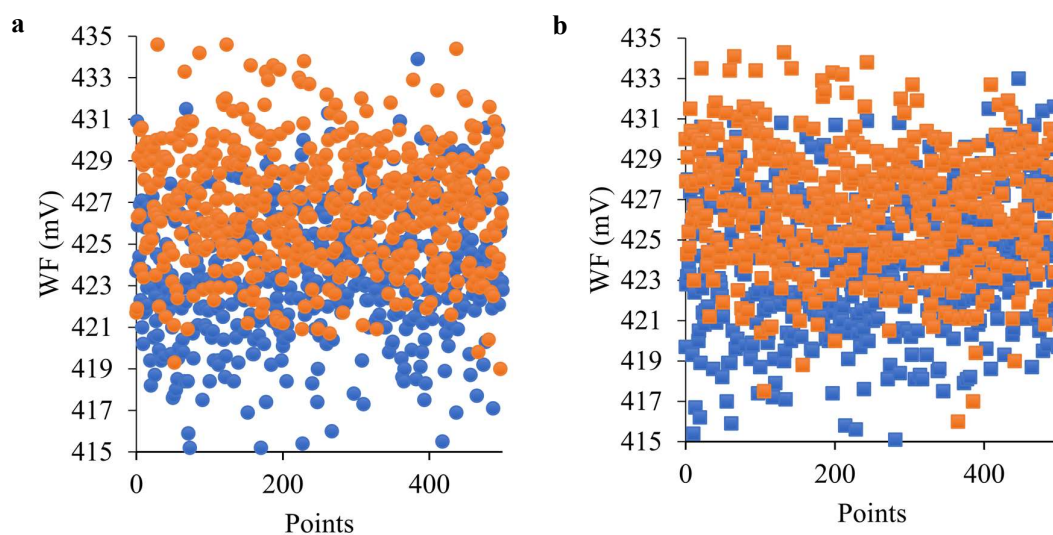


Fig. 3.31: Pre- and post-dark Kelvin probe experiment for NiO electrode dye. **a:** blue symbols pre-APS dark experiment, orange symbol post-APS dark experiment. **b:** blue symbols pre-APS illumination experiment, orange symbol post-APS illumination experiment.

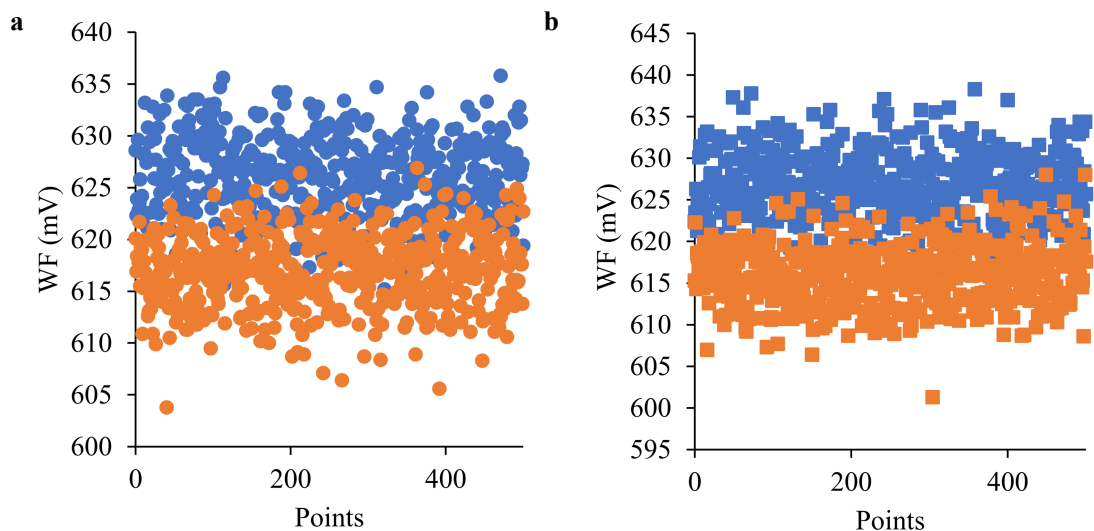


Fig. 3.32: Pre- and post-dark Kelvin probe experiment for the electrode sensitized with P1 dye. **a:** blue symbols pre-APS dark experiment, orange symbol post-APS dark experiment. **b:** blue symbols pre-APS illumination experiment, orange symbol post-APS illumination experiment.

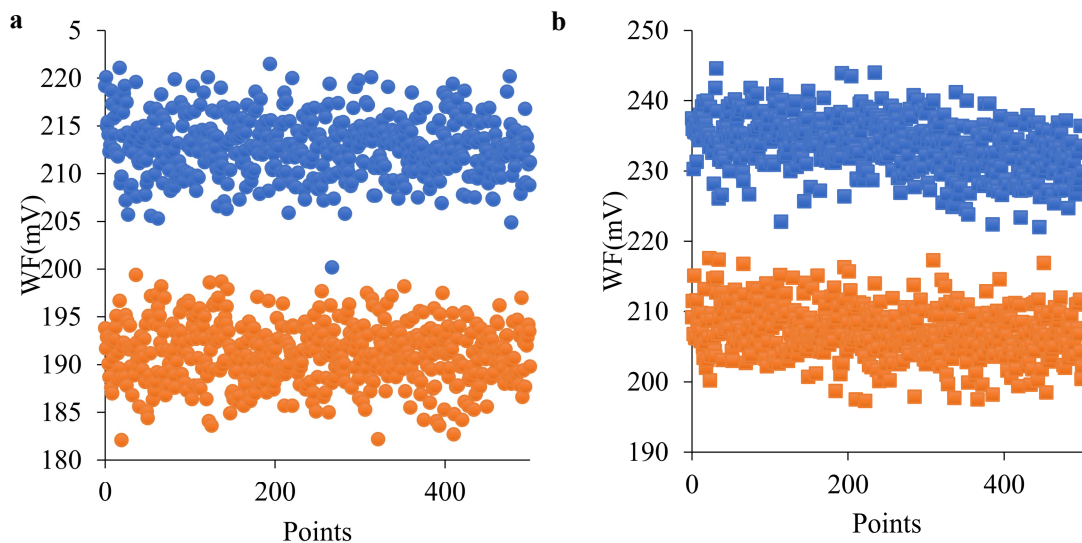


Fig. 3.33: Pre- and post-dark Kelvin probe experiment for the electrode sensitized with WOC53 dye. **a:** blue symbols pre-APS dark experiment, orange symbol post-APS dark experiment. **b:** blue symbols pre-APS illumination experiment, orange symbol post-APS illumination experiment

Experiment Name	Conditions of experiment		Number of points	mean	St. dev	min	max
NiO	Pre-APS	Illumination	500	422.8	3.32	415.4	433
	measurements	Dark		423.7	3.07	416	435.1
NiO	Post-APS	Illumination	500	427.9	3.12	415.2	433.9
	measurements	Dark		421.7	2.95	419	434.6
NiO with dye WOC53	Pre-APS	Illumination	500	237.5	3.51	222.8	244.6
	measurements	Dark		193.8	3.15	182.2	199.4
NiO with dye WOC53	Post-APS	Illumination	500	209.2	3.58	197.3	217.3
	measurements	Dark		219.2	3.27	200.2	221.5
NiO with dye P1	Pre-APS	Illumination	500	628.6	3.84	614.7	635.8
	measurements	Dark		622.4	3.94	613.9	638.3
NiO with dye P1	Post-APS	Illumination	500	620.1	3.42	626.9	603.4
	measurements	Dark		615.3	3.46	601.3	628.0

Table 3.11: Descriptive statistics for Kelvin probe (KP) measurements of NiO and NiO sensitized with WOC53 and P1 dyes.

In Fig 3.31 – 3.33a, b the Kelvin probe experiments for the NiO electrode and the sensitized NiO electrodes with P1 and WOC53 dyes can be observed. In Table 3.11 the descriptive statistics of all the measurements are presented. As observed from Table 3.11 for the KP experiments before and after APS experiments, under illumination or dark conditions, the standard deviation is very small (in the

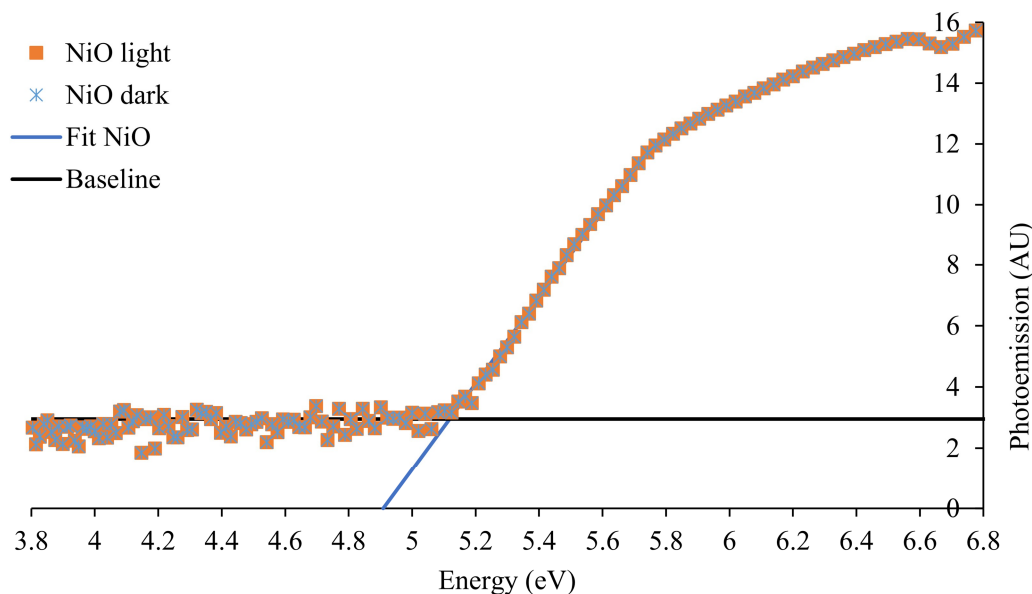


Fig. 3.34: APS measurement under dark and under illumination for NiO electrode.

order of 3.85 mV for all the samples). For the sample of blank NiO, the difference between the mean values of the KP experiments done before and after the APS experiment under illumination condition is very small and equal to 5.1 mV (Fig. 3.31b) and for the same experiment but under dark conditions the difference of the mean values is small as well and equal to 2 mV (Fig. 3.31a). For the sample of NiO sensitized with P1 dye, the difference of the mean values before the APS experiment and after, under illumination exhibit a difference of 8.5 mV (Fig. 3.32b) and for the same experiment under dark conditions a difference of 7.1 mV it is observed (Fig. 3.32a). The difference of the mean values for these two electrodes is very small and it is assumed that no significant changes on the composition of the surface is occurring after the APS experiments under dark or illumination conditions. For the NiO sample sensitized with WOC53 dye, the difference of the mean values for the measurement done before and after the APS experiment under illumination, is 28.3 mV (Fig. 3.33b). And for the same measurements

done under dark conditions a difference of 25.4 mV can be observed (Fig. 3.33a). This leads to the conclusion that some changes are occurring to the surface after being irradiated with the APS beam, an assumption maybe that the dye of the surface is photoexcited and does not have the time to relax

between the two Kelvin probe measurements. This hypothesis is further supported by the fact that no significant changes are occurring on the mean values of the sample of blank NiO when comparing the KP experiments before and after the APS experiment under illumination or dark conditions. For the NiO electrode sensitized with P1 dye the differences between the mean values are higher compared to what observed for the blank NiO electrode but still small. Thus, it can be concluded that the relaxation time of the P1 dye is faster compared to the WOC53 dye.

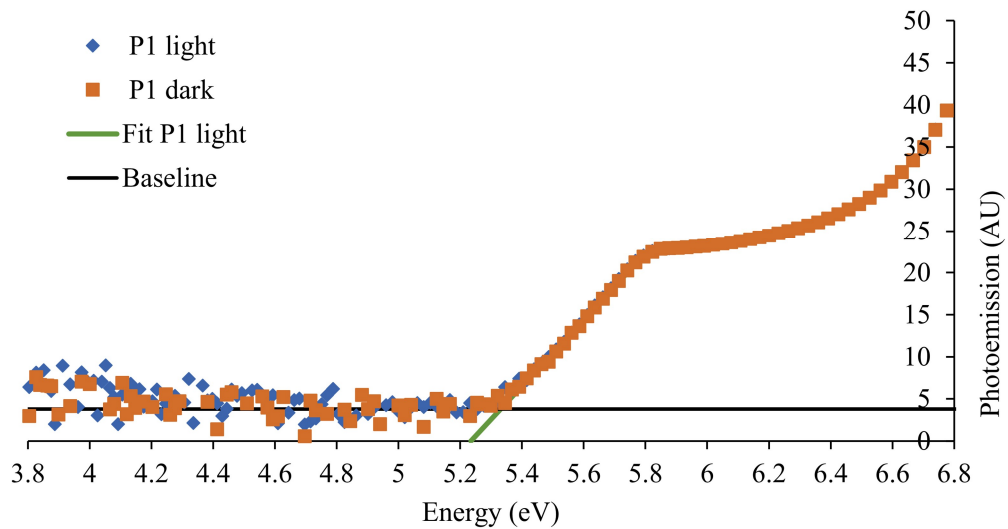


Fig. 3.35: APS measurement under dark and under illumination for electrode sensitized with P1 dye.

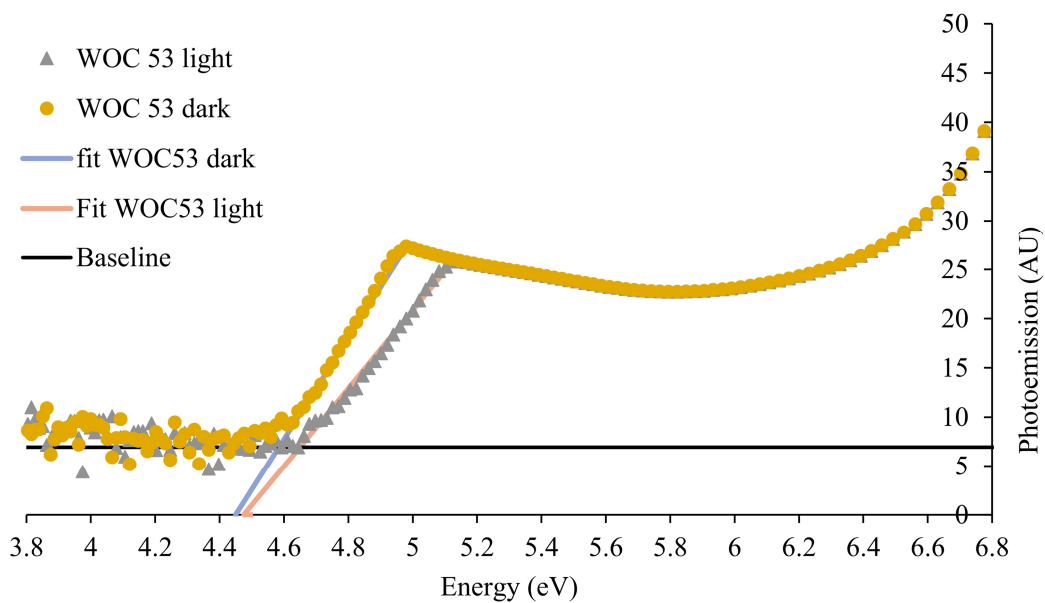


Fig. 3.36: APS measurement under dark and under illumination for electrode sensitized with WOC53 dye.

Experiment Name	Illumination Conditions	VB (eV)
NiO	Illumination	-5.12
	Dark	
NiO with dye P1	Illumination	-5.34
	Dark	
NiO with dye WOC53	Illumination	-4.66
	Dark	-4.62

Table 3.12: Valence band values from APS measurements of NiO and NiO sensitized with WOC53 and P1 dyes.

In Fig. 3.34-36 the APS measurement of the blank NiO and the NiO electrode sensitized with both sensitizers under dark and under illumination are shown. For most semiconductors the photoemission current increases with the cube root of the photon energy above the ionisation potential⁹³ so a plot of the cube root of the photoemission current against photon energy gives a curve, which at its higher slope part can be extrapolated towards the x-axis to give the valence band of the semiconductor⁹⁴. The values of the valence band under both sets of conditions are the same: -5.12 eV for the blank NiO electrode and -5.34 eV for the NiO electrode sensitized with P1 dye (Table 3.12) respectively. For the electrode sensitized with WOC53 dye the valence band for the measurement under illumination is -4.66 eV and under dark condition is -4.62 eV (Table 3.12). The difference between these two values is 0.04 eV and can be negligible.

The literature values for the valence band edge of NiO is at -5.14 eV⁹⁵ (Fig. 3.30) and agrees with the values found by this experiment of -5.12 eV. For the electrode sensitized with P1 the valence band is at higher energy value compared with the energy value found for the NiO sensitized with WOC53 dye, which suggest that a DSSC fabricates with NiO electrode sensitized with WOC53 dye and electrolyte comprised of a I⁻/I₃⁻ redox couple in the electrolyte in acetonitrile will exhibit a higher V_{OC} than a DSSC with a NiO sensitized with P1 dye and same electrolyte.

3.8 Tauc plot

This measurement was done by Jens Top at the lab of High-Performance Ceramics at Dübendorf EMPA. The Tauc plot is an optical absorption measurement with which the optical band gap of a semiconductor can be calculated. *Tauc et al*⁹⁶ found a method to calculate the band gap of a semiconductor material by plotting the square root of the absorption coefficient and photon energy versus the photon energy (eq. 3.9) and by extending with a straight line to the x-axis, the interception with the x-axis gives the band gap of the material. This theory was further investigated by the work of *Davis and Mott*^{97, 98}, who also validate the application of this way of calculating the band gap for amorphous semiconductors⁹⁹.

$$(ah\nu)^{1/n} = A_0(h\nu - E_g) \quad (3.9)$$

Where h is the Planck constant, ν is the photon's frequency, α is the absorption coefficient, E_g is the band gap, A_0 is the proportionality constant, n defines the nature of the electronic transition (allowed or forbidden and direct or indirect).

For direct allowed transition $n = 1/2$

For direct forbidden transition $n = 3/2$

For indirect allowed transition $n = 2$

For indirect forbidden transition $n = 3$

Solving equation 3.9 when taking under consideration that NiO has a direct band gap ($n=1/2$)¹⁰⁰, and the absorption data¹⁰¹ of a NiO electrode resulting in the plot in Fig. 3.37, where after extrapolating the plot at the x-axis, the band gap of NiO was found to be 2.83 eV.

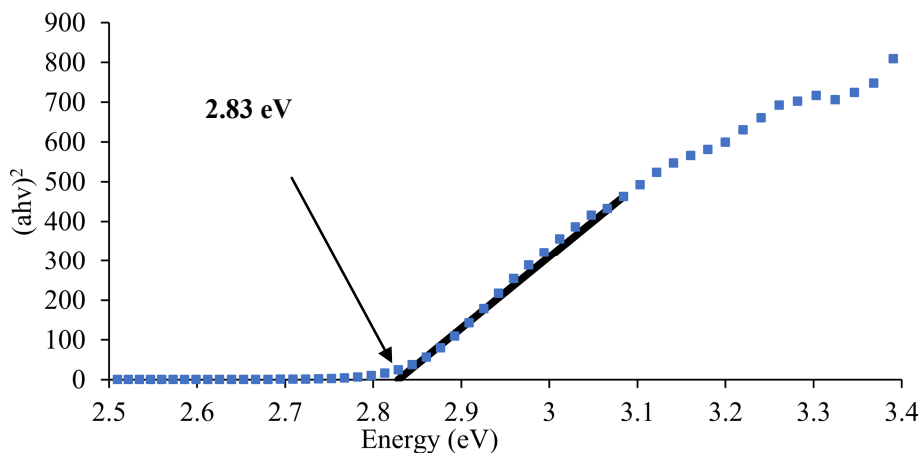
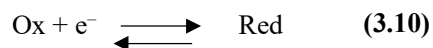


Fig. 3.37: Tauc plot of two screen printed layers of NiO electrode onto an FTO substrate with Ni(acac)₂ solution in AcCN as a pre-layer, sintered at 350 °C. The data were recorded in diffuse reflection and transformed to absorption using Kubelka-Munk equation ¹⁰¹.

3.9 Mott-Schottky analysis

As it has been mentioned before, the semiconductor is defined by electronic states including the valence band potential (E_{VB}), the conductive band potential (E_{CB}) and the Fermi level (E_f) (Fig. 3.38a). In the case of a liquid DSSC, the semiconductor it is in contact with the redox shuttle of the liquid electrolyte which can be described by the equation 3.10:



The energy of the redox shuttle is defined by whether the energy states are occupied (Red) or vacant (Ox) due to the different solvent-sheath energies λ (see Fig. 3.38a). The redox Fermi level of the electrolyte ($E_{f(\text{redox})}$) is the energy at which the probability of a state being occupied is 0.5. When a p-type semiconductor comes in contact with an electrolyte a downwards bending of the band or depletion (VB and CB) of the semiconductor occurs (Fig. 3.38b), and the Fermi level of the semiconductor bends “up” and equilibrium is observed when the Fermi level at both interfaces are the same ($E_{f \text{ equil.}}$). During this equilibrium process electrons from the Red of the electrolyte are transferred to the semiconductor, or holes from the semiconductor deplete into the electrolyte solution. This results in a negatively charged semiconductor. This equilibrium can be perturbed by applying different voltages with the help of a potentiostat, in a certain voltage the Fermi level of both the semiconductor and the electrolyte can be separate and the semiconductor can reach its flat band potential (ϕ_{fb}) where no band bending is observed as described before (Fig. 3.38c).

The Mott-Schottky equation (eq. 3.11) can be used for the calculation of the flat band potential of a semiconductor ¹⁰². In the case of a p-type semiconductor the potential that should be applied in order to reach the flat band potential should be more negative than the Fermi level of the semiconductor in order for the transition from the depletion to the flat band condition would be observed with the Mott-Schottky plot. In the case of NiO the applied potentials should be in the range of -0.3 to 0.6 V vs. NHE ⁴⁴ given that the literature value for the flat band potential of NiO varied between 0.3 to 1.04 V vs. NHE ^{98, 103, 104}.

$$\frac{1}{(C_{SC})^2} = -\frac{2}{e\epsilon_0 \kappa N_a A^2} \left(E_{app} - \varphi_{fb} - \frac{k_B T}{e} \right) \quad (3.11)$$

Where C_{SC} and A is the interfacial capacitance and area respectively, N_a the density of acceptors within the space region, E_{app} the applied voltage, k_B the Boltzman constant, ϵ_0 the vacuum permittivity, κ the dielectric constant, ($\kappa_{NiO} = 11.9$) ¹⁰⁵ T the absolute temperature and e the electronic charge.

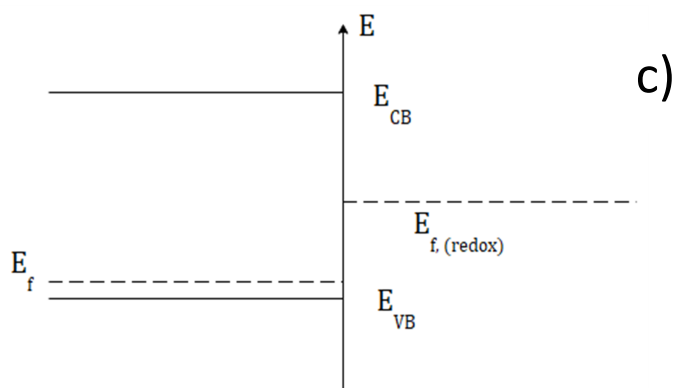
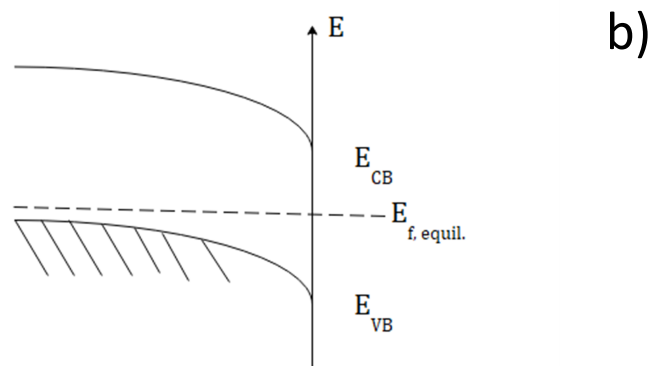
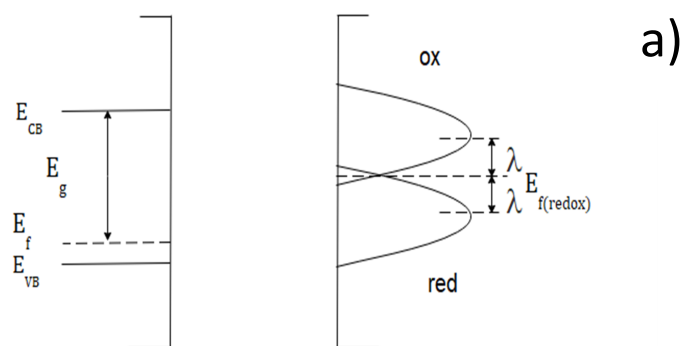


Fig. 3.38: **a:** Energy diagram for p-type semiconductor and redox states in solution **b:** electronic equilibrium between the p-type semiconductor and redox couple in solution. **c:** Situation when the semiconductor is at flat band potential.

In order to observe the flat band potential of NiO, a Mott-Schottky plot was made using the homemade NiO electrode (see section 3.3.6). Mott-Schottky plots were taken under illumination and dark conditions and three different electrodes were used, a blank NiO, NiO sensitized with P1 and NiO electrode sensitized with WOC53 dye. The electrolyte solution was 0.1 M phosphate buffer saline aqueous solution (mixed solution of sodium dihydrogen phosphate and disodium hydrogen phosphate) (pH 7) with 1 M potassium chloride as supporting electrolyte. The experiment was done in a ModuLab[®] XM PhotoEchem photoelectrochemical measurement system from Solartron Analytical. The AC frequency used for the plots was 10 Hz. The capacitance was extracted from the data using equation 3.12:

$$Z_{img} = \frac{1}{2\pi fC} \quad (3.12)$$

where Z_{img} is the imaginary part of the impedance obtained from the measurement, f is the frequency and C is the capacitance^{106, 107}. The density of acceptors can be calculated from the slope of the Mott-Schottky plots, which is determined from the first part of equation 3.11

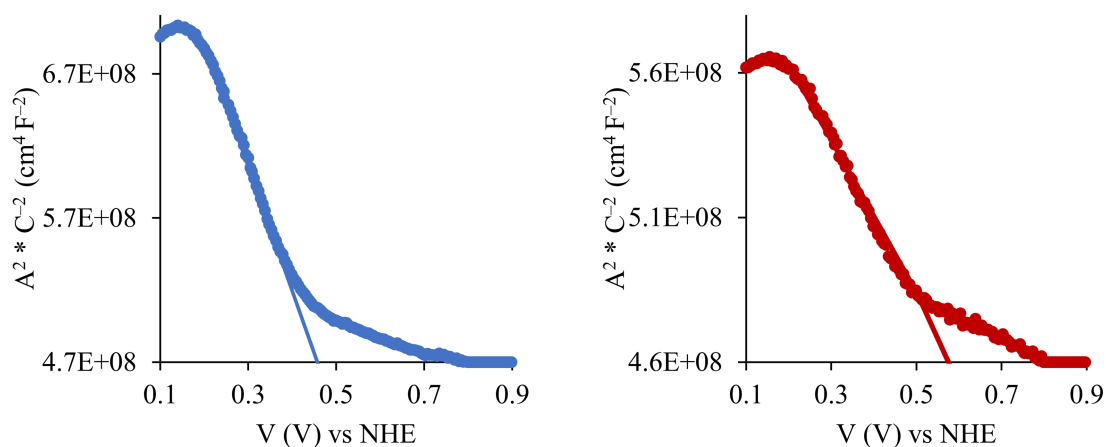


Fig. 3.39: Mott-Schottky plots for DSSC fabricated with an NiO electrode, and aqueous electrolyte containing 0.1 M NaH_2PO_4 and 1M KCl with a pH adjusted to 7. Blue symbol data taken under illumination and red symbol data taken under dark conditions.

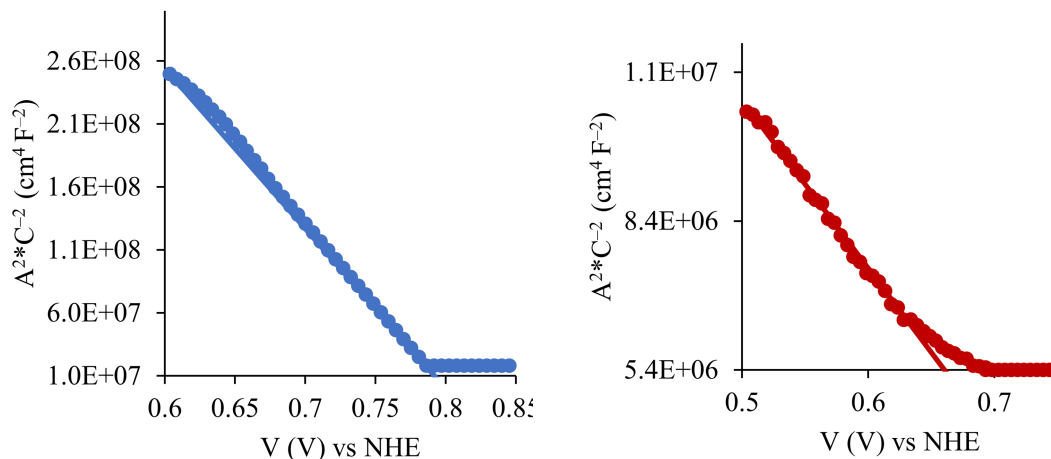


Fig. 3.40: Mott-Schottky plots for DSSC fabricated with an NiO electrode and sensitized with P1 dye with aqueous electrolyte containing 0.1 M NaH₂PO₄ and 1M KCl with a pH adjusted to 7. Blue symbol data taken under illumination and red symbol data taken under dark conditions.

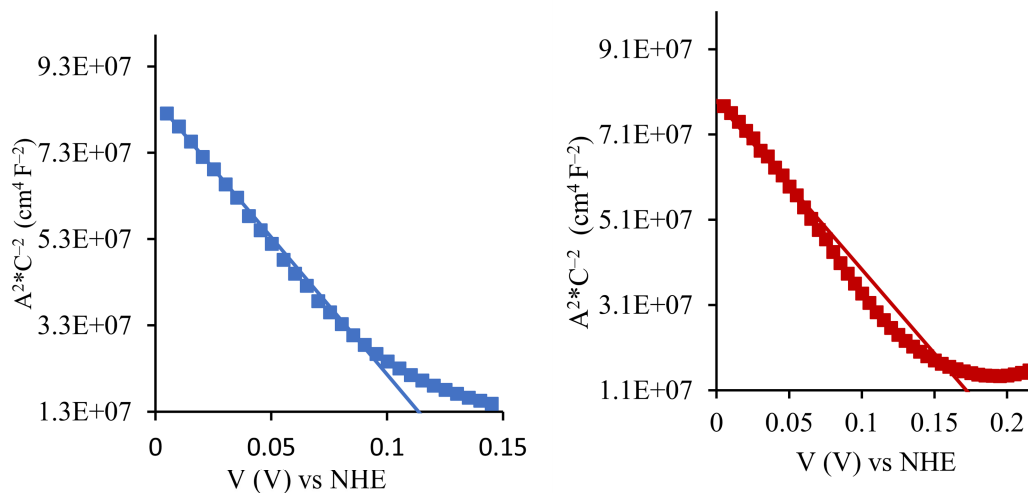


Fig. 3.41: Mott-Schottky plots for DSSC fabricated with an NiO electrode and sensitized with WOC53 dye with aqueous electrolyte containing 0.1 M NaH₂PO₄ and 1M KCl with a pH adjusted to 7. Blue symbol data taken under illumination and red symbol data taken under dark conditions.

The valence band position of a semiconductor will determine the open circuit voltage of the cell as the latest is the difference of the energy value of the valence band and the redox potential of the electrolyte. Thus, for the open circuit voltage to increase this difference should increase. The position of the valence band is of great importance and as seen from Fig. 3.42 ⁷⁶ the open circuit voltage will

increase for a certain electrolyte when the valence band potential vs. NHE will increase in value. The ϕ_{FB} , N_a and ϕ_{VB} were calculated using the Mott-Schottky plots (Fig. 3.39 - 41). For the calculation of the valence band potential (ϕ_{VB}) eq. 3.7 was used since the assumption $N_a/N_V \geq 0.05$ is not fulfilled and the semiconductor is not degenerated. The values of the extrapolated valence band potential for the three measured for which a value of $8.33 \times 10^{22} \text{ cm}^{-3}$ for the density of acceptors was recorded. The valence band potential for the NiO sensitized with P1 dye lies at $\phi_{VB} = 1.00 \text{ V vs. NHE}$ but a lower density of acceptors $6.24 \times 10^{22} \text{ cm}^{-3}$ compared with the NiO sensitized with WOC53 was observed. If taking under consideration the valence band potential found by this experiment and that the redox potential of the I^-/I_3^- redox couple of the electrolyte in acetonitrile is 0.35 V vs. NHE ¹⁰⁸, a DSSC fabricated with NiO sensitized with P1 and I^-/I_3^- redox couple in the electrolyte will exhibit a higher V_{OC} compared to a DSSC fabricated with NiO sensitized with WOC53 and the same electrolyte. In conclusion, the valence band potentials of the three samples calculated with Mott-Schottky plots lie in the literature range of $0.3 - 1.04 \text{ V vs. NHE}$ ^{98, 103, 104}. The dye sensitized electrodes tested, exhibit a good ϕ_{VB} and it could be assumed that since a difference is observed among the three different samples under the same conditions, the sensitizers have a doping role to the NiO material by tuning the valence band of the semiconductor.

From the results obtained with the APS measurement and the Mott-Schottky equation, the valence band potential of the three electrodes tested were calculated. Firstly, the valence band varies across the three samples and secondly regarding the prediction of the V_{OC} of the DSSCs fabricated with the sensitized NiO, we observed that in the case of the valence band calculated by the APS experiment the DSSC with WOC53 sensitizer and I^-/I_3^- redox couple in the electrolyte ^{109, 110} will exhibited the highest V_{OC} whereas when calculating the valence band potential from the Mott-Schottky equation the best predicted V_{OC} is attributed to the DSSC fabricated with the NiO sensitized with P1 and the same electrolyte. Thus, these contradicting results could be occurring from the fact that the APS is a surface measurement whereas the from the Mott-Schottky equation informations about the bulk material are calculated. electrodes (NiO, NiO sensitized with WOC53, NiO sensitized with P1) and the two different conditions of measurement (illumination and dark) are displayed in Table 3.13. For the blank NiO the calculated valence band potential lies at 0.66 V vs. NHE for the measurement done under illumination and at 0.82 V vs NHE when the measurement was done in dark conditions. These values are in agreement with the NiO valence band potential exhibited in the work of *Bach and co-workers* ⁹⁵ of 0.7 V vs. NHE . The lowest value of 0.34 V vs. NHE it is observed for the NiO sensitized with WOC53 dye under illumination

Experiment Name	Illumination Conditions	ϕ_{fb} (V vs. NHE measured at pH 7)	N_a ($\times 10^{22}/\text{cm}^3$)	ϕ_{VB} (V vs. NHE extrapolated at pH 7)
NiO	Illumination	0.45	6.24	0.66
	Dark	0.58	16.66	0.82
NiO with dye P1	Illumination	0.79	6.24	1.00
	Dark	0.66	6.09	0.87
NiO with dye WOC53	Illumination	0.12	8.33	0.34
	Dark	0.17	12.49	0.40

Table 3.13: Values for flat band potential, acceptor density and extrapolated valence band potential at pH 7 for NiO and sensitized NiO with WOC53 and P1 dye. The values of ϕ_{fb} were measured from Fig. 3.39-41. The values for N_a were measured from the slope of the curves of Fig. 3.39 - 41 and using eq. 3.11. The values for ϕ_{VB} were calculated using eq. 3.7.

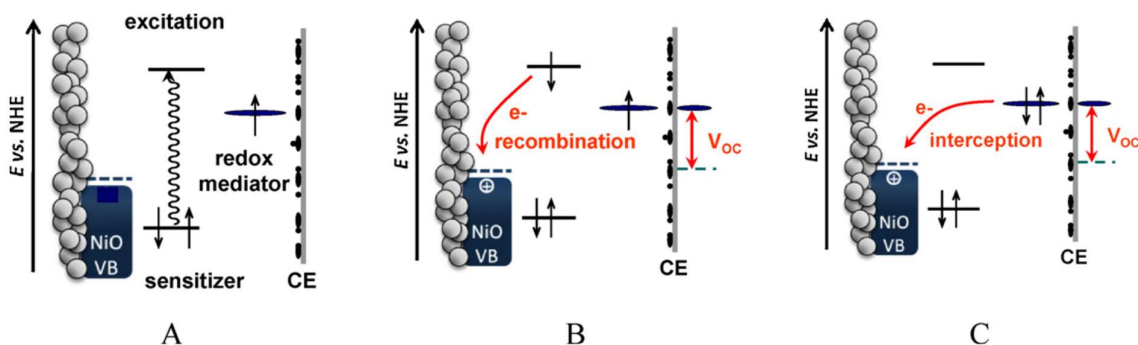


Fig. 3.42: Representation of charge transfer process in p-type DSSC, involving the recombination and the interception process with the dye and the electrolyte respectively. Reprinted with permission of *F. Odobel et al*⁷⁶, copyright royal society of chemistry, 2012.

3.10 Dyenamo electrodes

Electrodes from Dyenamo AB were also purchased. A benchmarking paper ⁷⁵, in which Dyenamo AB electrodes and P1 (Fig. 3.9) dye were used, gave the possibility to compare those results with the ones produced in our lab. The Dyenamo electrodes were screen printed, and had a surface area of 0.25 cm². Three different batches (Batch 1, Batch 2, and Batch 3) of electrodes were purchased from Dyenamo AB over a six-month period. FIB measurements showed that the first batch contained electrodes that were homogeneous and, of an optimum thickness and these electrodes gave DSSCs that performed well at the sun simulation measurements ¹¹¹. The following two batches purchased from the company (Batch 2 and Batch 3) presented irregularities on the surface and were of variable thickness. These features could be seen by eye. Moreover, the sun simulation measurements were worse in terms of current density compared with Batch 1. In this part of the discussion, FIB images, sun simulation measurements and EDX measurements are compared for the three batches of commercial electrodes. It is important to note that the specifications by Dyenamo of all three batches were the same (NiO thickness 2µm).

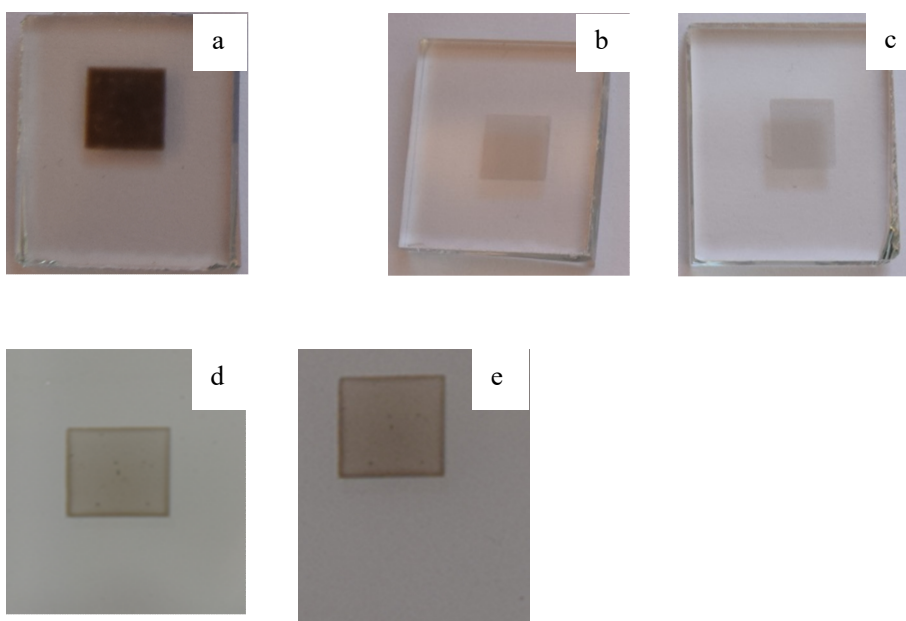


Fig. 3.43 **a:** Batch 1, Dyenamo electrodes after sintering at 450 °C. **b:** Batch 2, Dyenamo electrodes before sintering. **c:** Batch 2 of Dyenamo electrodes after sintering at 450 °C. **d:** Batch 3, batch of Dyenamo electrodes before sintering. **e:** Batch 3, of Dyenamo electrodes after sintering at 450 °C.

As can be seen from Fig. 3.43, there was a clear difference between the three batches of electrodes after sintering. Batch 1 appears very homogeneous and dark after sintering. Batch 2 appeared much lighter in colour which was attributed to the very thin NiO layer. Batch 3, was not homogeneous either, and appeared to be thinner in the middle of the electrode and thicker on the edges. In order to quantify these observations DSSC were fabricated out of the three batches of electrodes as described in table 3.14.

Name	Batch 1	Batch 2	Batch 3
Electrolyte	0.1M iodine I ₂ and 1M lithium iodide LiI in acetonitrile (Std III)		
Dye	WOC53 (1,2)	WOC53 (1,2)	WOC53 (1,2)
time in the dye solution	16h		
Sum Simulator settings	5.3vmV step, reverse scan rate of V, 1 mA range, inverted configuration, settling time of 360 ms		

Table 3.14: Description of experiments of DCCS fabricated with Dyenamo electrodes of Batch 1 2 and 3. The NiO electrodes were purchased by Dynamo AB and sintered at 450 °C.

Experiment Name	Jsc /mA cm ⁻²	Voc /mV	FF /%	η /%
Batch 1_1	4.06	95	36	0.139
Batch 1_2	4.13	92	36	0.136
Batch 2_1	1.86	104	41	0.080
Batch 2_2	1.79	108	40	0.077
Batch 3_1	2.83	104	39	0.114
Batch 3_2	2.86	97	37	0.102

Table 3.15: Parameters for the performance of duplicate DSSCs sensitized with WOC53 dye and with electrolyte comprising of 0.1M iodine and 1M lithium iodide in acetonitrile (Stnd III) and surface area of 0.25 cm².

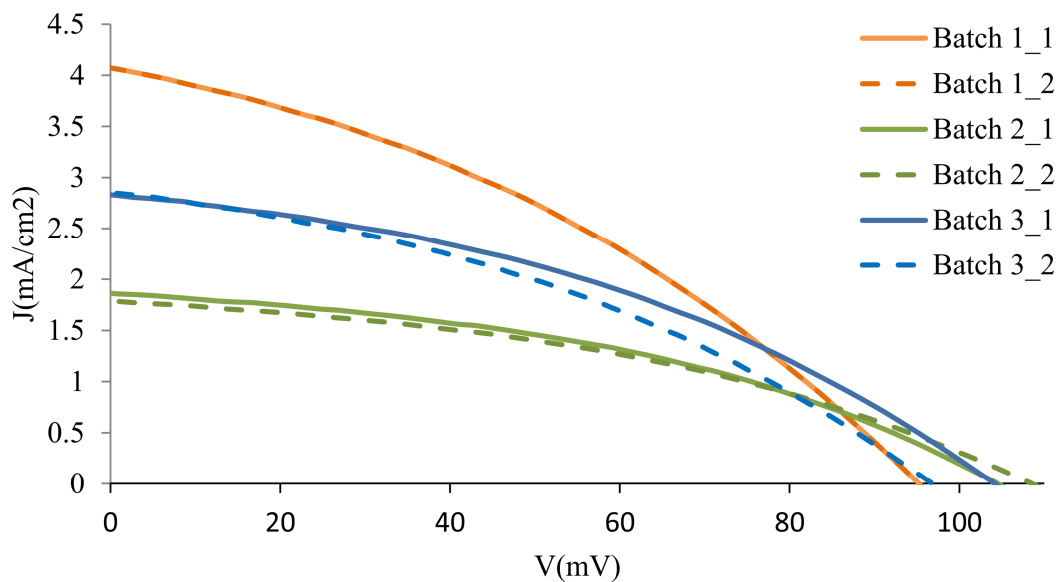


Fig. 3.44: JV curves for the duplicate DSSCs fabricated with the working NiO electrode form Table 3.12

From table 3.14 and Fig. 3.44 it is observed that the best performed DSSC were fabricated with Batch 1 ($\eta = 0.139\%$) electrodes, which appeared homogenous and dark after sintering (Fig. 3.44). Batch 2 electrodes produced DSSCs with the worst performance ($\eta = 0.080\%$) and DSSCs fabricated using

Batch 3 electrodes exhibit a small increase in performance ($\eta = 0.114\%$) compared with Batch 2. The decreasing performance in Batch 3 and 2 compared with Batch 1 is mainly due to a loss in J_{SC} , which can be attributed to the thinner electrode and ultimately to a lower dye loading.

3.10.1 FIB images

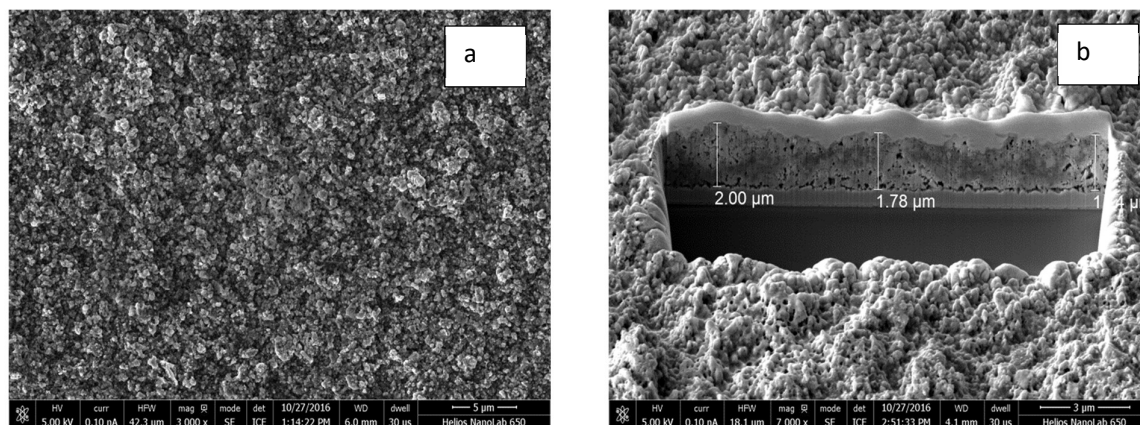


Fig. 3.45 a: FIB image of Dyenamo NiO electrode from the top before sintering **b:** FIB image of the cross section of the Dyenamo NiO electrode before sintering (platinum coating)

Fig. 3.45a, b shows that the thickness of the electrode is around 2 μm and the NiO is very homogeneous, before sintering. Also, there was a lack of porosity, which is due to the absence of sintering. Once the sample (Batch 1) had been sintered, a gain in porosity was observed (Fig. 3.46b), and the thickness of the electrode was measured to be 1.7 - 2.5 μm. The homogeneity of the surface

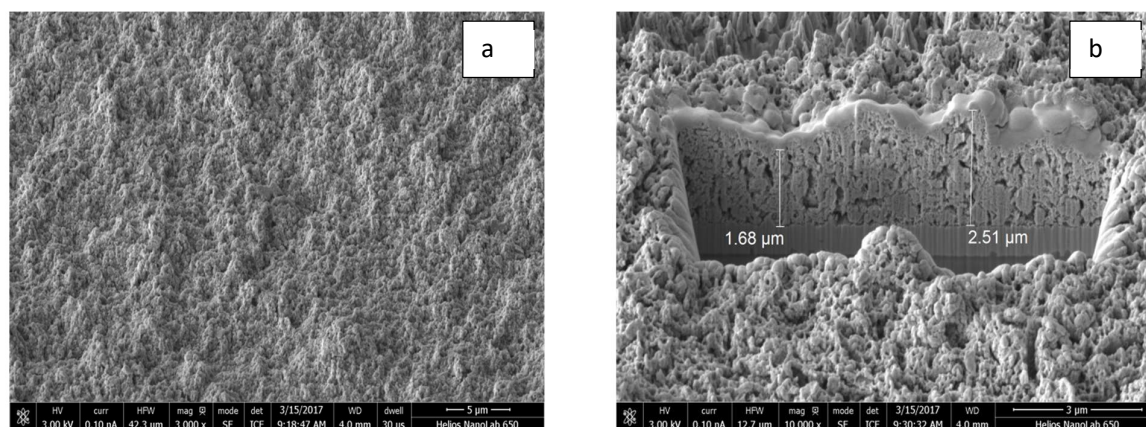


Fig. 3.46 a: FIB image of Dyenamo NiO electrode (Batch 1) from the top after sintering (350 °C) **b:** FIB image of the cross section with platinum coating of the Dyenamo NiO electrode after sintering (350 °C).

was not the same as before sintering as expected, but remains good. The electrodes of Batch 2 were also investigated using FIB as observed from Fig. 3.47, the thickness of the NiO electrode, before or after sintering was very small ($0.45\ \mu\text{m}$). This caused a very small current density in the finished cell as it was shown in table 3.15. The argument of a poor dye loading can be confirmed. Once more a difference in porosity before and after sintering was observed.

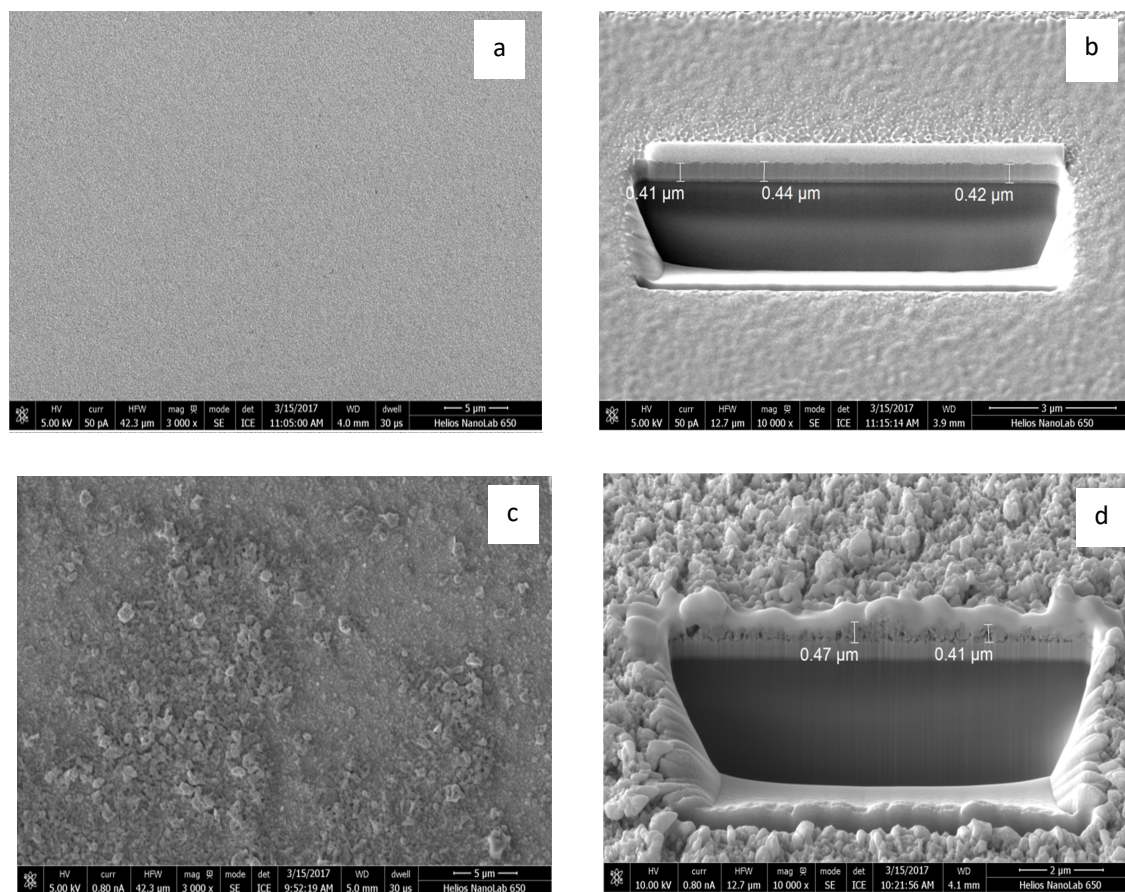


Fig. 3.47 **a:** Batch 2 of Dyenamo electrodes before sintering, top image. **b:** Batch 2 of Dyenamo electrodes before sintering, cross section. **c:** irregular batch of Dyenamo electrodes after sintering at $450\ ^\circ\text{C}$, top image. **d:** irregular batch of Dyenamo electrodes after sintering at $450\ ^\circ\text{C}$, cross section.

As it can be observed in Fig. 3.48 from the FIB images of Batch 3 Dyenamo electrode the NiO semiconductor was non-homogeneous as well. Their thickness did not meet the 2 μm required, moreover there was an obvious difference in the thickness of the electrode in the middle and at the edges.

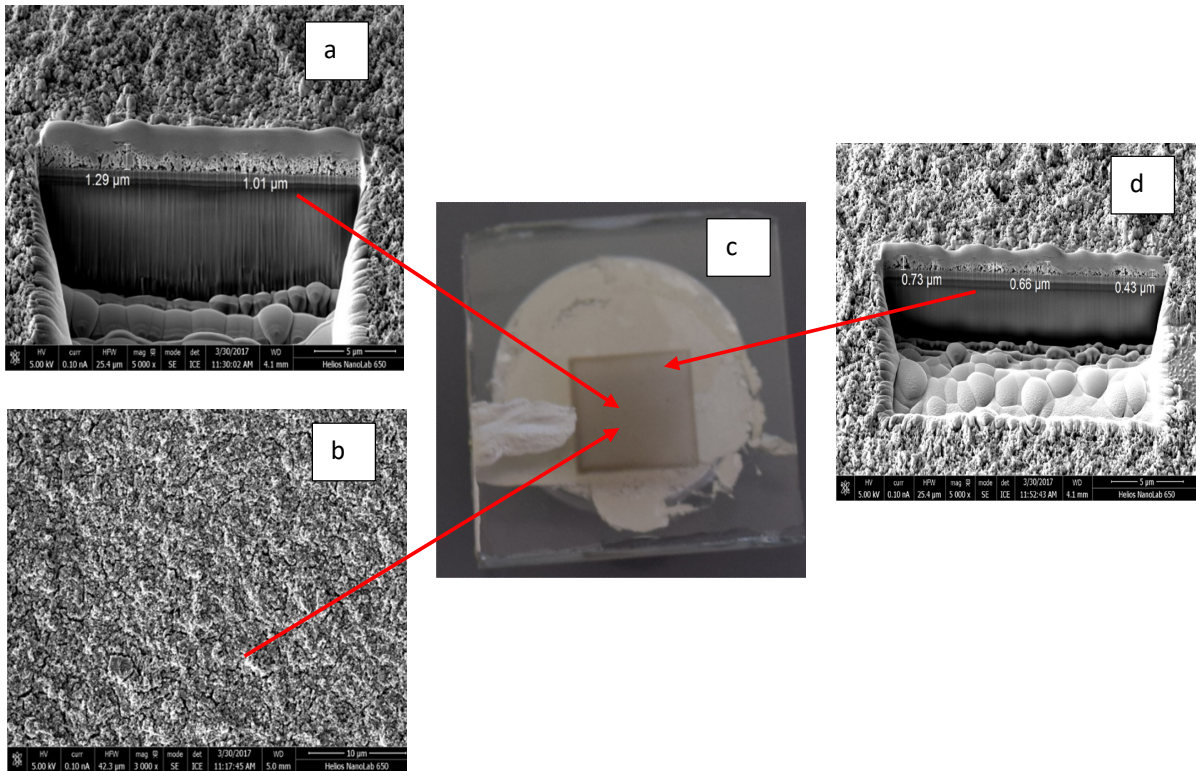
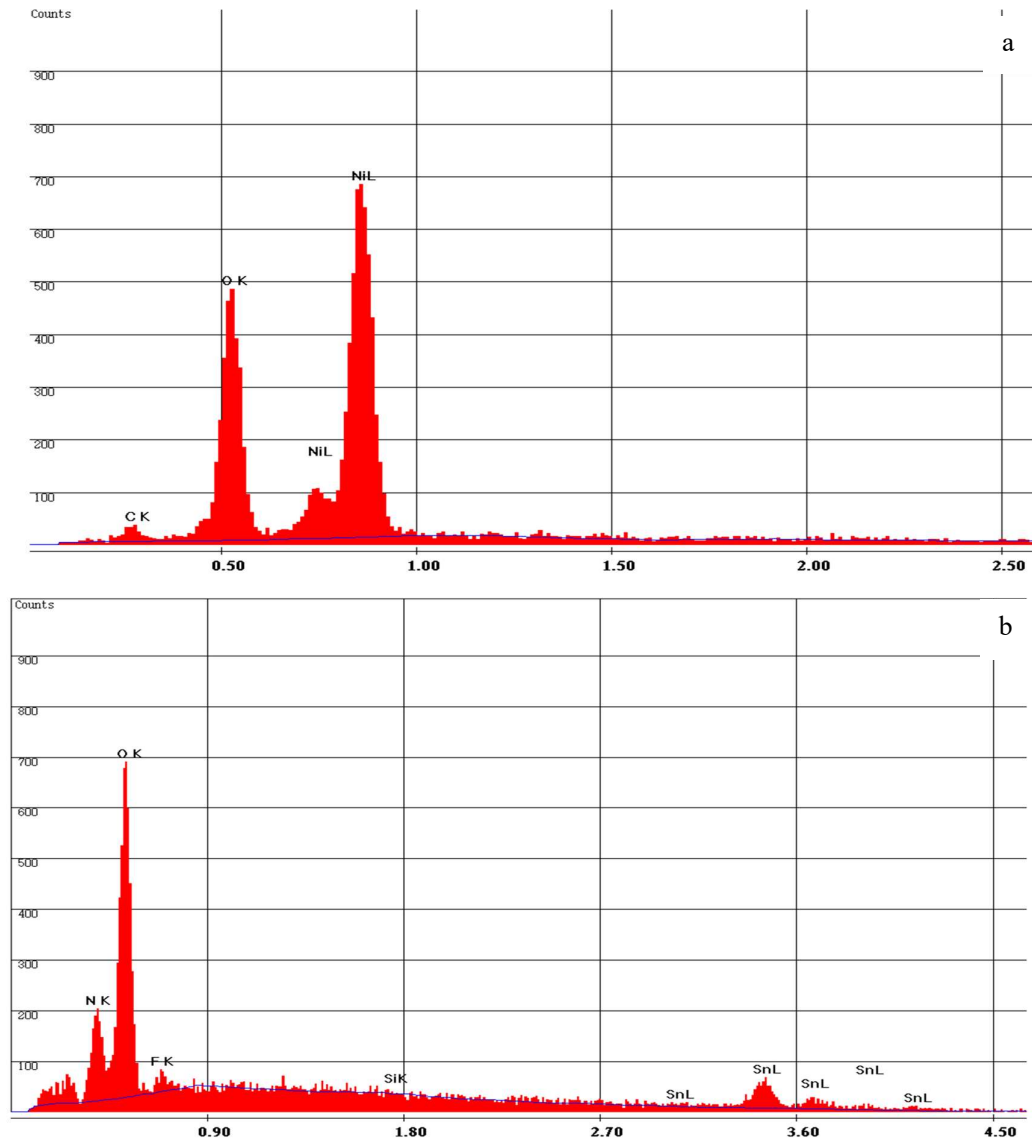


Fig. 3.48 a: FIB image of cross section of Batch 3 of Dayenamo electrodes after sintering at 450 °C **b:** FIB image of top image of Batch 3 of Dyenamo electrodes. **c:** picture of Batch 3 Dyenamo electrodes **d:** FIB image of cross section of Batch 3 of Dayenamo electrodes after sintering at 450 °C

3.10.2 Energy-dispersive X-ray spectroscopy (EDX) measurements

Energy-dispersive X-ray spectroscopy (EDX), measurement, is a technique used for the elemental analysis of a solid sample. During this measurement the sample is bombarded with a specific energy of X-rays, which may excite an electron from an inner shell of the atom and leave a vacancy which will be filled by an electron from a higher state which will cause the emission of an X-ray, characteristic of the element from which it was emitted ¹¹². EDX were performed on the Dyenamo batches 1 and 2 in



order to identify the composition of the NiO paste used.

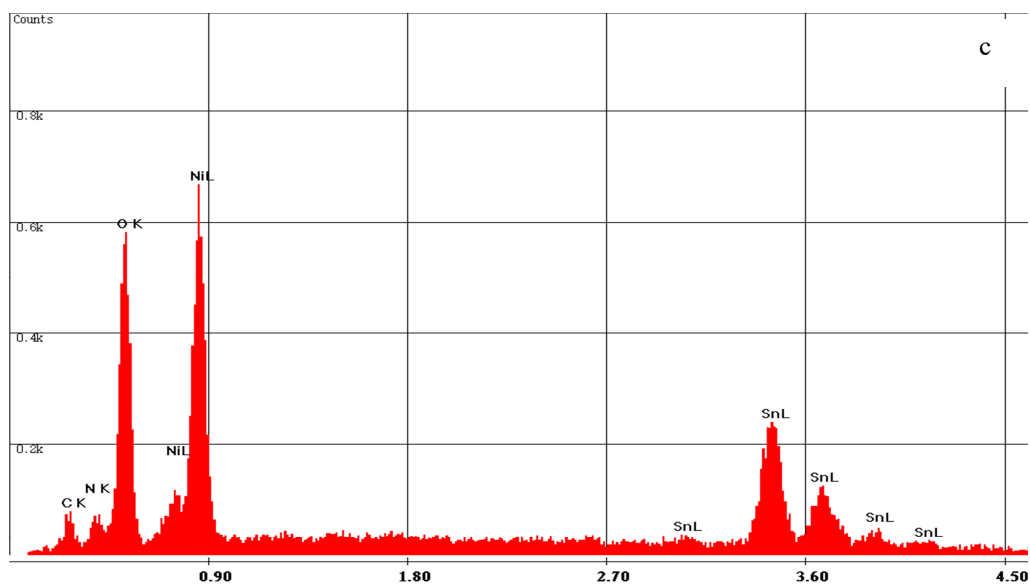


Fig. 3.49 a: EDX measurements of Batch 1 of Dyenamo electrodes after sintering at 350 °C. **b:** EDX measurements of Batch 2 of Dyenamo electrodes before sintering. **c.** EDX measurements of Batch 2 of Dyenamo electrodes after sintering at 450 °C

The EDX measurements, of the Batch 1 of Dyenamo electrodes presented in Fig. 3.49a, shows only nickel, oxygen and traces of carbon, most probably the solvent of the used paste. In Fig. 2.49b, the EDX spectra of Batch 2 of Dyenamo electrodes before sintering process is shown, from which no Ni peak was observed in contrast to the EDX spectra of Batch 1. The spectra of Batch 2 showed an Sn content which most certainly comes from the FTO layer. Both observations were consistent with the layer being very thin. In Fig. 3.49c Ni and Sn was both observed only to confirm the comments previously made. After discussing with the company Dyenamo, the above-mentioned results, the company confirmed that they could not guarantee reproducibility in their products, and in the best of our knowledge they withdraw the product from their catalogue. Once more it is confirmed that the fabrication of NiO electrodes is very challenging and the reproducibility of the layer's thickness is difficult to achieve.

3.11 Materials and Methods

3.11.1 Materials for the pre-treatment

Two different pre-layer materials were used: Ni(acac)₂ (ACROS) and Ni(OAc)₂ (ACROS) solutions (AcCN 0.05M). The application of those pre-treatments on the FTO (Solaronix TCO22-7, 2.2 mm thickness, sheet resistance = 7 Ω square⁻¹) glass vary as well. Before the pre-treatment, the glass with the coated FTO surface was cleaned by sonicating in Sonoswiss surfactant (2% in milliQ water), and rinsed with milliQ water and EtOH. The surface was activated in a UV-O₃ system (Model 256-220, Jelight Company Inc.) for 20 min. Then the solutions were dip-coated onto the glass, in more details this technique consisted of totally submerge the glass into a solution of one of the two pre-treatments and then let it dry in air, in a flat surface. In order to have completely coverage of all the surface, this procedure was repeated five times. The other method used was spin coating. The glass was putted in a spin coater (Sawatec SM180BT spin coater) the pre-treatment solution was added in the middle of the glass and two different speeds were used one at 2000 rpm and another at 3000 rpm.

3.11.2 Materials for screen printing

The paste used for the screen printed NiO electrodes was commercially available paste bought from Solaronix (Ni-Nanoxide N/SP, Solaronix). The electrodes were screen printed onto pre-treated FTO glass, the procedure of the pre-treatment is detailed in the section 3.11.1.

3.11.3 Materials for doctor blading

The paste used for the doctor bladed NiO electrodes was commercially available paste bought from Solaronix (Ni-Nanoxide N/SP, Solaronix). The electrodes were doctor bladed onto pre-treated FTO glass, the procedure of the pre-treatment is detailed in the section 3.11.1.

3.11.4 DSSCs assembly

The NiO electrodes were prepared by screen printing or doctor blading as described in section 3.11.2 and 3.11.3, then the electrode was washed with ethanol and heated at 300 °C for 30min and then cooled to 80 °C before immersing it to the dye bath. (0.3mM for the P1 dye bath in acetonitrile and 0.1mM for the WOC53 dye bath in ethanol). The electrodes were removed from the dye bath after 16 h. and washed with acetonitrile or ethanol accordingly. A commercial platinum counter electrode was used (Solaronix Test Cell Platinum Electrodes) which was washed with ethanol and heated at 450 °C for 30min. The DSSC were assembly by combing working and counter electrode using thermoplast hot-melt sealing foil (Solaronix, Meltonix 1170-25 Series, 60 mm thick) by heating while pressing

them together. The electrolyte was introduced by vacuum backfilling and the hole in the counter electrode was sealed by using a hot-melt sealing foil and cover glass.

3.11.5 Experimental Li⁺ doping

Li⁺ doped paste was created by adding aqueous LiCl (ACROS) solution in different concentration (1% and 0.1% with respect to the NiO nanoparticles) in the NiO paste (Ni-Nanoxide N/SP, Solaronix). Then the mixture was stirred for one day. Upon sintering the LiCl turn to the oxide form. Two different sintering temperatures were used, 350 °C and 450 °C. In order to assess the NiO surface, FIB images were taken. The counter electrode used were, commercial counter electrodes (Solaronix Test Cell Platinum Electrodes). The electrolyte comprised I₃⁻/I⁻ 10mM 1:1 in AcCN and TBA⁺ as a counter ion. The dye used was ([Ru(bpy)₂(H1)] WOC53. The experiment was carried, with electrodes with and without dye adsorbed on them, to have a better assess of real DSSC conditions

3.11.6 Cyclic voltammetry

Cyclic voltammetry measurements were performed in a CH instrument (Scanning Electrochemical Microscope). During both measurements done, (in aqueous and in organic solvent) the NiO electrode was used as the working electrode, a platinum electrode (Solaronix Test Cell Platinum Electrodes) was user as the counter electrode and a silver electrode was used as the reference.

3.11.7 Experimental doping with graphene oxide

Two different concentrations of graphene oxide, as doping material in NiO paste were investigated. Graphene oxide (Sigma-Aldrich, 2mg/ml dispersion in H₂O) was added in the NiO paste (Ni-Nanoxide N/SP, Solaronix), the first paste contained 3% w/w of graphene oxide and the second 8% w/w of graphene oxide (with respect to the NiO nanoparticles). Once the graphene oxide particles were added, the paste was stirred overnight.

3.11.8 Mott-Schottky

Three DSSC were prepared (with bare NiO, NiO sensitized with WOC53 and NiO sensitized with P1) the NiO electrodes were prepared as described in section 3.11.4. Commercial platinum counter electrode (Solaronix Test Cell Platinum Electrodes) were used previous to be washed with EtOH and then heated at 450 °C (hot plate) for 30 min to remove volatile organic impurities. The electrolyte used was 0.1 M NaH₂PO₄ and 1M KCl with a pH adjusted to 7 and was introduced from the hole of the counter electrode by vacuum backfilling and the hole in the counter electrode was sealed by using a hot-melt sealing foil and cover glass. The measurements were performed ModuLab[®] XM PhotEchem photoelectrochemical system from Sortatron Analytics, the frequency was kept constant at 10Hz.

Chapter 4 Dyes

4.1 Introduction

The dye or sensitizer is an organic or inorganic molecule that absorbs in the visible spectrum (400-700 nm), has at least one chromophore group and a conjugated system i.e. a structure with alternating double and single bonds and exhibit resonance of electrons, a stabilizing factor in organic compounds¹¹³. In a DSSC the dye has three main parts. First, the anchoring domain which is responsible for the attachment of the dye to the semiconductor surface as for example a carboxylic or a phosphonic acid. Second, a conjugated system providing a good charge mobility and third, one or more ancillary ligands facing towards the electrolyte for inorganic dyes or functional groups with electron donating or electron withdrawing properties in organic dyes in order to enable charge transfer with the electrolyte.

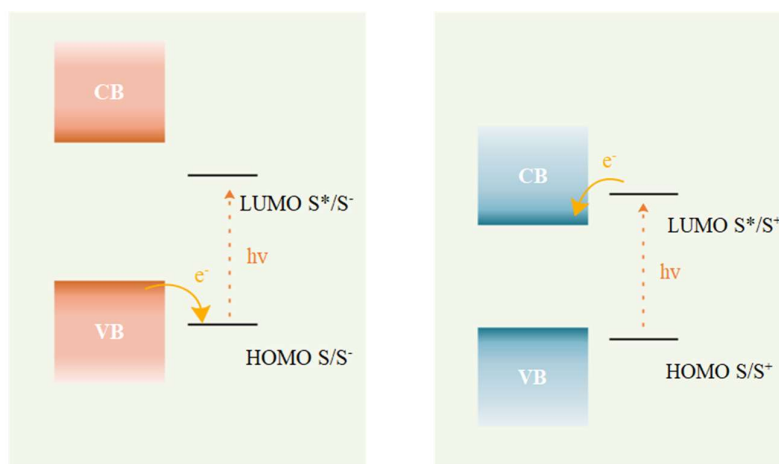


Fig. 4.1: Operating principles of a dye (S): photoexcitation and charge transfer from the semiconductor to the dye for a p-type DSSC (left) and from the dye to the semiconductor for a n-type DSSC (right).

In a p-type DSSC, the dye is excited by the sunlight and transfers an electron from the HOMO to the LUMO of the dye. Then an electron is injected from the valence band of the semiconductor to the

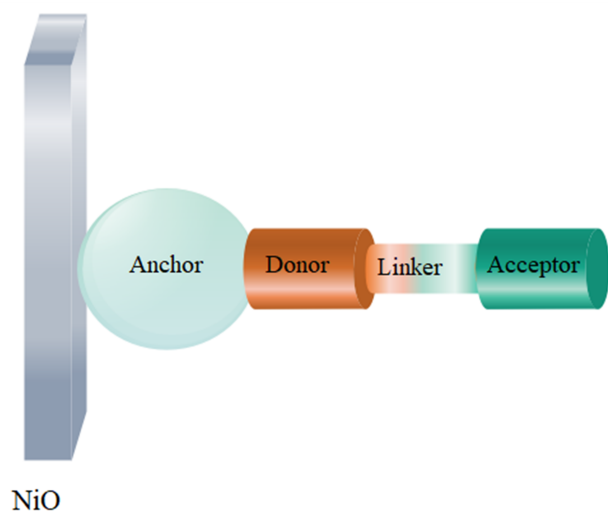


Fig. 4.2: Components of a push-pull dye for a p-type DSSC.

HOMO of the dye. The electron transferred to the LUMO of the dye will be intercepted by the electrolyte with the purpose of reducing the redox couple (Fig. 4.1 left). The constraints for those charge transfers is that firstly the HOMO of the dye should lie in a lower energetic state than the valence band of the semiconductor and secondly the LUMO of the dye should be positioned in a higher energetic level than the redox couple of the electrolyte. In order to deal with these constraints, p-type dyes were designed with a “push-pull” character. There is an electron donor close to the anchoring domain a linker which is a conjugated system for efficient electron transfer, and an electron acceptor remote from the anchor domain (Fig. 4.2)

4.2 Organic dyes for p-type DSSCs

Examples of dyes for p-type DSSCs are illustrated in Fig. 3^{56, 114, 115, 116}. During the work of *Sun and co-workers*¹¹⁴ the first synthesis of a “push-pull” system was reported (dye P1 Fig. 4.3). The triphenylamine moiety being the electron donor and thus “push”-ing side and the malonitrile moiety as electron acceptor and thus “pull”-ing side. DFT calculations during this study support this argument. The calculation shows that the HOMO of the dye is localized on the electron withdrawing part, and the LUMO on the electron accepting part. Various studies, followed the same thought by keeping the same “pull”-ing part and altering the functionalization on the “push”-ing moiety (Fig. 4.3 dyes O7, O2, PT3 and Table 4.1)^{114, 115, 116}. In a recent study, *Jousselem and co-workers*¹¹⁷ produced a series of organic “push-pull” dyes in an effort to tune the absorption spectra towards larger wavelength in order to obtain efficient dyes for tandem DSSCs which will not compete with the absorption of the photoanode. The synthesized dyes comprised of the electron rich triphenylamine moiety functionalized with different groups of increasing electron accepting character: naphthalimide (RBG-174) < 1,3-indandione (COCO) < 1,3-diethyl-2-thiobarbituric acid (BBTX) < 2-(3-oxo-indan-1-ylidene)-malonitrile (COCN). The best performing dye (Fig. 4.3, Table 4.1) of this series was BBTX which had a high absorption coefficient at $\lambda_{\text{max}} = 542$ nm. These sensitizers significantly increase the

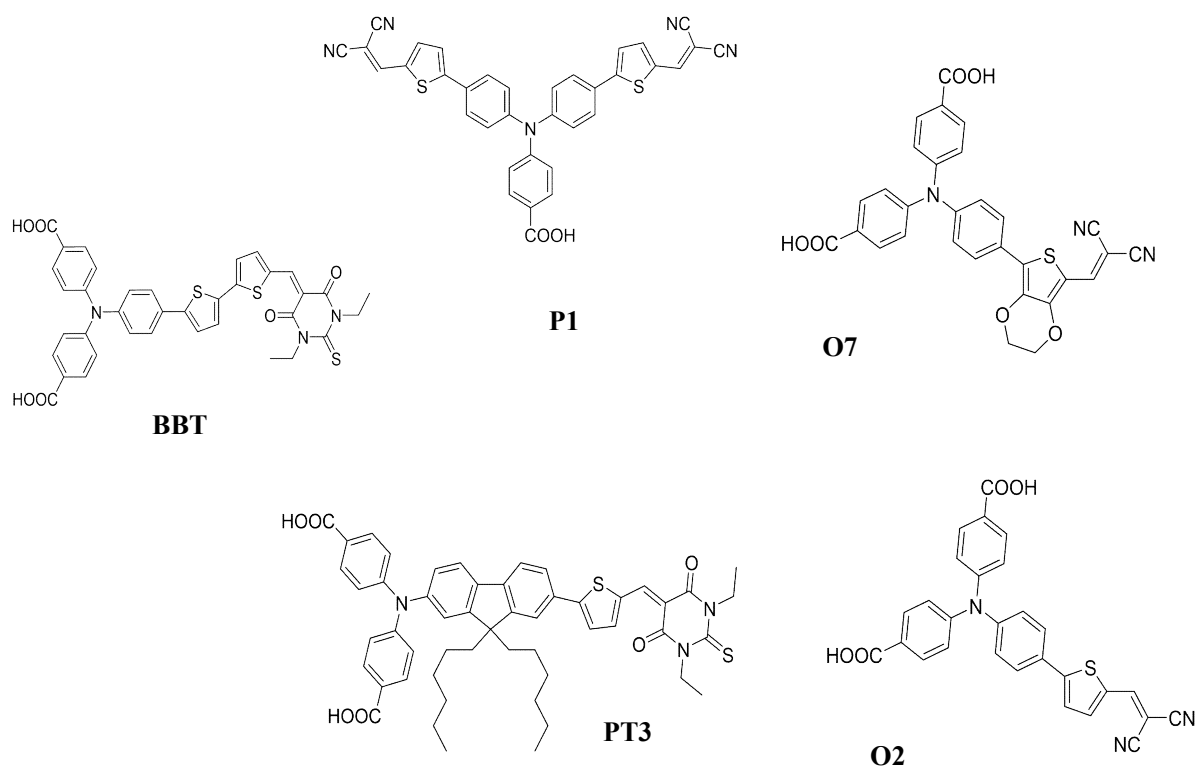


Fig. 4.3: Chemical structures of organic dyes used in p-type DSSCs with a “push-pull” character.

J_{SC} of the DSSCs but the rate of charge loss through recombination remain important. In order to address this problem, *Odobel and co-workers*^{118, 119} synthesized a series of dyes with a longer charge separation character by introducing a secondary electron acceptor moiety to the anchored chromophore part. The dyes were composed of a perylene mono-imide unit (PMI) and an electronically decoupled electron acceptor such as naphthalene diimide (NDI) or fullerene (C_{60}) (Fig. 4.4). These dyes consist of a donor-acceptor system (D-A) where their long-life charge separation depends on the different donors, acceptors and the linkage between them (Fig. 4.4, Table 4.1)^{110, 120, 77, 121}. Another efficient p-type organic dye containing a core of diketopyrrolopyrrole (DPP) (Fig. 4.5, EAG-DPP) functionalized with various electron accepting groups (i.e. Br, $(CN)_2$, NDI) was introduced by *Odobel and co-workers*^{122, 123}. These dyes show exceptional photostability and a strong absorption at 500 nm. In recent work of *Odobel and co-workers*⁵⁴ a replacement of the phenyl group on the DPP core by a thienyl moiety was made enabling an increase in the extinction coefficient along with a red shifted extension of the spectral absorption (Fig. 4.5, Th-DPP, Th-DPP-NDI).

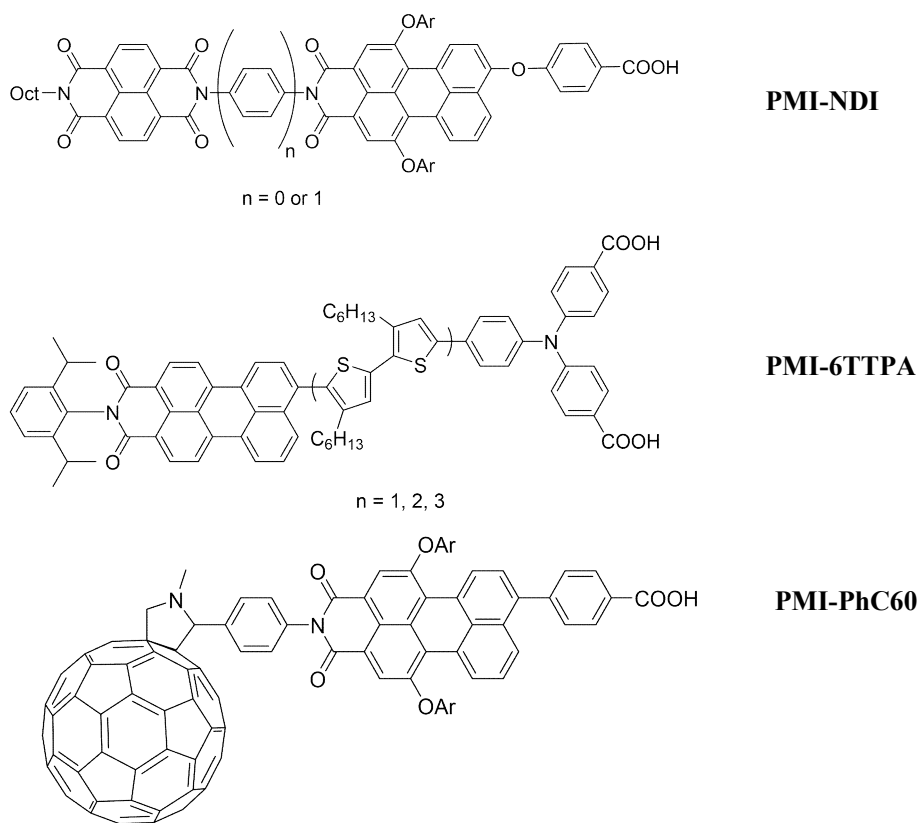


Fig. 4.4: Chemical structures of organic dyes used in p-type DSSC.

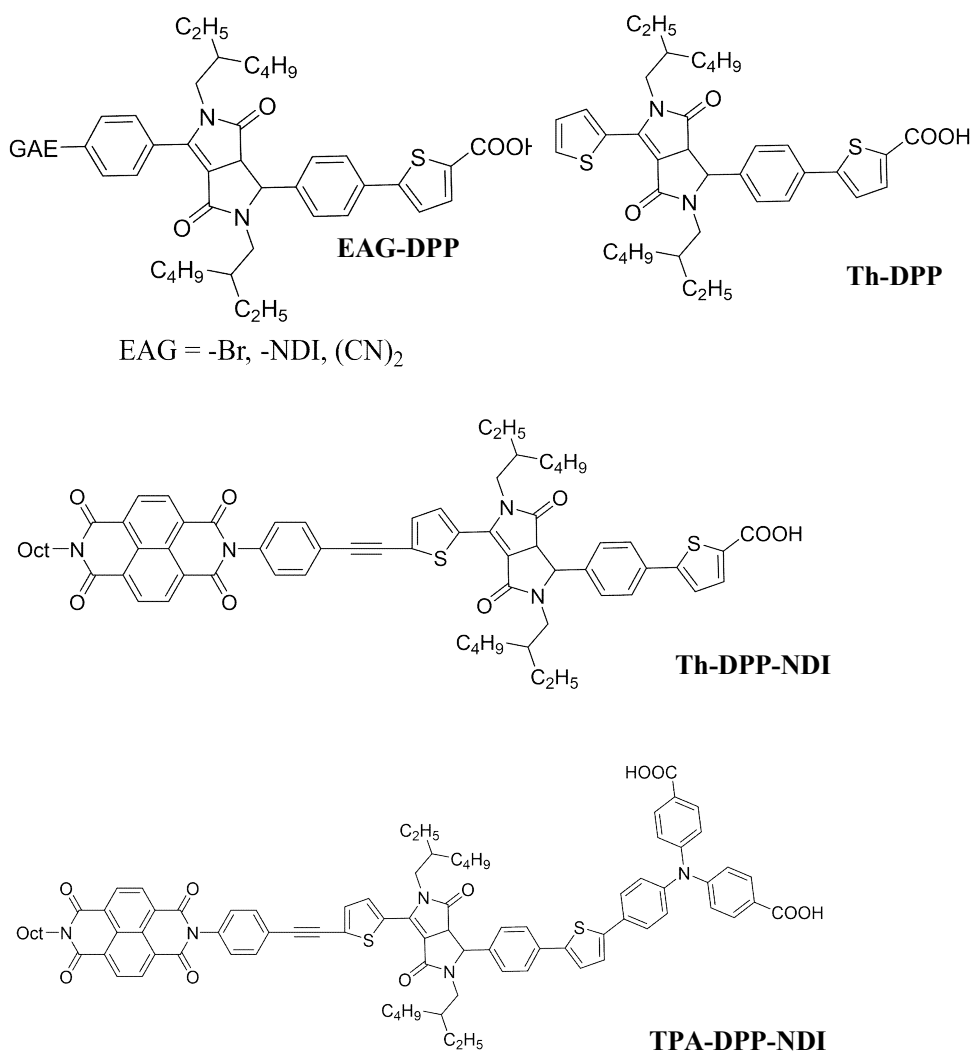


Fig. 4.5: Chemical structures of organic dyes used in p-type DSSCs with a DPP core.

The dye Th-DPP-NDI exhibited a record J_{sc} (Table 4.1) which lead to a good photoefficiency. However, the efficiency of the DSSCs can vary significantly with different electrolytes and the best performing p-type dye is with PMI-6TTPA in combination with $[Fe(acac)_3]^{3+/2+}$ redox couple.

Dyes used for the DSSCs	Electrolyte	$J_{sc}/mA\ cm^{-2}$	V_{oc}/mV	FF/%	$\eta/\%$
<i>P1</i>	I^-/I_3^- In AcCN	1.52	110mV	31	0.05
<i>O2</i>	0.1 M I_2 /1.0 M LiI /0.5 M TBP in AcCN	2.25	125	33	0.093
<i>O7</i>	I^-/I_3^-	1.74	90		0.060
<i>PT3</i>	0.1 M I_2 /1.0 M LiI /0.5 M TBP in AcCN	1.38	113	34	0.053
<i>BBTX</i>	0.1 M I_2 /1.0 M LiI in AcCN	4.32	88	33	0.126
<i>PMI-NDI</i>		1.76	120	34	0.073
<i>PMI-PhNDI</i>	1.0 M LiI / 0.1 M I_2 in PC	1.64	130	34	0.074
<i>PMI-PhC60</i>		1.88	95	32	0.058
<i>PMI-6TTPA</i>	0.03 M I_2 , 0.5 M TBP, 0.6 M BMIMI, 0.1 M GuSCN, AcCN, VN	5.11	294	41	0.61
<i>PMI-6TTPA</i>	0.20 M $nBu_4N[Fe(acac)_3]$, 0.05 M ($[Fe(acac)_3]$), 0.25 M (TBP), 0.05M (LiTFSI), 0.01 M chenodeoxycholic acid in AcCN	6.4	568	52	1.90
<i>DPP-NDI</i>	0.5 M DMBII 0.5 M LiI, 0.1 M I_2 , 0.5 M TBP and 0.1 M GuSCN in AcCN	1.23	135	33	0.05
<i>Th-DPP-NDI</i>	0.1 M I_2 /1.0 M LiI in AcCN	7.38	147	32	0.35
<i>TPA-DPP-NDI</i>		4.04	123	32	0.16

Table 4.1: Performance data with NiO/FTO electrodes. The data were taken from ref. 117-121, 54 and 127. Where: AcCN: acetonitrile, TBP: tert-butylpyridine, PC: propylene carbonate, BMIMI: 1-butyl-3-methylimidazolium iodine, LiTFSI: Lithium bis(trifluoromethanesulfonyl)imide, DMBII: 1-butyl -2,3-dimethyl-imidazolium iodides, GuSCN: guanidinium thiocyanate.

4.2.1 Effect of organic dyes in p-type DSSCs

From previous work done in our group with copper dyes for n-type DSSCs, ^{124, 125} it was proven that the dyes bearing a phosphonic acid group as an anchoring domain outperformed the dyes with a carboxylic acid anchor. During this study ¹²⁶ an organic dye bearing a phosphonic acid as an anchoring domain was synthesized and investigated as a p-type sensitizer. The organic dye (Fig. 4.6, PP1) was structurally related to the benchmarking dye P1 (Fig. 4.6). The synthesis was carried out by Dr. Maximilian Klein ¹²⁶. The synthetic route is described in Fig. 4.7.

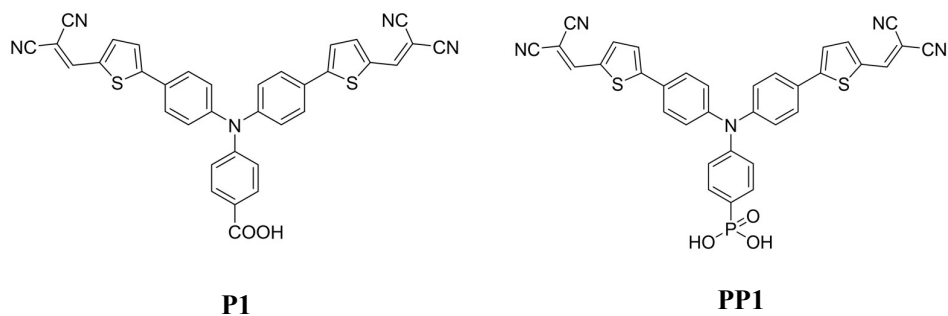


Fig. 4.6: Structure of dyes P1 and PP1.

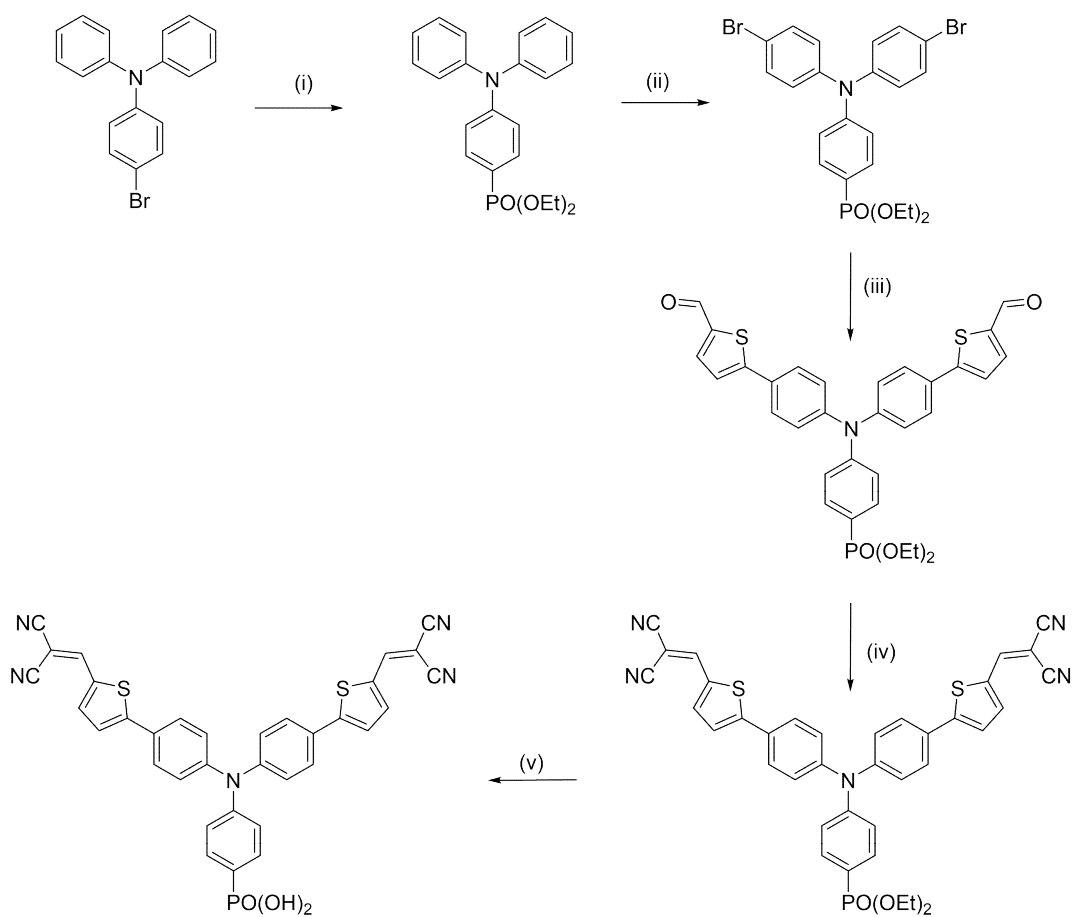


Fig. 4.7: Synthesis of PP1. Conditions: (i) $\text{HPO}(\text{OEt})_2$, Cs_2CO_3 , $[\text{Pd}(\text{PPh}_3)_4]$, dry THF ($120\text{ }^\circ\text{C}$, 20 min microwave reactor). (ii) NBS, THF $60\text{ }^\circ\text{C}$. (iii) 5-(4,4,5,5-tetramethyl-1,3,2-dioxaborolan-2-yl)thiophene-2-carbaldehyde, Cs_2CO_3 , $[\text{Pd}(\text{PPh}_3)_4]$ in dry toluene ($120\text{ }^\circ\text{C}$, 4 h, microwave conditions). (iv) malonitrile, Et_3N in dry AcCN . (v) Me_3SiBr , CH_2Cl_2 , room temperature, 12 h, addition of H_2O .

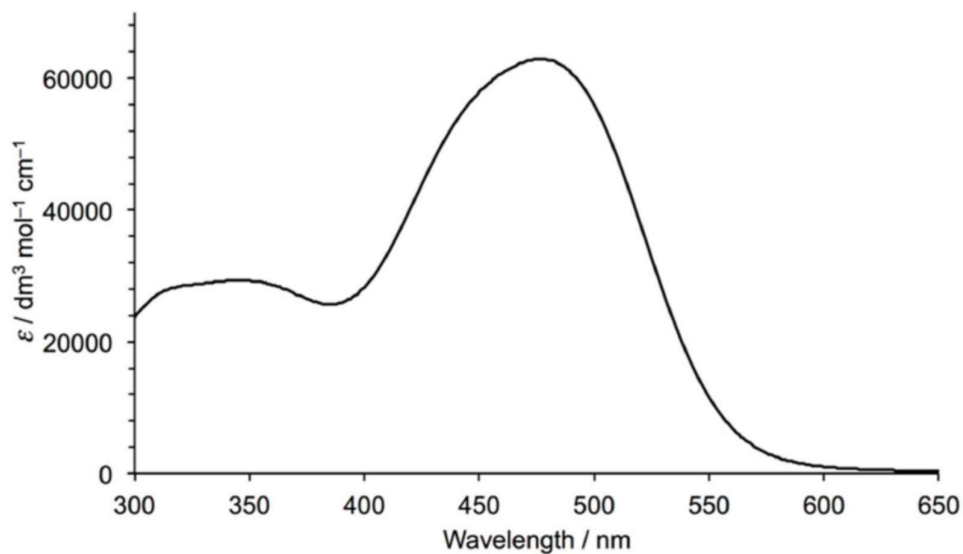


Fig. 4.8: Solution absorption spectrum of PP1 (AcCN, $1.18 \times 10^{-5} \text{ mol dm}^{-3}$)

The solution absorption spectrum of PP1 dye is illustrated in Fig. 4.8. A strong absorption at $\lambda_{\text{max}} = 478 \text{ nm}$, $\epsilon = 62,800 \text{ dm}^3 \text{ mol}^{-1} \text{ cm}^{-1}$ is observed which is similar to the absorption of P1 ($\lambda_{\text{max}} = 476 \text{ nm}$, $\epsilon = 44,559 \text{ dm}^3 \text{ mol}^{-1} \text{ cm}^{-1}$, Fig. 4.26 section 4.3.1). The solid-state UV-Vis absorption spectrum illustrated in Fig. 4.9. The absorption band for PP1 dye on NiO ($\lambda_{\text{max}} = 530 \text{ nm}$) is red-

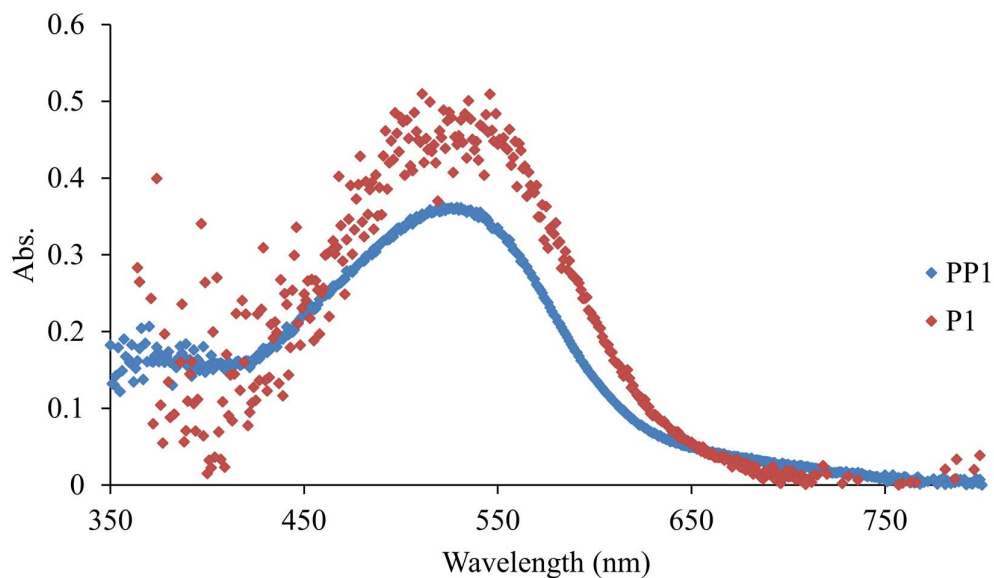


Fig. 4.9: Solid state UV-Vis absorption spectrum of NiO/FTO electrode sensitized with PP1 (blue curve) and P1 (red curve).

shifted with respect to the solution spectra. This red shift is also observed for P1 dye ($\lambda_{\text{max}} = 525 \text{ nm}$) and is attributed to the coupling of the dye with the NiO semiconductor⁵⁶. In order to assess the performance of the dyes as p-type sensitizers, five replicates of DSSCs were fabricated and their performances in terms of JV curves are illustrated in Fig. 4.10 and the data in Table 4.2.

Experiment Name	Jsc/mA cm⁻²	Voc/ mV	FF/%	η/%
P1_1	1.55	130	34	0.068
P1_2	1.80	128	33	0.076
P1_3	1.74	130	35	0.079
P1_4	1.64	125	34	0.071
P1_5	1.76	117	32	0.065
PP1_1	1.45	127	35	0.065
PP1_2	1.45	132	36	0.069
PP1_3	1.32	119	34	0.054
PP1_4	1.43	122	34	0.059
PP1_5	1.11	143	34	0.054

Table 4.2: Performance data for multiple cells and electrolyte comprising of 0.1 M I₂ /1.0 M LiI in AcCN (Std III). The active area of the cell was 0.237 cm². The measurements were done on the day of sealing the cells.

From the JV curves shown in Fig. 4.10 and the data in Table 4.2 we can see that the dyes behave similarly. The J_{SC} of the DSSCs with P1 dye lie in a range 1.55-1.80 mA cm^{-2} and for PP1 1.11-1.45 mA cm^{-2} , and the V_{OC} values are in the range of 117-170 mV for P1 and 119-143 mV for PP1. The comparable values of these two dyes are also reflected on their efficiency values as well as on their fill factor values.

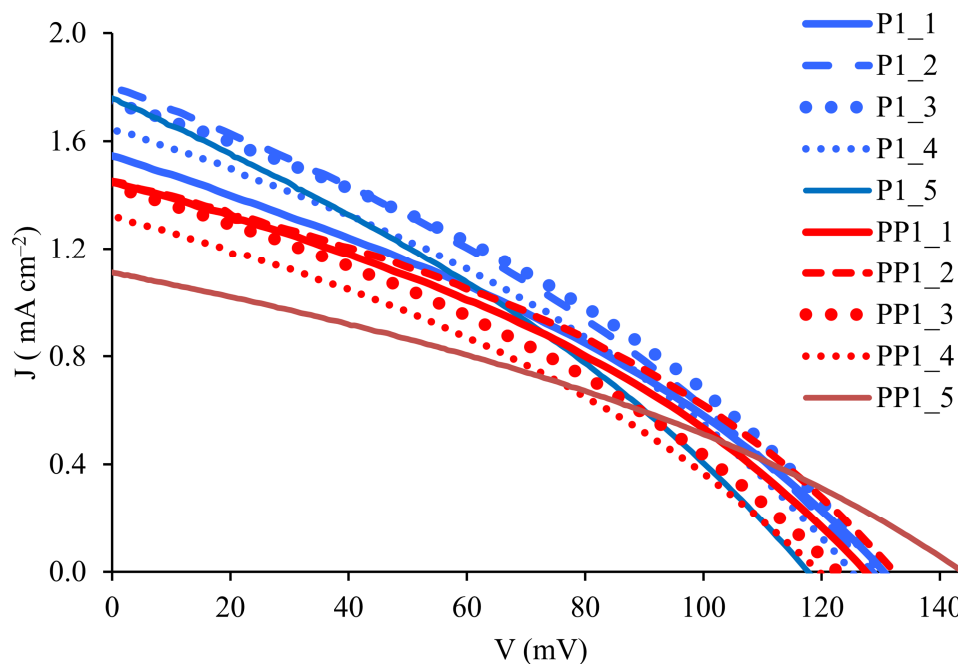


Fig. 4.10: JV curves of the DSSCs with electrolyte comprising of 0.1 M I_2 /1.0 M LiI in AcCN (Std III) and sensitized with P1 and PP1 dyes.

A further investigation of the performance of the DSSCs was made by external quantum efficiency measurements. The external quantum efficiency measurement (also known as incident photon to electron conversion efficiency, IPCE) contains information regarding the light harvesting efficiency (η_{HL}) of the cell, the charge injection efficiency (η_{inj}) and the charge collection efficiency (η_{col}) eq. 4.1

127, 128

$$EQE = \frac{J_{sc}(\lambda)}{q\phi(\lambda)} = \eta_{LH}(\lambda) \eta_{inj}(\lambda) \eta_{col}(\lambda) \quad (4.1)$$

In Fig. 4.11, the external quantum efficiency (EQE) spectra for DSSCs with P1 and PP1 dyes are shown. The spectra are broad (430-600 nm), consistent with charge-carrier injection over the full range of the light absorption for the dyes (see Fig. 4.9). For PP1, $EQE = 10\%$ at $\lambda_{max} \sim 500$ nm and for

P1, EQE = 13.5% at the same wavelength. This value is compared to the 18% reported by *Sun and co-workers*⁵⁶. The EQE data for PP1 and P1 confirm the similar performances of the two dyes, indicating that the replacement of the carboxylic acid anchor in P1 by the phosphonic acid unit in PP1 does not have a significant effect upon electron injection. During the measurement of EQE, the efficiency calculated also includes the reflected photons. In order to obtain a more precise value concerning the incident to electron conversion efficiency, the internal quantum efficiency (IQE) or the absorbed photon to electron conversion efficiency (APCE) must be calculated from equation 4.2, where R is the hemispherical reflectance and T the hemispherical transmittance at a specific wavelength.

$$IQE_{\lambda} = \frac{EQE_{\lambda}}{1-(R_{\lambda}-T_{\lambda})} \quad (4.2)$$

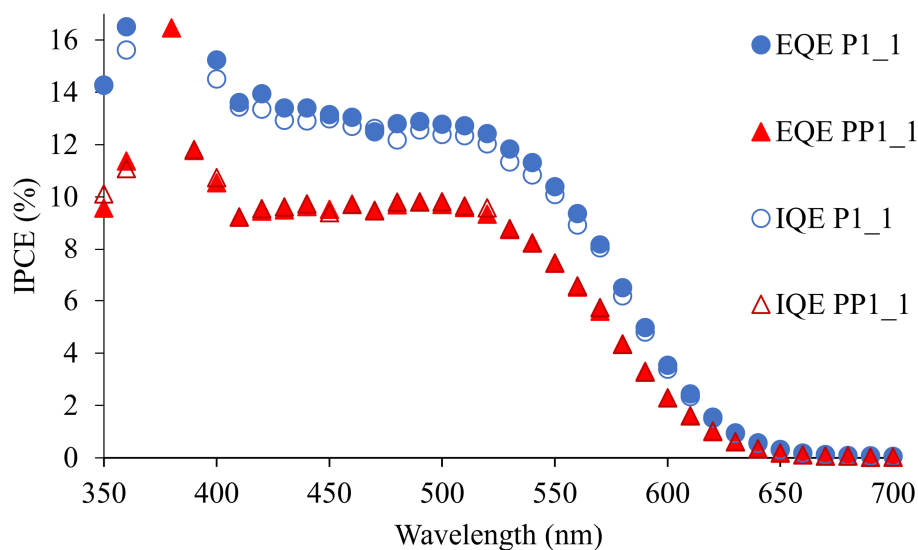


Fig. 4.11: EQE and IQE curves of the DSSCs with electrolyte comprising of 0.1 M I₂ / 1.0 M LiI in AcCN (Std III) and sensitized with P1 and PP1 dye.

From the IQE data points (Fig. 4.11) for the two dyes, it can be concluded that the majority of photons contributes to the J_{SC} of the cells.

In order to compare the performances of P1 and PP1 in more detail, EIS was used to investigate the internal processes and dynamics in each DSSC. A model based on an equivalent electrical circuit is used to represent the DSSC. Nyquist and Bode plots are used to depict the EIS results and parameters which can be extracted from the data include the recombination charge transfer resistance (R_{rec}), electron/hole transport resistance (R_t), charge-transfer resistance at the counter-electrode (R_{Pt}) and the

active layer surface chemical capacitance (C_μ). A Nyquist plot comprises three semicircles, but for p-type DSCs, typically only two semicircles are seen as a consequence of the relative magnitudes of the recombination and ion diffusion impedances. Fig. 4.12 shows the equivalent circuit used in the investigation, and is composed of a series resistance (R_s), a distribution element that consists of the R_t , R_{rec} and constant phase element (CPE, Q_μ) of the NiO/electrolyte interface ¹²⁹. Values of R_t , R_{rec} and Q_μ are derived from the individual values of r_t , r_{rec} and q_μ ^{130, 131, 132} and the resistance and constant phase element of the platinum counter electrode (R_{CE} , Q_{CE}). In this study, a resistance - constant phase element (R-CPE) circuit was employed, because of the surface irregularities of the NiO electrode ¹³³.

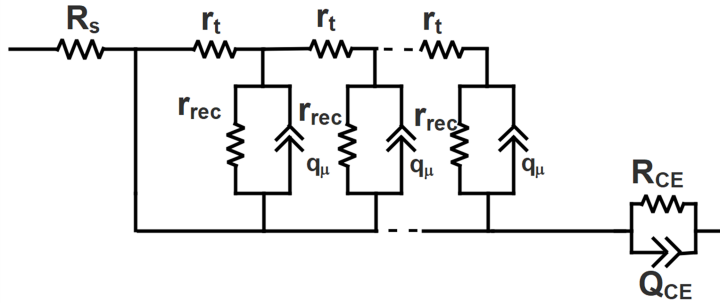


Fig. 4.12: Equivalent circuit used to fit the EIS data.

To account for this, the pre-factor term Q of the CPE was corrected using eq. 4.3 ^{134, 133} in which α is an empirical constant, to calculate the capacitance. Fig. 4.13 shows Nyquist plots for DSSCs sensitized

$$C_\mu = \{(R_{rec})^{1-\alpha} Q\}^{1/\alpha} \quad (4.3)$$

with P1 or PP1, and parameters obtained from the fitting are presented in Table 4.3. The first semicircle at high frequencies (seen in the expansion in Fig. 4.13b) is attributed to the platinum counter electrode charge transfer process while the semicircle at lower frequencies is ascribed to charge transfer processes at the NiO/electrolyte interface. Table 4.3 shows that the DSSC sensitized with PP1 exhibits a higher recombination resistance (R_{rec}) while the DSSC containing P1 exhibits a lower transport resistance and a much higher capacitance. The similar overall performances of the DSSCs (Table 4.2) indicate that these factors essentially offset one another. The Bode plots for DSSCs with the two dyes are shown in Fig. 4.14. Since the hole lifetime is inversely related to the value of the maximum frequency (f_{max}) ¹³⁵, the Bode plots demonstrate that the cell sensitized with PP1 ($f_{max} = 31.6$ Hz) exhibits a smaller hole lifetime (τ_n) than that containing the carboxylic acid-anchored dye P1 ($f_{max} = 9.9$ Hz). Indeed, from eq. 4.4, ¹³⁶ the hole lifetime can be calculated and it was found that the hole

$$\tau_n = R_{rec} C_\mu \quad (4.4)$$

life time of DSSC sensitized with PP1 is shorter ($\tau_n = 0.096$ ms vs. 0.32 ms for DSSC sensitized with P1 dye).

Cell Name	R_s/Ω	R_{Pt}/Ω	$C_{Pt}/\mu F$	R_t/Ω	R_{rec}/Ω	$C_\mu/\mu F$	a
P1_1	17.7	4.8	7.9	1.9	507.1	485.6	0.70
PP1_1	11.1	2.0	20	8.3	729.9	96.5	0.88

Table 4.3: EIS data obtained from measurements at a light intensity of 22 mW cm⁻² of p-type DSSCs containing FTO/NiO working electrodes, sensitized with P1 or PP1 and electrolyte comprising of 0.1 M I₂, 1 M LiI in AcCN.

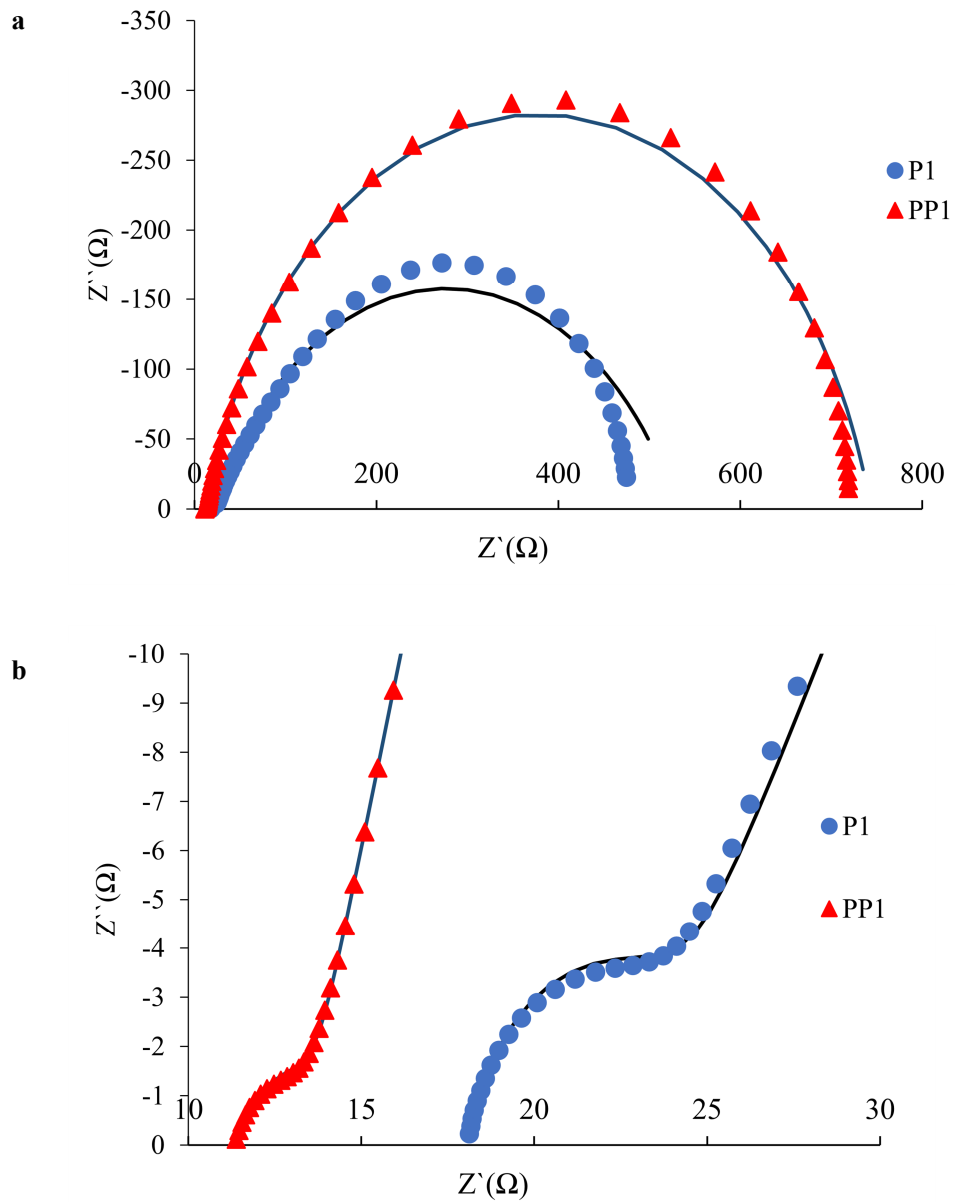


Fig. 4.13: **a.** Nyquist plots and **b.** expansion of Nyquist plots up to $Z' = 30 \Omega$ for DSSCs with NiO/FTO electrodes and electrolyte comprising of 0.1 M I_2 , 1 M LiI in AcCN. The NiO electrodes were sensitized with P1 or PP1.

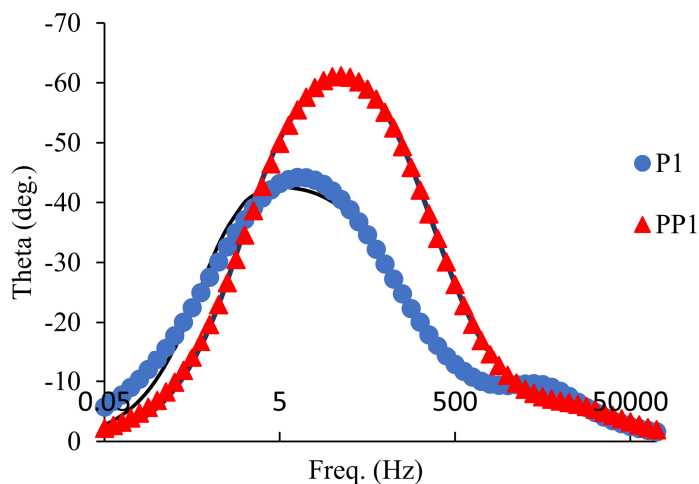


Fig. 4.14: Bode plots for DSSCs with NiO/FTO electrodes and electrolyte comprising of 0.1M I₂, 1M LiI in AcCN. The NiO electrodes were sensitized with P1 or PP1.

Under open-circuit voltage conditions, the band gap between the valence band and the conduction band of the semiconductor is at its lowest value, and the rates of charge-carrier injection and recombination are equal. From eq. 4.5, the lifetime of the charge, τ_n , can be extracted^{137 138}. However, since the photovoltage decay is a dark measurement, the data concern only the recombination process with the electrolyte and not the recombination path with the anchored dye¹³⁹.

$$\tau_n = -\frac{k_B T}{e} \left(\frac{dV_{OC}}{dt} \right)^{-1} \quad (4.5)$$

Fig. 4.15a displays the voltage decay profiles for DSSCs containing dyes P1 or PP1, and demonstrates that the decay of V_{OC} is more rapid for PP1 than for P1. By using eq. 4.5, the lifetime versus voltage plot shown in Fig. 4.15b is obtained which shows that the lifetime of the P1-sensitized DSSC remains longer with increased voltage. The DSSC sensitized with PP1 exhibits a greater drop in lifetime at lower voltages which in turn translates to a more dominant charge recombination process with the electrolyte for PP1 versus P1.

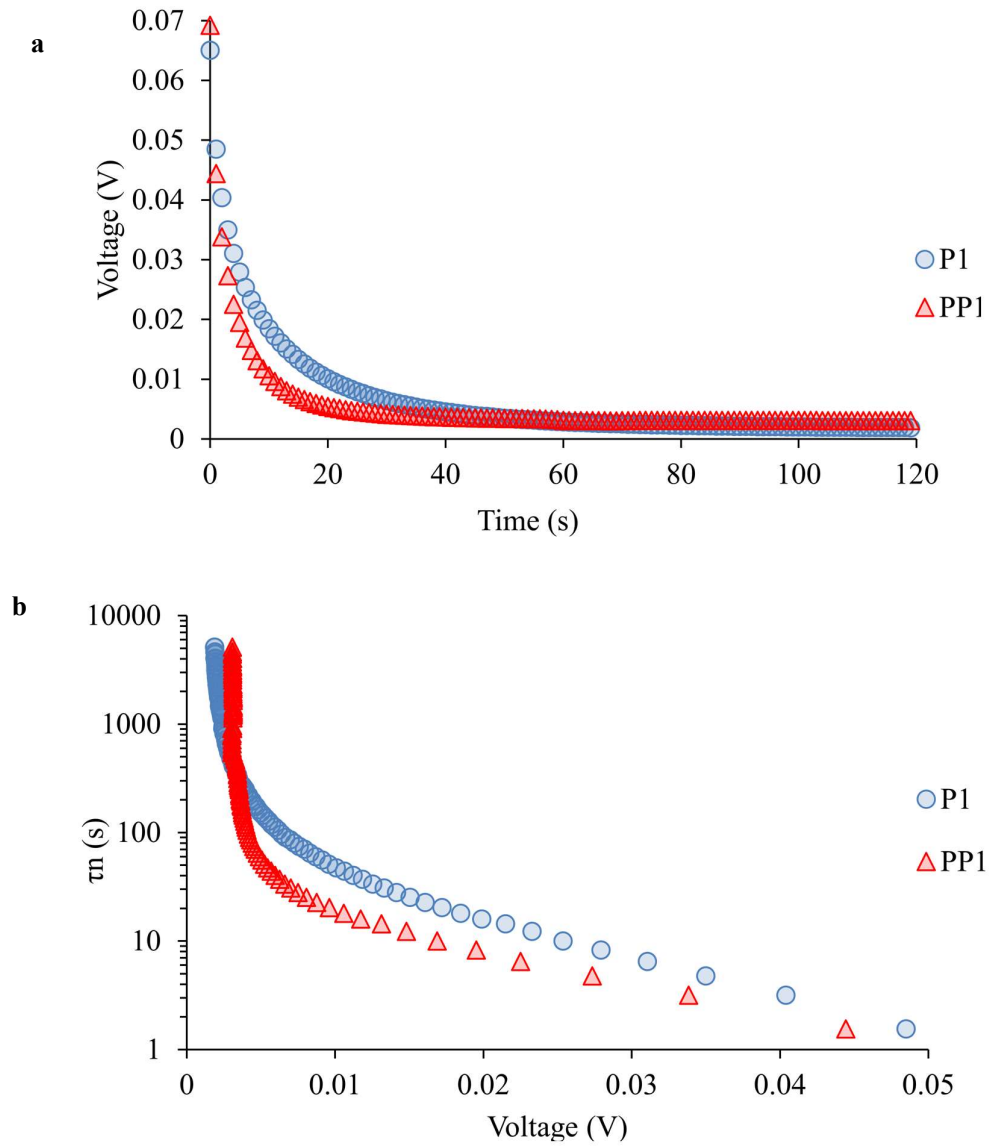


Fig. 4.15: **a.** Open-circuit voltage decay vs. time. **b.** Electron lifetime vs. open circuit voltage at light intensity of 22 mW cm⁻².

The diffusion length (L_d) of the charge in the NiO semiconductor is also important in defining the efficiency of the DSSC and can be calculated from eq. 4.6^{136, 139} where τ_0 is the free charge lifetime and D_0 is the free charge diffusion coefficient.

$$L_d = \sqrt{\tau_0 D_0} \quad (4.6)$$

In an n-type DSSC, the diffusion length should be 2-3 times larger than the thickness of the TiO_2 semiconductor for efficient charge collection¹³⁷. However, in p-type DSSCs, this ratio is difficult to achieve due to the intrinsic properties of the p-type semiconductor²⁶. Intensity-modulated photocurrent spectroscopy (IMPS)^{140 141} at different light intensities was used to calculate the chemical diffusion coefficient (D_n) of the P1 and PP1 sensitized cells. During this measurement, the cell is potentiostatically controlled and the photocurrent is measured with no bias applied. Since the measurement is done under short-circuit conditions, the semiconductor band gap is at a maximum and no charge is exchanged at the semiconductor /electrolyte/dye interface. As a consequence, charges migrate to the back layer of the photocathode where most reactions occur, so the charge transport time, as well as the diffusion length coefficient can be calculated¹³⁹. From Fig. 4.16, it can be seen that the diffusion lengths of both the P1 and PP1-sensitized cells are similar and follow the same trend, only increasing slightly as the light intensity increases. This indicates a similar mechanism for the movement of the charge in the semiconductor for both dyes. The dependence of D_n on light intensity is not as great for p-type as in n-type DSSCs²⁸, attributed to different mechanisms for the migration of

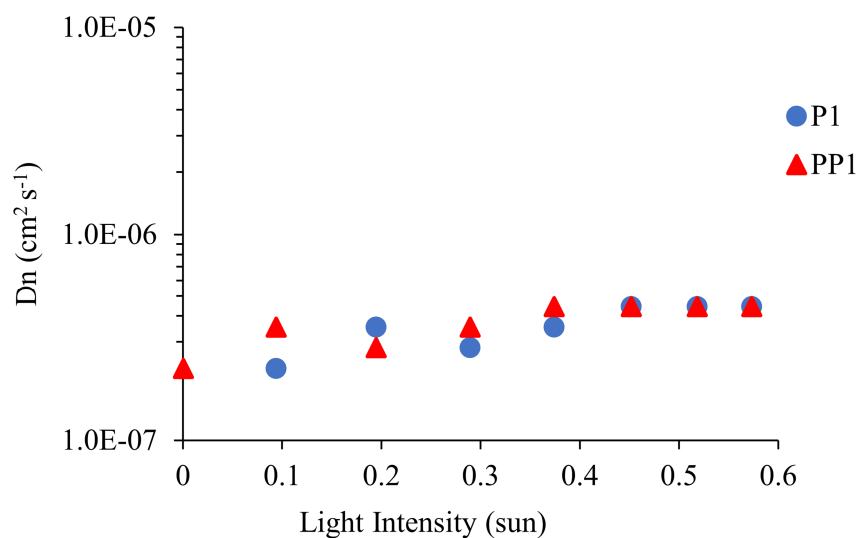


Fig. 4.16: Chemical diffusion coefficient for DSSCs with P1 or PP1 at different light intensities.

charge carriers (hopping as opposed to a trapping-detrapping mechanism)^{142 143}.

In conclusion, the first organic dye, PP1 for p-type DSSCs bearing a phosphonic acid anchor was synthesized. The DSSCs with P1 or PP1 performed similarly but from EIS measurements the hole lifetime for the DSSC sensitized with PP1 was greater compared with the P1-sensitized cell. Moreover, from open circuit voltage decay measurements a more significant charge recombination with the LiI/I₂ electrolyte was observed for the DSSC sensitized with PP1.

4.3 Inorganic dyes for p-type DSSCs

Inorganic dyes are known to have a better thermal and chemical stability compared to organic dyes. Moreover, due to the metal-to-ligand charge transfer in inorganic dyes a broader absorption spectrum

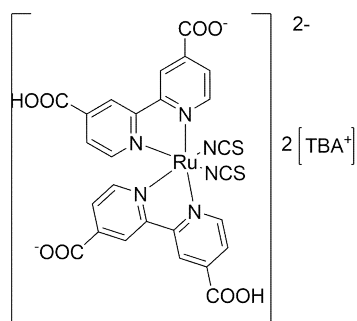


Fig. 4.17: Chemical structure of N719 dye¹⁰.

can be expected. The first n-type DSSC reported by O'Regan and Grätzel¹⁰, was sensitized by a Ru(II) complex (N719, Fig. 4.17) in which the anchoring domains consisted of carboxylate groups attached to the N[^]N (bpy) domains where the LUMO character is localized. For an efficient cyclometallated Ru(II) p-type dye, according to Fig. 4.2 in order to obtain an efficient charge separation the LUMO should be localized at the ancillary ligands and the HOMO onto the anchoring domain. In cyclometallated Ru(II) as such in Fig. 4.18, after DFT calculations (Fig. 4.19) the HOMO was found to be localized on the anchoring domain of the dye due to the strong σ -donating properties of the carbon anion in the anionic C[^]N ([ppy]⁻) ligand and the LUMO was localized on the N[^]N (bpy) domain¹⁵⁶. Such dyes were reported by *Wu and co-workers*¹⁴⁴ (Fig. 4.18 dyes: O8, O11, O12). The J_{SC} (Table 4.4) of DSSC fabricated using these dyes increases with increased phenyl spacer (J_{SC O6} < J_{SC O11} < J_{SC O12}) which indicates a better charge separation by adding longer spacers. Later work done by *Wu and co-workers*¹⁴⁵ aimed at an increase of J_{SC} after inserting a triphenylamine moiety (Fig. 4.18 dye: O3). By changing the N[^]N ligand to 1,10-phenanthroline (O13) or 4,7-diphenylphenanthroline (O17), the absorption of the dye increased but not the J_{SC} (Table 4.4).

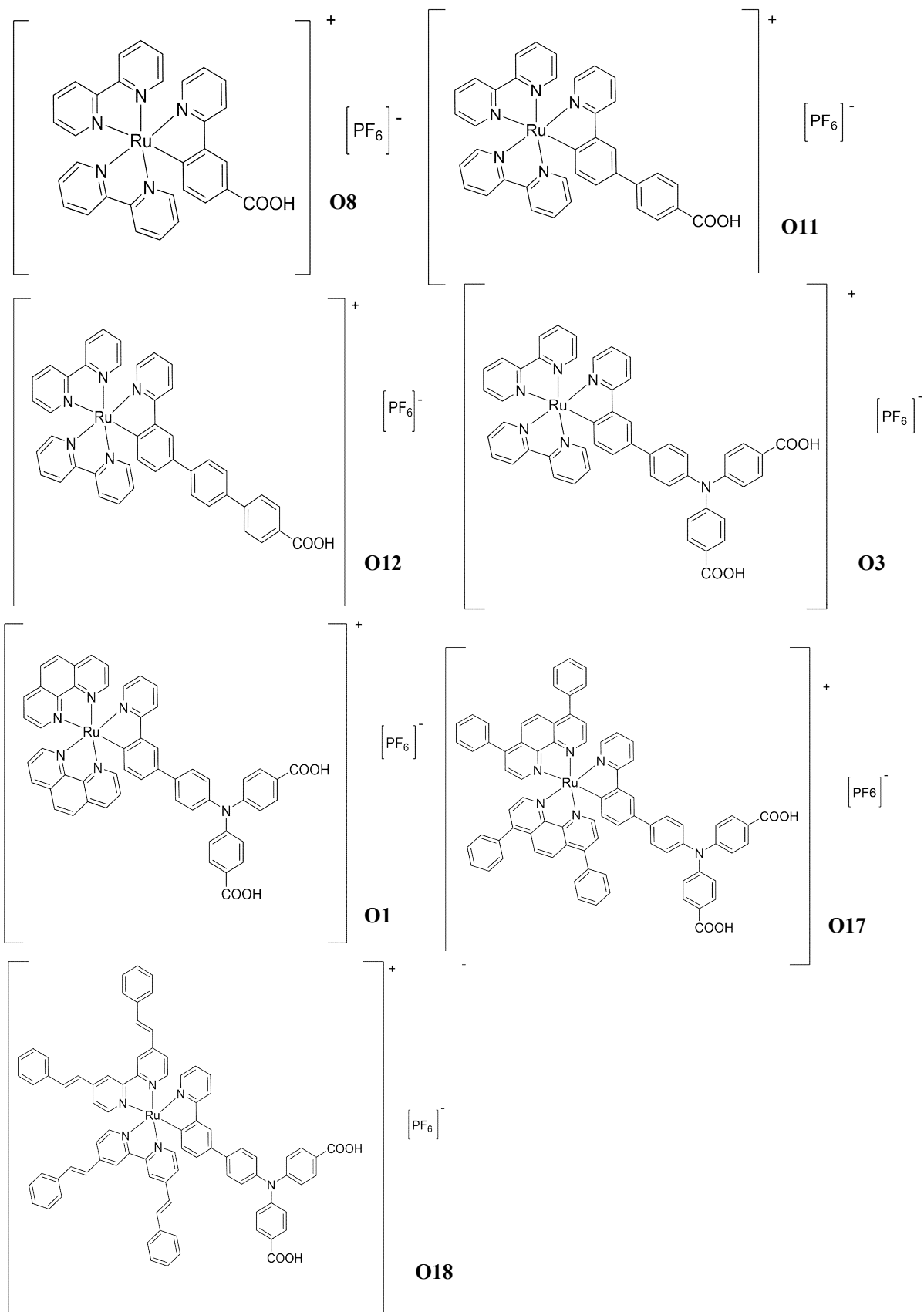


Fig. 4.18: Chemical structures of cyclometallated Ru(II) dyes synthesized in the work of *Wu and co-workers*¹⁴⁴⁻¹⁴⁶.

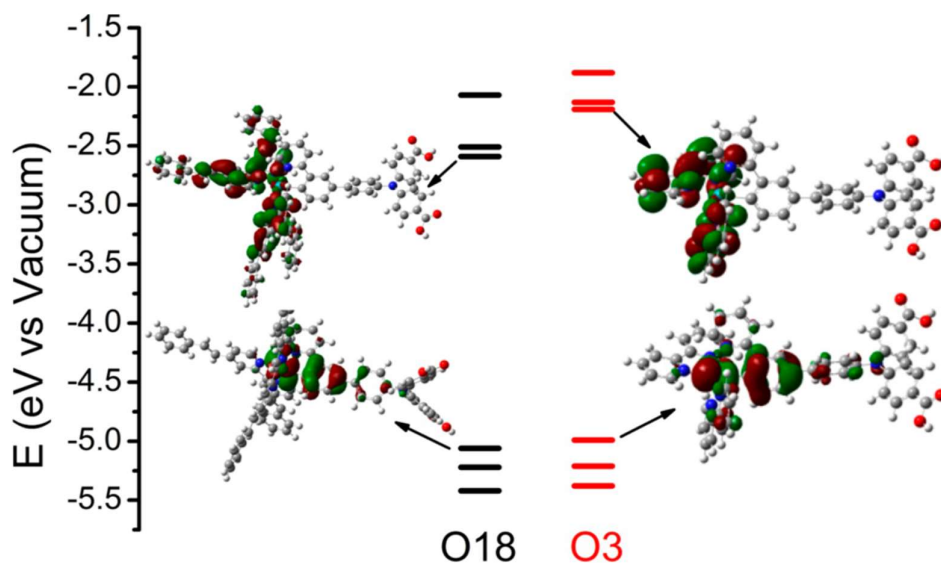


Fig. 4.19: Isodensity plots of HOMO and LUMO and the energy levels of the frontier orbital obtained by TD-DFT calculation for dyes O3, O18 (see Fig. 4.18). Reprinted with permission from *Wu and co-workers*¹⁴⁶. Copyright 2014 American Chemical Society

In a more recent study Wu and co-workers¹⁴⁶ synthesized a panchromatic cyclometallated Ru(II) dye (O18, Fig. 4.18) with the highest $J_{SC} = 3.43 \text{ mA cm}^{-1}$ among this series (Table 4.4). The good performance of O18 dye was due to the extension of the MLCT absorption spectra compared to the next best dye synthesised by this group O3 (593 vs. 543 nm for O18 and O3 dye accordingly). DFT calculations showed that the HOMOs for both dyes were localized on the Ru centre and partially delocalized onto the anionic C⁻N ligands as seen in Fig. 4.19. The LUMOs of the dyes were localized on the bpy ligands of the dyes but for O18, a decrease of 0.4 eV was observed which explains the

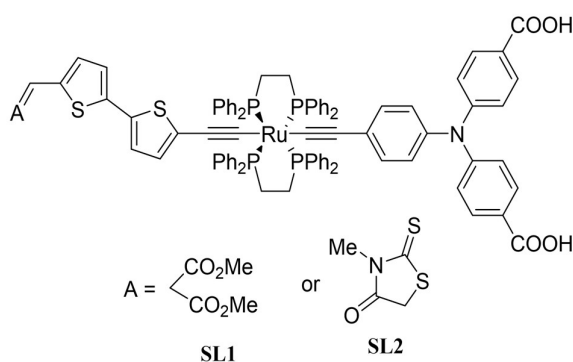


Fig. 4.20: Chemical structures of SL1 and SL2 p-type dyes¹⁴⁷

extension of the π -conjugated system of this dye¹⁴⁶ (Fig. 4.19). In a more recent work, neutral organometallic ruthenium complexes with a “push-pull” character were synthesised from *Odobel and co-workers*¹⁴⁷. These dyes consist of a ruthenium-diacetylide complex with a triphenylamine functionalized with two carboxylic groups in the role of the anchoring ligand and an electron withdrawing group (acrylic ester or rhodanine) separated by bithienyl spacers (Fig 4.20, SL1 and SL2). The most efficient dye among the

The most efficient dye among the

two tested did not exceed an efficiency of 0.079% (Table 4.4) that was due to moderate hole injection driving forces. In the work of *Odobel and co-workers*¹⁵³ different anchoring domains, on trisbipyridine Ru(II) complexes were tested (Fig. 4.21, Table 4.4). It was concluded that replacing the carboxylic acid anchor by a methyl phosphonic acid Ru(bpy)₃CH₂PO₃H anchor or a catechol moiety Ru(bpy)₃C₂H₂C₆H₃(OH)₂ increased the efficiency of the cells. These results were justified due to a better binding affinity with the NiO surface of the dye bearing a methyl phosphonic acid anchor or due to an enhance in the electron coupling with the semiconductor of the dye bearing a catechol anchor. Other metals have also been used for the preparation of inorganic p-type dyes.

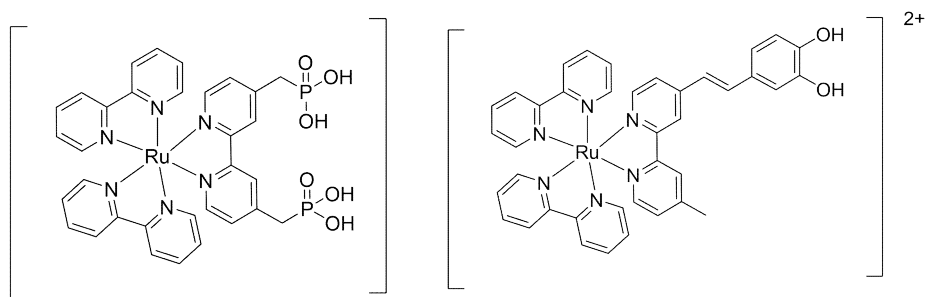


Fig. 4.21: Chemical structures of trisbipyridine Ru(II) complexes¹⁵³

Reports for cyclometallated iridium(III) complexes¹⁴⁸, (Fig. 4.22, IrDPQCN2) exhibit a low J_{SC} but a very high V_{OC} (Table 4.4) due to the $Co^{2+/3+}$ redox couple in the electrolyte used. In other work, cyclometallated iridium(III) complexes (Fig. 4.22, AS14) showed a higher photocurrent density when combined with an iodine/triiodide redox couple in the electrolyte but an overall lower efficiency¹⁴⁹ (Table 4.4). Studies have also been conducted for the synthesis of zinc-porphyrin p-type sensitizers. *Spicca and co-workers*¹⁵⁰ incorporated triphenylamine with two carboxylic acids as the electron acceptor and perylenemonoimide as the electron donor moiety. In order to enhance the charge separation, fluorene with two aliphatic hexyl chains was introduced between the porphyrin and the triphenylamine moiety. The efficiency of the cells showed an improvement compared to previous studies. This is mainly due to the exceptional $J_{SC} = 4.4 \text{ mA cm}^{-2}$ (Table 4.4).

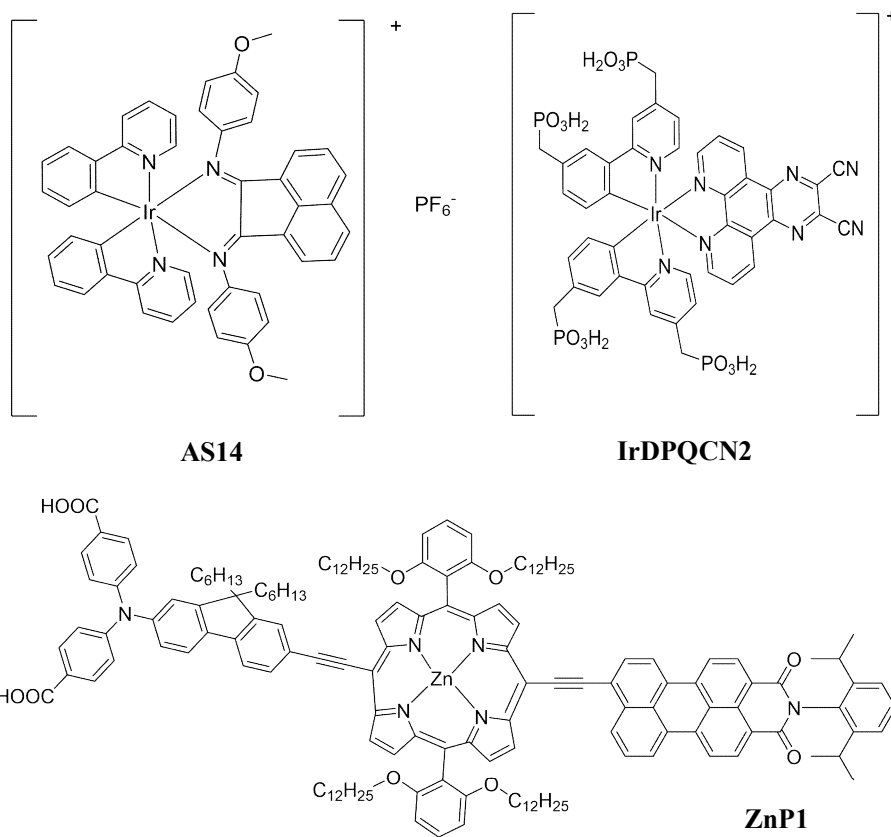


Fig. 4.22: Chemical structures of cyclometallated Ru(II), Ir(III) and Zn-porphyrin dyes used in p-type DSSCs ¹⁶⁰⁻¹⁶²

Dyes used for the DSSCs	Electrolyte	Jsc/mA cm ⁻²	Voc/ mV	FF/%	η/%
O8	0.1 M I ₂ /1.0 M LiI in AcCN	0.44	63	36	0.009
O11		1.16	79	36	0.033
O12		1.84	82	34	0.051
O3		3.04	93	35	0.099
O13		2.66	89	31	0.074
O17		2.69	92	34	0.085
O18		3.43	100	36	0.104
Ru(bpy) ₃ MePO ₃ H	0.1 M I ₂ /1.0 M LiI in AcCN	0.78	95	34	0.025
Ru(bpy) ₃ phen(OH) ₂		0.65	85	32	0.018
SL1	0.6 M DMBII 0.03 M I ₂ , 0.5 M TBP and 0.1 M GuSCN in AcCN	2.25	104	34	0.079
AS14	0.1 M I ₂ /1.0 M LiI in AcCN	1.12	100	36	0.043
IrDPQCN 2	Co(dtbp) ₃ ^{3+/2+}	0.25	508	54	0.068
ZnP1	0.20 M ⁿ Bu ₄ N[Fe(acac) ₃], 0.05 M [Fe(acac) ₃], 0.25 M TBP, 0.05M LiTFSI, 0.01 M chenodeoxycholic acid	4.4	465	45	0.92

Table 4.4: Performance data for p-type DSSCs with NiO/FTO electrode the data were taken from ref. 146-162, 164. Where: AcCN: acetonitrile, TBP: tert butylpyridine, DMBII: 1-butyl -2,3-dimethylimidazolium iodides, GuSCN: guanidinium thiocyanate, LiTFSI: Lithium bis(trifluoromethanesulfonyl)imide, Co(dtbp)₃^{3+/2+}: 4,4'-di-tert-butyl-2,2'-bipyridine)-cobalt(II/III).

4.3.1 Effects of using cyclometallated ruthenium(II) dyes in p-type DSSCs

During this thesis, p-type cyclometallated ruthenium(II) dyes were synthesized by Felix Brunner¹⁵¹ and Cedric Wobill¹⁵². For the first time, a phosphonic acid was introduced as the anchoring domain in cyclometallated dyes. The approach followed to introduce the anchoring domain can be applied for a variety of anchors. This synthetic step consists of a Suzuki reaction between 2-bromo-4-chloropyridine and phenyl boronic acid to produce H1 (defined in Fig. 4.24) and a cyclometallation reaction to synthesize $[\text{Ru}(\text{bpy})_2(\mathbf{1})][\text{PF}_6]$, followed by a Suzuki-Miyaura coupling of $[\text{Ru}(\text{bpy})_2(\mathbf{1})]^+$ with 4-carboxylic acid phenylborate ester or 4-phosphonic acid phenylborate ester using SPhos Pd G2 as catalyst to synthesize the two ruthenium(II) cyclometallated complexes shown in Fig. 4.24. The protonation states of the anchoring groups in the two complexes were initially investigated by electrospray ionization mass spectrometry (ESI-MS). A peak at m/z 724.2 and at 688.1 for the cyclometallated ruthenium(II) phenyl phosphonic acid complex and for the cyclometallated ruthenium(II) phenyl carboxylic acid complex respectively were detected. These results were not clear since the peak at m/z 724.2, could arise from either $[\text{M} + \text{H}]^+$ for M being the zwitterion WOC53 (as shown in Fig. 4.24) or from $[\text{M} - \text{PF}_6]^+$ where M is the salt with the phosphonic acid in its full protonation state. Also, the peak at m/z 688.1 could arise from either the $[\text{M} - \text{PF}_6]^+$ where M is the salt WOC58 as shown in Fig. 4.24, or $[\text{M} + \text{H}]^+$ where M is the zwitterion carrying a carboxylate group. Elemental analysis for the cyclometallated ruthenium(II) phenyl phosphonic acid complex agreed with the zwitterion structure, which was further supported by the ^{31}P NMR spectrum for which the isolated cyclometallated ruthenium(II) phenyl phosphonic acid complex showed no signal for PF_6^- and a signal at $\delta +10.8$ ppm. After the addition of vapours of trifluoroacetic acid (TFA), this peak shifted to $\delta +15.2$ ppm. The addition of solid K_2CO_3 to the same NMR tube shifted the peak to lower frequency again (Fig. 4.23). This observation led to the conclusion that the complex was the zwitterion WOC53. The ^{31}P NMR spectrum of the cyclometallated ruthenium(II) phenyl carboxylic acid complex showed a septet at $\delta -144.7$ ppm characteristic of the hexafluoridophosphate anion so it was concluded that the complex was the salt WOC58 illustrated in Fig. 4.23¹¹⁵.



Fig. 4.23: 162 MHz $^{31}\text{P}\{^1\text{H}\}$ NMR spectrum of WOC53 (*) in CD_3OD and spectra taken after the addition of (i) $\text{CF}_3\text{CO}_2\text{H}$ (TFA, blue) (ii) K_2CO_3 (green) (iii) $\text{CF}_3\text{CO}_2\text{H}$ followed by K_2CO_3 (red). Reprinted with permission from *Housecroft and co-workers*¹⁵¹. Copyright 2016, Royal Society of Chemistry.

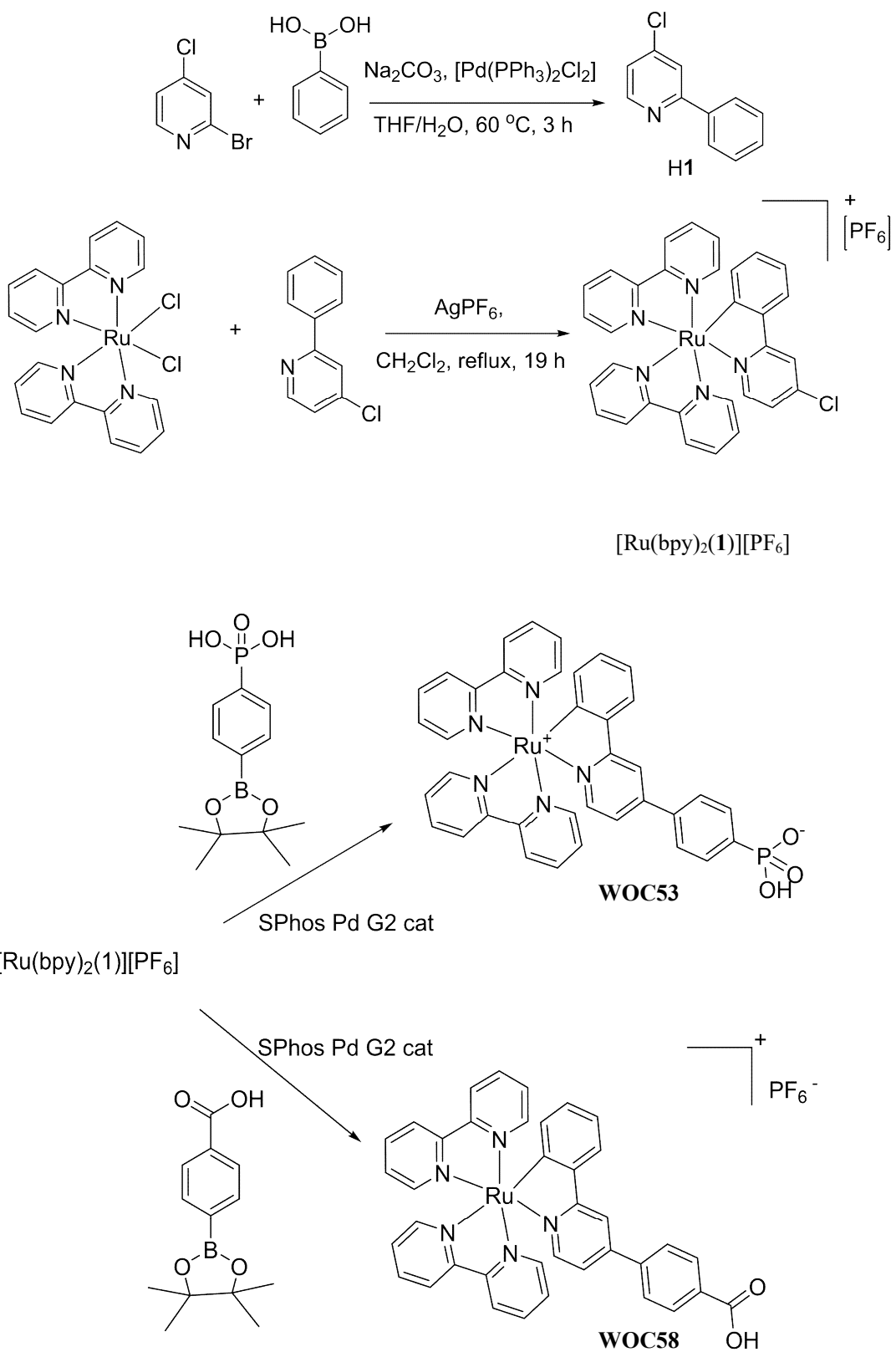


Fig. 4.24: i) Suzuki reaction to produce **H1** ii) cyclometallation reaction to synthesize $[\text{Ru}(\text{bpy})_2(\mathbf{1})][\text{PF}_6]$ iii) Suzuki-Miyaura coupling to synthesize **WOC53** and **WOC58**.

Moreover, DFT calculations performed by Prof. Catherine Housecroft, (Fig. 4.25), showed that the HOMO of the dye WOC53, is localized on the anchoring domain located on the cyclometallating ring and the LUMO on the bpy domains. These results indicate that WOC53 follows the conformed chemical structure for p-type ruthenium(II) cyclometallated dyes as was explained in section 4.3.1.

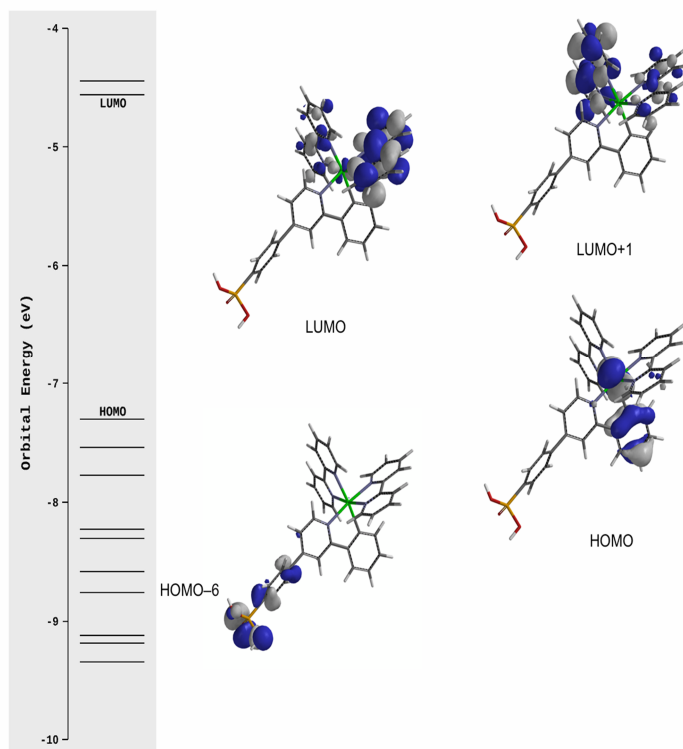


Fig. 4.25: Results of a DFT calculation for the cyclometallated ruthenium(II) dye WOC53, with the phosphonic acid anchoring group in his fully protonated state. The structure was optimised at PM3 semi-empirical level then this structure was used as the input file for a ground state energy calculation

The cyclic voltammetry (CV) measurements made by Felix Brunner for WOC53 and WOC58 are illustrated in Table 4.5.

Complex	$E^{\text{ox}}_{1/2}/\text{V}$	$E^{\text{red}^1}_{1/2}/\text{V}$	$E^{\text{red}^2}_{1/2}/\text{V}$	$E^{\text{red}^3}_{1/2}/\text{V}$	$\Delta E_{1/2}/\text{V}$
WOC53	0.63	1.31	1.60	2.20	2.64
WOC58	0.70	1.33	1.58	2.19	2.66

Table 4.5: Redox potentials for WOC53 (degassed DMSO solution) and WOC58 (degassed AcCN solution) vs. Fc/Fc^+ and calculated for NHE, 0.1 $[\text{nBu}_4\text{N}][\text{PF}_6]$ as supporting electrolyte and scan rate of 0.1 V s^{-1} .

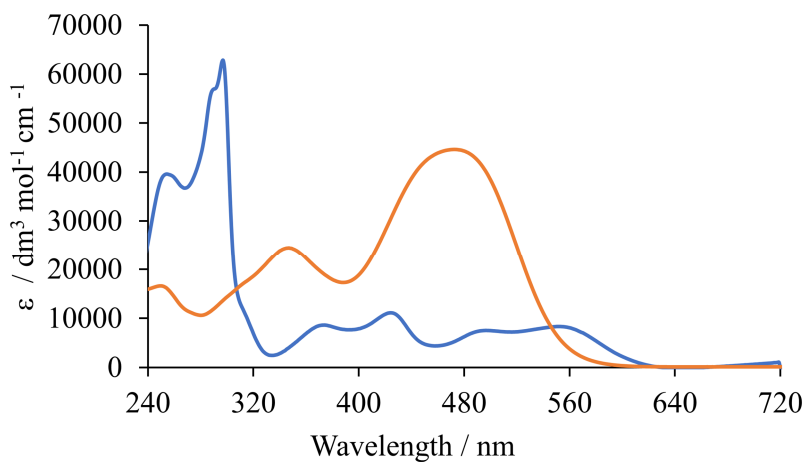


Fig. 4.26: Solution UV-Vis absorption spectrum of WOC53 (MeOH $1 \times 10^{-5} \text{ mol dm}^{-3}$, blue curve) and P1 (AcCN, $3 \times 10^{-5} \text{ mol dm}^{-3}$, orange curve)

The solution absorption spectra of WOC53 and P1 (Fig. 4.3) are shown in Fig. 4.26. The intense bands (240-320 nm) are assigned to ligand-centred $\pi^* \leftarrow \pi$ transitions. The broad bands at lower intensity absorptions (350-430 nm and 430-620 nm) in the spectrum of the metal complex are characteristic of $[\text{Ru}(\text{bpy})_2(\text{C}^{\wedge}\text{N})]^+$ cations and are ascribed to the metal-to-C[^]N and metal-to-bpy MLCT transitions respectively. The commercially available P1 dye that was used as a reference exhibits an absorption as described in the literature ¹¹⁴. DSSCs were fabricated by immersing the NiO/FTO electrode into a

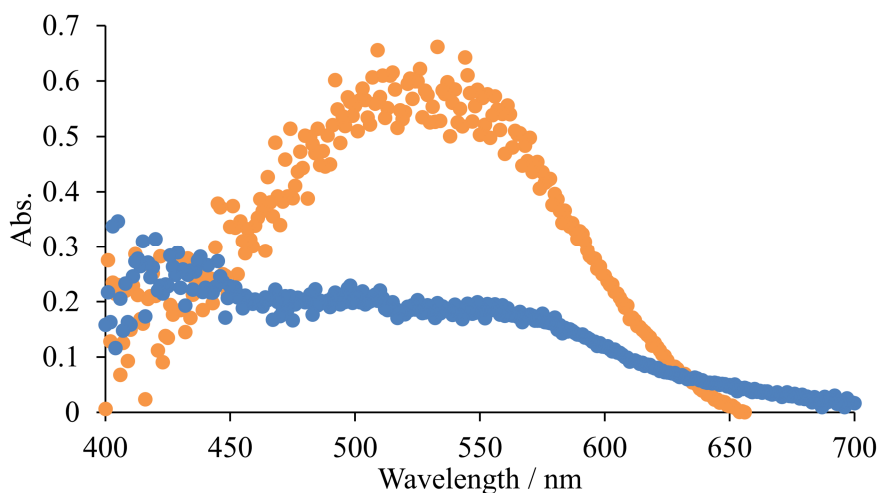


Fig. 4.27: Solid state UV-Vis absorption spectra of NiO/FTO electrodes sensitized with WOC53 (blue curve) and P1 (orange curve).

solution of the dyes (see section 4.4.4). The solid state UV-Vis absorption spectra of the sensitized NiO/FTO electrodes were recorded (Fig. 4.27) and showed an accordance with the absorption spectra of the dyes in solution (Fig. 4.26) with a small red-shifting on going from the solution to the solid. Duplicate DSSCs using both dyes were fabricated to confirm the reproducibility of the measurement and JV curves were plotted (Fig. 4.28)

Experiment Name	Jsc/mA cm ⁻²	Voc/ mV	FF/%	η/%
P1_1	1.84	88	35	0.057
P1_2	1.96	82	32	0.051
WOC53_1	3.38	95	36	0.116
WOC53_2	3.34	95	34	0.109

Table 4.6: Performance data for duplicate cells and electrolyte comprising of 0.1 M I₂/1.0 M LiI in AcCN (Std III). The active area of the cell was 0.237 cm². The measurements were done on the day of sealing the cells.

From Fig. 4.28 and Table 4.6 it is observed that WOC53 performs better than P1 (η = 0.116 % vs. 0.057 %) the difference in performance of these two DSSCs arises mainly from their different J_{sc} values (3.38 vs 1.96 mA cm⁻² for DSSC sensitized with WOC53 and P1 respectively). Last, the

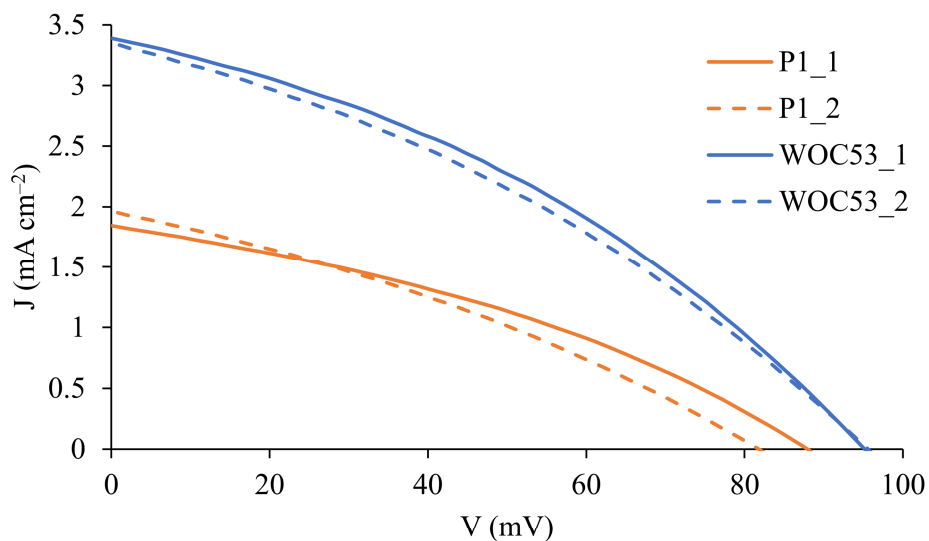


Fig. 4.28: JV curves of the DSSCs with electrolyte comprising of 0.1 M I₂/1.0 M LiI in AcCN (Std III) and sensitized with P1 and WOC53 dyes.

WOC53_1 performance is comparable with the best values reported for cyclometalated Ru(II) dyes (Table 4.4, O18) ¹⁴⁶.

4.3.2 Effect of different anchoring ligands on the performance of p-type DSSCs with cyclometalated ruthenium(II) dyes

During this study, a performance comparison of DSSCs sensitized with different cyclometalated ruthenium(II) dyes bearing different anchoring domains was investigated. The dyes were synthesized by Cedric Wobill ¹⁵² and their performances were compared to the commercially available P1 dye (Fig. 4.3).

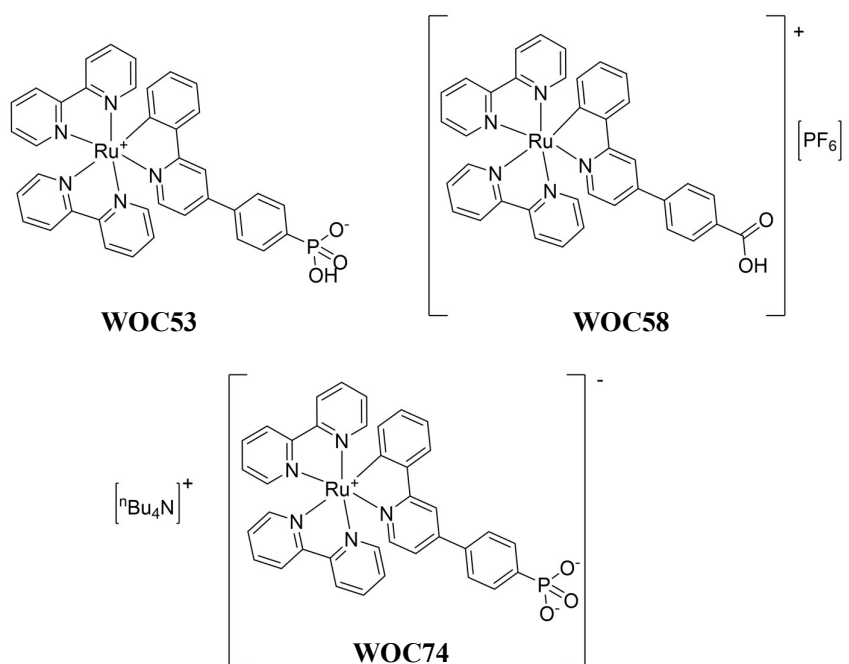


Fig. 4.29: Structures of dyes WOC53, WOC54 and WOC74

The three different anchoring groups investigated were located on the phenyl ring of the [ppp]⁻ ligand and consisted of a mono deprotonated phosphonic acid, carboxylic acid and double deprotonated phosphonic acid (Fig. 28). Moreover, two different compositions of organic solvent in the electrolyte were used and investigated, 0.1 M I₂/1.0 M LiI in AcCN and 3:1 AcCN/propionitrile. The synthetic routes used for the synthesis of WOC53 and WOC58 have been described in section 1.3.1. The synthesis of WOC74 was done by deprotonation of WOC53 and addition of ⁿBu₄NOH. Unfortunately, an isolation of pure WOC74 was not possible. Nevertheless, the impure compound with excess ⁿBu₄NOH was used as a dye. Duplicate DSSCs were fabricated with each dye to confirm reproducibility.

Experiment Name	Jsc/mA cm ⁻²	Voc/ mV	FF/%	η/%
WOC53_1	3.24	102	35	0.116
WOC53_2	2.91	98	35	0.100
WOC74_1	2.37	95	34	0.076
WOC74_2	1.99	94	33	0.062
WOC58_1	1.20	63	34	0.026
WOC58_2	1.38	73	34	0.035
P1_1	2.28	91	30	0.063
P1_2	2.01	89	31	0.055

Table 4.7: Performance data for duplicate cells and electrolyte comprising of 0.1 M I₂/1.0 M LiI in AcCN (Std III). The active area of the cell was 0.237 cm². The measurements were done on the day of sealing the cells.

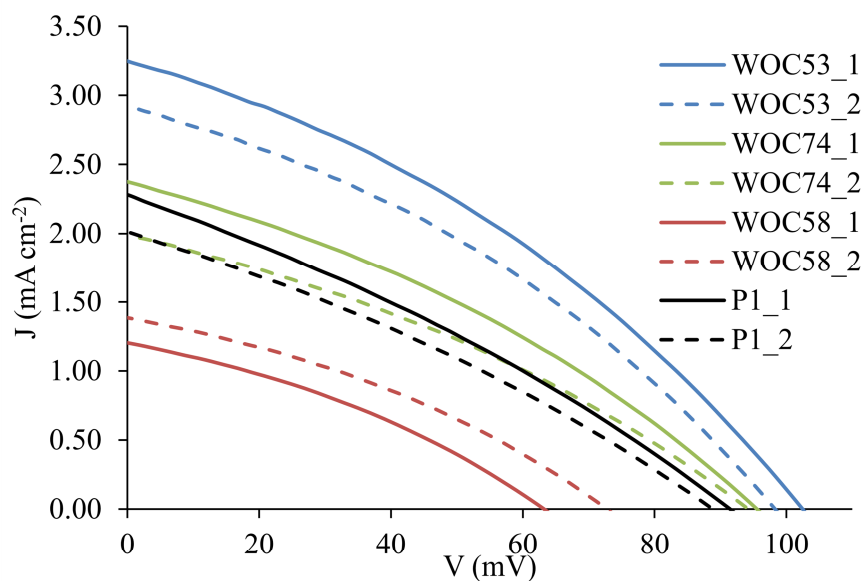


Fig. 4.30: JV curves of the DSSCs with electrolyte comprising of 0.1 M I₂/1.0 M LiI in AcCN (Std III) (see Table 4.6).

Experiment Name	Jsc/mA cm ⁻²	Voc/ mV	FF/%	η /%
WOC53P_1	2.50	105	34	0.091
WOC53P_2	2.91	99	34	0.099
WOC74P_1	2.10	102	35	0.075
WOC74P_2	2.07	100	34	0.070
WOC58P_1	1.10	71	35	0.027
WOC58P_2	1.09	72	35	0.028
P1P_1	2.18	103	31	0.069
P1P_2	2.12	103	31	0.068

Table 4.8: Performance data for duplicate cells and electrolyte comprising of 0.1 M I₂/1.0 M LiI in 3 : 1 AcCN/propionitrile (PN1). The abbreviation -P was added at the end of the experiments name to differentiate the cells backfilled with PN1 from those backfilled with Stnd III electrolyte (see Table 4.7). The active area of the cell was 0.237 cm². The measurements were done on the day of sealing the cells.

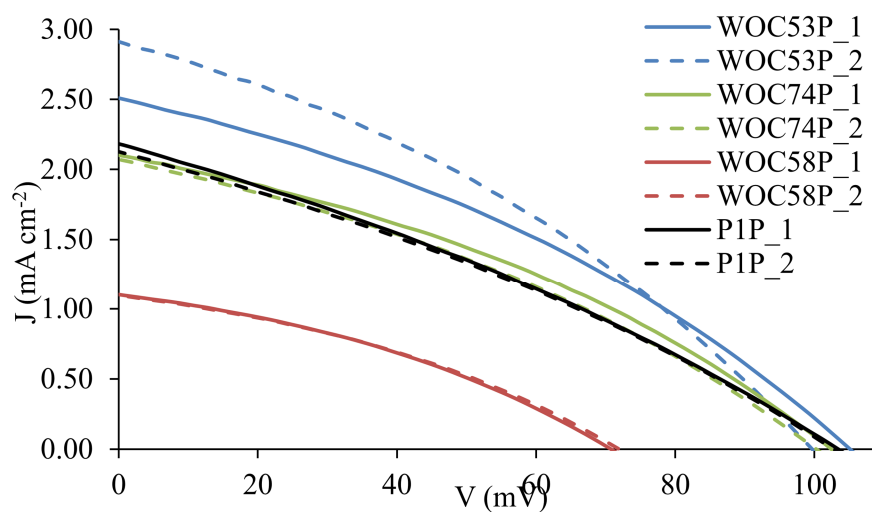


Fig. 4.31: JV curves of the DSSCs with electrolyte comprising of 0.1 M I₂ /1.0 M LiI in 3 : 1 AcCN/propionitrile (PN1). The abbreviation -P was added at the end of the experiments name to differentiate the cells back field with PN1 from those backfilld with Stnd III electrolyte (see Table 4.7).

The DSSCs performances follow the trend WOC53 > WOC74 > P1 > WOC58, regardless of the electrolyte used (Table 4.7, 4.8 and Fig. 4.30, 4.31). The performance of the DSSC sensitized with P1 is consistent with the values reported by *Gibson and co-workers*⁷⁵ in their benchmarking investigation. The cells with Stnd III electrolyte exhibit an overall better performance compared with the cells filled with PN1 electrolyte due to a higher J_{sc} (3.24 vs. 2.91 mA cm⁻² for WOC53_1 and WOC53P_2 respectively) which is consistent with our work described in chapter 5.4.1. In spite of the problems in purification of the WOC74 dye that was mentioned above, the results obtained from the sun simulation measurements show a distinctive difference between the performance of WOC53 and the doubly deprotonated WOC74 with the latter performing worse due to a drop in J_{sc} . The DSSC containing WOC58 with a carboxylic anchoring domain has the lowest performance among the studied series. This is consistent with previous work of *Odobel and co-workers*¹⁵³ that demonstrated that Ru(bpy)₃²⁺ based dyes with phosphonic acid anchors performed better than those with carboxylic acid. To investigate the stability of the DSSCs sensitized with the three Ru(II) dyes and with P1, their performance was measured 7 days after the sealing.

Experiment Name	$J_{sc}/\text{mA cm}^{-2}$	Voc/ mV	FF/%	$\eta/\%$
WOC53_1	3.23	102	33	0.109
WOC53_2	3.01	97	34	0.098
WOC74_1	2.54	95	32	0.077
WOC74_2	2.09	94	31	0.060
WOC58_1	1.15	68	35	0.027
WOC58_2	1.32	71	35	0.033
P1_1	1.60	90	30	0.043
P1_2	1.68	87	30	0.044

Table 4.9: Performance data for duplicate cells and electrolyte comprise of 0.1 M I₂ /1.0 M LiI in AcCN (Stnd III). The active area of the cell was 0.237 cm². The measurements were done 7 days after the sealing the cells.

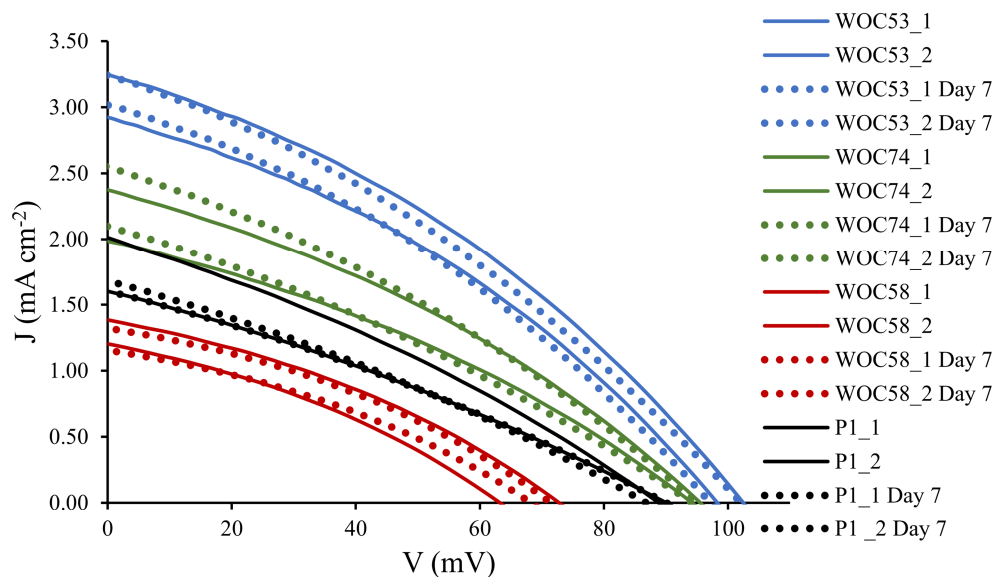


Fig. 4.32: JV curves of the DSSCs with electrolyte comprised of 0.1 M I₂/1.0 M LiI in AcCN (Std III) on the day of the sealing and 7 days after, and sensitized with WOC53, WOC74 and P1 dyes.

Experiment Name	J _{sc} /mA cm ⁻²	V _{oc} / mV	FF/%	η/%
WOC53P_1	2.72	106	35	0.100
WOC53P_2	2.97	99	34	0.100
WOC74P_1	2.22	96	36	0.077
WOC74P_2	2.33	99	34	0.079
WOC58P_1	1.04	72	36	0.027
WOC58P_2	1.08	74	37	0.030
P1P_1	1.54	94	30	0.044
P1P_2	1.69	99	32	0.054

Table 4.9: Performance data for duplicate cells and electrolyte comprised of 0.1 M I₂/1.0 M LiI in 3 : 1 AcCN/propionitrile (PN1). The active area of the cell was 0.237 cm². The measurements were done 7 days after the sealing the cells.

In Table 4.8, 4.9 and Fig. 4.32, 4.33 the ageing of the DSSCs is exhibited. It can be observed that the performance of all DSSCs with both electrolytes sensitized with cyclometallated ruthenium(II) stays rather stable but that the performance of the DSSC with P1 dye drops significantly. Those results argue favourably over the better ageing of the inorganic dyes over the organic one.

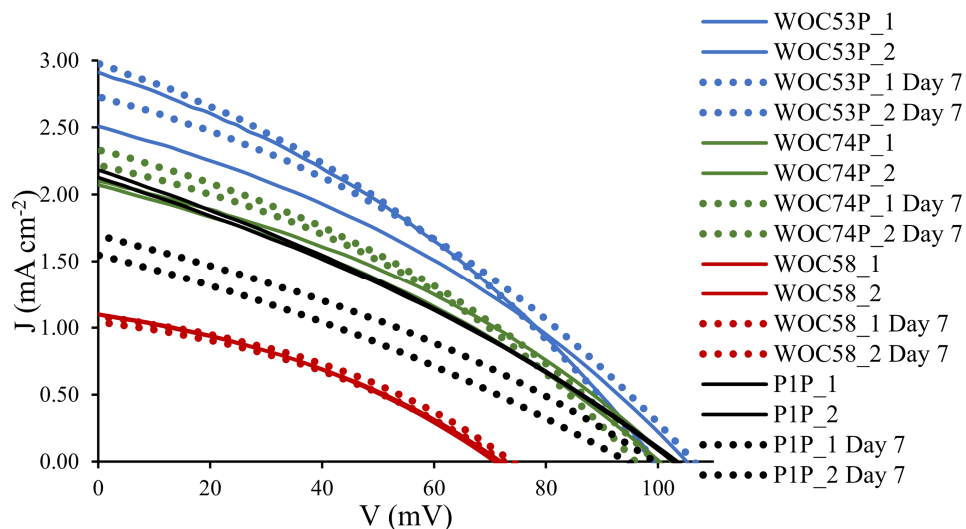


Fig. 4.33: JV curves of the DSSCs with electrolyte comprise of 0.1 M I_2 /1.0 M LiI in 3 : 1 AcCN/propionitrile (PN1) and sensitized with WOC53, WOC74 and P1 dyes. The measurements were done on the day of the sealing the cells and 7 days after.

Further analysis for the better understanding of the behaviour of the three Ru(II) dyes were carried on with EIS measurements. The equivalent circuit to fit the EIS data is presented in Fig. 4.34. In this study, a resistance - constant phase element (R-CPE) circuit was employed, because of the surface irregularities¹³³ of the NiO electrode. To account for this pre-factor term Q of the CPE was corrected using eq. 4.3 (section 4.2.1) The equivalent circuit is consisting of a series resistance (R_s), the resistance (R_{FTO}) and capacitance (C_{FTO}) of the FTO/NiO interface, a distribution element that includes the sum of recombination (R_{rec}) and transport resistance (R_t) and the capacitance (C_μ) of the NiO electrode. Furthermore, a Warburg (Z_d) element and the resistance (R_{CE}) and capacitance (C_{CE}) of the counter electrode. The EIS data for the better performing cell of each pair are summarized in Table 4.10 and Nyquist plots are presented in Fig. 4.35. From Table 4.7 is observed that the values of V_{OC} among the Ru(II) sensitized DSSCs follows the trend : WOC53_1 > WOC74_1 > WOC58_2. This trend is reflected in the EIS measurements when observing the transport resistance which follows the opposite trend (Table 4.10). The values of R_{rec} in Table 4.10 follow the same trend as R_t , which is to be expected since

the lower J_{SC} (Table 4.7) indicates fewer charge carriers being injected into the NiO, therefore fewer holes are available for recombination, leading to a higher R_{rec} . The increase in capacitance follows the trend $WOC74_1 > WOC58_2 > WOC53_1$ and is also consistent with WOC53 being the best performing dye. As expected, the series resistance, R_s is constant for all three cells (Table 4.10).

Cell Name	R_s/Ω	R_{Pt}/Ω	$C_{Pt}/\mu F$	R_{rec}/Ω	R_t/Ω	$C_\mu/\mu F$	$\tau n/ms$	$\tau t/ms$	a
WOC53_1	12.2	2.2	5.9	97.8	75.7	529.4	51.8	40.1	0.868
WOC74_1	13.6	5.0	3.5	185.7	89.1	532.4	98.8	47.4	0.879
WOC58_2	15.1	1.5	4.1	632.6	83.2	850.8	538.2	70.8	0.847

Table 4.10: EIS data obtained from measurements at a light intensity of 22 mW cm^{-2} of p-type DSSCs containing FTO/NiO working electrodes, sensitized with WOC53, WOC74 and WOC58 and electrolyte comprising of $0.1 \text{ M I}_2, 1 \text{ M LiI}$ in AcCN.

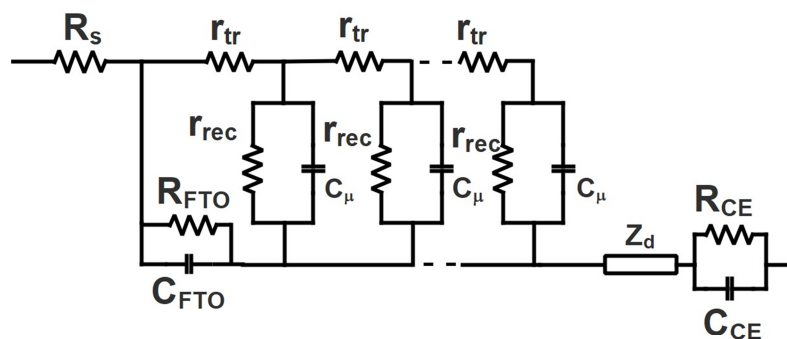


Fig. 4.34: Equivalent circuit used to fit the EIS data.

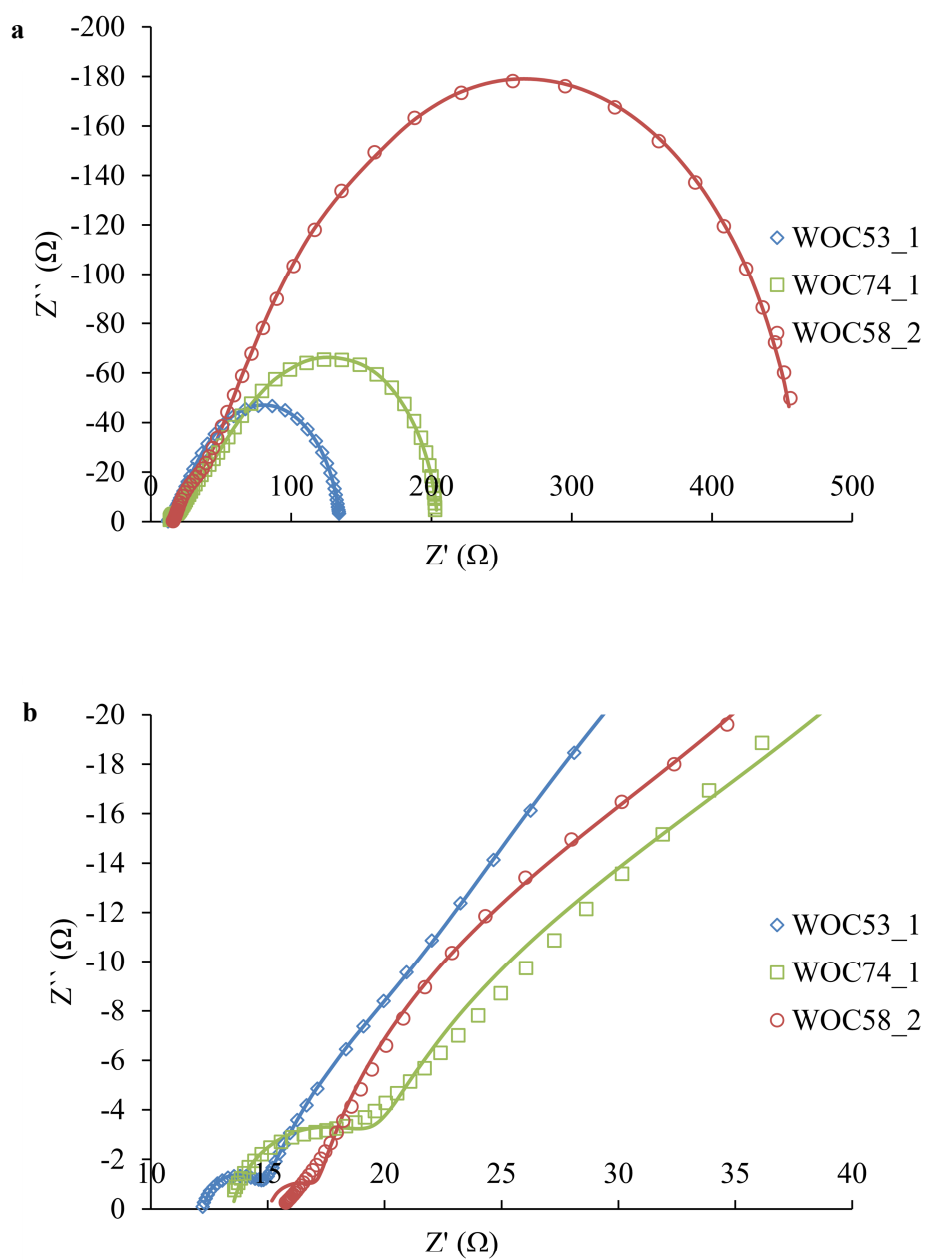


Fig. 4.35: **a.** Nyquist plots and **b.** expansion of Nyquist plots for $0 < Z' < 40 \Omega$ for DSSCs with NiO/FTO electrodes and electrolyte comprising of 0.1 M I_2 , 1 M LiI in AcCN. The NiO electrodes were sensitized with WOC53, WOC74 and WOC58.

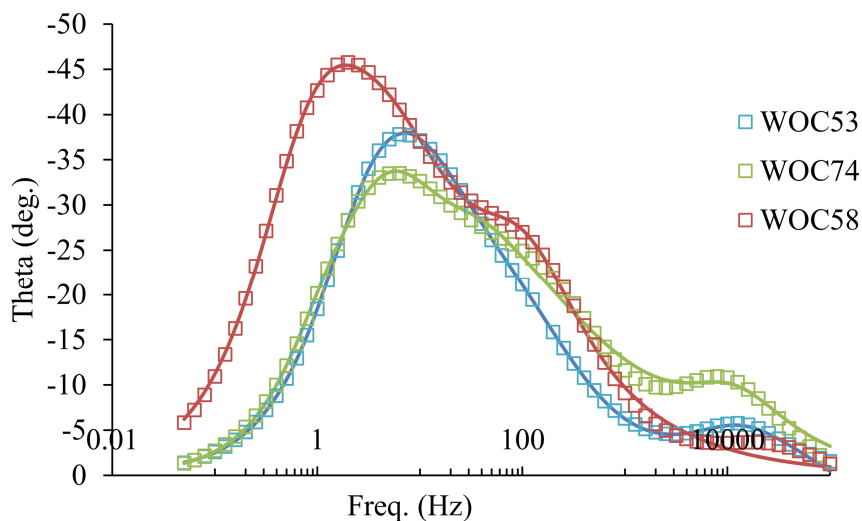


Fig. 4.36: Bode plots for DSSCs with NiO/FTO electrodes and electrolyte comprising of 0.1M I₂, 1M LiI in AcCN. The NiO electrodes were sensitized with WOC53, WOC74 and WOC58.

The hole life time, τ_h , can be calculated using eq. 4.4 (section 4.2.1). Table 4.10 shows that the best performing dye WOC53 has the shortest hole lifetime as expected. Since the hole lifetime is inversely related to the value of the maximum frequency f_{max} ¹³², it follows that the trend in values of τ_h can also be seen in the Bode plot Fig. 4.36. The cell sensitized with WOC58 has the lowest frequency peak position ($f_{max} = 1.99$ Hz) compared to the cells sensitized with WOC74 and WOC53 ($f_{max} = 5.0$ and 6.3 Hz, respectively). The transport time is calculated from eq. 4.7 and the trends τ_t in Table 4.10 are consistent with the performance of the dyes (Table 4.7).

$$\tau_t = R_t C_\mu \quad (4.7)$$

R_{FTO} and C_{FTO} represent the resistance and the capacitance at the FTO/NiO-electrolyte interface. These terms are related to the incomplete coverage of the FTO substrate by the semiconductor and can cause of current leakage¹³⁰. At low voltages, when NiO becomes less conductive the R_{FTO} and C_{FTO} terms have the greatest significance, whereas under open circuit voltage conditions, the dominating process is that taking place at the NiO/electrolyte interface since the hole transfer resistance is much smaller compared to the FTO resistance^{132, 154}. The effects of different applied potentials on the DSSC containing WOC53 and Std III electrolyte is revealed in the Bode plot in Fig. 4.37. An increase in charge density is observed on going to more positive potentials (direction of the arrow in Fig. 4.37). At open circuit conditions ($V_{OC} = 102$ mV from Table 4.7), the frequency peak involving the NiO/electrolyte interface is at 6.3 Hz and as the applied potential is increased, the peak in the Bode

plot for the same process moves toward higher frequencies, indicating that there is an increase of the number of holes associated with this process^{132, 155}. This increase can be explained by the decrease of the band gap at the NiO semiconductor, this frequency peak can be assigned to the charge transfer process taking place in the semiconductor which is described at the second semi-circle observed at the Nyquist plot (Fig. 4.35). The second peak in higher frequencies can be attributed to the charge transfer process at the counter electrode/electrolyte interface that as it is seen stays stable at the same frequency for all the applied potentials.

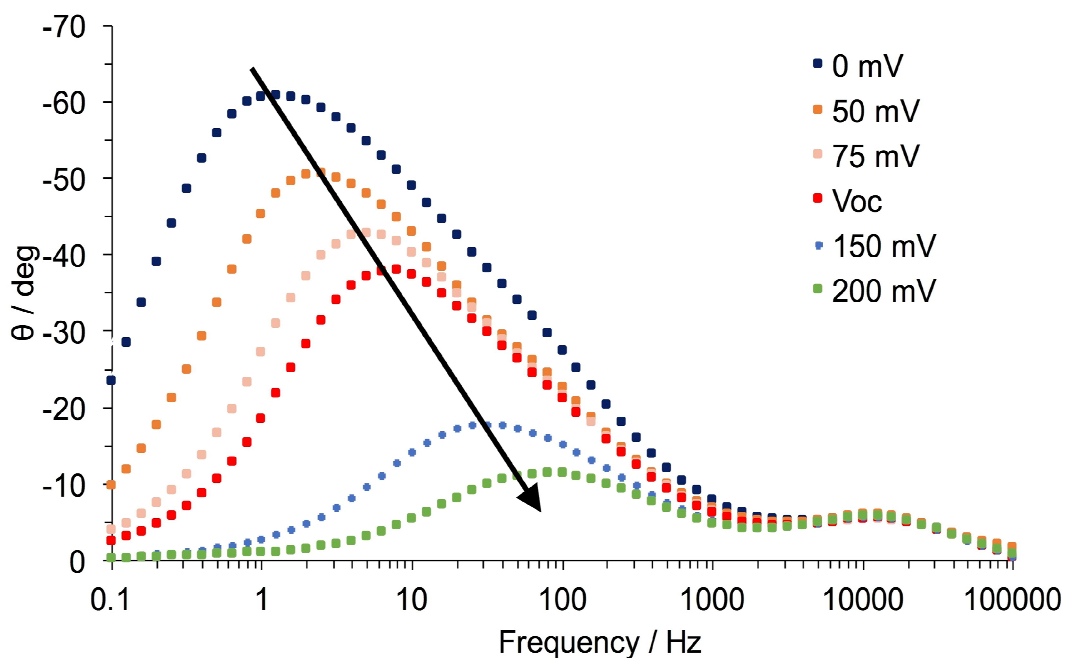


Fig. 4.37: Bode plots of the DSSC with WOC53 and electrolyte comprising of 0.1M I₂, 1M LiI in AcCN under different applied potentials (22 mW cm⁻² irradiation).

From the comparison of the three cyclometallated ruthenium(II) dyes and the standard P1 dye, it is concluded that WOC53 is the best performing, confirming that the monodeprotonated phosphonic acid used as an anchoring ligand is the best among the others used in this experiment which leads to enhanced values of J_{SC} and photoconversion efficiencies. Removal of a second proton to give WOC74 dye results in a lower J_{SC} and overall photoconversion efficiency. A change from Std III to PN1 electrolyte has a small influence on the device performance and all DSSCs sensitized with Ru(II) dyes exhibit good stability over a period of 7 days.

4.4 Materials and Methods

4.4.1 Solar cells measurements

The solar cell measurements were made using unmasked cells with an active area of 0.237 cm^2 . The DSSCs were sun-soaked from the anode side for 20 min at 1 sun irradiation. The cell was then inverted and measured immediately with a LOT Quantum Design LS0811 instrument ((LOT-QuantumDesign GmbH, Darmstadt, Germany) ($100 \text{ mW cm}^{-2} = 1 \text{ sun}$ at AM1.5 and $23 \text{ }^\circ\text{C}$) to obtain the current density–voltage (JV) curves. The instrument software was set to a p-type measurement mode (inverted configuration), with a 360 ms settling time and a voltage step of 5.3 mV. The voltage was scanned from negative to positive values.

4.4.2 External quantum efficiency (EQE) measurements

The external quantum efficiency (EQE) measurements were made using a Spe-Quest quantum efficiency instrument (Rera Systems, Nijmegen, The Netherlands) equipped with a 100 W halogen lamp (QTH) and a lambda 300 grating monochromator (L.O.T.-Oriol GmbH & Co. KG, Darmstadt, Germany). The monochromatic light was modulated to 1 Hz by using a chopper wheel (ThorLabs Inc., Newton, NJ, USA). The cell response was amplified with a large dynamic range IV converter (Melles Griot B.V., Didam, The Netherlands) and measured using a SR830 DSP Lock-In amplifier (Stanford Research Systems Inc., Sunnyvale, CA, USA).

4.4.3 Electrochemical impedance (EIS), open circuit voltage and intensity modulated photocurrent spectroscopy (IMPS) measurements

EIS and IMPS measurements were carried out on a ModuLab® XM PhotoEchem photoelectrochemical measurement system (Solartron Metrology Ltd, Leicester, UK). The impedance was measured around the open-circuit potential of the cell at different light intensities (590 nm) in the frequency range 0.05 Hz to 400 kHz using an amplitude of 10 mV. The impedance data were analysed using ZView® software (Scribner Associates Inc., North Carolina, USA). The IMPS measurements were performed using a small perturbation ($> 5\%$) of the steady state illumination. Voltage decay was measured on a Modulab XM electrochemical system (Solartron Metrology Ltd, Leicester, UK)

4.4.4 Electrodes preparation

Working NiO electrodes were prepared as follows for the experiment described on section 1.2.1. An FTO glass plate (TCO22-7, 2.2 mm thickness, sheet resistance = $7 \text{ } \Omega \text{ square}^{-1}$, Solaronix SA, Aubonne, Switzerland) was cleaned by sonicating in surfactant (2% in milliQ water), rinsed with milliQ water and EtOH and then sonicated for 10 min in acidified EtOH. The surface was sintered at

450 °C for 30 min. A pretreatment of NiO was prepared by spin-coating (3000 rpm for 1 min) onto the clean substrates a Ni(OAc)₂ solution (0.5 M) containing ethanolamine (0.5 M) in methoxyethanol. After spin-coating, the plate was sintered at 500 °C for 30 min. A layer of NiO paste (Ni-Nanoxide N/SP, Solaronix SA, Aubonne, Switzerland) was screen-printed (90 T, Serilith AG, Switzerland) onto the pretreated FTO plate, which was then placed in an EtOH chamber for 3 min to reduce surface irregularities, and dried (125 °C heating plate, 6 min). In total, two cycles of screen printing were carried out and the resultant two-layer plate was sintered by gradually heating from room temperature to 450 °C over a period of 30 min, maintained at 450 °C for 30 min, then allowed to cool over 2 h to room temperature. The NiO electrodes were soaked in an EtOH solution of Ni(OAc)₂ (20 mM) containing 1% ethanolamine for 30 min at 60°C followed by EtOH rinsing and drying in air. The sintered FTO/NiO plates were then cut to form electrodes (1 × 2 cm). The thickness of the NiO layer (≈1.0–2.5 μm) was confirmed using focused ion beam (FIB) scanning electron microscopy (REM-FEI Helios NanoLab 650).

Working NiO electrodes were prepared as follows for the experiment described on section 1.3.1 and 1.3.2. An FTO glass plate (Solaronix TCO22-7, 2.2 mm thickness, sheet resistance =7 Ω square⁻¹) was cleaned by sonicating in surfactant (2% in milliQ water), and rinsed with milliQ water and EtOH. The surface was activated in a UV-O₃ system (Model 256-220, Jelight Company Inc) for 20 min. The plate was then dipped five times into a solution of [Ni(acac)₂] (ACROS) in AcCN (0.5 mM) and air dried after each dipping. A layer of NiO paste (Ni-Nanoxide N/SP, Solaronix) was screen-printed (90T, Serilith AG, Switzerland) onto the pre-treated FTO plate, and was then placed in an EtOH chamber for 3 min to reduce surface irregularities, then dried (125 °C heating plate, 6 min). Two cycles of screen printing were carried out. The NiO was sintered by gradually heating from room temperature to 350 °C over a period of 30 min, kept at 350 °C for 30 min, then allowed to cool over 2 h to room temperature. The sintered FTO/NiO plates were then cut to form electrodes (1 cm × 2 cm). The thickness of the NiO layer (~1.0–2.5 μm) was confirmed using focused ion beam (FIB) scanning electron microscopy (REM-FEI Helios NanoLab 650).

4.4.5 Assembly of DSSCs

DSSCs were assembled as follows. The FTO/NiO electrodes were heated at 250 °C (20 min), then cooled to 80 °C before being immersed in an AcCN solution (0.3 mM) of P1 (Dyemaco AB), an acetone solution (0.3 mM) of PP1 or EtOH solution (0.1 mM) of the respective ruthenium dye for 20 h. The electrodes were removed from the solutions, washed with EtOH, then dried in an N₂ stream. Commercial counter electrodes (Solaronix Test Cell Platinum Electrodes) were washed with EtOH and then heated at 450 °C (hot plate) for 30 min to remove volatile organic impurities. The DSCs were fabricated by combining working and counter electrodes using thermoplast hot-melt sealing foil (Solaronix, Meltonix 1170-25 Series, 60 μm thick) by heating while pressing them together. The

electrolyte comprised I₂ (0.1 M), LiI (1 M) in AcCN or I₂ (0.1 M), LiI (1 M) in AcCN/propionitrile 3:1 and was added to the DSC by vacuum backfilling. The hole in the counter electrode was then closed using a hot-melt sealing foil and cover glass.

4.4.6 Synthesis of dyes

The syntheses of the dyes described in this chapter are summarized in the following papers:

Y. M. Klein, N. Marinakis, E. C. Constable, C. E. Housecroft, *Phosphonic acid anchoring analogue of the dye P1 for p-type dye-sensitized solar cells*, *Crystals*, 2018, **8**, 389.

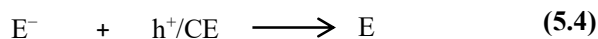
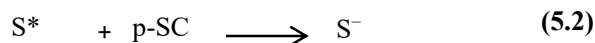
F. Brunner, N. Marinakis, C. Wobill, M. Willgert, C. D. Ertl, T. Kosmalski, M. Neuburger, B. Bozic-Weber, T. Glatzel, E. C. Constable, C. E. Housecroft, *Modular synthesis of simple cycloruthenated complexes with state-of-the-art performance in p-type DSCs*, *J. Mater. Chem. C*, 2016, **4**, 9823.

N. Marinakis, C. Wobill, E. C. Constable, C. E. Housecroft, *Refining the anchor: Optimizing the performance of cyclometallated ruthenium(II) dyes in p-type dye sensitized solar cells*, *Polyhedron*, 2018, **140**, 122.

Chapter 5 Electrolytes

5.1 Introduction

An important component of a DSSC is the electrolyte, which is responsible for the charge transport between the working electrode and the counter electrode, and the efficient charge diffusion in the nanoporous oxide semiconductor. In a p-type DSSC, upon photoexcitation of the (S) dye (eq. 5.1) an electron is transferred from the HOMO to the LUMO orbital of the dye. Then an electron is injected from the valence band of the semiconductor to the HOMO of the dye (S^-) (Fig. 5.2). The electron in the LUMO orbital of the dye, is intercepted from the redox mediator (E) thus, the redox couple is being reduced (eq. 5.3). A hole is transferred to the counter electrode from the external circuit and regenerates the electrolyte through oxidation (eq. 5.4). The procedures can be described with the following equations:



An electrolyte should fulfil the following criteria (i) chemical, optical thermal and electrochemical stability under dark and under illumination (ii) it should not absorb in the visible light (iii) high dielectric constant so the salt present in the electrolyte can dissolve and exists in the dissociated state. (iv) Good solubility for the redox mediator (v) low viscosity in order to achieve an optimal diffusion coefficient (vi) low toxicity and environmental hazard ¹⁵⁶.

5.1.1 Liquid electrolytes

There are three main categories of electrolyte used for the fabrication of DSSCs: 1. liquid electrolyte 2. quasi solid-state electrolyte and 3. solid state electrolyte. The first category is the one mostly explored. A liquid electrolyte consists of a redox couple, one organic solvent or a mixture of organic solvents, or an ionic liquid, in which all the solid components are dissolved and different additives consisting of chemical species that are absorbed onto the electrode/electrolyte interphase thus shifting the semiconductor's conduction band and enhance the efficiency of the cell. In the paper of *O'Regan* and *Grätzel* in 1991 ¹⁰ they report a DSSC with a liquid electrolyte comprised of a redox couple of

triiodide/iodide dissolved in a mixture 8:2 ethylene carbonate : acetonitrile; this device had a

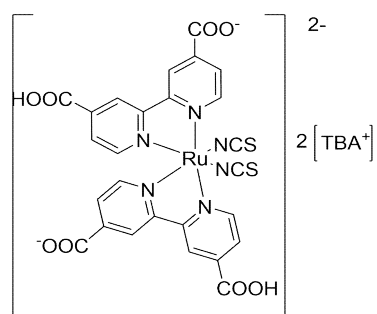


Fig. 5.1: Chemical structure of N719 dye ¹⁰.

photoconversion efficiency of 7.9%. Later on, with the same dye (Fig. 5.1 N719) but with a different composition of electrolyte consisting of the same redox couple dissolved in a different mixture of organic solvents plus some additives, the cell achieved an efficiency of 12% ¹⁰. The redox couple plays a very important role in the performance of the cell. Firstly, the potential difference between the Fermi level of the illuminated semiconductor and the

redox potential of the redox species defines the open circuit voltage of the cell. In order to obtain a high open circuit voltage in the p-type DSSC, the redox potential of the electrolyte should lie close to the HOMO level of the dye S/S^- , and at the same time it should lie away from the valence band of the semiconductor (Fig. 5.2) in order to obtain a quick dye regeneration. On the other hand, the energy level of the redox species should have a sufficient difference with the LUMO energy level of the S^*/S^- in order to produce enough driving force to regenerate the dye ¹⁵⁷, this behaviour is often described as an “asymmetric behaviour”. Furthermore, another reason why the redox potential of the electrolyte should lie away from the valence band of the semiconductor is the reduction of the hole by the electrolyte at the surface of the semiconductor, a process called interception (Fig. 5.2 red arrow 2.) It is another form of charge loss or recombination of the hole which will lead to an increase in the dark current. Last, a redox couple should enable a fast charge transfer to the counter electrode with a minimal over potential ¹⁵⁸. The most frequently used redox shuttle in a DSSC is the triiodide/iodide which exhibits good characteristics for the n-type DSSC such as, good kinetic properties leading to the “asymmetric behaviour” previously described and good chemical long-term stability. On the other hand, the disadvantages of this redox couple are the absorption of the visible light at 430 nm and corrosion of the noble metal (e.g. Pt and Au) ¹⁵⁹. For the p-type DSSC the redox shuttle of triiodide/iodide does not exhibit the asymmetric behaviour since its redox potential (I_3^-/I^- , 0.354 V vs NHE in acetonitrile) ¹¹⁰ lies close to the Fermi level of the semiconductor leading to a low open circuit voltage. For the same reason, interception of the hole (Fig. 5.2 red arrow 2) is more plausible leading to an increase in dark current.

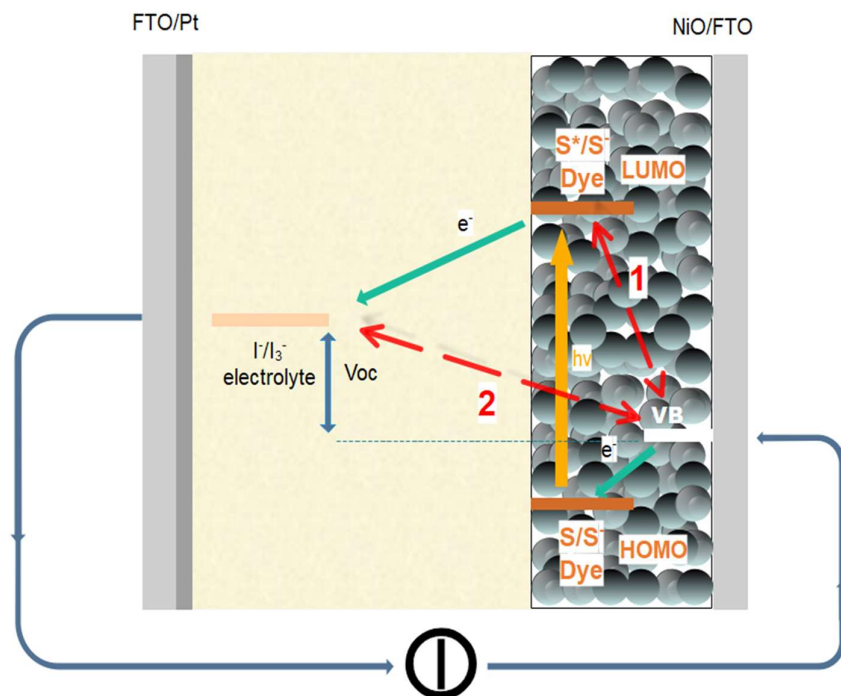


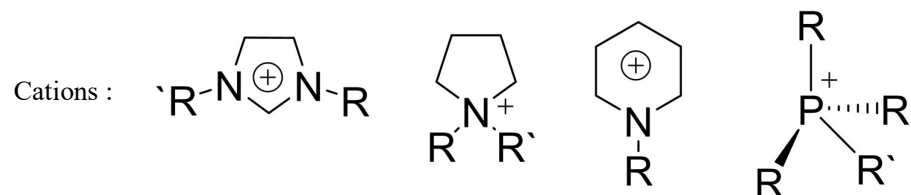
Fig. 5.2: Charge transport process in p-type DSC. Red dotted arrow 1: recombination of the hole with the valence band and 2: interception of the hole by the electrolyte.

Aside from the redox couple, the organic solvent that it is used to dissolve the solid materials present in the electrolyte, has been investigated thoroughly. Having in mind the characteristics previously mentioned, the most popular are the solvents of the nitrile family. For example, acetonitrile is commonly used; this solvent is also considered to be the best solvent for electrochemical studies since its electrochemical stability window ¹⁶⁰ is more than 4 V. Other solvents extensively studied are valeronitrile, propionitrile and mixtures of these, and also nitriles with methoxy groups, for example methoxyacetonitrile and 3-methoxypropionitrile with a higher viscosity than acetonitrile. Other alternatives are alcohols such as ethanol or lactones and even water due to its chemical stability, abundance and low environmental hazards.

5.1.2 Ionic liquids and quasi-solid-state electrolytes

The risk of evaporation due to leakage of the sealing remains a major issue regardless of the effort to employ high viscosity organic solvents. As a result, new media have been investigated. Ionic liquids are non-volatile at room temperature and have a great chemical stability and a wide electrochemical window ¹⁶¹. Ionic liquids are salts consisting of an aromatic or non-aromatic organic cation and various anions, which can be used instead of the organic solvent or in a mixture with the latter (Fig. 5.3). Ionic liquids can be tuned in terms of conductivity, hydrophobicity, melting point and solubility by changing the substitutive group on the cation or on the anion part ¹⁶². The most studied ionic liquids

are the ones based on imidazolium cations ¹⁶³ and frequently used examples are 1-propyl-3-methylimidazolium iodide (PMImI), or mixtures of this and 1-ethyl-3-methylimidazolium thiocyanate (EMImSCN) ¹⁶⁴.



Anions : Cl^- , Br^- , I^- , PF_6^- , BF_4^- , CF_3COO^- , CF_3SO_3^- , $[\text{N}(\text{CN})_2]^-$

Fig. 5.3: Selected cations and anions used for ionic liquids.

In order to overcome the problem of the long-term stability of DSSCs due to the leakage and evaporation of the organic solvent or the ionic liquid, quasi-solid electrolytes have been developed. The three main ways to prepare these semi-solid electrolytes from liquid electrolytes are (i) addition of organic polymer gelators (ii) addition of inorganic gelators (iii) or polymerization of the ionic liquid ¹⁶⁵. Despite the fact that the efficiency of the DSSC with quasi-solid-state electrolyte are worse than the one using liquid electrolyte due to increase charge diffusion ¹⁶⁶, they provide long-term stability and better sealing process.

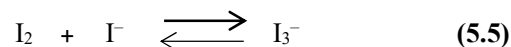
5.1.3 Solid state electrolytes

The last category is the solid-state electrolyte. These were initially developed using inorganic hole transporting materials (HTM) or p-type semiconductors such as CuI, CuBr or CuSCN ^{167, 168, 169, 170}. Moreover, those cells were unstable due to the degradation of the copper to Cu₂O and/or CuO ¹⁷¹. Later on, organic HTMs were used such as 2,2',7,7'-tetrakis(N,N-di-4-methoxyphenylamino)-9,9'-spirofluorene (spiro-OMe-TAD) ¹⁷² which showed better long-term stability and good efficiency when the TiO₂ was sensitized with a Ru(II) dye ¹⁷³ but with the disadvantage of a high cost of this material and the poor hole mobility. In order to overcome those problems, conjugated polymers (CPs) were investigated, which had a good thermal stability, great conductivity, good solubility and tuneable optoelectronic properties ¹⁷⁴.

5.2 Electrolytes used in p-type cells

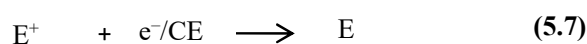
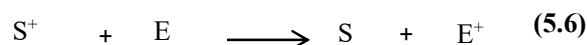
5.2.1 Introduction: Redox couple

In p-type DSSCs, different redox couples have been investigated. The most investigated among these is the iodine/triiodide redox couple in different mixtures of organic and ionic liquid media. When I₂ is in solution it binds an iodide ion to form triiodide (I₃⁻) (eq. 5.5) ¹⁷⁵.

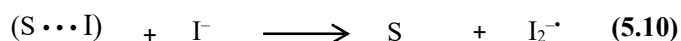
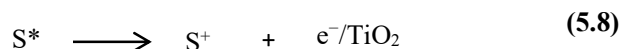


Due to the high equilibrium constant ¹⁷⁶ $K = [\text{I}_3^-]/[\text{I}_2] [\text{I}^-] = 10^{6.78}$ of this reaction most iodine molecules will react with I⁻ and the free iodine concentration is low ¹⁷⁵.

In n-type DSSCs, the electrolytes will regenerate the oxidized dye, S, and then the electrolyte will be regenerated at the counter electrode interface by an electron from the external circuit as shown in equations 5.6 and 5.7.



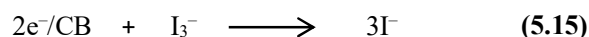
In the case of iodine/triiodide as a redox couple, the dye regeneration can be described as follows. The dye is excited by the light and an electron is injected into the conduction band of the semiconductor (eq. 5.8). The oxidized dye is regenerated by iodide (eq. 5.9) and forms a complex. Upon the introduction of a second iodide ion, the complex dissociates and regenerated dye is formed (S) as well as a diiodide radical (eq. 5.10). Finally, two diiodide radicals react and form triiodide and iodide (eq. 5.11)



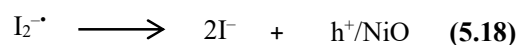
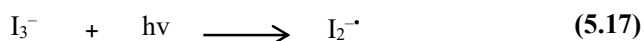
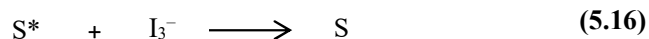
Moreover, the iodine/triiodide electrolyte has a yellow-brown colour, and thus absorbs visible light. When iodine is photoexcited, the following decomposition reactions take place:



Regarding the n-type DSSCs the driving force for the dye regeneration is given by the difference between the redox potential of the dye $E^{\circ}(\text{S}^+/\text{S})$ and $E^{\circ}(\text{I}_2^{\cdot-}/\text{I}^-)$, $E^{\circ} = 0.79$ V vs. NHE in AcCN)¹¹⁰. The formation of the species I_3^- (eq. 5.11 and 5.14) corresponds to a potential loss due to interception of the injected electron in the conduction band of TiO_2 by the triiodide species (eq. 5.15)^{175, 110}.



In p-type DSSCs the regeneration of the dye follows a different mechanism which is illustrated in Fig. 5.4. The light photoexcites the dye, which transfers his energy to a triiodide ion (eq. 5.16) the triiodide radical forms diiodine radicals (eq. 5.17) which will inject holes into the NiO semiconductor (eq. 5.18)¹⁷⁷.



In the p-type DSC the driving force for the regeneration of the dye is dictated by the potential difference between $E^{\circ}(\text{S}^+/\text{S})$ and $E^{\circ}(\text{I}_3^-/\text{I}_2^{\cdot-})$ ^{178, 179, 180} with a redox potential of 0.08 V vs. NHE in acetonitrile¹¹⁰. In the case of p-type DSSCs the photodissociation of triiodide (eqs. 5.12-5.14) can have a beneficial effect by injecting holes into the semiconductor. Thus, by increasing the concentration of triiodide in the electrolyte of a p-type DSSC an increase of the J_{SC} of the cell can be observed as it has been shown from the work of *Gibson and co-workers*²¹¹. During this work the effect of different I_2 and $\text{I}_{2, \text{free}}$ concentrations was investigated where $\text{I}_{2, \text{free}}$ is the iodine present in nanomolar scale in the organic solvent. The results show that an increase of I_2 concentration in the electrolyte provokes an increase in J_{SC} and in V_{OC} .

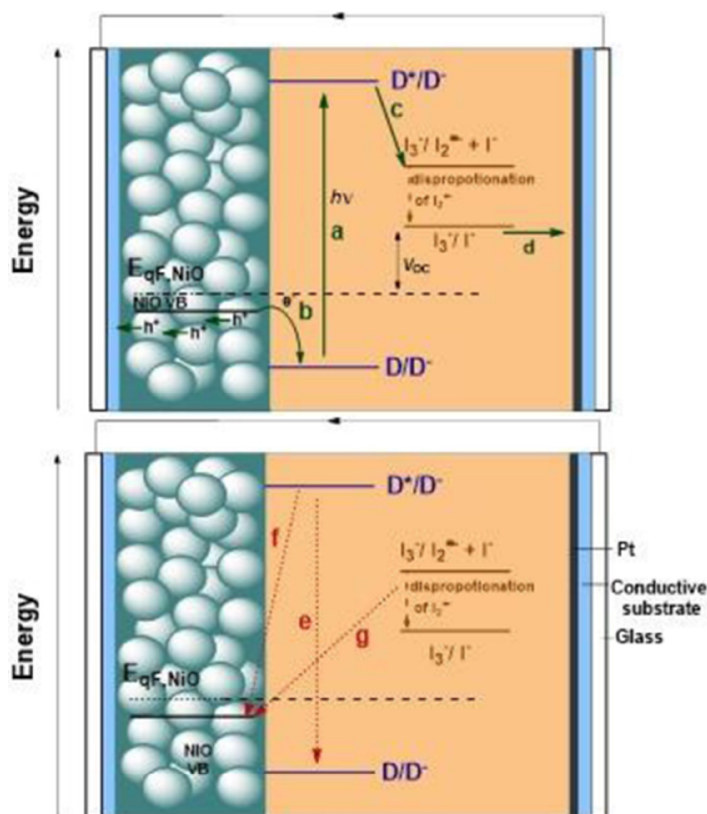
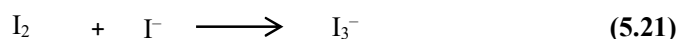
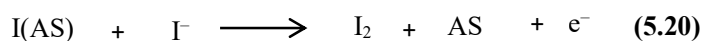


Fig. 5.4: Schematic illustrations of the current-generating (top) and recombination processes (bottom) in a p-type dye-sensitized solar cell. a) The dye is excited by visible light b) the excited dye accepts an electron from NiO c) I_3^- accepts an electron from the reduced dye to form I_2^- , which disproportionate to form I^- and I_3^- d) I^- diffuses to the counter electrode, at which it is oxidized to I_3^- e) the excited dye relaxes radiatively or nonradiatively to the ground state f) holes in NiO react with electrons in the reduced dye g) holes in NiO oxidize the electrolyte. Reprinted with permission from E.A. Gibson and co-workers *ChemElectroChem* 2016, **3**, 1827²¹¹, Copyright 2016, John Wiley and Sons.

However, when increasing the $I_{2, \text{free}}$ concentration, a decrease in J_{SC} and of V_{OC} was observed. The decrease of J_{SC} was due to an increase in recombination reactions. The lowering of the V_{OC} was attributed to the presence of I^- that negatively shifts the Fermi level of the semiconductor surface by reducing the Ni^{3+} sites of it. These reactions have been described by *Arvia and co-workers*¹⁸¹ as follows:



where AS is an absorption site on the NiO semiconductor.

The lithium cation present in an LiI/I₂ electrolyte induce a positive shift of the valence band of the NiO thus increasing the V_{OC} as is described in section 3.4 of this thesis.

5.2.2 Effect of different iodine concentrations

We now move from the background information to experiments conducted to investigate the effects of different electrolyte composition on performance of p-type DSSCs. In the first investigation, three different compositions of iodine-based electrolytes were investigated. All three electrolytes have been

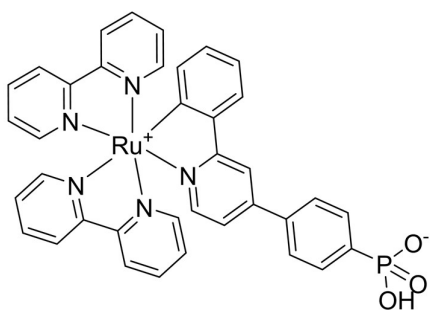


Fig. 5.5: Chemical structure of WOC53

broadly used for n and p-type DSSCs^{173, 110, 182, 183} The dye used for sensitization was the ruthenium cyclometallated complex WOC53¹⁵¹ (Fig. 5.5) and duplicate cells were made to confirm reproducibility of the measurements. Their iodine/triiodide concentrations were varied systematically. The first electrolyte (**Stnd I**) comprised of 0.3 M iodine I₂, 0.6 M 1-butyl-3-methylimidazoliumiodine (BMIMI), 0.1 M guanidinium thiocyanate (GuSCN) and 0.5 M 4-tert-butylpyridine (4-TBP) in acetonitrile

The second electrolyte (**Stnd III**) comprised of 0.1 M iodine I₂ and 1 M lithium iodide LiI in acetonitrile and the third electrolyte (**Stnd IV**) comprised of 0.03 M iodine I₂, 0.6 M tetrabutylammonium iodide (TBAI), 0.1 M guanidinium thiocyanate (GuSCN) and 0.5 M 4-tert-butylpyridine (4-TBP) in acetonitrile. From Fig. 5.6 and Table 5.1 the cells with Stnd III electrolyte and higher concentration of iodine/triiodide have a better performance than the others. Namely, for the better DSSC of each pair, the η of the cells with Stnd III electrolyte is 0.138% compared to 0.051% for Stnd I and 0.023% for Stnd IV electrolyte, i.e. 2.5 times and 6 times higher respectively. Each of the three different electrolytes (Stnd I, III, IV) was investigated further by changing the iodine/triiodide concentration in each series.

Experiment Name	Jsc/ mA cm ⁻²	Voc/mV	FF/%	η/%
Stnd I_1	0.96	104	32	0.031
Stnd I_2	1.45	109	32	0.051
Stnd III_1	3.80	104	35	0.138
Stnd III_2	3.62	103	35	0.129
Stnd IV_1	0.77	98	31	0.023
Stnd IV_2	0.75	95	31	0.022

Table 5.1: Performance data for duplicate cells for three different electrolytes. The NiO electrodes were fabricated as described in section 3.3.5 of this thesis. The measurements were done on the day of sealing. The cells active area was 0.237 cm².

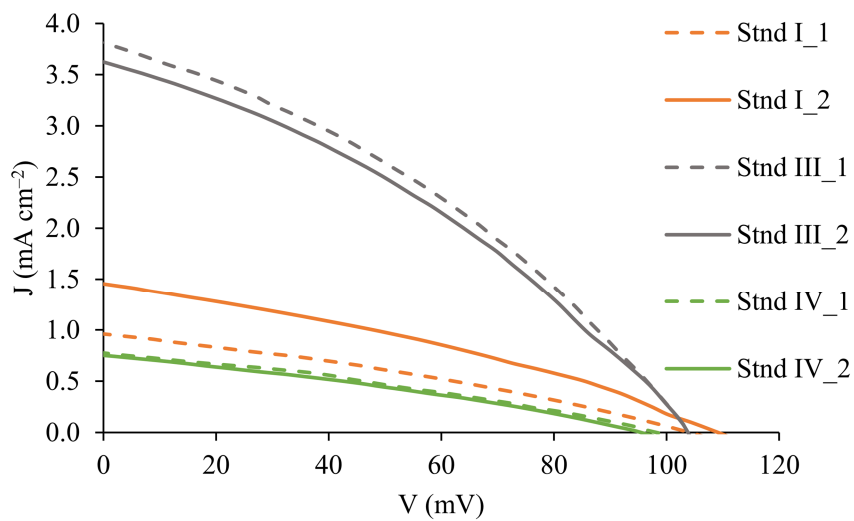


Fig. 5.6: JV curves of the duplicate DSSCs with the three different electrolytes Stnd I, Stnd III and Stnd IV.

5.2.3 Varying the concentration of iodine/triiodide ions in Stnd I electrolyte

Cell name	Description of the electrolyte
Stnd III	0.1 M I ₂ , 1 M LiI
Stnd I	0.03 M I ₂ , 0.6 M (BMIMI), 0.1 M GuSCN, 0.5M 4-TBP
I90	0.1 M I₂ , 0.6 M (BMIMI), 0.1 M GuSCN, 0.5M 4-TBP
I91	0.03 M I ₂ , 1 M (BMIMI) , 0.1 M GuSCN, 0.5M 4-TBP
I92	0.1 M I₂, 1 M (BMIMI) , 0.1 M GuSCN, 0.5M 4-TBP

Table 5.2: Summary of electrolyte compositions for changes made to electrolyte Stnd I.

Experiment Name	Jsc/ mA cm ⁻²	Voc/mV	FF/%	η /%
Stnd I_1	0.96	104	32	0.031
Stnd I_2	1.45	109	32	0.051
Stnd III_1	3.80	104	35	0.138
Stnd III_2	3.62	103	35	0.129
I90_1	2.61	109	32	0.092
I90_2	2.23	106	32	0.075
I91_1	1.46	106	33	0.051
I91_2	1.25	100	31	0.038
I92_1	1.39	101	29	0.041
I92_2	2.61	110	34	0.096

Table 5.3: Performance data for duplicate cells sensitized with WOC53 and for changes made to electrolytes Stnd I and Stnd III. The NiO electrodes were fabricated as described in section 3.3.5 of this thesis. The cells active area of the cell was 0.237 cm².

From Fig. 5.7 and Table 5.3, it is observed that when the concentration of iodine was increased, the efficiency of the cells increases (efficiencies of 0.092% for I90_1 and 0.096% for I92_2 compared with 0.051% for Stnd I_2). When only the concentration of the ionic liquid BMIMI was increased, the

performance of the cell did not overpass the Stnd I_2 (efficiencies of 0.051% for the I 90_1 compare with 0.051% for Stnd I_2).

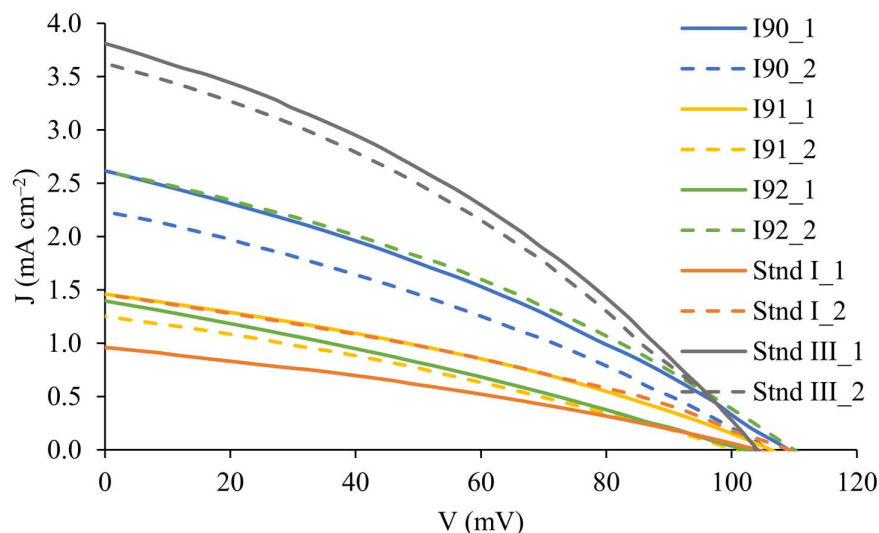


Fig. 5.7: JV curves of the DSSCs with changes made to electrolyte Stnd I compared to DSSCs containing Stnd III.

5.2.4 Varying the concentration of iodine/triiodide ions in Stnd IV electrolyte

Cell name	Description of the electrolyte
Stnd III	0.1 M I ₂ , 1 M LiI
Stnd IV	0.03 M I ₂ , 0.6 M (TBAI), 0.1 M GuSCN, 0.5M 4-TBP
I93	0.1 M I₂ , 0.6 M (TBAI), 0.1 M GuSCN, 0.5M 4-TBP
I94	0.03 M I ₂ , 1 M (TBAI) , 0.1 M GuSCN, 0.5M 4-TBP
I95	0.1 M I₂, 1 M (TBAI) , 0.1 M GuSCN, 0.5M 4-TBP

Table 5.4: Summary of electrolyte composition for changes made to electrolyte Stnd IV

From Fig. 5.8 and Table 5.5 it is observed that once more the cells I93 with a higher concentration of iodine performed better compared with the Stnd IV_1 cell (efficiencies of 0.052% compare with 0.023%). Cells I95 in which the concentrations of both iodine and ionic liquid were increased exhibit a higher open circuit voltage of 125 mV (Table 5.5).

Experiment Name	Jsc/ mA cm⁻²	Voc/mV	FF/%	η/%
Stnd IV_1	0.77	98	31	0.023
Stnd IV_2	0.75	95	31	0.022
Stnd III_1	3.80	104	35	0.138
Stnd III_2	3.62	103	35	0.129
I 93_1	1.48	115	31	0.052
I 93_2	1.32	115	29	0.044
I 94_1	0.55	99	32	0.017
I 94_2	0.48	106	32	0.016
I 95_1	0.79	124	30	0.030
I 95_2	0.78	125	32	0.031

Table 5.5: Performance data for duplicate cells sensitized with WOC53 and for changes made to electrolyte Stnd IV and cells Stnd III. The NiO electrodes were fabricated as described in section 3.3.5 of this thesis. The cells active area of the cell was 0.237 cm².

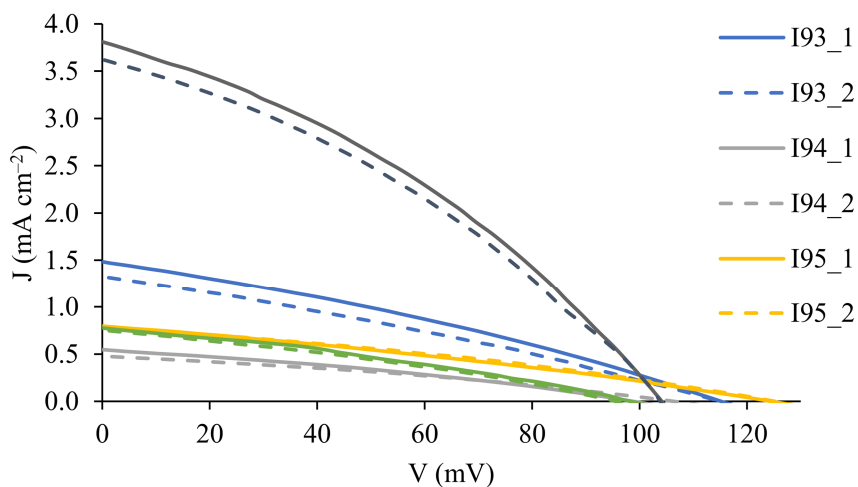


Fig. 5.8: JV curves of the DSSCs with changes made to electrolytes Stnd IV compared to DSSCs containing Stnd III.

In this study it was concluded that, the best iodine/triiodide electrolyte of those investigated p-type cells is the Stnd III which has a high concentration of iodine and LiI and no ionic liquid. The cells filled with an electrolyte containing TBAI (I93_1) or BMIMI (I90_1), exhibited the worst overall performances. An explanation for this could be the large size of the cation (TBAI⁺, BMIM⁺) which worsens the diffusion of the electrolyte in the semiconductor.

5.3 Background of varying the cation size in the electrolyte

Numerous studies on the counter ion effect of the I_3^-/I^- electrolyte have been done in order to investigate the role and the behaviour of different cations in a DSSC. In n-type DSSCs the counter ion has a double role; it intercalates and/or absorbs at the TiO_2 /electrolyte interface¹⁸⁴, this leads to enhanced charge compensation of the electron accumulation in the conductive band of the TiO_2 semiconductor. The intercalation and/or absorption of the cation leads to a flat band modification of the TiO_2 ¹⁸⁵. This was proven in the study of *Lindquist and co-workers*¹⁹⁹, during which an increase in V_{OC} was observed with increase cation size $Li^+ < Na^+ < K^+ < Rb^+ < Cs^+$ ¹⁸⁶. In p-type DSSCs similar studies have shown that the intercalation of Li^+ in the NiO semiconductor could contribute to the modification of the valence band energy and thus to the increase of the V_{OC} but only in a small extend⁴². During work of *Boschloo and co-workers*²⁰⁰ the effect of Li^+ , Na^+ and TBA^+ counterions was tested and it was observed that the hole transport time and hole lifetime decreased with increasing cation size (Fig. 5.9).

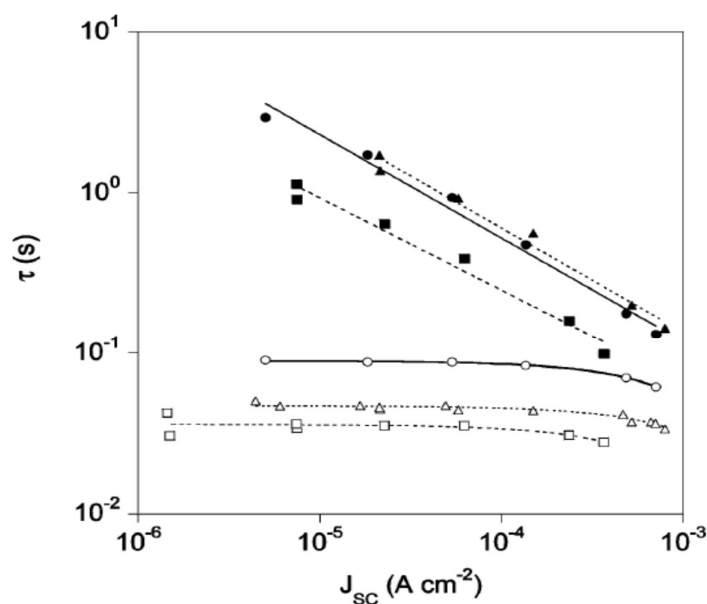


Fig. 5.9: Hole transport times (open symbols) and lifetimes (filled symbols) in C343-sensitized mesoporous NiO solar cells as function of short-circuit current density. The electrolyte was 0.5 M of LiI (circles), NaI (triangles), or TBAI (squares) and 0.1 M I_2 in 3-methoxypropionitrile. Work reported by *Boschloo and co-workers*²⁰⁰. Reproduce with permission from ACS, copyright 2007.

5.3.1 Effect of varying the cation size in the electrolyte

During the present work, counter ions differing in size were tested for the triiodide/iodide redox couple of the electrolyte in acetonitrile. The NiO electrodes were fabricated as described in section 3.3.5 of this thesis. The NiO was sensitized with WOC53 (Fig. 5.5). Table 6 summarises the electrolyte composition and DSSCs parameters. JV curves were produced after sun simulation measurements and the data were evaluated.

Experiment Name	Electrolyte composition	Jsc/ mA cm ⁻²	Voc/mV	FF/%	η /%
LiI_1	0.1M I ₂ ,1M LiI in	3.38	95	36	0.116
LiI_2	acetonitrile	3.34	95	34	0.109
NaI_1	0.1M I ₂ ,1M NaI in	3.22	83	29	0.078
NaI_2	acetonitrile	3.67	74	29	0.080
TBAI_1	0.1M I ₂ ,1M TBAI in	1.53	65	31	0.031
TBAI_2	acetonitrile	1.32	64	32	0.028

Table 5.6: Performance data for duplicate cells sensitized with WOC53 dye and with different cations in the I₃⁻/I⁻ electrolyte. The cells active area of the cell was 0.237 cm².

From Figure 5.10 and Table 5.6 it can be observed that the efficiency of the DSSC decreases with increasing cation size $\text{Li}^+ < \text{Na}^+ < \text{TBA}^+$. A significant drop in J_{SC} and V_{OC} was observed when comparing the cells LiI_1 and TBAI_1 which suggests that the bigger size of the TBA^+ compared to the Li^+ ion significantly reduces the charge transfer which results in a low J_{SC} . On the other hand, the cell with LiI_2 displays a similar or even slightly higher J_{SC} compared with the NaI_1 cell (3.67 vs 3.38 mA cm^{-2} for NaI_2 and LiI_1 respectively) but also a drop in V_{OC} (95 vs. 83 mV for LiI_2 and NaI_1 respectively) and a significant drop in fill factor (36 vs. 29 % for LiI_2 and NaI_1 respectively).

In conclusion, this study agrees with the results in the literature, small size cations (Li^+) have more beneficial effect compared with larger cations (TBA^+) on the charge transport mechanism at the interface of the sensitized NiO and the electrolyte.

5.4 Introduction: Organic solvents

As mentioned in the introduction of this chapter, the medium in which all the compounds of the electrolyte are dissolved is an important parameter defining the performance of the solar cell. Besides the volatility and the chemical stability, other characteristics such as for example the donor number, the dielectric constant (ϵ_r) and the viscosity coefficient (ζ) of the organic solvent have been investigated. The Gutmann donor number (DN), is the characteristic solvent donation electron capacity,¹⁸⁷ higher DN means stronger basicity of the solvent. During the work of *Han and co.*¹⁸⁸ the DN in n-type DSC was investigated and the results showed that by increasing the DN of the solvent, the V_{oc} of the cell was increased and the J_{sc} decreased. This result was due to the fact that a basic solvent will decrease the number of the surface-bound protons, which will lead to a more negatively charged TiO_2 and effectively will increase the flat-band potential (Φ_{fb}) of the semiconductor¹⁸⁹. This

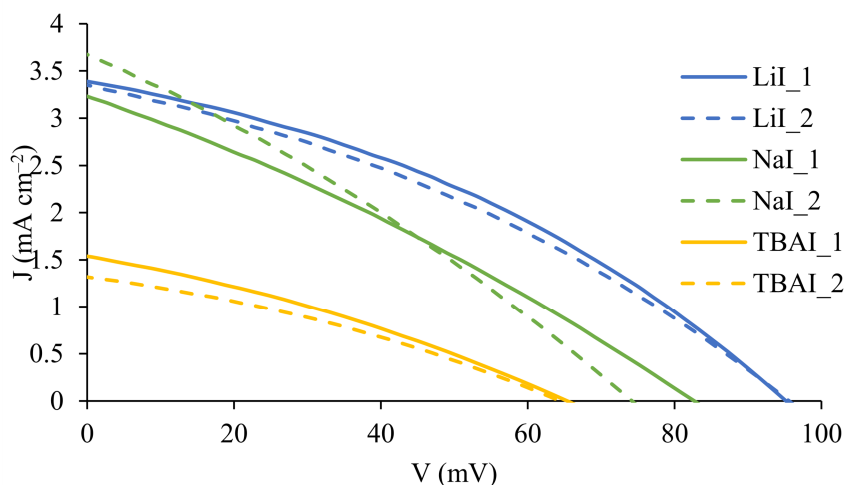


Fig. 5.10: JV curves of the DSSCs with different electrolytes displayed in Table 5.6.

in turn, will decrease the driving force of the electron transfer from the excited dye to the semiconductor which will result in a decrease of the J_{sc} . But the potential difference between the electrolyte redox shuttle and the valence band of the semiconductor, will increase leading to a higher V_{oc} . Something analogous to this had not yet been investigated for p-type DSSCs when we began our investigation.

5.4.1 Effect of different organic solvent

During this experiment, five organic electrolyte solvents (Table 5.7) and mixtures of these were tested and the effect on the performance of the p-type DSSC build was monitored in terms of J_{sc} , V_{oc} and efficiency. Moreover, EIS tests were performed which gave a better understanding about the different procedures happening at the various interfaces within the cells.

Solvent	Structure	Boiling point/ $^{\circ}\text{C}$	Viscosity/ mPa s^{a}	Donor number ^b
Acetonitrile (AN)	CH_3CN	82	0.33 (at 30 $^{\circ}\text{C}$)	14.1
Propionitrile (PN)	$\text{CH}_3\text{CH}_2\text{CN}$	97	0.39 (at 30 $^{\circ}\text{C}$)	16.1
Valeronitrile (VN)	$\text{CH}_3(\text{CH}_2)_3\text{CN}$	139	0.78 (at 19 $^{\circ}\text{C}$)	
3-methoxypropionitrile (MPN)	$\text{CH}_3\text{OCH}_2\text{CH}_2\text{CN}$	164	2.5 (at 25 $^{\circ}\text{C}$)	16.1
N-Methylpyrrolidone (NMP)		203	1.65 (at 25 $^{\circ}\text{C}$)	27.3

Table. 5.7: Chosen organic solvents for this experiment.

^a data from ref ¹⁵⁶ and ¹⁶⁵ $1\text{cp}=1\text{mPa s}$ ^b Gutmann number ¹⁸⁷

For this experiment two types of electrodes were used, the house made screen printed NiO/FTO using Solaronix NiO paste (see section 3.3.5) and the commercial Dyenamo NiO/FTO electrodes. The electrolyte comprises of iodine 0.1 M and lithium iodide 1 M in the organic solvent shown in Table 5.7. The sensitizer used was WOC53 (Fig. 5.5).

Experiment Name	Jsc/ mA cm ⁻²	Voc/mV	FF/%	η/%
AN_1	3.38	95	36	0.116
AN_2	3.34	95	34	0.109
PN_1	2.18	115	40	0.099
PN_2	2.16	118	39	0.100
VN_1	0.64	149	36	0.033
VN_2	0.64	148	34	0.031
MPN_1	1.48	106	36	0.053
MPN_2	1.47	113	36	0.056
NMP_1	0.41	65	30	0.008
NMP_2	0.44	70	31	0.009

Table 5.8: Performance data for duplicate cells with in-house screen printed NiO/FTO electrodes. The active area of the cell was 0.237 cm².

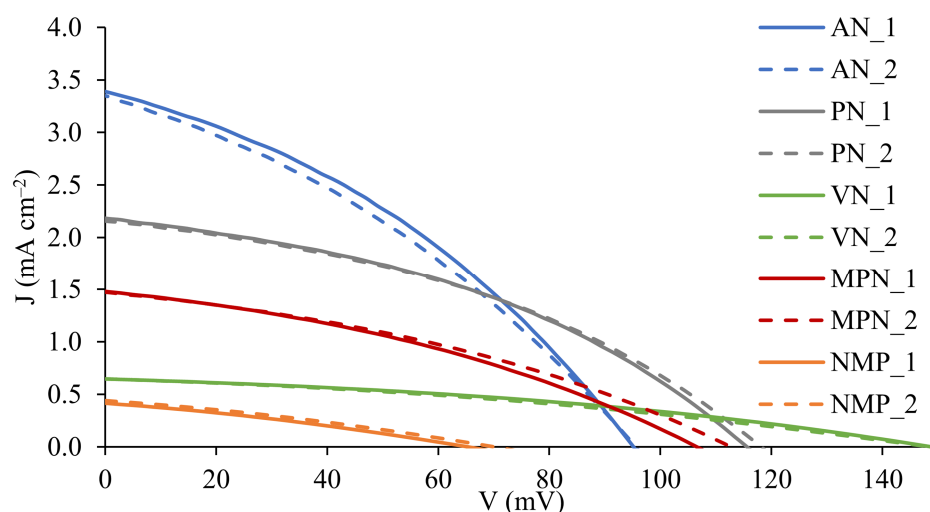


Fig. 5.11: JV curves for duplicate DSSCs containing in-house screen printed NiO/FTO

From the results in Fig. 5.11 and Fig. 5.12 it was deduced that the cells with AN as an organic solvent exhibit the highest efficiency (0.139% for the cells with Dyenamo electrode and 0.116% for the in-house screen printed NiO/FTO electrode See Tables 5.8 and 5.9). This is mainly due to the high short circuit current of those cells (4.06 and 3.38 mA cm⁻² for the cells with the Dyenamo electrodes and the in-house electrode respectively). Nevertheless, the cells with PN (PN_2) as an organic solvent exhibit

a higher open circuit voltage of 118 mV compare with the best performing cell (AN_1) in terms of efficiency which achieve a Voc of 95 mV.

Experiment Name	Jsc/ mA cm ⁻²	Voc/mV	FF/%	η/%
AN_1	4.06	95	36	0.139
AN_2	4.13	92	36	0.136
PN_1	2.63	115	39	0.117
PN_2	2.51	119	39	0.117
VN_1	1.04	139	42	0.060
VN_2	0.98	141	41	0.057
MPN_1	1.79	100	36	0.064
MPN_2	1.77	104	38	0.070
NMP_1	0.41	78	33	0.010
NMP_2	0.40	79	33	0.011

Table 5.9: Performance data for duplicate cells with commercial Dyenamo NiO/FTO electrodes. The active area of the cell was 0.25 cm².

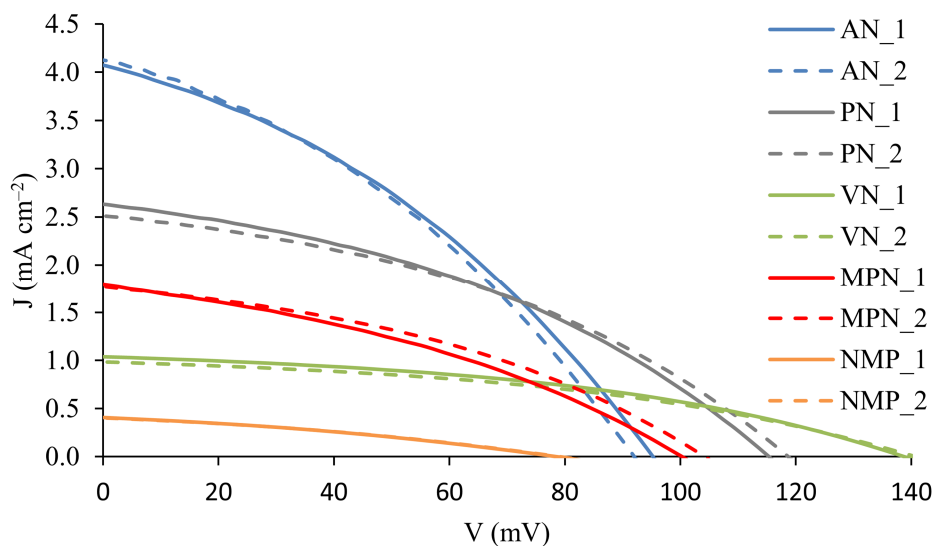


Fig. 5.12: JV curves for duplicate DSSCs containing commercial Dyenamo NiO/FTO electrodes.

Moreover, the Voc of the cells with VN achieve an impressive value of 141 mV for the cells with a Dyenamo NiO electrode and 149 mV for the cells with the in-house screen-printed NiO electrode. Besides the initial performance of the DSSCs on the day of the sealing the long-term stability is also a very important factor that should be taken into consideration when designing the components of a DSSC.

Experiment Name	Jsc/ mA cm⁻²	Voc/mV	FF/%	η/%
AN_1	3.17	89	34	0.096
AN_2	4.15	82	35	0.121
PN_1	3.17	119	41	0.154
PN_2	2.99	119	41	0.146
VN_1	1.18	148	44	0.077
VN_2	1.14	146	43	0.071
MPN_1	1.69	91	38	0.058
MPN_2	1.61	97	40	0.063
NMP_1	0.55	95	34	0.018
NMP_2	0.56	96	35	0.019

Table 5.10: Performance data for duplicate cells with commercial Dyenamo NiO/FTO electrodes on day 33 or 34 after the sealing. The active area of the cell was 0.25 cm².

Experiment Name	Jsc/ mA cm⁻²	Voc/mV	FF/%	η/%
AN_1	3.00	86	34	0.088
AN_2	3.81	83	32	0.102
PN_1	3.04	122	40	0.148
PN_2	2.96	118	41	0.142
VN_1	1.25	153	41	0.079
VN_2	1.06	155	39	0.065
MPN_1	1.37	89	29	0.035
MPN_2	1.38	101	31	0.043
NMP_1	0.57	102	35	0.020
NMP_2	0.58	101	35	0.021

Table 5.11: Performance data for duplicate cells with commercial Dyenamo NiO/FTO electrodes on day 57 or 58 after the sealing. The active area of the cell was 0.25 cm².

During this work the stability of the cells was tested after 33 or 34 and 57 or 58 days (Table 5.10 and 5.11). The cells were kept under ambient conditions in the dark between JV curves measurements. From Fig. 5.13 and Table 5.10 and 5.11, it is observed that most cells display a great long-term stability, except for one cell containing AN electrolyte which exhibits a drop of Jsc. Remarkably, the majority of the cells not only stay stable through time but, their performance increases. Namely, cells with PN and VN increase in efficiency over time from 0.117 to 0.146% and from 0.060 to 0.079% respectively. This is mainly due to the increase in Jsc in both cases. This phenomenon, is also known for n-type DSSCs sensitized with Ru(II) or Cu(I) complexes and it is attributed to the dye-aggregates which reorganize on the surface of the electrode over a period of time ¹⁹⁰.

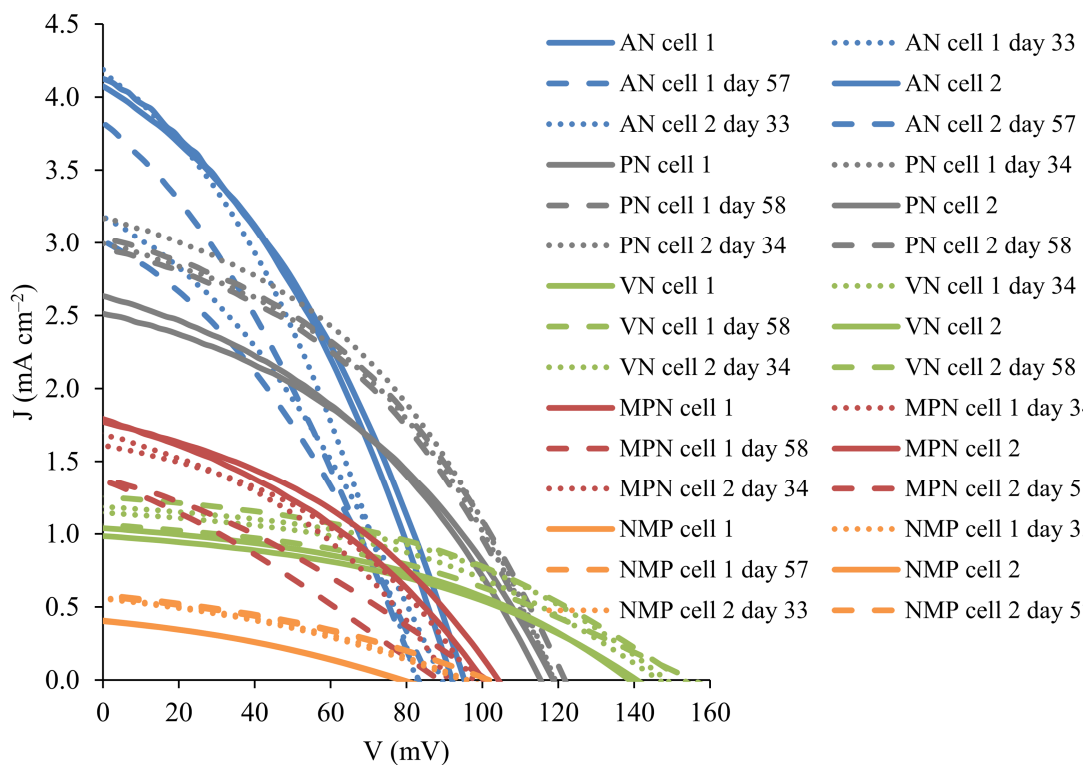


Fig. 5.13: JV curves for duplicate DSSCs containing commercial Dyenamo NiO/FTO electrodes.

Although that the cells with AN perform better on the day of the sealing, the cells with more viscous organic solvents have a better stability over time and a higher open circuit voltage. In order to harvest the benefits of both cases, mixtures of solvents were prepared (see later). This method has been broadly used in n-type DSSC¹⁵⁶.

In order to further investigate the DSSCs with AN, PN or MPN solvents EIS measurements were performed. Those measurements were done and analysed by Dr. Markus Willgert¹¹¹. The main factor that differentiates the performance of the DSSCs with different organic solvents (Table 5.9) is the different J_{SC} values. For the EIS study, DSSCs with three different organic solvents with the same donor number were chosen in order to exclude one variable and better investigate the solvent viscosity which follows the order AN < PN < MPN. The J_{SC} values of those cells follow the inverse trend.

Experiment Name	R_t/Ω	R_{rec}/Ω	$C_\mu/\mu F$	R_{Pt}/Ω	$C_{P\mu}/\mu F$	τ/ms
AN_1	39.6	87.9	2107.5	7.3	3.4	185
AN_2	40.4	80.1	1883.4	7.1	3.7	151
PN_1	96.4	146.3	1685.4	8.2	4.0	247
PN_2	109.0	129.3	1451.7	12.9	3.7	188
MPN_1	70.4	332.2	2170.3	20.4	4.0	721
MPN_2	56.6	248.6	2160.5	18.4	3.8	537

Table 5.12: EIS data obtained from measurements at light intensity of 22 mW cm^{-2} of p-type DSSCs containing Dyanamo NiO/FTO working electrodes, sensitized with WOC53 dye and I_3^-/I^- electrolyte in different solvents.

The diffusion coefficient for the redox mediator in the electrolyte decreases with increasing viscosity of the organic solvent ¹⁹¹. As can be observed in Table 5.12 and Fig. 5.14, the recombination resistance R_{rec} increases with increasing viscosity of the organic solvent which is due to the fewer charge carriers available for back reactions. Moreover, the chemical capacitance C_μ of the cells with MPN as an organic solvent has the highest value which in combination with the previous observation about the recombination resistance will result in a long charge carrier lifetime. The lowest transport resistance R_t value is observed for the cells with AN electrolyte and intermediate for the cells with MPN electrolyte. This suggests that the cells with MPN have a higher density of charge carrier trap state, which in turn agrees with the decreased J_{SC} for those cells. In addition, the platinum resistance R_{Pt} of the cells with MPN is more than twice as large than the R_{Pt} of the cells field with AN electrolyte which is another explanation for the low J_{SC} observed on the cells with MPN electrolyte. The cells with PN electrolyte exhibit a high transport resistance R_t which suggest a high density of states of charge carrier trap states and together with the low chemical capacitance is a good explanation regarding the moderate performance of those cells.

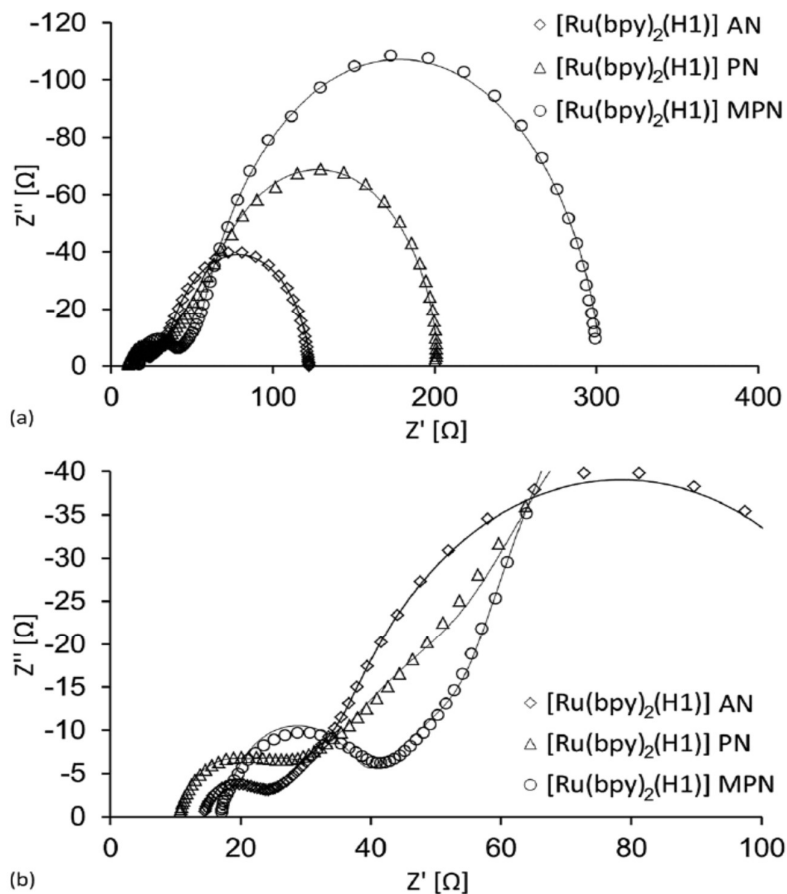


Fig. 5.14: **a.** Nyquist plot and **b.** Expansion of Nyquist plots for DSSC with Dyenamo electrode NiO/FTO, sensitized with WOC53 and different electrolyte ($[Ru(bpy)_2(H1)] = WOC53$). This work was reported by *Housecroft and co-workers*¹¹¹, Reproduce with permission from Royal Society of Chemistry. Copyright 2017.

We now turn to the effect of mixed solvents. The data in Table 5.13 give DSSCs performance parameters for duplicate cells sensitized with WOC53 (Fig. 5.5) and with I_3^-/I^- redox couple. JV curves are shown in Fig. 5.14-16.

Experiment Name	Jsc/ mA cm ⁻²	Voc/mV	FF/%	η /%
AN_1	4.06	95	36	0.139
AN_2	4.13	92	36	0.136
AN : PN 3:1_1	3.64	99	38	0.138
AN : PN 3:1_2	3.60	100	38	0.137
AN : PN 1:1_1	3.34	115	37	0.142
AN : PN 1:1_2	3.36	112	37	0.140
AN : PN 1:3_1	2.79	106	38	0.111
AN : PN 1:3_2	2.86	105	38	0.113
PN_1	2.63	115	39	0.117
PN_2	2.51	119	39	0.117
AN : VN 3:1_1	3.14	115	39	0.141
AN : VN 3:1_2	3.27	115	40	0.148
AN : VN 1:1_1	2.43	119	40	0.115
AN : VN 1:1_2	2.38	121	40	0.115
AN : VN 1:3_1	1.58	133	42	0.087
AN : VN 1:3_2	1.58	133	39	0.081
VN_1	1.04	139	42	0.060
VN_2	0.98	141	41	0.057
AN : MPN 3:1_1	2.97	102	37	0.112
AN : MPN 3:1_2	2.90	97	39	0.109
AN : MPN 1:1_1	2.74	111	38	0.117
AN : MPN 1:1_2	2.85	104	38	0.112
AN : MPN 1:3_1	2.25	112	39	0.097
AN : MPN 1:3_2	2.21	106	38	0.089
MPN_1	1.79	100	36	0.064
MPN_2	1.77	104	38	0.070

Table 5.13: Performance data on day of the sealing for duplicate cells with commercial Dyenamo NiO/FTO electrodes and mixtures ratios are volume ratios of organic solvents in the electrolyte. The active area of the cell was 0.25 cm².

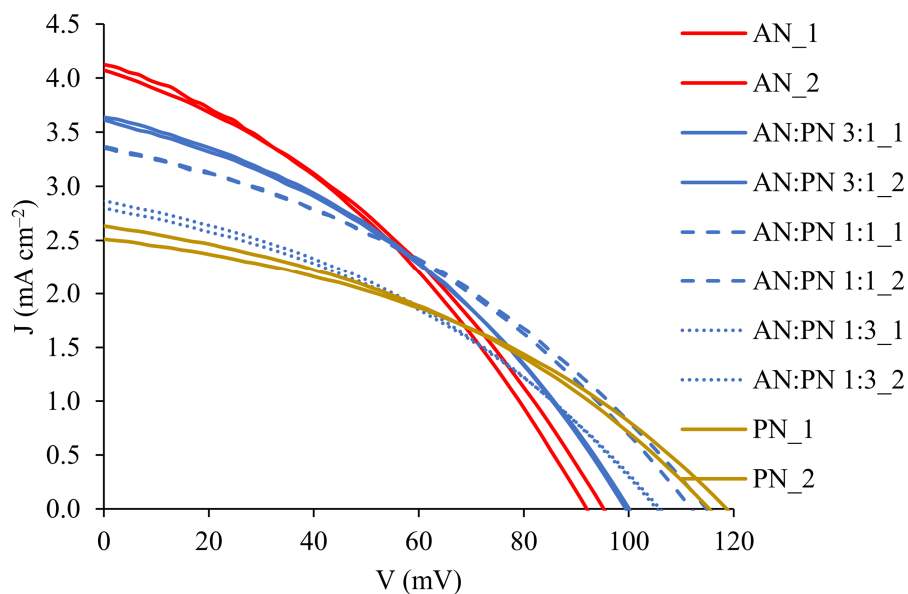


Fig. 5.14: JV curves for duplicate DSSCs containing commercial Dyenamo NiO/FTO electrodes and sensitized with WOC53. AN, PN or AN/PN mixed solvents.

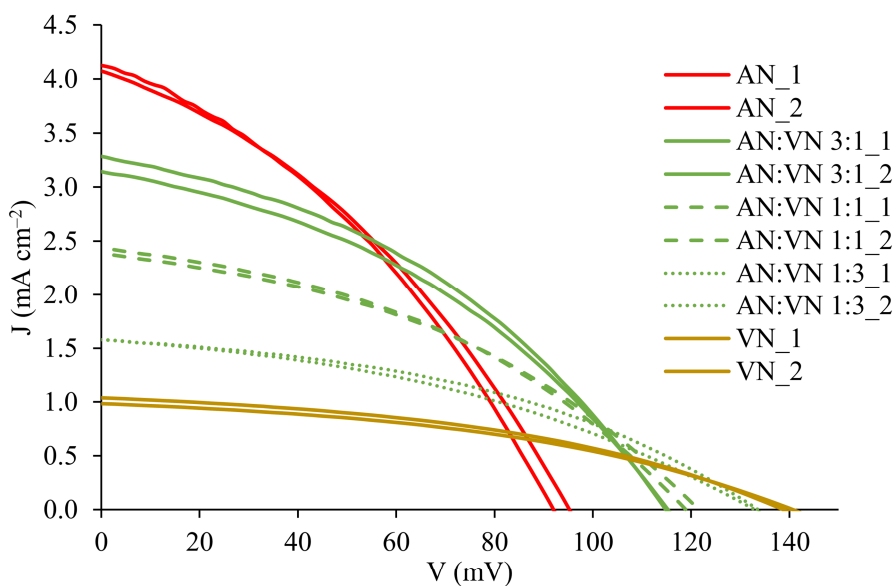


Fig. 5.15: JV curves for duplicate DSSCs containing commercial Dyenamo NiO/FTO electrodes and sensitized with WOC53. AN, VN or AN/VN mixed solvents.

With the addition of PN, VN or MPV to AN a decrease in the J_{sc} is observed especially with the mixture of AN and VN (Table 5.13, and Fig. 5.14-16). At the same time, there is an increase of the V_{oc} which agrees with the general observation that an increase in the donor number induces a decrease of the J_{sc} and an increase in V_{oc} ¹⁵⁶. For PN, a small change is observed upon increase of PN

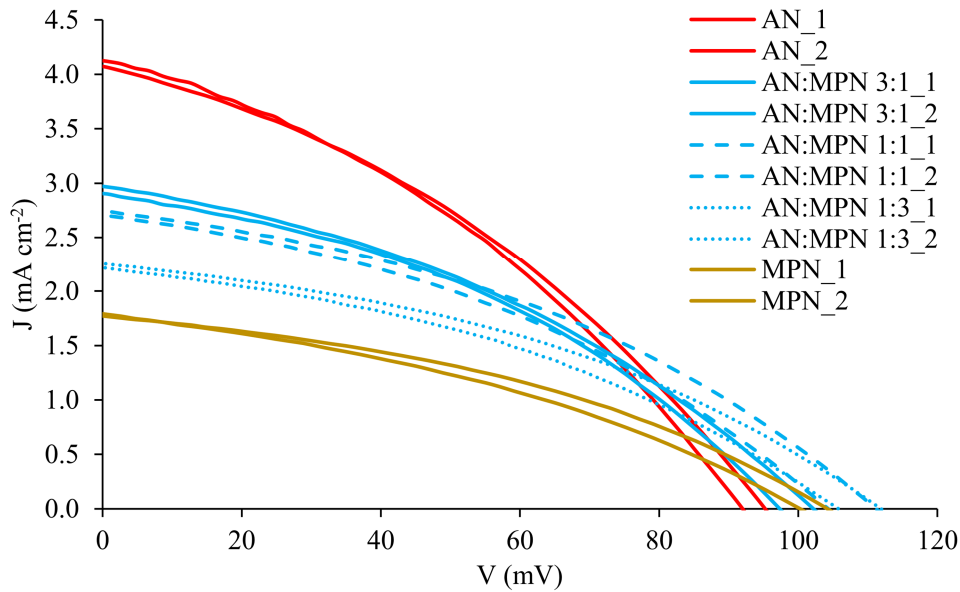


Fig. 5.16: JV curves for duplicate DSSCs containing commercial Dyenamo NiO/FTO electrodes and sensitized with WOC53. AN, MPN or AN/MPN mixed solvents

with the mixture AN : PN 1:1 having the best efficiency (Table 5.13, Fig. 5.14). For VN and MPN a decrease of the efficiency of the cells is observed upon increase of their volumes (Table 5.13, Fig. 5.15, 5.16). It is noticeable that for MPN, the higher V_{oc} is obtained with the mixture of 1:3 and 1:1 rather than pure MPN (Table 5.13, Fig. 5.16). In conclusion, all the results agree that the optimal solvent for this electrolyte is a mixture of AN : PN 1:1. The long term stability of the cells with this electrolyte was tested on day 39 and 63 from the day of sealing and the results are summarized in Table 5.14 and Fig. 5.17.

Experiment Name	Jsc/ mA cm ⁻²	Voc/mV	FF/%	η/%
On day 0				
AN : PN 3:1_1	3.64	99	38	0.138
AN : PN 3:1_2	3.60	100	38	0.137
AN : PN 1:1_1	3.34	115	37	0.142
AN : PN 1:1_2	3.36	112	37	0.140
On day 39				
AN : PN 3:1_1	3.86	97	38	0.142
AN : PN 3:1_2	3.88	100	41	0.158
AN : PN 1:1_1	3.86	107	39	0.162
AN : PN 1:1_2	3.89	105	40	0.162
On day 63				
AN : PN 3:1_1	3.52	97	32	0.111
AN : PN 3:1_2	3.62	99	38	0.138
AN : PN 1:1_1	3.49	108	31	0.118
AN : PN 1:1_2	3.59	111	35	0.139

Table 5.14: Performance data for duplicate cells with commercial Dyenamo NiO/FTO electrodes and a mixture of organic solvents in the electrolyte on day 39 and 63 of the sealing. The active area of the cell was 0.25 cm².

As can be observed from Table 5.14 and Fig. 5.17 the J_{SC} increases while the V_{OC} remains stable (3:1 ratio) or decrease (1:1 ratio), the fill-factor remains stable so the overall result is that the efficiency increases, with the best efficiency being 0.162% for the DSSCs filled with the electrolyte of AN:PN 1:1_1 and 2. The J_{SC} (3.86 and 3.89 mA cm⁻²) of these cells approach the current density of those recorded for DSSCs on the day of cell fabrication in which the solvent is pure AN (Table 5.13). Further ageing results in decrease in performance due to a decrease in fill factor (31-38%) which suggests

deterioration of the cell. In conclusion the mixed solvent leads to noticeably better long-term stability than the DSSCs containing only AN (Table 5.14 vs. Table 5.10) that was due to the increased viscosity of the organic solvent in the electrolyte by replacing a volume of the volatile AN with the less volatile PN.

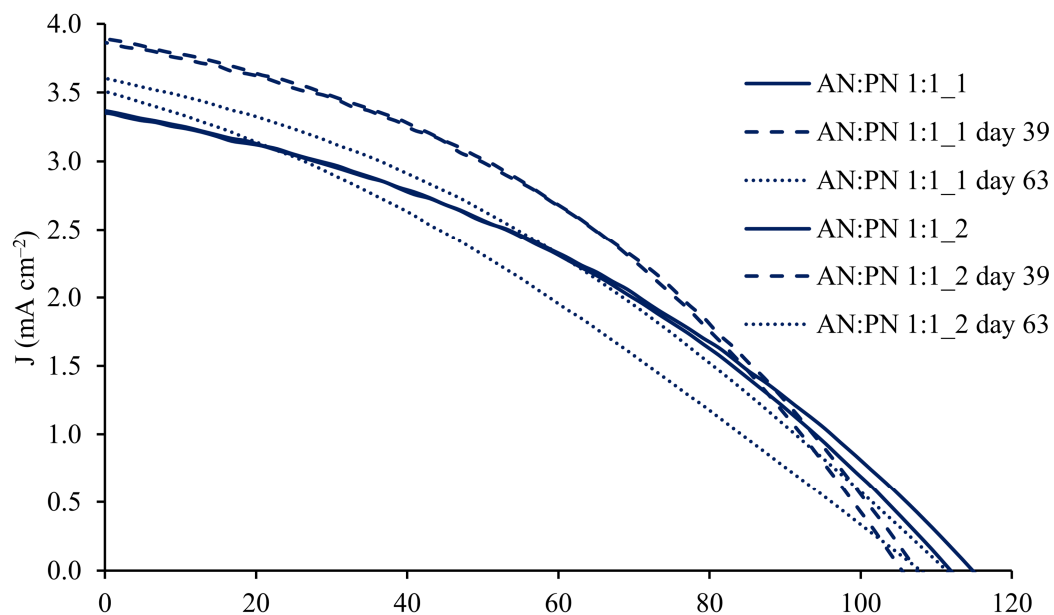


Fig. 5.17: JV curves for duplicate DSSCs containing commercial Dyenamo NiO/FTO electrodes and sensitized with WOC5 and electrolyte containing iodine/triiodide redox couple in the electrolyte in a mixture of organic solvents AN : PN 1:1 on day 0, 39 and 63 of the sealing.

5.5 Additives background

Numerous investigations have been done on the effects of additives in the electrolyte. The additives are typically cations or compounds that are supposed to adsorb on the surface of the semiconductor¹⁵⁶.

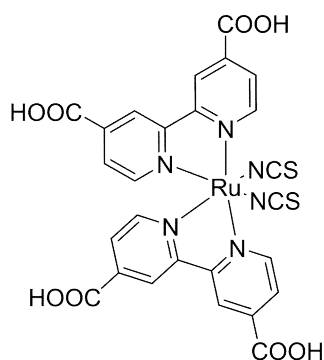


Fig. 5.18: Chemical structure of N3 dye

Thereby changing the surface charge characteristics^{192,193}, and shifting the band edge (the conductive band CB, or valence band VB). This can affect recombination kinetics, and by consequence affect the photovoltaic parameters and the efficiency of the cell. 4-tert-butylpyridine (TBP) is an additive first used by *Grätzel and co-workers*¹⁹⁴ which improve the efficiency of the cell by increasing the V_{oc} . Later on, it was proven by in-situ Raman spectroscopy that the additives, like the dye, anchors on the surface of the semiconductor¹⁹⁵.

According to the work of *Hagfeldt and co-workers* the increase of the V_{oc} , can be attributed to a simultaneous shift of the band-edge of the semiconductor towards higher energy levels and the increase of the electron lifetime in the TiO_2 conduction band¹⁹⁶.

A different type of additive is the guanidinium salts (e.g.: guanidinium thiocyanate GSCN) which has a beneficial effect on the performance of n-type DSSC but operates in a different way compared to the aforementioned TBP. The use of guanidinium ions results in an increase in J_{sc} due to an increase in electron injection yield³⁶. The reason for this is the formation of a compact monolayer on the surface of the TiO_2 comprised of the guanidinium ions and the dye (Fig. 5.18, N3) that reduces electron recombination¹⁹⁷. During the work of *Gibson and co-workers* on the effect of GuSCN in p-type cells¹⁹⁸ it was shown that the guanidinium ions do not adsorb on the NiO surface, and have a rather negative affect on the performance of the cell. This was attributed to the formation of a complex between SCN^- and I_2 , which lowers the concentration of I_3^- and leads to a decrease in the J_{sc} . Moreover, lithium cations have been used as additives in n-type cells¹⁹⁹ this work indicates that the CB of TiO_2 is shifted toward more positive potentials due to adsorption of the cations on the surface of TiO_2 and increasing the electron injection yield due to intercalation of Li^+ . Similar work was performed for p-type DSSCs⁴², during which it was observed that by doping the NiO semiconductor a positive tuning of the valence band could be realized with a significant increase of the V_{oc} . On the other hand, when the Li^+ concentration was increased in the electrolyte of the DSSC, no beneficial effects on the V_{oc} were seen. In another study, *Odobel and co-workers*²⁵ affirm that the simple addition of Li^+ in the electrolyte as an additive can have beneficial results in the photoefficiency of the DSSCs. This can be due to the small size of the lithium cation that allows to intercalate easily on the bulk of the NiO and efficiently transport the charge at the semiconductor. Indeed, the work of *Boschloo and co-workers*²⁰⁰ proved that the larger the size of the counter cation in the electrolyte, the

worse the hole life time and hole transport time. The small size of the lithium ion lead to the best performance among the counterions studied in this work (section 5.3, Fig. 5.9).

5.5.1 Effect of different concentrations of additives in p-type DSSCs

We now move from the background information to the investigation conducted in our lab during which an investigation on the behaviour of GuSCN and TBP additives was conducted for p-type DSSCs. The concentration of both GuSCN and TBP was systematically modified in an electrolyte comprised of 0.3 M iodine I₂, 0.6 M 1-butyl-3-methylimidazoliumiodine (BMIMI), 0.1 M guanidinium thiocyanate (GuSCN) and 0.5 M 4-tert-butylpyridine (4-TBP) in 85:15 acetonitrile, valeronitrile (**EL1**). This work was done before the optimization of the organic solvent described in section 5.4.1 which is the reason of this choice of organic solvents for the electrolyte. The different concentration of GuSCN were 0, 0.05, 0.1 and 0.2 M and for TBP, 0, 0.25, 0.5 and 1 M NiO was used as the p-type semiconductor and the photocathode were made in-house by screen-printing as described

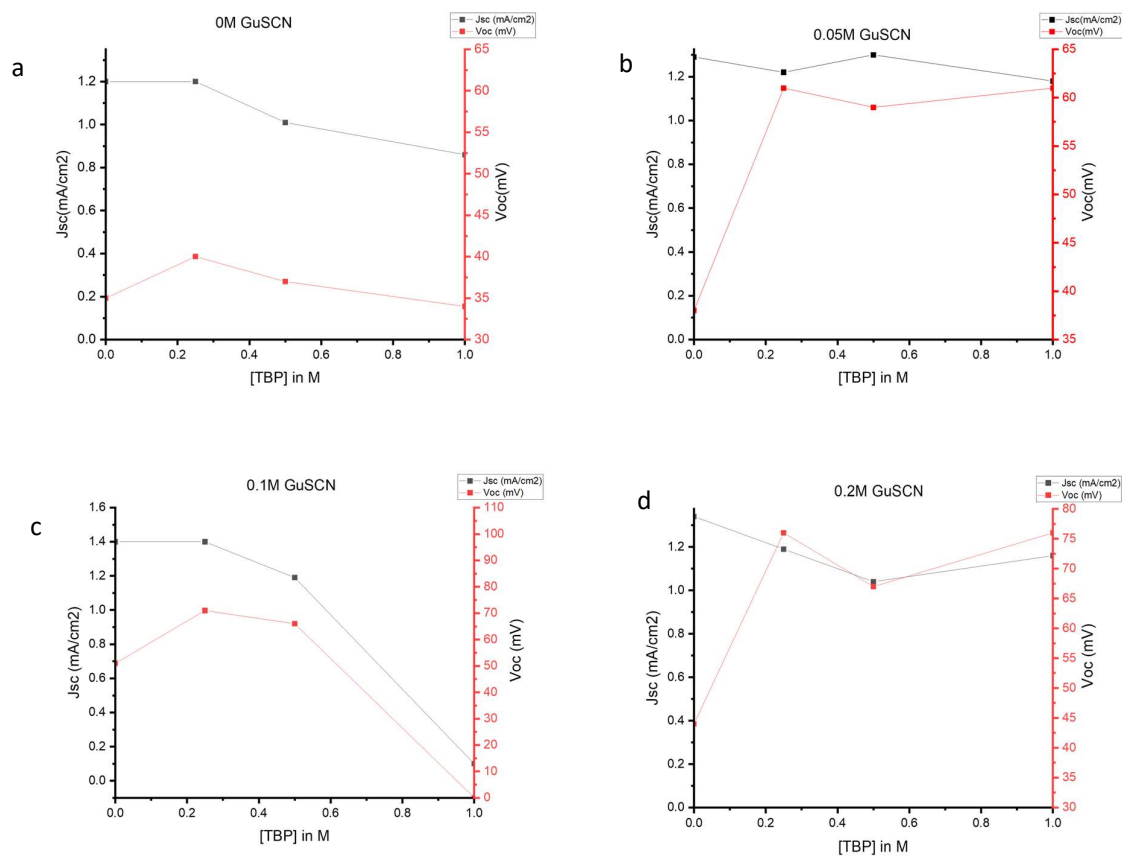


Fig. 5.19: Plots of V_{oc} vs. J_{sc} with changing TBP concentrations, the concentration of GuSCN is constant for each graph and indicated as a headline. The photocathode was in-house made NiO/FTO (see section 3.3.5) and sensitized with WOC53 dye. The electrolyte was **EL1**. The measurement was done on the day of the sealing and the cells were masked with an aperture of 0.05951 cm².

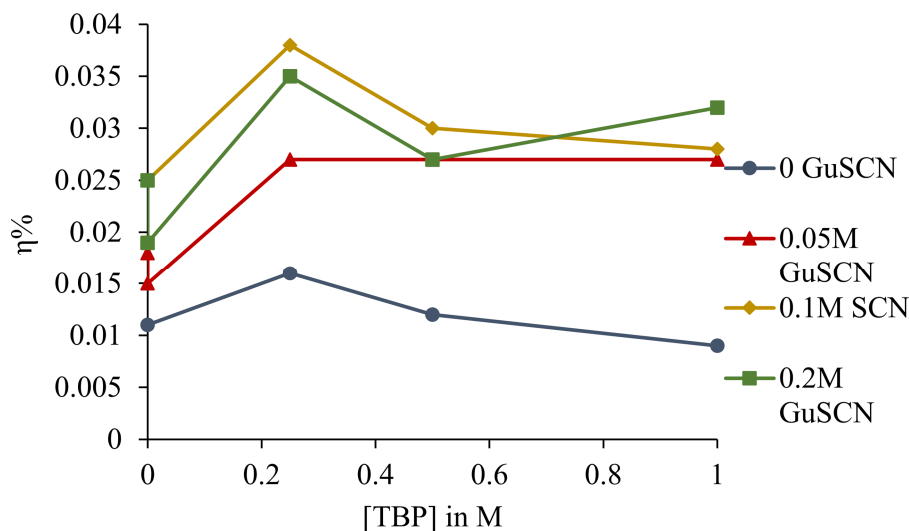


Fig. 5.20: Plots of photoefficiencies vs. changing TBP concentrations, each plot represents a different GuSCN concentration. The photocathodes used in-house made NiO/FTO and sensitized with WOC53 dye. The electrolyte was **EL1**. The measurement was done in day 0 of the sealing day and the cells were masked with an aperture of 0.05951 cm².

From Fig. 5.19 it is observed that the efficiency drops when the concentration of TBP increases. The cell with the higher efficiency for this electrolyte composition is the one that contains 0.25 M TBP and 0.1M GuSCN. Nevertheless, from Fig. 5.19, it is clear that when increasing the concentration of TBP for each set of cells the J_{sc} drops. Instead, for the V_{oc} , the best value is observed at a concentration of 0.25 M TBP regardless the concentration of GuSCN (Fig. 5.19). This trend is also reflected on the values of the efficiency of the cells (Fig. 5.20).

During the in more depth investigation of the following experiment, the TBP or GuSCN or both were excluded from electrolytes Stnd I and Stnd IV. Also, since electrolyte Stnd III in the best performing one the addition of one or the other or both additives were tested as well (Table 5.15).

Cell Name	Electrolyte composition	Jsc/mA cm ⁻²	Voc/ mV	FF/%	η /%
Std I	0.3M I ₂ , 0.6M BMIMI 0.1M GuSCN 0.5M 4-TBP in acetonitrile	1.32	121	38	0.061
I96	0.3M I ₂ , 0.6M BMIMI 0.5M 4-TBP in acetonitrile	1.23	77	30	0.029
I97	0.3M I ₂ , 0.6M BMIMI 0.1M GuSCN in acetonitrile	1.48	128	37	0.070
I98	0.3M I ₂ , 0.6M BMIMI in acetonitrile	1.19	102	31	0.038
Std III	0.1M I ₂ , 1M LiI in acetonitrile	3.80	104	35	0.138
I106	0.1M I ₂ , 1M LiI, 0.1M GuSCN in acetonitrile	2.80	116	36	0.117
I107	0.1M I ₂ , 1M LiI, 0.5M 4-TBP in acetonitrile	2.46	103	35	0.089
I105	0.1M I ₂ , 1M LiI, 0.1M GuSCN, 0.5M 4-TBP in acetonitrile	2.32	119	37	0.102
Std IV	0.03M iodine I ₂ , 0.6M TBAI, 0.1M GuSCN and 0.5M 4-TBP in acetonitrile	0.78	128	34	0.034
I99	0.03M iodine I ₂ , 0.6M TBAI, 0.5M 4-TBP in acetonitrile	1.20	81	32	0.031
I100	0.03M iodine I ₂ , 0.6M TBAI, 0.1M GuSCN in acetonitrile	1.18	134	37	0.058
I101	0.03M iodine I ₂ , 0.6M TBAI, in acetonitrile	1.25	84	32	0.034

Table 5.15: Performance data for DSSCs with different I₃⁻/I⁻ redox couple based electrolytes and sensitized with WOC53 dye. The measurements were done on the day of sealing the cells. The active area of the cell was 0.237 cm².

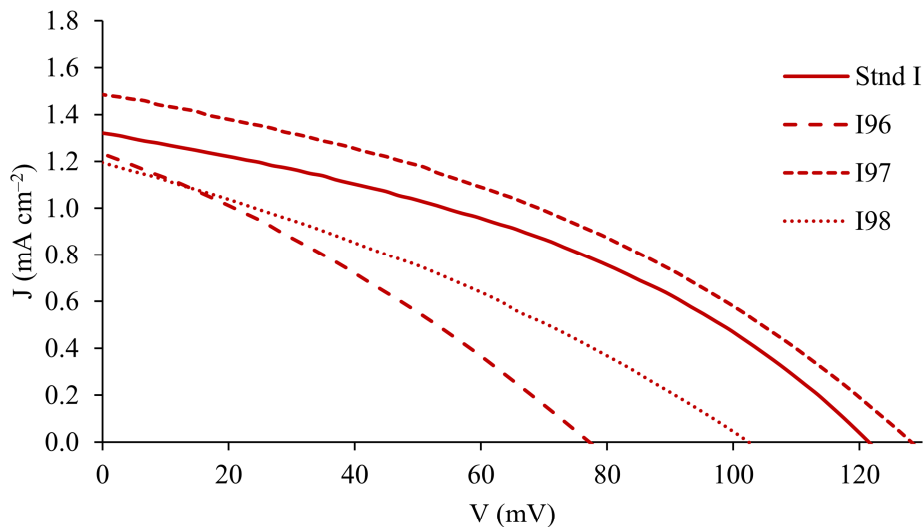


Fig. 5.21: JV curves for cells comprising electrolytes Stnd I, I96, I97 and I98. The photocathodes were in-house made NiO/FTO. The dye was WOC53

From Fig. 5.21 and Table 5.15, it is observed that the cell which contains the electrolyte without the TBP (I97) additive has the best performance in terms of both V_{oc} (128 mV) and J_{sc} (1.48 mA cm^{-2}) among the cells of this series. Indeed, the cell with I96 electrolyte, which contains only TBP and no GuSCN, has a much lower V_{oc} (77 mV) and also a lower J_{sc} (1.23 mA cm^{-2}). As for the cell with I98 electrolyte which does not contain any additives, a J_{sc} which is similar with the I96 is observed (1.19 mA cm^{-2}) but the V_{oc} is higher (102 mV). This suggests, that GuSCN is beneficial for the performance of the cell and leads to an increase in both the V_{oc} and the J_{sc} . TBP worsens the performance in terms of both V_{oc} and J_{sc} .

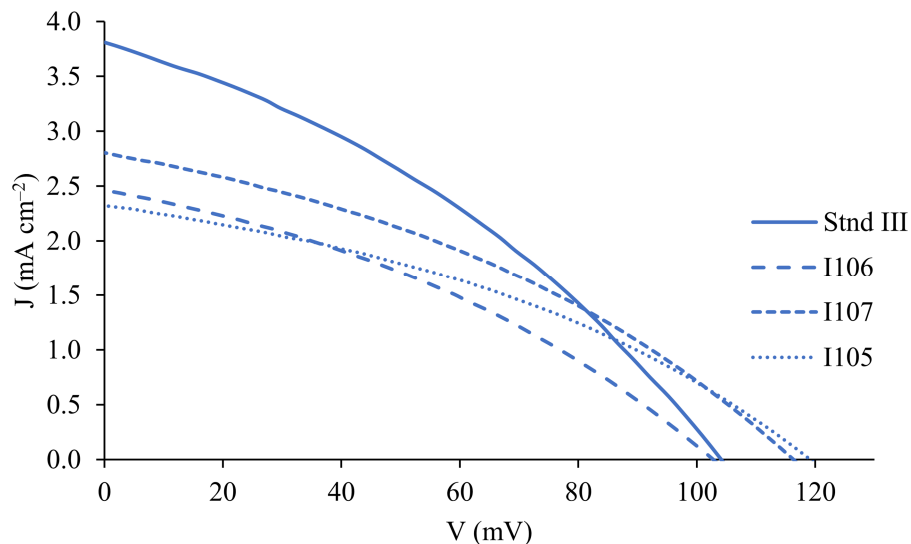


Fig. 5.22: JV curves for cells comprising electrolytes Stnd III, I106, I107 and I105. The photocathodes were in-house made NiO/FTO. The dye was WOC53.

Looking through the series of the cells in which Stnd III electrolyte was modified by adding TBP or GuSCN to the original composition (Fig. 5.22, Table 5.15), it is observed that although the cells with GuSCN as an additive in the electrolyte (I106) performed better compared with the one with only TBP (I107) (with a $V_{oc} = 116$ vs 103 mV and a $J_{sc} = 2.80$ vs 2.46 mA cm⁻²), they still do not match the performance of the cells with Stnd III electrolyte. This is mainly due to the higher J_{sc} that the Stnd III cells exhibits (3.80 mA cm⁻²). From the JV curves in Fig. 5.22, it is concluded that although the addition of GuSCN as an additive in Stnd III may increase the V_{oc} of the cell, there is a significant decrease in J_{sc} , so overall, the efficiency of the cell is worse.

From Fig. 5.23 the same trend as before is repeated. The addition of GuSCN has a beneficial effect on the performance of the cell (I100) by increasing both V_{oc} and J_{sc} . The absence of GuSCN (I101) or only the addition of TBP (I99) decreases the total performance of the cells by negatively affecting only the V_{oc} but not the J_{sc} .

In conclusion, from both experiments, two main trends are observed. One trend is when an ionic liquid is used as for example the BMIMI, and the other trend when there is no ionic liquid in the electrolyte

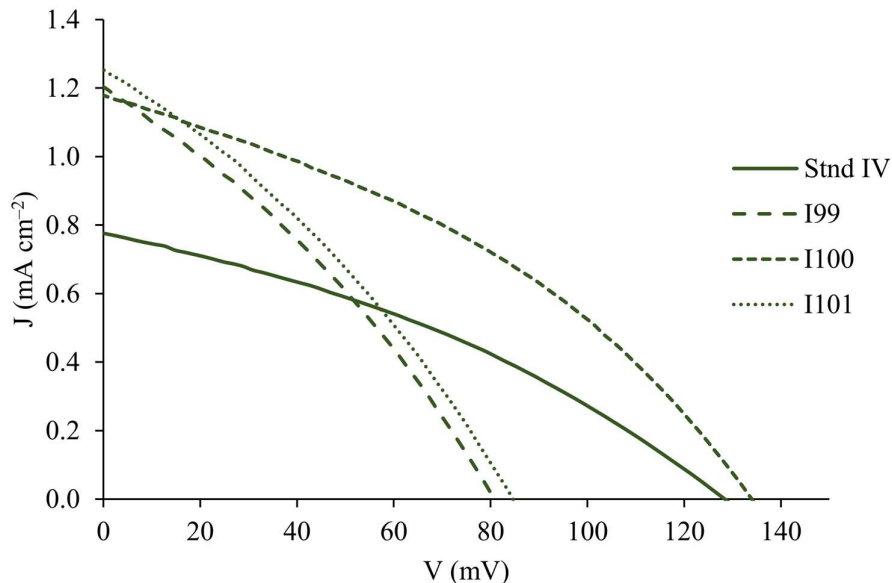
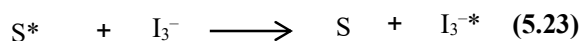
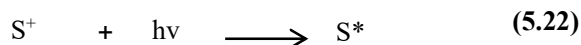


Fig. 5.23: JV curves for cells comprising electrolytes Stnd IV, I99, I100 and I10. The photocathodes were in-house made NiO/FTO. The dye was WOC53

but rather a much smaller lithium iodide salt. For the first trend that concerns the series of electrolyte Stnd I and Stnd IV, it is observed that GuSCN have a beneficial effect by boosting both V_{oc} and J_{sc} , and on the other hand TBP has negative effect mainly on the V_{oc} of the cells (Table 5.15, Fig 5.20, 5.21, 5.23). For the second trend, that concerns the series of cells with Stnd III electrolyte, both additives worsen the performance of the cell (Table 5.15, Fig. 5.22). Stnd III with its simple composition stays the best performing electrolyte.

5.5.2 Dyes as additives in the electrolyte, background

In the work of *Boschloo and co-workers*²⁰⁰, another very interesting mechanism regarding the charge transport in p-type DSSC was introduced: a dye was used as an additive in the electrolyte. The coumarin family are well known dyes and more specifically coumarin 343 (Fig. 5.24) has been broadly used in the p-type DSSCs. Although coumarin 343 has the ability to anchor on the NiO surface with the carboxylic anchoring, part coumarin 337 (Fig. 5.24) does not anchor on the surface of the NiO. Nevertheless, an increase in the photocurrent was observed for cells with coumarin 337 which was due to the contribution of the coumarin 337 in the electrolyte as an additive.



The excited dye (eq. 5.22) transfers energy to triiodide which then will form diiodide radicals (eq. 5.23) that can inject holes in the semiconductor and ultimately contribute to the increase of the photocurrent. With these results in mind we decided to carry out similar experiments which were carried on in order to assess the influence of the dyes as additives in the electrolyte and to compare different dyes on this function.

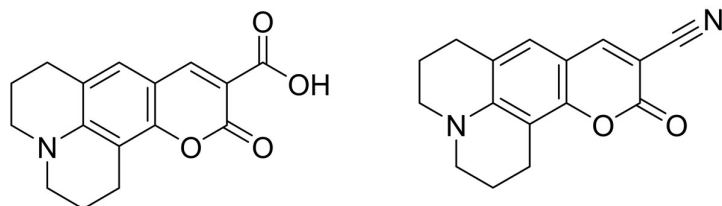


Fig. 5.24: Chemical structure of coumarin 343 (C343) on the left and coumarin 337 (C337) on the right.

5.5.3 Effect of dyes as additives in the electrolyte

It was decided to investigate the effect of introducing coumarin dyes C337 and C343 (Fig. 5.24), a p-type dye P1 and an n-type dye SQ2 (Fig. 5.25) to the electrolyte in p-type DSSCs sensitized with WOC53. The electrolyte composition comprised of 0.1 M iodine I_2 and 1 M lithium iodide LiI in acetonitrile and in acetonitrile: propionitrile 1:1 mixture, which previous experiments had shown to be the best solvents (see section 5.4.1). The dyes C343 and P1 were expected to sensitize the NiO surface instead the C337 dye cannot anchor on the surface and therefore will not sensitize the NiO electrode. When SQ2 is used as an n-type dye in a device consisted of TiO_2 working electrode and I_3^-/I^- electrolyte it exhibits an efficiency of $\eta = 3.28\%$, with a $J_{SC} = 9.46 \text{ mA cm}^{-2}$ and $V_{OC} = 504 \text{ mV}$ ²⁰¹

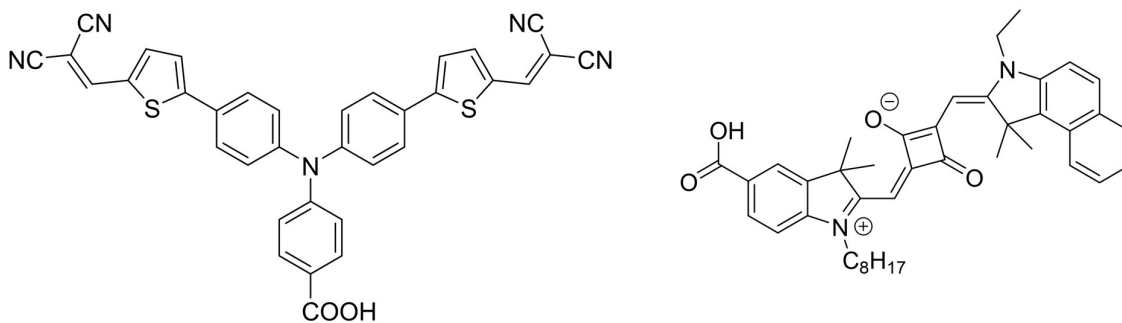


Fig. 5.25: Chemical structures of P1 dye on the left and SQ2 dye on the right.

SQ2 was chosen because, as a dye for n-type DSSCs, it was not expected to function as a sensitizer at the p-type semiconductor interface. It could therefore be used to assess the role of a dye as an additive in the electrolyte. All dyes were commercially available. The homemade (see section 3.3.5) and commercially available Dyenamo (DN-S01) NiO/FTO electrode were used as working electrodes. For the sensitization of the NiO semiconductor WOC53 dye was used. Initially, DSSCs were made with all 4 dyes previously mentioned and WOC53 as sensitizers plus a blank (without sensitizer) in order to monitor their performance.

Cell Name	Jsc/ mA cm^{-2}	Voc/ mV	FF/%	η /%
WOC53_1	3.38	95	36	0.116
WOC53_2	3.34	95	34	0.109
P1_1	2.28	91	30	0.063
P1_2	2.01	89	31	0.055
C343_1	0.94	107	36	0.036
C343_2	0.94	107	36	0.036
SQ2_1	1.14	74	34	0.029
SQ2_2	1.18	76	35	0.032
C337_1	0.69	71	40	0.020
C337_2	0.70	69	38	0.019
Blank (no dye)	0.79	84	42	0.027

Table 5.16: Performance data for duplicate cells with homemade NiO/FTO electrodes and, Stnd III electrolyte and different dyes which are indicated by the name of the cells. The measurements were done on the day of sealing the devices. The active area of the cell was 0.237 cm^2 .

The values compared here are for the better cell of each pair. From Fig. 5.26 and Table 5.16 it is clear that the cells sensitized with the WOC53 have the best performances ($\eta = 0.116\%$) followed by the cells sensitized with P1 ($\eta = 0.063\%$). The C343 sensitized cells have a low performance due mainly to a low J_{SC} (0.94 mA cm^{-2}) but a good V_{OC} (107 mV). The cells sensitized with C337 have the lowest

performance ($\eta = 0.019\%$) which is even lower than the blank cell ($\eta = 0.027\%$) mainly due to a low J_{SC} which is a strong argument regarding the statement that C337 do not anchor on the NiO so cannot be used as a traditional sensitizer. Last the cells sensitized with SQ2, exhibit a low performance due to a low V_{OC} but with an efficiency ($\eta = 0.032\%$) that exceeds the efficiency of the blank cell.

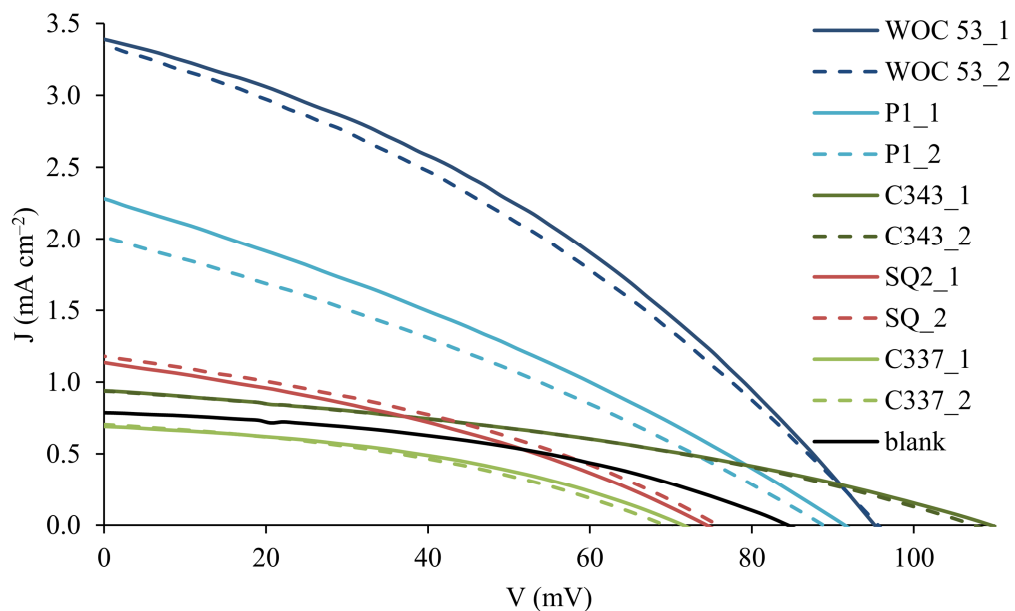


Fig. 5.26: JV curves for cells with homemade NiO/FTO electrodes and Std III electrolyte, sensitized with dyes WOC53, P1, SQ2, C337, C343 and no dye.

Cell Name	Electrolyte composition	J _{sc} /mA cm ⁻²	V _{oc} / mV	FF/%	η/%
WOC53_1	Std III	3.38	95	36	0.116
WOC53_2		3.34	95	34	0.109
I71_1	0.1M I ₂ ,1M LiI + 0.5mM	3.19	98	35	0.111
I71_2	C343	3.01	101	35	0.107
I72_1	0.1M I ₂ ,1M LiI + 0.5mM P1	2.40	99	31	0.074
I72_2		2.90	100	34	0.098
I75_1	0.1M I ₂ ,1M LiI + 0.1mM	3.31	110	36	0.130
I75_2	SQ2	3.50	106	36	0.132
I77_1	0.1M I ₂ ,1M LiI + 0.5mM	3.09	105	34	0.111
I77_2	C337	2.81	103	34	0.099

Table 5.17: Performance data for duplicate cells with homemade NiO/FTO electrodes and different electrolytes comprised of 0.1 M I₂,1 M LiI and different dyes as additives in acetonitrile. The NiO electrode was sensitized with WOC53. The measurements were done on the day of sealing the devices. The active area of the cell was 0.237cm².

From Fig. 5.27 and Table 5.17 is shown that the cells to which SQ2 dye was added in the electrolyte (I75_2) achieved the best performance with an efficiency of 0.132%, which exceeds the efficiency of the cell without SQ2 (WOC53_1) as an additive (0.116%) and the performance of the cell (SQ2_2) that was sensitized only with SQ2 (0.032%). This suggests that SQ2 behaves as an additive in the electrolyte rather than a sensitizer. The same goes for all the cells, for which a significant increase of J_{sc} and V_{oc} it is observed (I71_1, I72_2, I77_1). In order to gain a better understanding of the results, EIS measurements were performed on the best performing cells (I71_1, I72_2, I75_2, I77_1) with dyes as additive in the electrolyte and were compared to the best performing cell without dyes as additives in the electrolyte (cell WOC53_1).

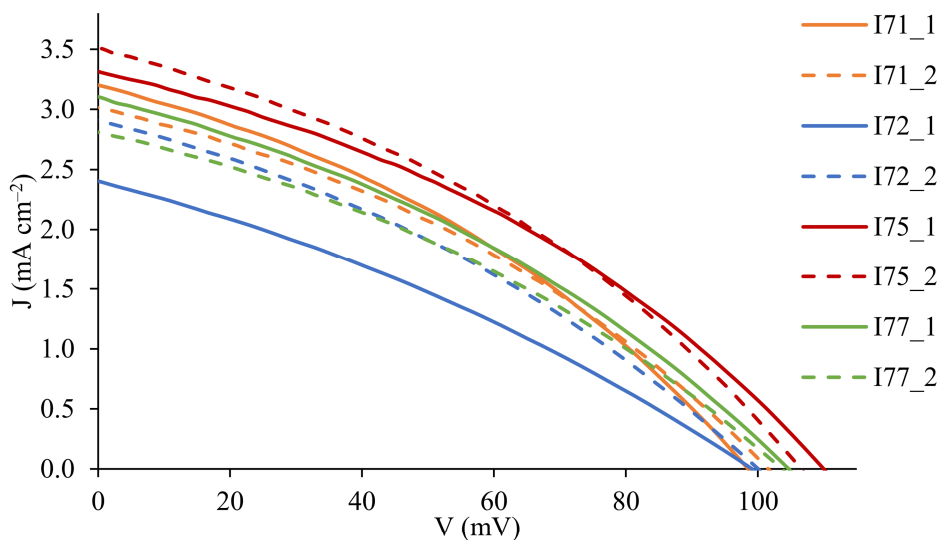


Fig. 5.27: JV curves for duplicate cells with homemade NiO/FTO electrodes and different electrolytes comprised of 0.1 M I₂, 1 M LiI and different dyes in acetonitrile, the NiO electrode was sensitized with WOC53. The measurements were done on the day of the sealing of the devices. The active area of the cell was 0.237cm².

Cell Name	Rs/ Ω	R _{Pt} / Ω	C _{Pt} / μ F	R _{rec} / Ω	Rt/ Ω	C _{μ} / μ F	Ws/ Ω	WsT/mF	τ n/ms	τ t/ms	Ld/ μ m	a
WOC 53_1	12.5	1.8	7.6	60.3	52.2	860.2	52.2	378.2	51.9	44.9	1.4	0.950
I71_1	12.9	3.1	6.4	31.7	10.0	1432.2	134.6	327.7	45.4	14.3	4.5	0.998
I72_2	11.6	53.9	4.7	125.0	59.3	1132.7	49.0	39.1	141.6	67.2	3.6	0.953
I75_2	6.7	4.8	9.1	89.9	32.5	1057.9	26.6	59.9	95.1	34.4	4.2	0.990
I77_1	10.6	4.9	6.0	67.4	70.1	860.9	64.4	337.7	58.0	60.4	2.5	0.927

Table 5.18: EIS data obtained from measurements at light intensity of 22 mW cm⁻² of p-type DSSCs containing FTO/NiO working electrodes, sensitized with WOC53, and different electrolytes which are denoted in Table 5.17.

For the fitting of the EIS data the equivalent circuit showing on Fig. 5.28 was used. The equivalent circuit was composed of a series resistance and is seen in the Nyquist plot on the abscissa from zero to the start of the first semicircle (Fig. 5.29). An R/Q element in order to calculate the resistance and

capacitance of the platinum electrode, which is attributed at the first semicircle on the Nyquist plot which occurs in high frequency regions (Fig. 5.29b) and an extended distribution element from which parameters about recombination charge transfer resistance, active layer chemical capacitance and charge transport resistance were calculated in intermediate frequency regions and is represented as the second semicircle on the Nyquist plot (5.29). Furthermore, the Warburg element (Z_d) was used to model the diffusion process in the high frequency region. During this study a constant phase element

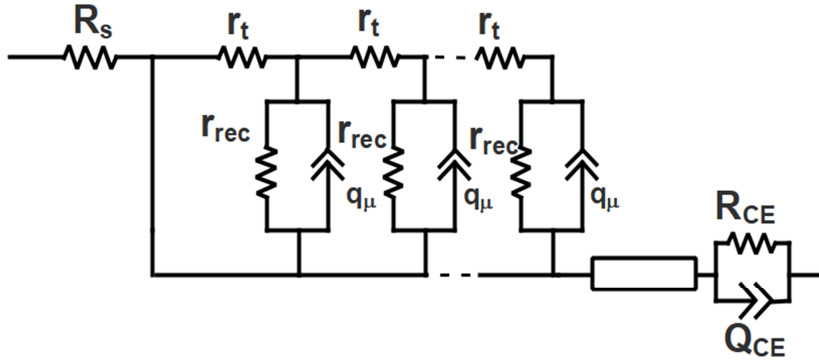


Fig. 5.28: Equivalent circuit used to fit the EIS data.

(CPE) was used instead of a capacitor for fitting the capacitance of the NiO and the platinum electrode. That was due to the porosity of these surfaces¹³³

Thus, a pre-factor term Q of the CPE was calculated and then it was corrected using eq. 5.24 in order to obtain the real capacitance of the DSSC.

$$C_{\mu} = \{(R_{rec})^{1-\alpha} Q\}^{1/\alpha} \quad (5.24)$$

Where α is an empirical constant²⁰²

$$\tau_n = R_{rec} C_{\mu} \quad (5.25)$$

$$\tau_t = R_t C_{\mu} \quad (5.26)$$

$$L_d = d(R_{rec}/R_t)^{1/2} \quad (5.27)$$

Where d is the thickness of the semiconductor in μm .

The parameters concerning recombination and transport time and diffusion length were calculated using eq. 5.25-27 accordingly.

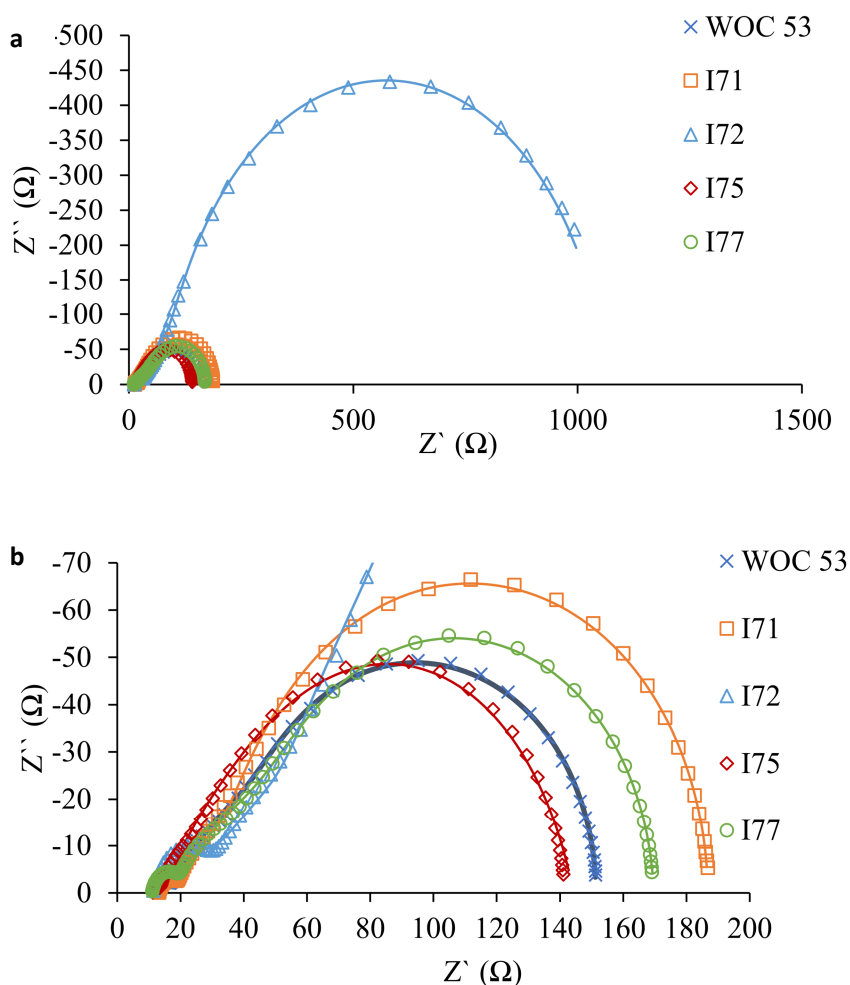


Fig. 5.29: **a.** Nyquist plot and **b.** Expansion of Nyquist plots for DSSC with homemade NiO/FTO electrode and, different electrolyte (See Table 5.15) comprised of 0.1 M I_2 , 1 M LiI and different dyes in acetonitrile, the NiO electrode was sensitized with WOC53.

From the EIS data (Table 5.18, Fig. 5.27) it is observed that I75_2 which has the best performance ($\eta = 0.132\%$) also exhibits a low transport resistance, a low Warburg resistance and a high recombination resistance. The good performance of this cell is also reflected in the low transport time and the high lifetime obtained by those measurements. The cells I71_1 and I77_1 which display the same efficiency (0.111%) for almost the same J_{SC} and V_{OC} values (3.19 vs. 3.09 mA cm^{-2} and 98 vs. 105 mV for I71_1 and I77_1 accordingly), shows very different trends regarding the EIS values. I71_1 has the lowest R_t among this series of cells and a low R_{rec} but the highest C_{μ} , instead I77_1 has a high R_t for a high R_{rec} and a low C_{μ} . One explanation could be that in I71_1 a fraction of the dye C343

which was added in the electrolyte, anchors on NiO in sites that WOC53 dye fails to fill. As a consequence, it will act as a co-sensitizer by injecting directly charges carriers into the semiconductor thus increasing the capacitance. That suggestion it is also reflected in the very low transport time (Fig. 5.31c). Nevertheless, charge recombination with the dyes or electrolyte is very fast and as a consequence, the life time of the charge is very low as well. On the other hand, from the data of the cell I77_1 it is concluded that the transport

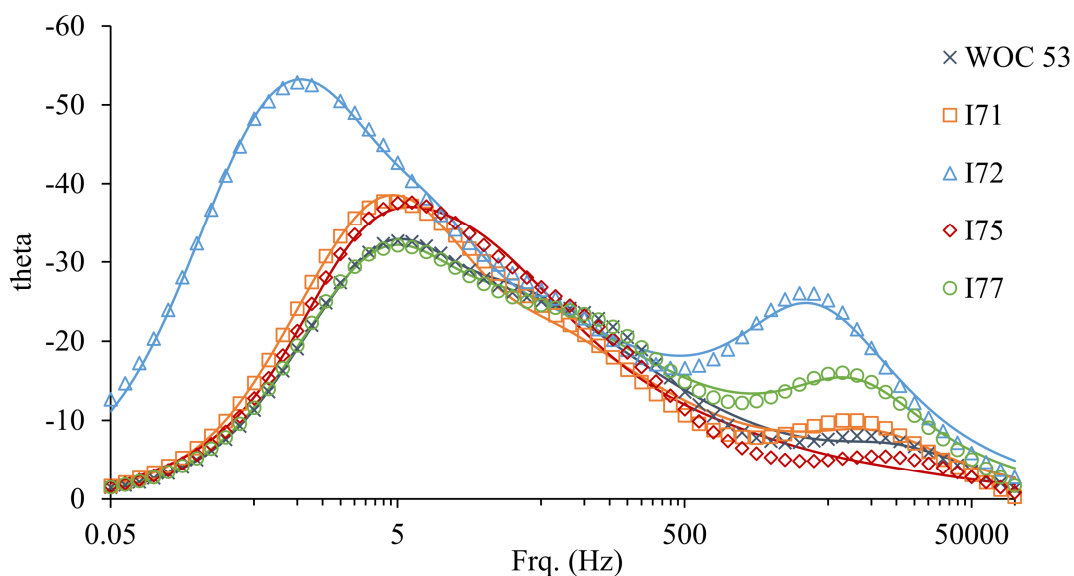


Fig. 5.30: Bode plots for DSSCs with homemade NiO/FTO electrodes and different electrolyte comprising of 0.1 M I₂, 1 M LiI and different dyes in acetonitrile. The NiO electrodes were sensitized with WOC53.

of the charge through the semiconductor is a slow process for this cell but the charge has a better life time compared with I71_1. The same experiment but with commercial Dyenamo NiO electrodes is described below.

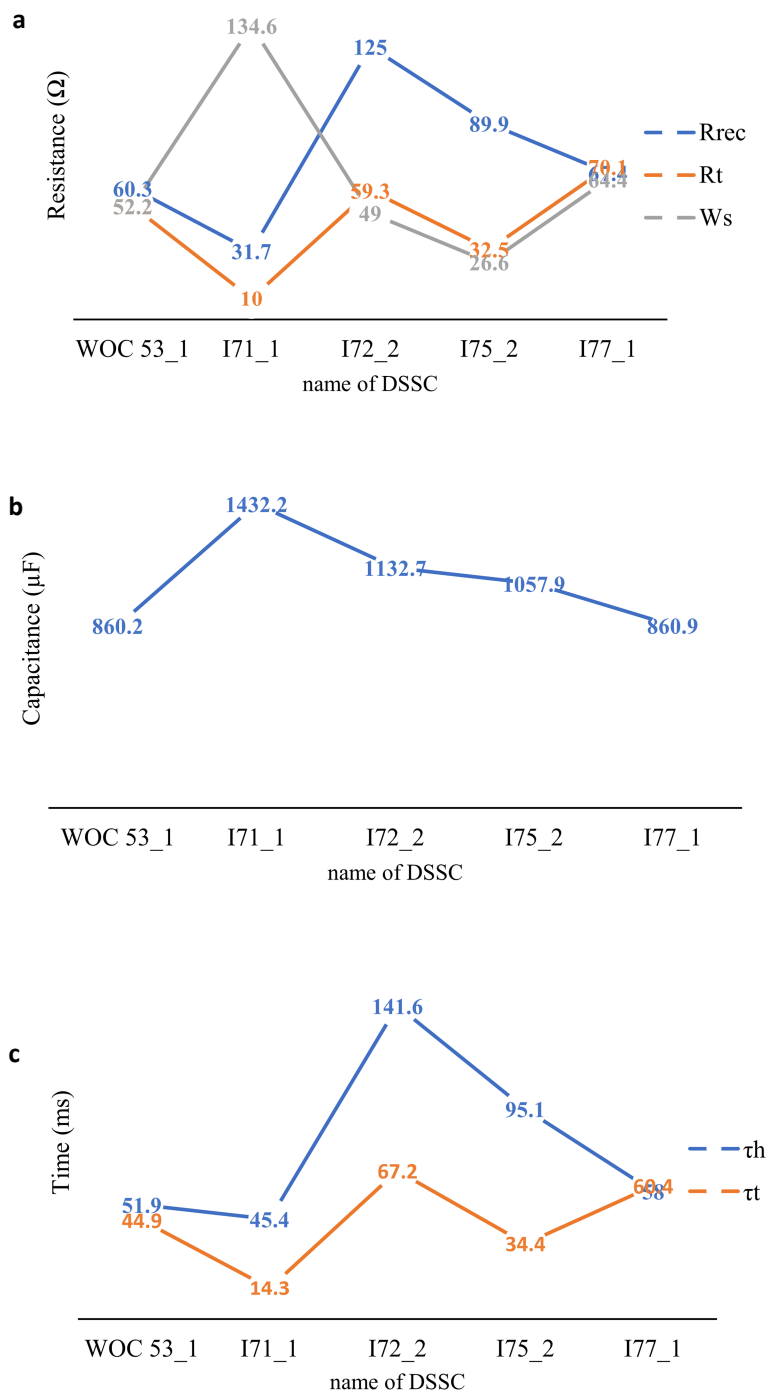


Fig. 5.31: **a.** Recombination, transport and Warburg resistance **b.** chemical capacitance **c.** and recombination and transport time values plotted from values in Table 5.18.

Cell Name	Electrolyte composition	Jsc/ mA cm^{-2}	Voc/ mV	FF/%	$\eta/\%$
DWOC53_1	Stnd III	4.06	95	36	0.139
DWOC53_2	Stnd III	4.13	92	36	0.136
DP1_1	Stnd III	2.76	92	33	0.085
DP1_2	Stnd III	2.42	97	34	0.079
DSQ2_1	Stnd III	1.32	68	34	0.031
DSQ2_2	Stnd III	1.35	68	35	0.032

Table 5.19: Performance data for duplicate cells with commercial Dyenamo NiO/FTO electrodes and Stnd III electrolyte and different dyes which are indicated by the name of the cells. The measurements were done on the day of sealing the cells. The active area of the cell was 0.25 cm^2 .

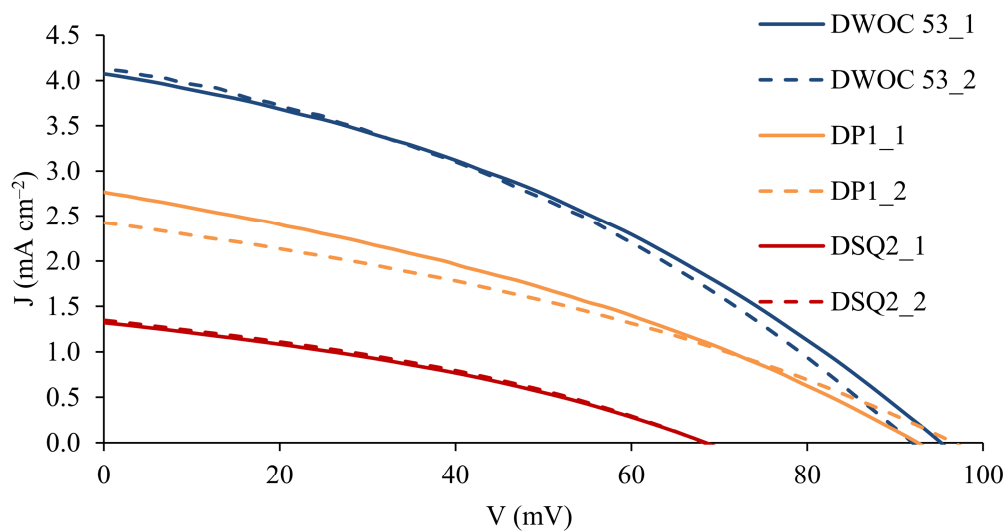


Fig. 5.32: JV curves for duplicate cells with commercial Dyenamo NiO/FTO electrode. The electrolytes Stnd III, and dyes were WOC53, P1, SQ2.

Cell Name	Electrolyte composition	Jsc/mA cm ⁻²	Voc/ mV	FF/%	η/%
DWOC53_1	Std III	4.06	95	36	0.139
DWOC53_2		4.13	92	36	0.136
DI71_1	0.1M I ₂ , 1M LiI + 0.5mM C343	4.39	83	39	0.142
DI71_2		4.61	89	40	0.165
DI72_1	0.1M I ₂ , 1M LiI + 0.5mM P1	4.27	87	40	0.148
DI72_2		4.25	81	38	0.130
DI75_1	0.1M I ₂ , 1M LiI + 0.1mM SQ2	4.94	92	39	0.175
DI75_2		4.87	91	38	0.170

Table 5.20: Electrolyte and performance data for duplicate cells with Dyenamo NiO/FTO electrodes and different electrolytes comprised of 0.1 M I₂, 1 M LiI and different dyes as additives in acetonitrile. The NiO electrode was sensitized with WOC53. The measurements were done on the day of sealing the devices. The active area of the cell was 0.25 cm².

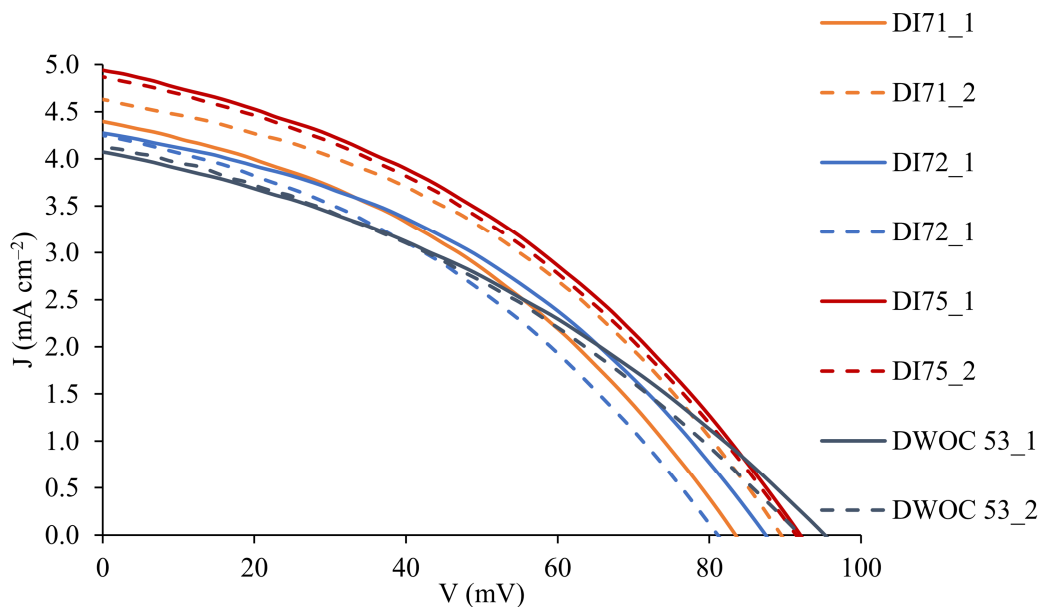


Fig. 5.33: JV curves for duplicate cells with commercial Dyenamo NiO/FTO electrode and, different electrolyte comprised of 0.1 M I₂, 1 M LiI and different dyes in acetonitrile, the NiO electrode was sensitized with WOC53. The measurement was done on the day of the sealing. The area of the cell was 0.25cm².

The same trends with higher efficiencies are observed when commercial Dyenamo NiO electrodes are used (Table 5.20 and Fig. 5.33). The cell with SQ2 as an additive in the electrolyte achieves a record efficiency of 0.175% which is mainly due to the very high J_{sc} of 4.94 mA/cm². By comparing the efficiencies of the cells sensitized with SQ2 (DSQ_1 and _2, Table 5.19 and Fig. 5.32) with those with SQ2 as additive (DI75_1 and 2) it is obvious that the SQ2 has a different function than as a sensitizer and the hypothesis made earlier (eqs. 5.22 - 5.23) can be confirmed. Unfortunately, Dyenamo stopped producing the electrodes and the series could not be finished with C337 as an additive. Nevertheless, EIS measurements were done in order to further investigate the effect of the dyes as additives. The equivalent model used for the fitting of the EIS data was the same as the one presented for the previous experiment (Fig. 5.28)

Cell Name	R_s/Ω	R_{Pt}/Ω	$C_{Pt}/\mu F$	R_{rec}/Ω	R_t/Ω	$C_{\mu}/\mu F$	W_s/Ω	W_sT/mF	τ_h/ms	τ_t/ms	$Ld/\mu m$	a
DWOC 53_1	11.95	7.1	3.7	80.14	40.4	1881.0	1.51E-05	737.4	150.7	76.0	2.5	0.908
DI71_1	8.3	3.4	12.4	55.8	9.3	3275.4	10.7	424.1	182.7	30.5	6.1	0.937
DI72_2	9.3	4.0	11.6	69.4	6.3	3764.2	11.4	501.8	261.2	23.5	8.3	0.940
DI75_2	10.2	4.1	19.5	53.6	13.1	3608.5	11.4	521.8	193.5	47.4	5.1	0.937

Table 5.21: EIS data obtained from measurements at light intensity of 22 mW cm^{-2} of p-type DSSCs containing commercial Dyenamo FTO/NiO working electrodes, WOC53 sensitizer and different electrolytes as denoted in Table 5.15. The active area of the cell was 0.25 cm^2 .

In Fig. 5.34 and 5.35 the Nyquist and the Bode plots of the EIS measurements are shown. The same trend for the analogous cells with homemade NiO electrodes is observed. The best performing cell (DI75_1) has a low transport resistance and in combination with a high recombination resistance and high capacitance achieves a record J_{SC} (4.94 mA cm^{-2}).

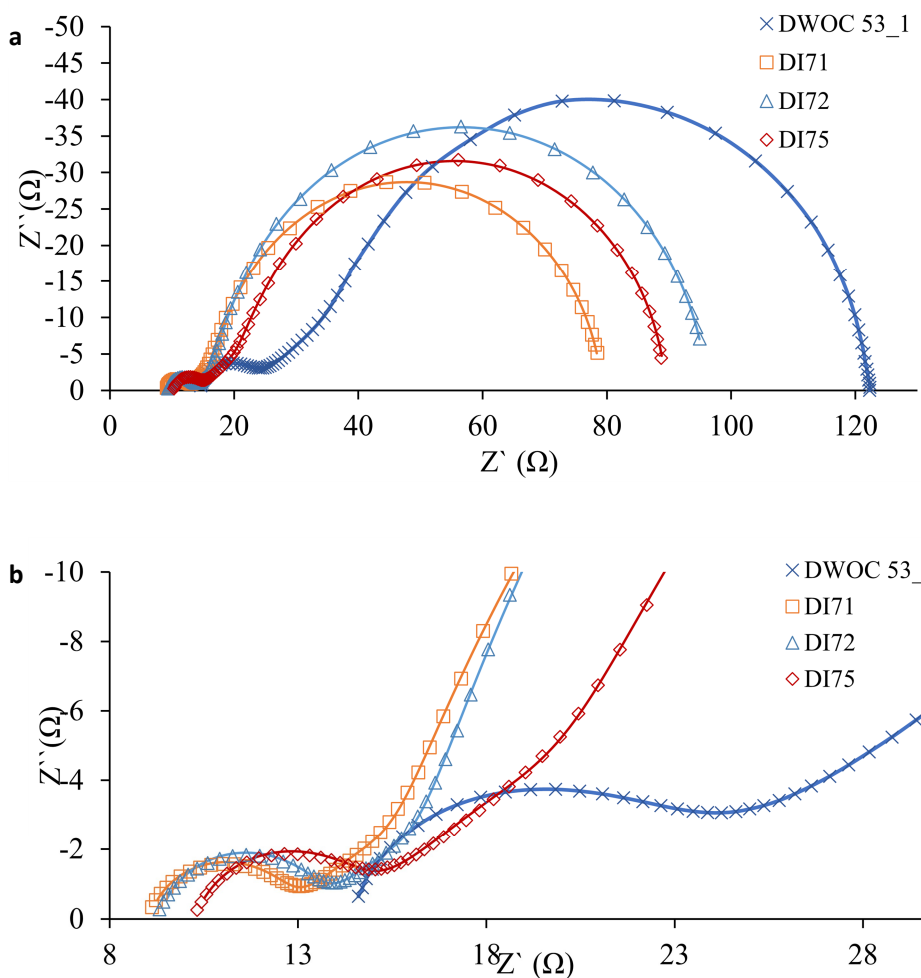


Fig. 5.34: **a.** Nyquist plot and **b.** Expansion of Nyquist plots for DSSC with Dyenamo NiO/FTO electrode and, different electrolyte comprised of 0.1 M I_2 , 1 M LiI and different dyes in acetonitrile, the NiO electrode was sensitized with WOC53.

In Fig. 5.36a, b, the values of recombination, transport and Warburg resistance and life and transport time of the two best performed cells for the two series (homemade and Dyenamo NiO/FTO electrode, I75_2, DI75_2) are compared. The R_t and W_s of cell DI75_2 is much lower compared to the values of I75_2 which can be a significant factor for the better J_{SC} that is observed for DI75_2 cell. On the other hand, the recombination resistance of DI75_2 is lower compared to the R_{rec} of I75_2 but it can be assumed that since the lifetime of the charge of DI75_2 is higher ultimately, less charge will be lost by recombination on this cell compared to I75_2 cell. In conclusion, since the only difference between those two cells is the NiO electrode, it can be deduced that the Dyenamo NiO electrode have a better charge conductivity than the homemade NiO electrode. From Fig. 5.37, the same behaviour as the one previously described for the experiment with the homemade NiO electrode was observed. The cells to which p-type dyes were added as additives (DI71_1 and DI72_2) in the electrolyte have a co-

sensitization behaviour (low R_{rec} and R_t , and high C_{μ}) in contrast, the cell DI75_2 with SQ2 which is designed as a dye for n-type DSSCs as an additive do not exhibit this behaviour.

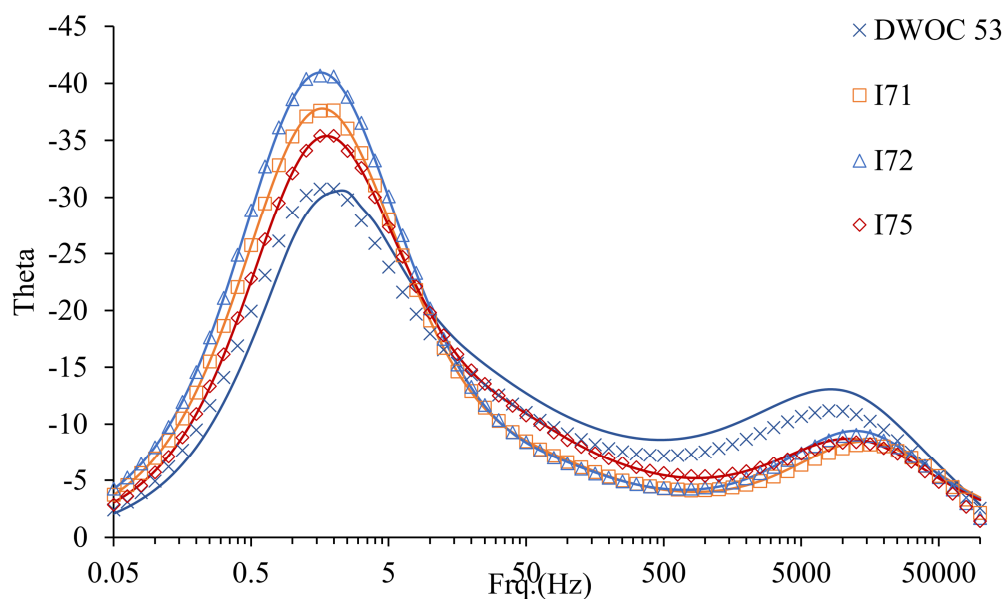


Fig. 5.35: Bode plots for DSSCs with Dyenamo NiO/FTO electrodes and different electrolytes comprised of 0.1M I_2 , 1M LiI and different dyes in acetonitrile. The NiO electrodes were sensitized with WOC53.

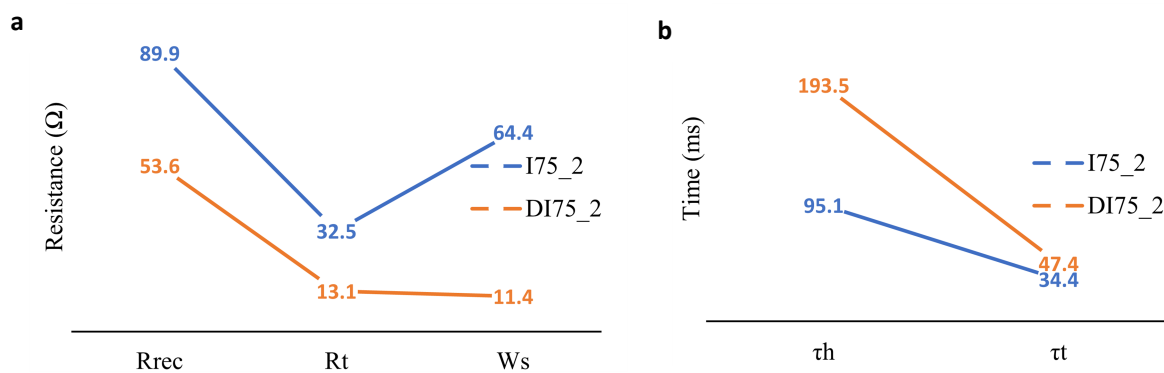


Fig. 5.36: **a.** Recombination, transport and Warburg resistance **b.** and recombination and transport time values plotted from values in Table 5.15 and 5.16 for I75_2 and DI75_2 cells.

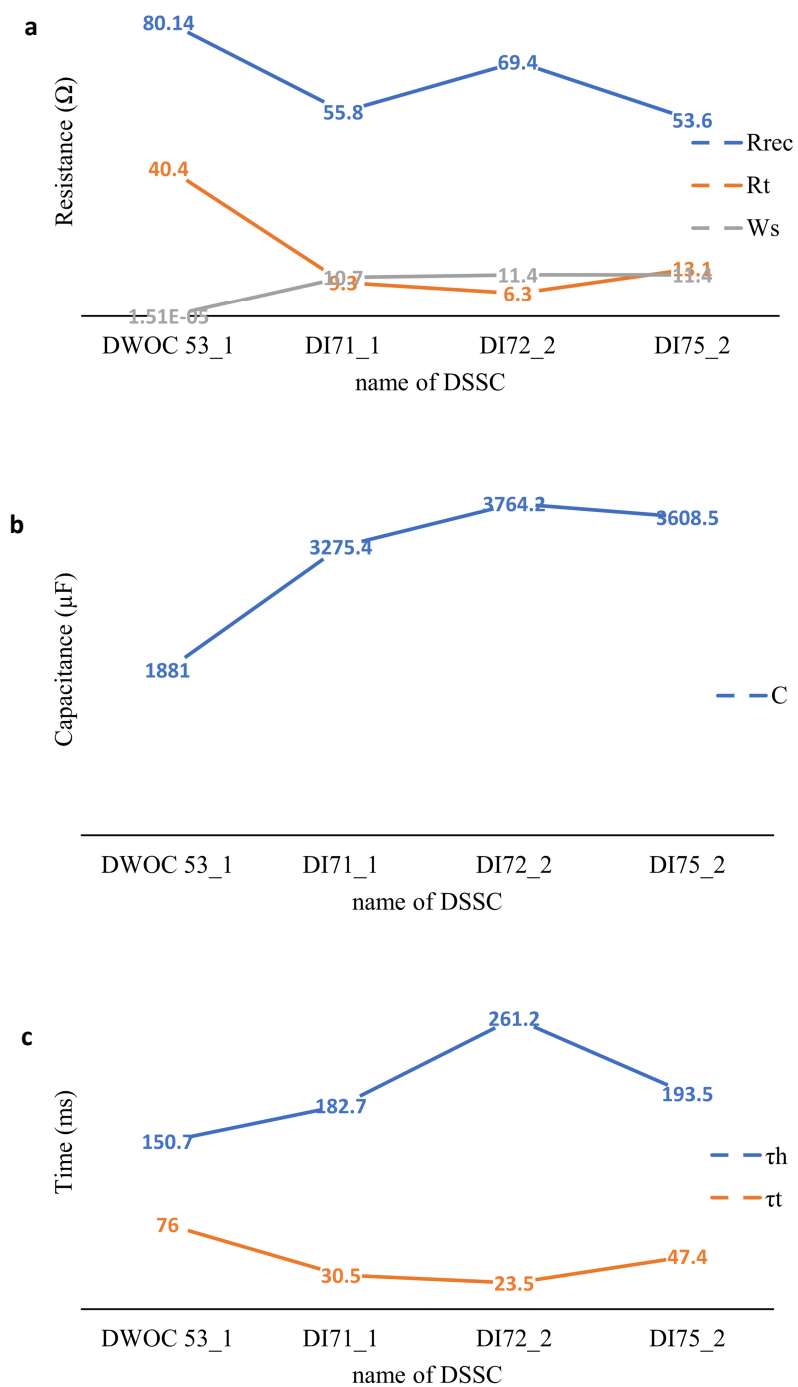


Fig. 5.37: **a.** Recombination, transport and Warburg resistance **b.** chemical capacitance **c.** and recombination and transport time values plotted from values in Table 5.21.

5.6 Co-adsorbants background

Another way to tune the performance of a p-type DSSC was introduced in the work of *Zaban and co-worker*²⁰³. These researchers introduced polar molecules to the NiO surface to shift the band gap to more positive potential and consequently increase the Voc of the cell. The NiO electrode was first sensitized with the coumarin C343 dye and then dipped for one hour in solutions containing polar molecules. Two different polar molecules were used for comparison, 4-nitrophenylphosphonic acid and 4-methoxybenzoic acid, the nitro group being electron withdrawing and the methoxy group being electron donating. The first one will shift the valence band of the NiO towards more positive potentials and the second one towards more negative potentials.

5.7 Effect of the addition of a co-adsorbant on the semiconductor surface

Based on the above idea, different polar molecules functionalized with different electron withdrawing groups were used as additives in the electrolyte and the performances of the cells were monitored. After theoretically screening of several molecules with similar characteristics, a phenyl group with a withdrawing group (CN- or NO₂-) in the 4 position and an anchoring moiety in position 1 (phosphonic acid, boronic acid or carboxylic acid), two were selected 4-nitrophenylphosphonic acid and 4-cyanophenyl phosphonic acid. The selection was based on a quick preliminary test which pointed out the best candidates. After DFT calculations made by Prof. Catherine Housecroft, the dipole moment of 4-nitrophenylphosphonic acid was calculated at 3.22 D and the dipole moment of 4-cyanophenylphosphonic acid was found to be 2.61 D, which suggest a good electron withdrawing ability of additives NO₂-Ph P.A. and CN-Ph P.A. (Fig. 5.38).

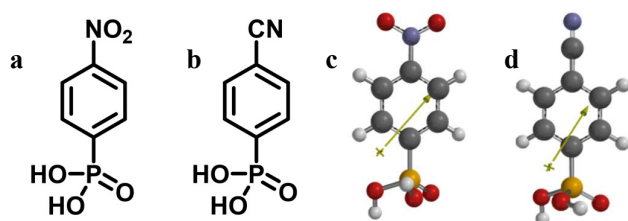


Fig. 5.38 **a:** 4-nitrophenylphosphonic acid (NO₂-Ph P.A.) and **b:** 4-cyanophenylphosphonic acid (CN-Ph P.A.) **c:** dipole moment of 4-nitrophenylphosphonic acid **d:** dipole moment of 4-cyanophenylphosphonic acid

Cell Name	Electrolyte composition	Jsc/mA cm ⁻²	Voc/ mV	FF/%	η /%
WOC53_1	Stnd III	3.80	104	35	0.138
WOC53_2		3.62	103	35	0.129
I108_1	Stnd III + 5x10 ⁻³ M CN-Ph P.A.	2.27	98	28	0.063
I108_2		2.88	94	31	0.085
I109_1	Stnd III + 10 ⁻² M CN-Ph P.A.	3.58	105	35	0.131
I109_2		3.92	102	34	0.137
I110_1	Stnd III + 2x10 ⁻² M CN-Ph P.A.	1.41	93	29	0.038
I110_2		1.08	92	29	0.029
I111_1	Stnd III + 5x10 ⁻³ M NO ₂ -Ph P.A.	3.41	102	33	0.116
I111_2		3.46	102	35	0.122
I112_1	Stnd III + 10 ⁻² M NO ₂ -Ph P.A.	3.50	100	34	0.118
I112_2		3.39	98	34	0.113
I113_1	Stnd III + 2x10 ⁻² M NO ₂ -Ph P.A.	0.97	105	31	0.032
I113_2		0.19	72	29	0.004

Table 5.22: Performance data for duplicate cells with homemade NiO/FTO electrodes and different electrolytes comprising of 0.1 M I₂, 1 M LiI and different co-adsorbants in acetonitrile. The NiO electrodes were sensitized with WOC53 (see Fig. 5.5). The measurements were done on the day of sealing of the cells. The active area of the cell was 0.237 cm².

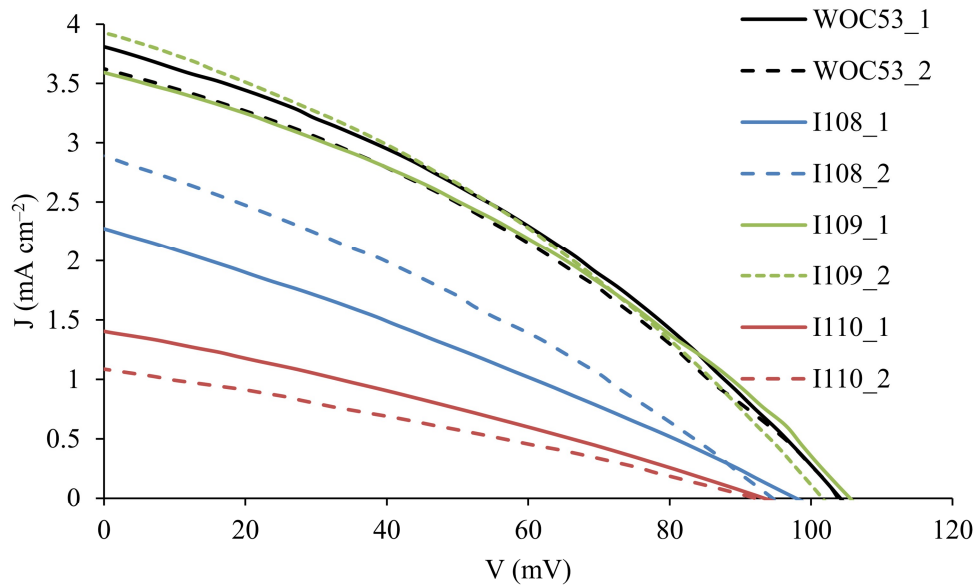


Fig. 5.39: JV curves for duplicate cells with homemade NiO/FTO electrodes and different electrolyte comprising of 0.1M I₂, 1M LiI and CN-Ph P.A. co-adsorbants in acetonitrile. The NiO electrode were sensitized with WOC53. The measurements were done on the day of sealing of the cells. The active area of the cell was 0.237 cm².

From Table 5.22 and Fig. 5.39 it was observed that the cell I109_1,2 with 10⁻² M CN-Ph P.A. additive in the electrolyte exhibited a similar efficiency compared with a DSSC the WOC53_1 cell without co-adsorbants ($\eta = 0.137$ vs. 0.138%). The cells with lower (I108) or higher (I110) concentration of CN-Ph P.A. additive displayed a worse performance.

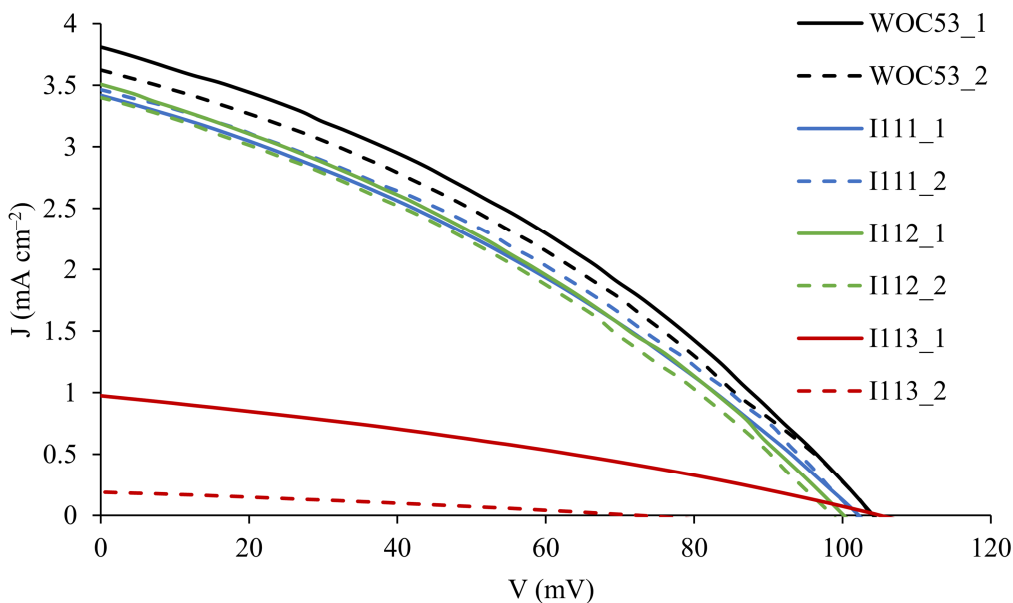


Fig. 5.40: JV curves for duplicate cells with homemade NiO/FTO electrodes and different electrolyte comprising of 0.1M I₂, 1M LiI and NO₂-Ph P.A. co-adsorbants in acetonitrile. The NiO electrode were sensitized with WOC53. The measurements were done on the day of sealing of the cells. The active area of the cell was 0.237cm².

From Table 5.22 and Fig. 5.40 it was observed that among the series with NO₂-Ph P.A. additive no DSSC exceeded the efficiency of the DSSC without additive (WOC53_1, 2). This is due to a drop of J_{SC}, the V_{OC} stays fairly stable without significant fluctuations. A further investigation was done with EIS measurements in order to better assess the results taken from the sun simulation measurements. From Table 5.22 and Fig. 5.40 it was observed that among the series with NO₂-Ph P.A. additive no DSSC exceeded the efficiency of the DSSC without additive (WOC53_1, 2). This is due to a drop of J_{SC}, the V_{OC} stays fairly stable without significant fluctuations. A further investigation was done with EIS measurements in order to better assess the results taken from the sun simulation measurements. During the EIS measurements the WOC53_1 cell was compared with the best performing cells of the CN-Ph P.A. series (I109_2) and NO₂-Ph P.A. series (I111_2). The equivalent circuit shown in Fig. 5.43 was used to fit the Nyquist and the Bode plot (Fig. 5.41 and 5.42). And was the same as previously reported (section 5.5.3, Fig. 5.28) but without the Warburg element. The chemical capacitance, recombination and transport resistances and the diffusion length were calculated using eqs. 5.24 - 5.27 (section 5.5.3). The EIS data from Table 5.23 indicate that the trend of the charge transport resistance (R_t) and chemical capacitance (C_μ) of the cells agrees with their J_{SC} values (Table 5.22) and follows the reverse and the same trend respectively. On the other hand, the recombination resistance disagrees with the J_{SC} values of the cell following the trend I111_2 > I109_2 > WOC53_1.

Cell Name	R_s/Ω	R_{Pt}/Ω	$C_{Pt}/\mu F$	R_{rec}/Ω	R_t/Ω	$C_\mu/\mu F$	τ_n/ms	τ_t/ms	$Ld/\mu m$	a
WOC 53_1	8.9	6.7	98.9	127.6	73.1	838.4	106.9	61.2	1.5	0.891
I109_2	8.1	9.4	87.6	161.0	62.4	585.1	94.2	36.4	1.2	0.877
I111_2	7.5	8.9	130.5	220.7	78.6	496.2	109.5	38.9	0.1	0.892

Table 5.23: EIS data obtained from measurements at light intensity of 22 mW cm^{-2} of p-type DSSCs containing commercial homemade FTO/NiO working electrodes, WOC53 sensitizer and different electrolytes denoted in Table 5.22 The active area of the cell was 0.25 cm^2 .

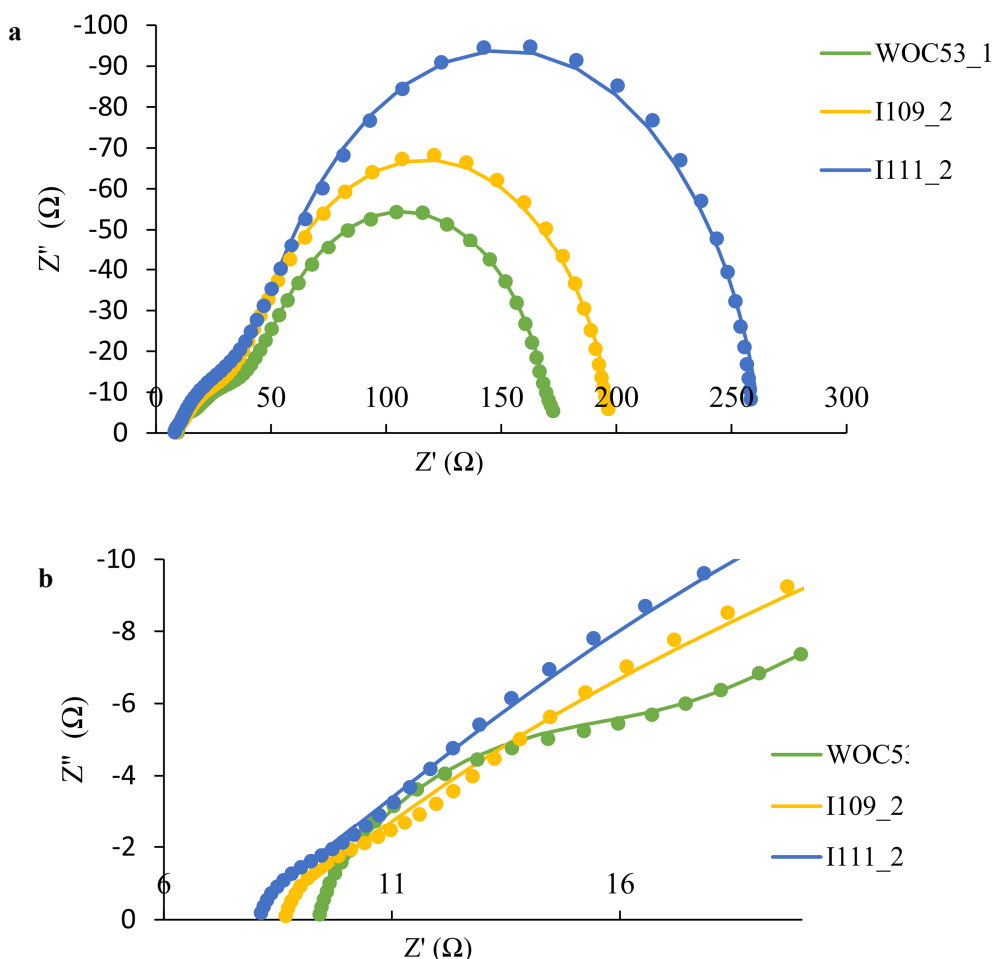


Fig. 5.41: **a:** Nyquist plots and **b:** expansion of Nyquist plots for DSSCs with homemade NiO/FTO electrode and different electrolytes comprising of $0.1M \text{ I}_2, 1M \text{ LiI}$ and different co-adsorbants in acetonitrile. The NiO electrode was sensitized with WOC53.

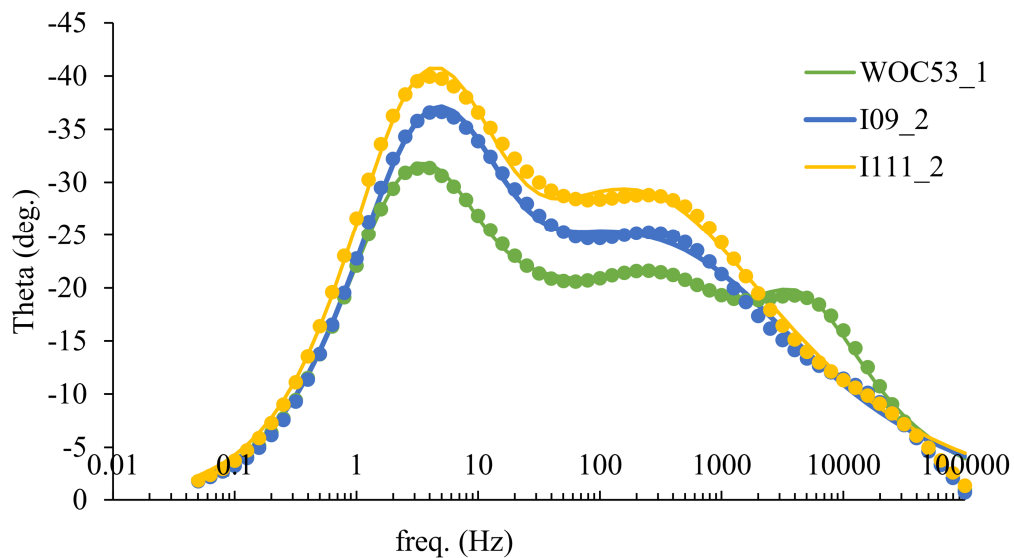


Fig. 5.42: Bode plots for DSSCs with homemade NiO/FTO electrodes and, different electrolytes comprising of 0.1 M I₂, 1 M LiI and different co-adsorbants in acetonitrile. The NiO electrode was sensitized with WOC53.

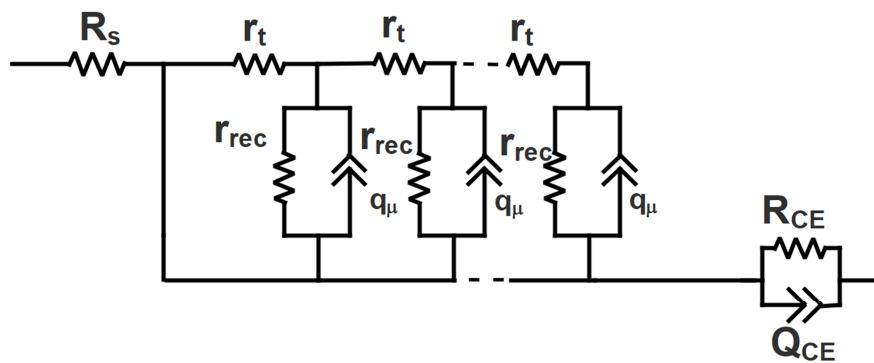


Fig. 5.43: Equivalent circuit used to fit the EIS data.

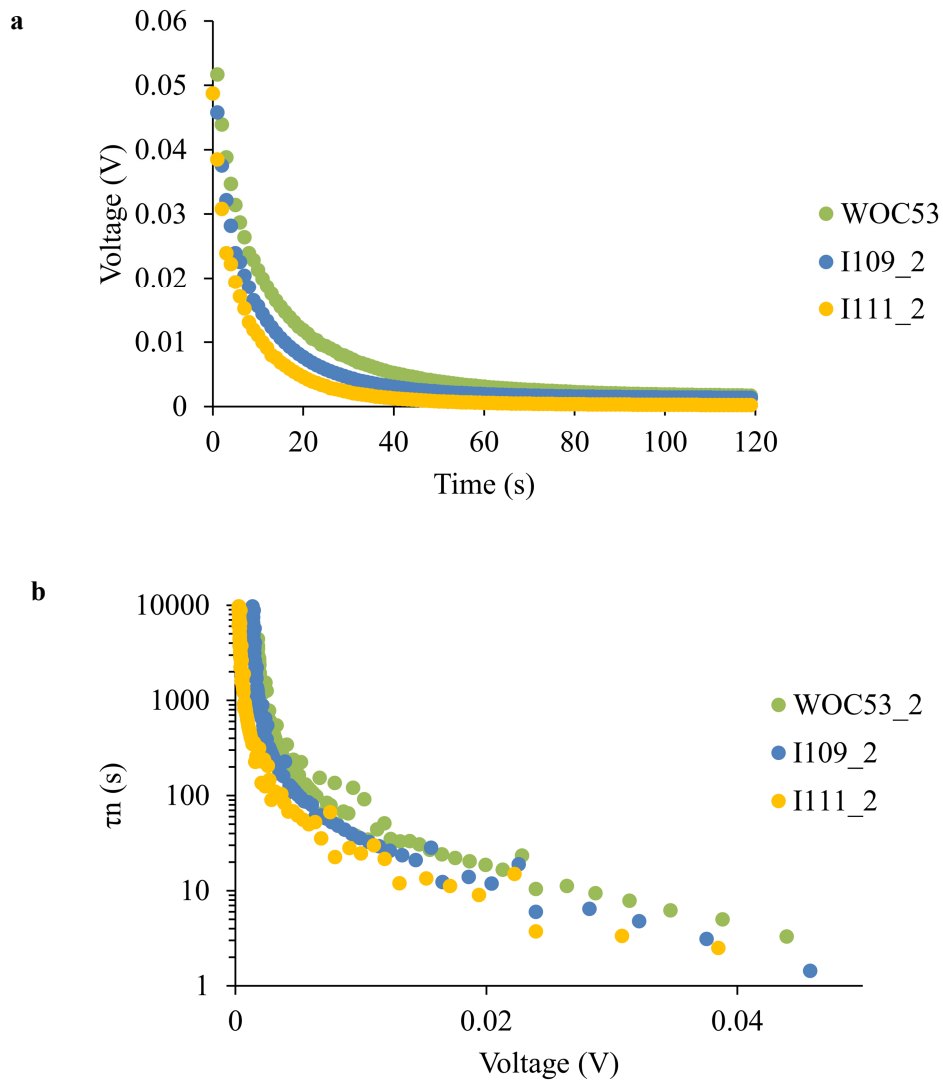


Fig. 5.44: **a:** Open-circuit voltage decay vs. time **b:** Electron life time vs. open circuit voltage at light intensity of 22 mW cm^{-2} for DSSC with Dyenamo NiO/FTO electrode and, different electrolyte comprised of 0.1M I_2 , 1M LiI and different co-absorbants in acetonitrile, the NiO electrode was sensitized with WOC53.

In order to decouple the recombination processes between the hole in the semiconductor and the dye and the hole and the electrolyte (Fig. 5.2), open circuit voltage decay measurements were performed. Under open-circuit voltage conditions, the band gap between the valence band and the conduction band of the semiconductor is at its lowest value, and the rates of charge-carrier injection and recombination are equal. From eq. 5.28, the lifetime of the charge, τ_n , can be extracted^{137, 138}.

However, since the photovoltage decay is a dark measurement, the data concern only the recombination process with the electrolyte and not the recombination path with the anchored dye ¹³³.

$$\tau_n = -\frac{k_B T}{e} \left(\frac{dV_{OC}}{dt} \right)^{-1} \quad (5.28)$$

Fig. 5.44a displays the voltage decay of the DSSCs over time and it can be observed that the I111_2 demonstrates a more rapid voltage decay followed by I109_2 and WOC53_1. After solving eq.20 the lifetime vs. voltage plots shown in Fig. 5.44b are obtained. This indicates that the lifetime of DSSC with WOC53 retains a higher value of V_{OC} for a longer time. In contrast, I109_2 exhibits a more significant drop in lifetime at lower voltage and I111_2 an even greater. These results can be translated as a more important charge recombination process with the electrolyte for cells I109_2 and I111_2.

In conclusion, the DSSC with 0.1 M I_2 , 1 M Li electrolyte in acetonitrile and a concentration of 10^{-2} M of CN-Ph P.A. co-adsorbant (I109_2) exhibited a moderately increased efficiency compared with the cell that no co-adsorbant (WOC53_1). That was due to the higher J_{SC} of the I109_2. Moreover, no increase of the V_{OC} was observed as was suggested by the work of *Zaban and co-workers* ²⁰³ From the open circuit voltage decay measurements combined with the results obtained from the EIS measurements, it can be concluded that the recombination of the hole on the semiconductor by the electrolyte (interception process) is more pronounced when the additives were added in the electrolyte (Fig. 5.38a, b), on the other hand it can be suggested that the co-adsorbant do indeed anchor on the NiO surface creating a layer and thus by passivation of the NiO layer minimizing the recombination with the anchored dye resulting in an overall smaller recombination (Table 5.23).

5.8 Materials and Methods

5.8.1 DSSCs assembly

The NiO electrodes were prepared by screen printing as described in section 1.11.2. Then each electrode was washed with ethanol and heated at 300 °C for 30 min and then cooled to 80 °C before immersing it in the dye bath (0.3 mM for the P1 dye bath in acetonitrile and 0.1 mM for the WOC53 dye bath in ethanol). The electrodes were removed from the dye bath after 16 h. and washed with acetonitrile or ethanol accordingly. A commercial platinum counter electrode was used (Solaronix Test Cell Platinum Electrodes) which was washed with ethanol and heated at 450 °C for 30 min. The DSSCs were assembled by combining working and counter electrode using thermoplast hot-melt sealing foil (Solaronix, Meltonix 1170-25 Series, 60 mm thick) by heating while pressing them together. The electrolyte was introduced by vacuum backfilling and the hole in the counter electrode was sealed by using a hot-melt sealing foil and cover glass

5.8.2 Sun simulation measurements

The DSSCs were sun-soaked from the anode side for 20 min at 1 sun irradiation. The cell was then inverted and measured immediately with a LOT Quantum Design LS811 instrument ($100 \text{ mW cm}^{-2} = 1$ sun at AM 1.5 and 23 °C) to obtain the current density-voltage (JV) curves. The instrument software was set to a p-type measurement mode (inverted configuration), with 360 ms settling time, and voltage step of 1.5 mV. The voltage was scanned from the negative to positive values.

5.8.3 Electrochemical impedance spectroscopy (EIS)

EIS measurements were carried out on a ModuLab[®] XM PhotoEchem photoelectrochemical measurement system from Solartron Analytical. The impedance was measured around the open-circuit potential of the cell at different light intensities (590 nm) in the frequency range 0.05 Hz to 400 kHz using an amplitude of 10 mV. The impedance data were analysed using ZView[®] software from Scribner Associates Inc. Voltage decay was measured on a Modulab XM electrochemical system.

Chapter 6 Tandem DSSCs

6.1 Introduction

The evolution of photovoltaic devices from the first report of *Bell* in 1954²⁰⁴ to modern discoveries motivated *Green*²⁰⁵ to adopt a classification method. First generation photovoltaic devices refer to the silicon pn-junction. Modern silicon cells achieve photoconversion efficiencies of up to 25%. The second generation refers to devices of low manufactured cost but low conversion efficiency such as the DSSC. Devices that could exceed the efficiency of the first-generation silicon pn-junction with the same or lower manufactured cost as the second-generation devices, are characterized as third-generation photovoltaic devices. Example of third-generation devices are tandem DSSCs, which are composed of an n-type DSSC as photoanode and a p-type DSSC as photocathode. The photoanode side of the tandem DSSC was reported in 1991 on the paper of *O'Regan and Grätzel*¹⁰, while *Lindquist and co-workers*²⁴ presented for the first time a p-type DSSC using NiO as a semiconductor, with a reverse charge operation than the n-type DSSC. Both n- and p-type photoelectrodes can work in

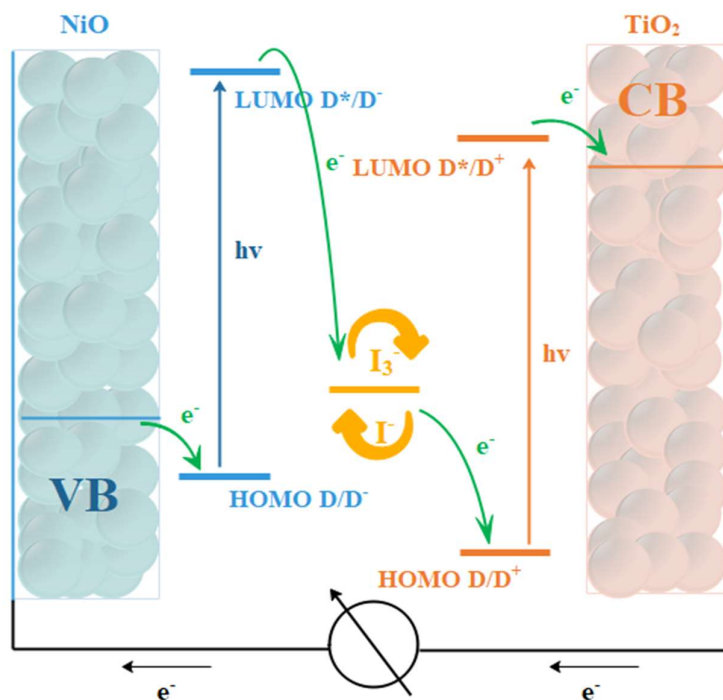


Fig. 6.1: Electron transfer processes occurring in the tandem DSSC.

a cooperative way producing a tandem DSSC (Fig. 6.1). The highest efficiency achieved by n-type DSSCs is ~14%²⁰⁶ and for p-type DSSCs the record efficiency is 2.5%¹⁸². The drive for the fabrication of a tandem DSSC lies in the higher theoretical efficiency that can be achieved by this device. The maximum theoretical efficiency of DSSCs is limited due to the band gap energy of the

semiconductor and is referred to as the Shockley-Queisser limit²⁰⁷ which is 31% for a single junction DSSC. For a tandem device this limit has been calculated to be 43%²⁰⁸. The charge transfer processes in a tandem DSSC are illustrated in Fig. 6.1. When irradiation takes place from the photocathode side, the dye anchored on TiO₂ absorbs light and is excited. Excitation of an electron and injection into the conduction band of the TiO₂ occurs. An electron is transferred from the redox couple to the oxidized dye to regenerate it. The oxidized redox couple accepts an electron from the excited state of the dye anchored on the p-type NiO semiconductor. In turn, an electron is transferred from the valence band of NiO to regenerate the dye on the p-type side of the cell. This quite simple picture of the tandem cell, is of course, made more complicated by the competitive recombination events and the different rates of electron transfer. As illustrated in Fig. 6.1, the n-type electrode and p-type electrode are mounted in a series configuration. The V_{OC} for this tandem device will be determined from the sum of the V_{OC} of

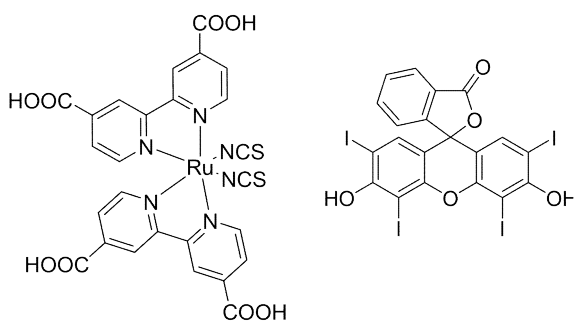


Fig. 6.2: Chemical structures of the N3 dye (left) and erythrosine B dye (right).

each half cell $V_{OC\ tandem} \approx V_{OC\ n-type} + V_{OC\ p-type}$ which is equal to the difference between the quasi-Fermi level of the valence band of the photocathode and the quasi-Fermi level of the conduction band of the photoanode. Thus, the photovoltage of the tandem cell is independent of the redox potential of the electrolyte. The J_{SC} of a tandem DSSC will be dictated by the lower performing dye²⁵ so the current density of both electrodes should be matched. The first reported

tandem device with the TiO₂ being sensitized with N3 dye and NiO with erythrosine B dye (Fig. 6.2) and an I⁻/I₃⁻ redox couple in the electrolyte, reached an efficiency of 0.39%²⁰⁹. The low efficiency was due to the low J_{SC} produced by the p-type of the device. Later work of *Bach and co-workers*²¹⁰, reported a tandem DSSC with an efficiency of 1.91% and with a record $V_{OC} = 1079$ mV and a $J_{SC} = 2.40$ mA cm⁻². The TiO₂ side was sensitized with N719 dye and the NiO was sensitized with PMI-6TTPA dye (Fig. 6.3).

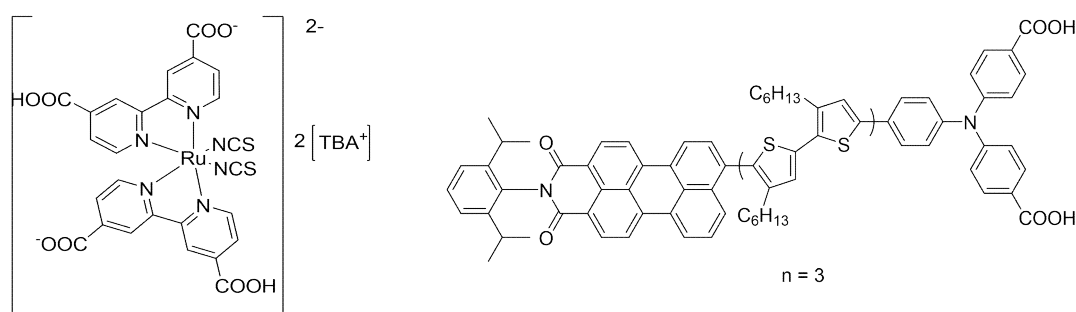


Fig. 6.3: Chemical structures of N719 dye (left) and PMI-6TTPA dye (right).

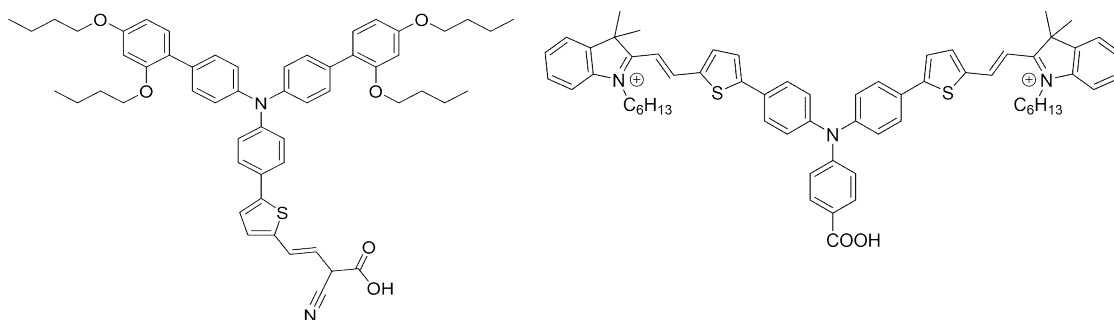


Fig. 6.4: Chemical structure of D35 dye (left) and CAD 3 dye (right).

More recent work of *Gibson and co-workers*²¹¹ achieved an efficiency 1.7% for a tandem DSSC with a record $J_{SC} = 5.15 \text{ mA cm}^{-2}$ and $V_{OC} = 613 \text{ mV}$. This was achieved with NiO sensitized with the dye CAD 3 ($\lambda_{max} = 614 \text{ nm}$) which with the D35 dye ($\lambda_{max} = 500 \text{ nm}$) (Fig. 6.4) used as a sensitizer for the TiO_2 reached a broader spectral absorbance over the visible region. In order to harvest as much of the visible part of the spectrum as possible *Kim and co-workers*²¹² used two commercially available

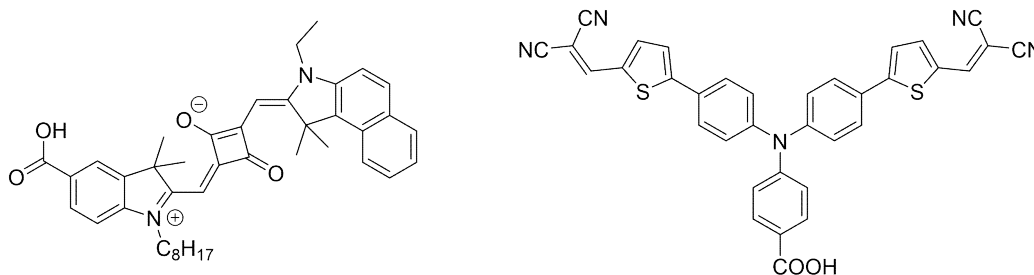


Fig. 6.5: Chemical structures of SQ2 dye on the left and P1 dye on the right.

organic dyes; SQ2 sensitized TiO_2 with an absorption at $\lambda_{max} = 645 \text{ nm}$ and P1 was used for the sensitization of the NiO and an absorption at $\lambda_{max} = 466 \text{ nm}$ (Fig. 6.5). With this combination of dyes and a $\text{Co}^{2+/3+}$ redox mediator, the tandem DSSCs achieved an efficiency of 1.91% with a $J_{SC} = 4.78$

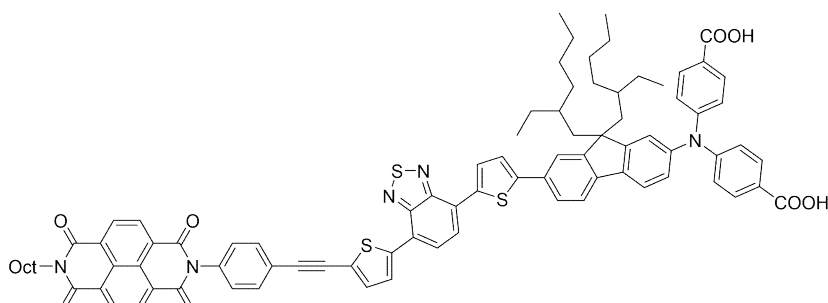
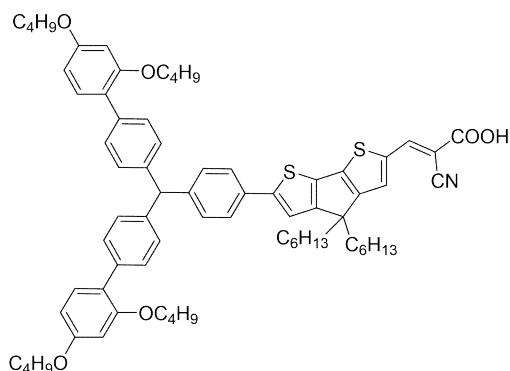


Fig. 6.6: Chemical structure of PP2-NDI dye.

mA cm⁻² and V_{OC} = 678 mV. During the work of *Odobel and co-workers*²¹³, a record efficiency of 2.86% with a J_{SC} = 5.07 mA cm⁻² and V_{OC} = 896 mV was reached for tandem DSSCs when using the dye D35 anchored on the TiO₂ electrode (Fig. 6.4) and PP2-NDI with λ_{max} = 501 nm (Fig. 6.6) on the NiO electrode with an I⁻/I₃⁻ redox couple in the electrolyte.

During the past years, several efforts have been made towards the goal of replacing the non-abundant



ruthenium metal on the dyes of DSSCs²¹⁴ or the I⁻/I₃⁻²¹⁵ redox couple, with more abundant metals such as copper. n-Type DSSCs with heteroleptic copper complexes and I⁻/I₃⁻ redox couple have achieved efficiencies of > 3%²¹⁶ and an efficiency of more than 8% was achieved when combining an organic dye (LEG4 Fig. 6.7) with [Cu(dmphen)₂]⁺²⁺ redox shuttle in the electrolyte (dmphen = 2,9-dimethyl-1,10-phenanthroline)²¹⁷. In a recent

Fig. 6.7: Chemical structure of LEG4 n-type dye

study done in our group the combination of copper dye and copper based redox couple in n-type DSSCs was reported²¹⁸. An efficiency of 2.06% with J_{SC} = 4.01 mA cm⁻² and V_{OC} = 684 mV was achieved for the combination of [Cu(dmbpymethoxy)(ALP1)] as a dye and [Cu(dmbpymethoxy)₂]⁺²⁺ (Fig. 6.8) as a redox couple (dmbpymethoxy = 6, 6'-dimethyl-4,4'-dimethoxy-2,2'-bipyridine, ALP1 = ((6,6'-dimethyl-[2,2'-bipyridine]-4,4'-diyl)bis(4,1-phenylene))bis(phosphonic acid)). During this study several ancillary ligands were investigated with different homoleptic copper redox shuttles in the electrolyte. The J_{SC} of these DSSCs covered a range from 1.10 to 4.01 mA cm⁻². Given that the photocurrent of these n-type DSSCs approximately matches the photocurrent obtained by the p-type DSSCs fabricated during this thesis (1.76 and 3.38 mA cm⁻² for DSSCs sensitized with P1 and WOC53 dye accordingly) a first

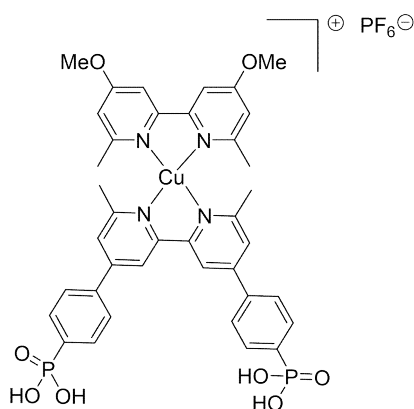


Fig. 6.8: Chemical structure of [Cu(dmbpymethoxy)(ALP1)] n-type dye

attempt for the fabrication of a tandem DSSC was initiated using copper dyes as sensitizers of the TiO₂ and WOC53 or P1 as sensitizers for the NiO, with a Cu^{+/2+} redox couple in the electrolyte.

6.2 Preliminary results of tandem DSSCs

During our investigation, tandem DSSCs were fabricated using Cu^{+/Cu²⁺} (Fig. 6.9) redox couple in the electrolyte and two different heteroleptic copper(I) dyes (Fig. 6.10) were tested as sensitizers for the

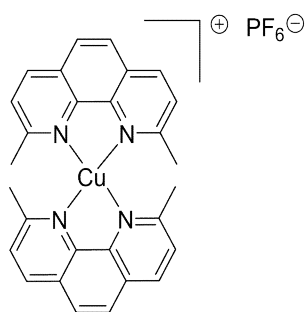


Fig. 6.9: Chemical structure of copper(I) complex used in the electrolyte, [Cu(dmphen)₂]⁺²⁺.

TiO₂ electrode. The heteroleptic copper(I) dyes used in this study are shown in Fig. 6.10. Using the same dyes and electrolyte, n-type DSSCs were also fabricated for comparison with the tandem cells. The NiO side was sensitized with cyclometalated Ru(II) dye WOC53 (Fig. 6.11) or with an organic commercially available P1 dye (Fig. 6.5). Prior to that, p-type DSSCs were fabricated using the two p-type dyes (WOC53 and P1) with the Cu^{+/Cu²⁺} electrolyte. The NiO electrodes were homemade and the fabrication procedure was described in chapter 3

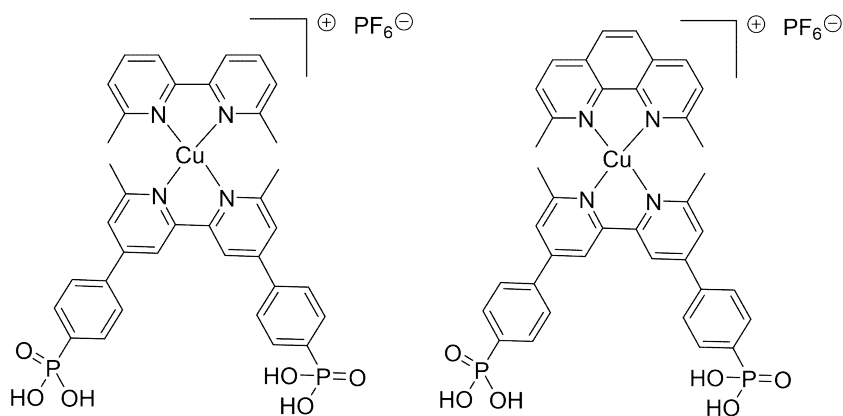


Fig. 6.10: Chemical structure of [Cu(ALP1)(dmbpy)]⁺ (left) dye and [Cu(ALP1)(dmphen)]⁺ (right) dye.

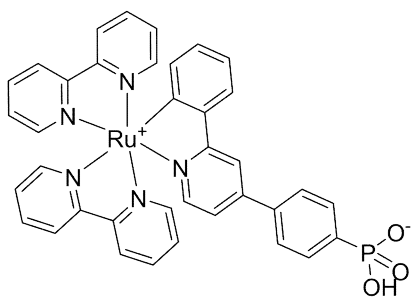


Fig.6.11: Chemical structure of WOC53 used on the p-type electrode

section 3.3.8. The FTO/TiO₂ electrodes were screen printed in our lab ²¹⁸. This work was done in collaboration with Dr. Annika Büttner responsible for the fabrication of TiO₂ electrodes and the synthesis of the n-type ²¹⁹ dyes and Cedric Wobill ²¹⁸ responsible for the synthesis of the copper complexes for the electrolyte.

6.2.1 Synthesis of dyes and redox couple for the electrolyte

The synthesis of the ALP1 anchoring domain was performed by Dr. Annika Büttner and it is described in Fig. 6.12.

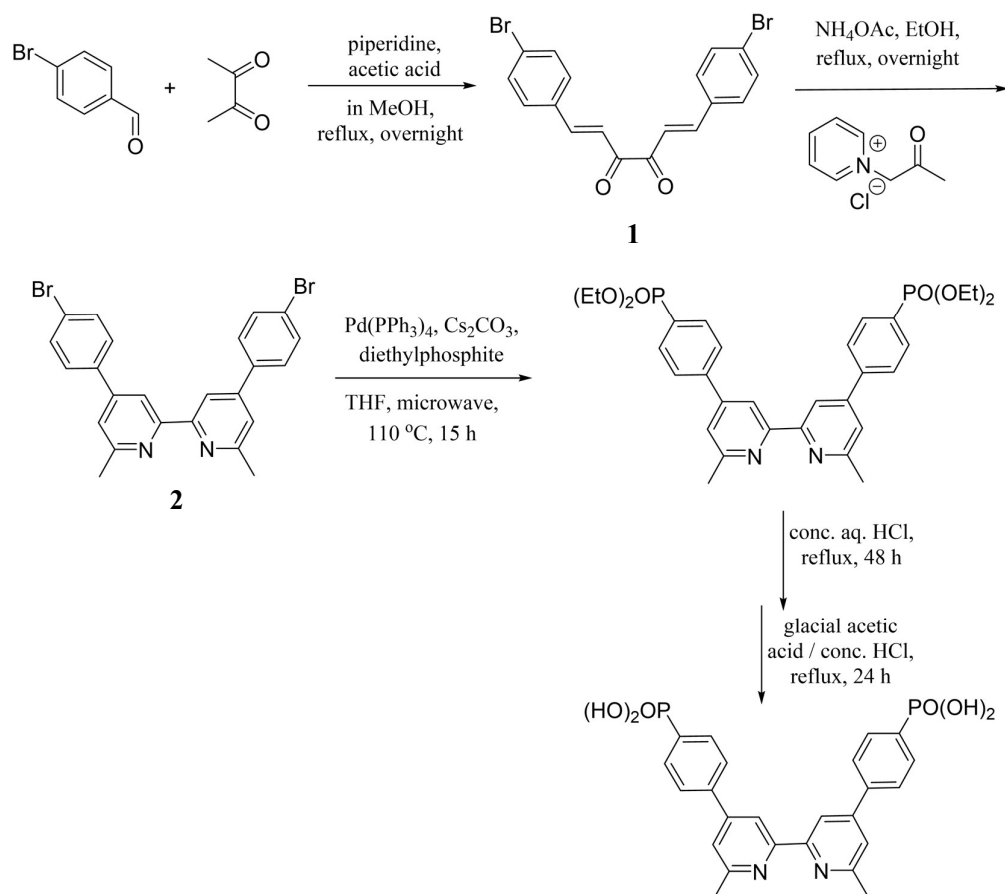


Fig. 6.12: Synthesis of the ALP1 anchoring ligand.

Compounds **1** and **2** were prepared according to the literature using the Kröhnke method ²²⁰. Compound **2** was treated with diethylphosphite in the presence of a catalytic amount of Pd(PPh₃)₄ and Cs₂CO₃ as a base before the reaction in a microwave reactor. The phosphonic ester was obtained and the deprotection to the phosphonic acid was performed by addition of acetic acid in the presence of HCl.

The ligands dmbpy (6,6'-dimethyl-2,2'-bipyridine) and dmphen (2,9-dimethyl-1,10-phenanthroline) were commercially available and purchased from Merck in a purity of 99%. The homoleptic $[\text{Cu}(\text{dmbpy})_2][\text{PF}_6]$ was synthesized as reported in the literature ⁷⁴ (Fig. 6.13). $[\text{Cu}(\text{NCMe})_4][\text{PF}_6]$ was dissolved in a mixture of acetonitrile and dichloromethane and 6,6'-Dimethyl-2,2'-bipyridine (0.456 mmol, 2 eq.) was added. The solution turned red, and it was stirred overnight. The volume of solvent was reduced in a rotary evaporator and the product precipitated after the addition of diethyl ether. The solid was redissolved in acetonitrile and precipitated again with diethyl ether. The dark red product was collected by filtration and was washed with diethyl ether and dried in a stream of air.

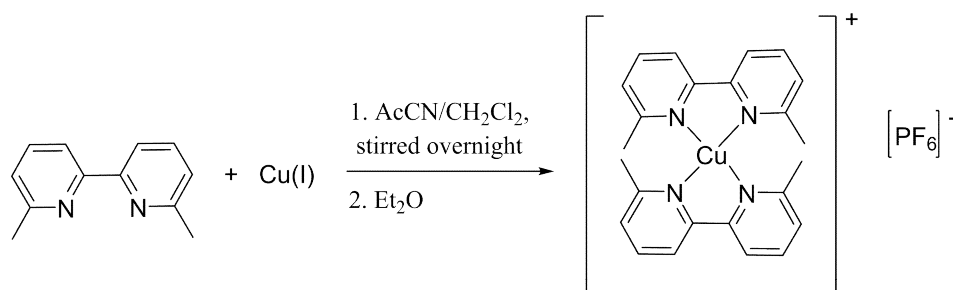


Fig. 6.13: Synthesis of the $[\text{Cu}(\text{dmbpy})_2][\text{PF}_6]$ complex.

$[\text{Cu}(\text{dmphen})_2][\text{PF}_6]$ was synthesized as reported in the literature ^{221, 222} (Fig. 6.14). 2,9-Dimethyl-1,10-phenanthroline (2 eq.) was dissolved in 10 ml of acetonitrile under argon stir. This solution was added while stirring to solid $[\text{Cu}(\text{NCMe})_4][\text{PF}_6]$ under argon atmosphere. An orange-red colour was observed, and the reaction mixture was stirred for 10 min. The product was precipitated by addition of diethyl ether under an argon atmosphere. The solid was filtered onto a glass frit and redissolved in a minimum volume of dichloromethane.

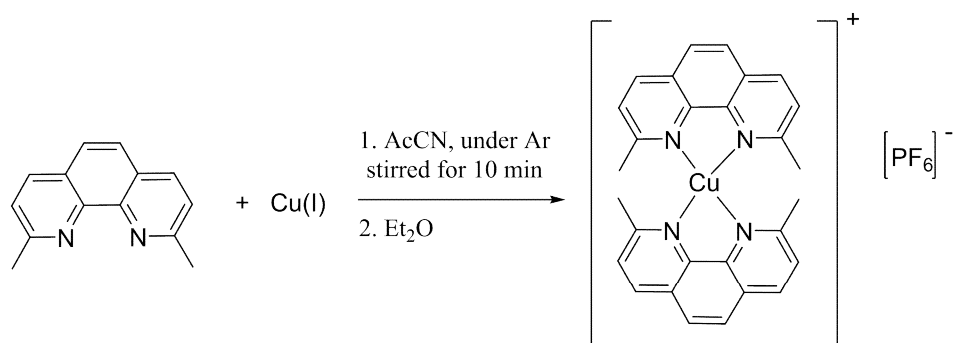


Fig. 6.14: Synthesis of the $[\text{Cu}(\text{dmphen})_2][\text{PF}_6]$ complex.

$[\text{Cu}(\text{dmphen})_2][\text{PF}_6]_2$ was prepared by oxidation of $[\text{Cu}(\text{dmphen})_2][\text{PF}_6]$ (Fig. 6.15). $[\text{Cu}(\text{dmphen})_2][\text{PF}_6]$ was dissolved in dry acetonitrile and $[\text{NO}][\text{BF}_4]$ was added. Over a period of 1 hour stirring, the solution turned green. After addition of a methanol solution of NH_4PF_6 , diethyl ether was then added to the solution to precipitate the Cu(II) complex, which were collected by filtration and washed with water and diethyl ether.

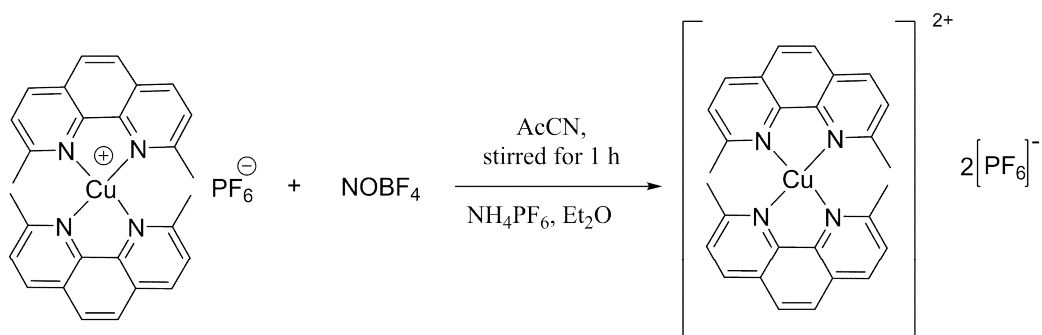


Fig. 6.15: Synthesis of the $[\text{Cu}(\text{dmphen})_2][\text{PF}_6]_2$ complex.

The synthesis of WOC53 has been described in section 4.3.1. The dye P1 is commercially available and was purchased from Dyenamo.

6.2.2 Cyclic voltammetry and solid-state UV-Vis. spectroscopy

The cyclic voltammetry data (CV) recorded by Cedric Wobill showed that the redox couple used in the electrolyte during this study ($[\text{Cu}(\text{dmphen})_2]^{+/2+}$, Fig. 6.9) has an oxidation potential of $E^{\text{ox}}_{1/2} = +0.41 \text{ V}$ and $E_{\text{pc}} - E_{\text{pa}} = 66 \text{ mV}$ vs Fc/Fc^+ in CH_2Cl_2 solution with $[\text{nBu}_4\text{N}][\text{PF}_6]$ as supporting electrolyte at a scan rate of 0.1 V s^{-1} ²⁴⁵. This value compares with $+0.93 \text{ V}$ vs. SHE from the work of *Freitag and co-workers*²⁴⁷ and with $+0.50 \text{ V}$ vs. Fc/Fc^+ from the work of *Pallenberg and co-workers*²²³. From the solid-state UV-Vis absorption spectra of the sensitized TiO_2/FTO electrode with $[\text{Cu}(\text{ALP1})(\text{dmbpy})]^+$ and $[\text{Cu}(\text{ALP1})(\text{dmphen})]^+$ it is observed that both dyes have a broad absorption spectrum between $400 - 520 \text{ nm}$ with a maximum at $\lambda_{\text{max}} = 470 \text{ nm}$ (Fig. 6.16). On the other hand, the solid-state absorption of NiO/FTO electrodes sensitized with the p-type dyes absorb at longer wavelength with a maximum at $\lambda_{\text{max}} = 540 \text{ nm}$ for P1 and a less intense but broader band for WOC53 between $\lambda_{\text{max}} = 430 - 620 \text{ nm}$.

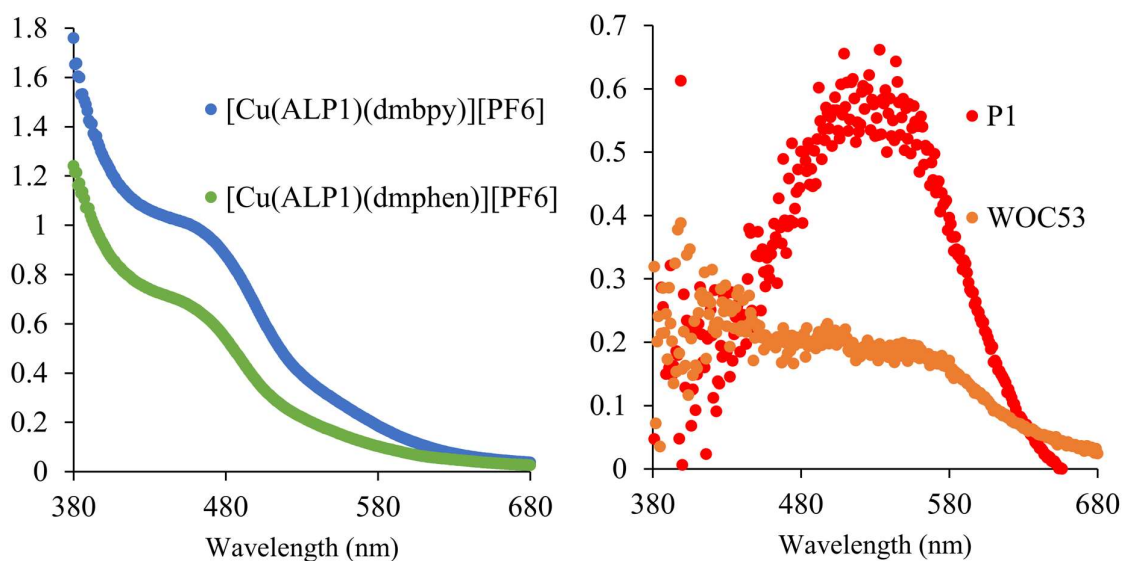


Fig. 6.16: Solid state UV-Vis. absorption spectrum of TiO_2/FTO electrode sensitized with $[\text{Cu}(\text{ALP1})(\text{dmbpy})]^+$ (blue curve) and $[\text{Cu}(\text{ALP1})(\text{dmphen})]^+$ (green curve) on the left and NiO/FTO electrode sensitized with WOC53 (blue curve) and P1 (orange curve) on the right.

6.2.3 Sun simulation and External quantum efficiency (EQE)

measurements

Duplicate DSSCs were fabricated for each combination of dyes, and electrolyte and the JV curves were measured (Table 6.1, Fig. 6.17). In Fig. 6.17, only the best performing DSSC out of the duplicate sets is exhibited. All cells were vacuum back filled with the electrolyte comprising 0.2 M $[\text{Cu}(\text{dmphen})_2][\text{PF}_6]$, 0.04 M $[\text{Cu}(\text{dmphen})_2][\text{PF}_6]_2$, 0.1 M LiPF_6 , 0.5 M 4-tert-butylpyridine in

acetonitrile. The best performing tandem DSSC (NMA-504_1) exhibits an efficiency of $\eta = 1.17\%$ with a $J_{SC} = 2.00 \text{ mA cm}^{-2}$ and $V_{OC} = 797 \text{ mV}$. Comparing this DSSC with the analogous n-type DSSC (NMA-564_1) bearing the same dye which displays an efficiency of 0.88% with a $J_{SC} = 1.87 \text{ mA cm}^{-2}$ and $V_{OC} = 760 \text{ mV}$, an increase in efficiency for the tandem DSSC can be seen. This increase is

Experiment Name	<i>n-type dye</i>	<i>p-type dye</i>	Jsc/ mA cm⁻²	Voc/mV	FF/%	η/%
NMA-504_1	[Cu(ALP1)(dmbpy)] ⁺	WOC53	2.00	797	73	1.17
NMA-504_2	[Cu(ALP1)(dmbpy)] ⁺	WOC53	2.04	788	71	1.15
NMA-562_1	[Cu(ALP1)(dmbpy)] ⁺	P1	1.95	792	71	1.11
NMA-562_2	[Cu(ALP1)(dmbpy)] ⁺	P1	1.57	793	68	0.85
NMA-508_1	[Cu(ALP1)(dmphen)] ⁺	WOC53	1.87	743	58	0.81
NMA-508_2	[Cu(ALP1)(dmphen)] ⁺	WOC53	1.74	776	67	0.91
NMA-563_1	[Cu(ALP1)(dmphen)] ⁺	P1	1.50	729	62	0.67
NMA-563_2	[Cu(ALP1)(dmphen)] ⁺	P1	0.72	605	46	0.20
NMA-564_1	[Cu(ALP1)(dmbpy)] ⁺	–	1.85	760	63	0.88
NMA-564_2	[Cu(ALP1)(dmbpy)] ⁺	–	1.71	722	55	0.68
NMA-565_1	[Cu(ALP1)(dmphen)] ⁺	–	1.23	752	65	0.60
NMA-565_2	[Cu(ALP1)(dmphen)] ⁺	–	1.21	727	54	0.48
NMA-566_1	–	WOC53	0.14	12	25	0.00
NMA-566_2	–	WOC53	0.07	20	25	0.00
NMA-567_1	–	P1	0.02	22	25	0.00
NMA-567_2	–	P1	0.02	9	24	0.00

Table 6.1: Performance data for duplicate tandem (irradiated from the TiO₂ side), n-type (irradiated from the TiO₂ side) and p-type (irradiated from the NiO side) DSSCs. The measurements were done on the day of sealing. The active area of the cell was 0.0597 cm^2 .

justified by an increase of the V_{OC} of the tandem cell which is equal to $V_{OC\ tandem} \approx V_{OC\ n-type} + V_{OC\ p-type}$ and a small increase of the J_{SC} which is justified by the wider range of light absorption when combining the n- and p-type dyes ($[Cu(ALP1)(dmbpy)]^+$ and WOC53). The last argument is confirmed when considering the tandem DSSC sensitized with the same n-type dye and p-type dye P1 (NMA-562_1) which also displays an increase of the J_{SC} compared with the analogous n-type dye (NMA-564_1) (1.106 vs 0.878 $mA\ cm^{-2}$ for NMA-562_1 and NMA-564 respectively). When

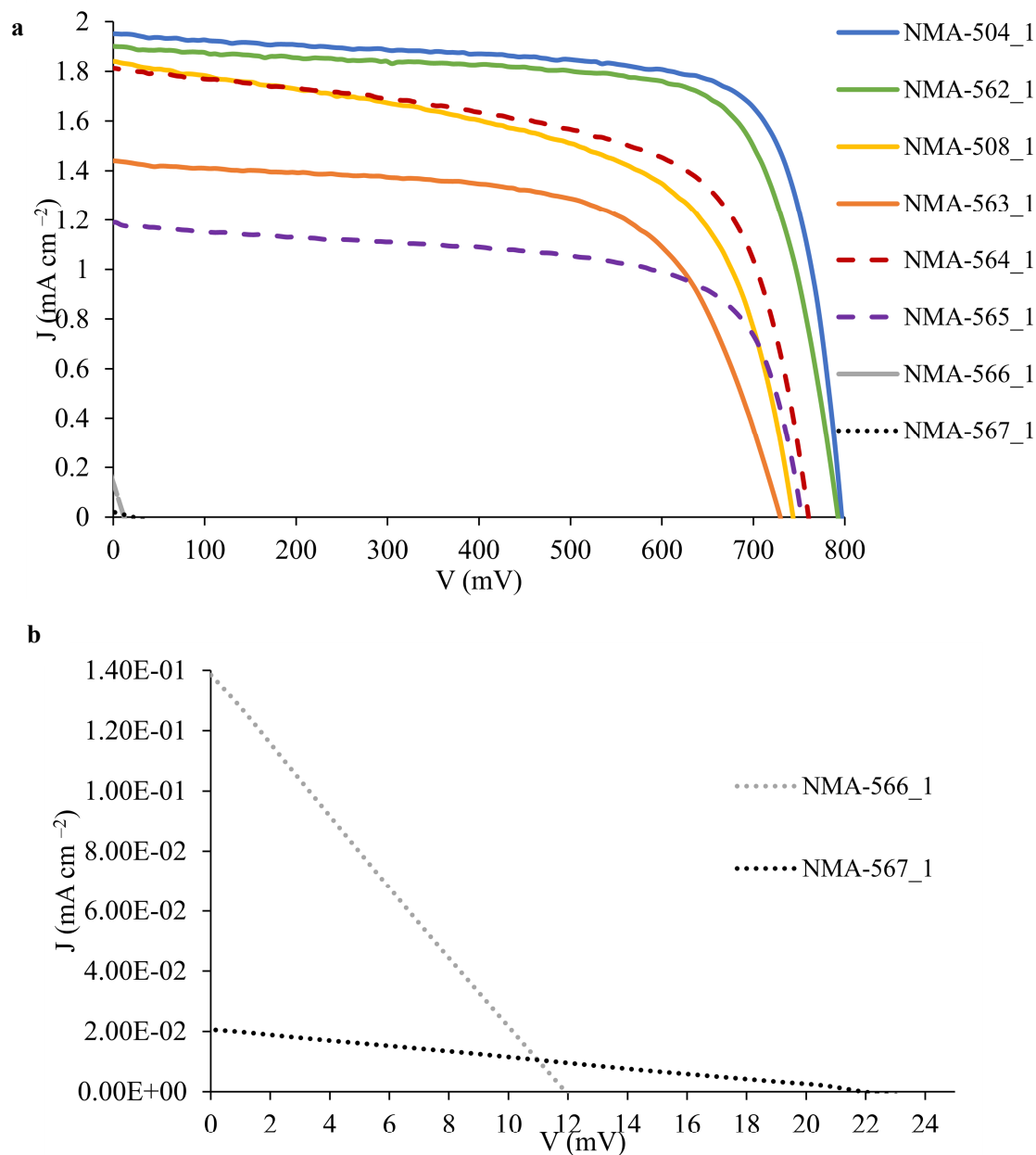


Fig. 6.17: **a.** JV curves of tandem DSSCs (full lines) n-type DSSC (dashed lines) p-type DSSCs (dotted lines) **b.** expansion of JV plots for the p-type DSSCs. The composition of the cells is described in Table 6.1.

[Cu(ALP1)(dmphen)]⁺ dye was used as an n-type dye for a tandem DSSC (NMA-508_1) a decrease in the efficiency was observed compared to the tandem DSSC NMA-504_1 ($\eta = 1.168\%$ vs. 0.808% for NMA-504_1 and NMA-508_1 respectively). But the tandem DSSC with n-type [Cu(ALP1)(dmphen)]⁺ dye and p-type WOC53 or P1 dyes (NMA-508_1 or NMA-563_1 accordingly) was more efficient compared to the analogous n-type DSSC (NMA-565_1). This was mainly reflected in the better J_{SC} of the tandem DSSC (1.87 or 1.50 vs 1.23 mA cm^{-2} for NMA-508_1 or NMA-563_1 vs NMA-565_1 respectively).

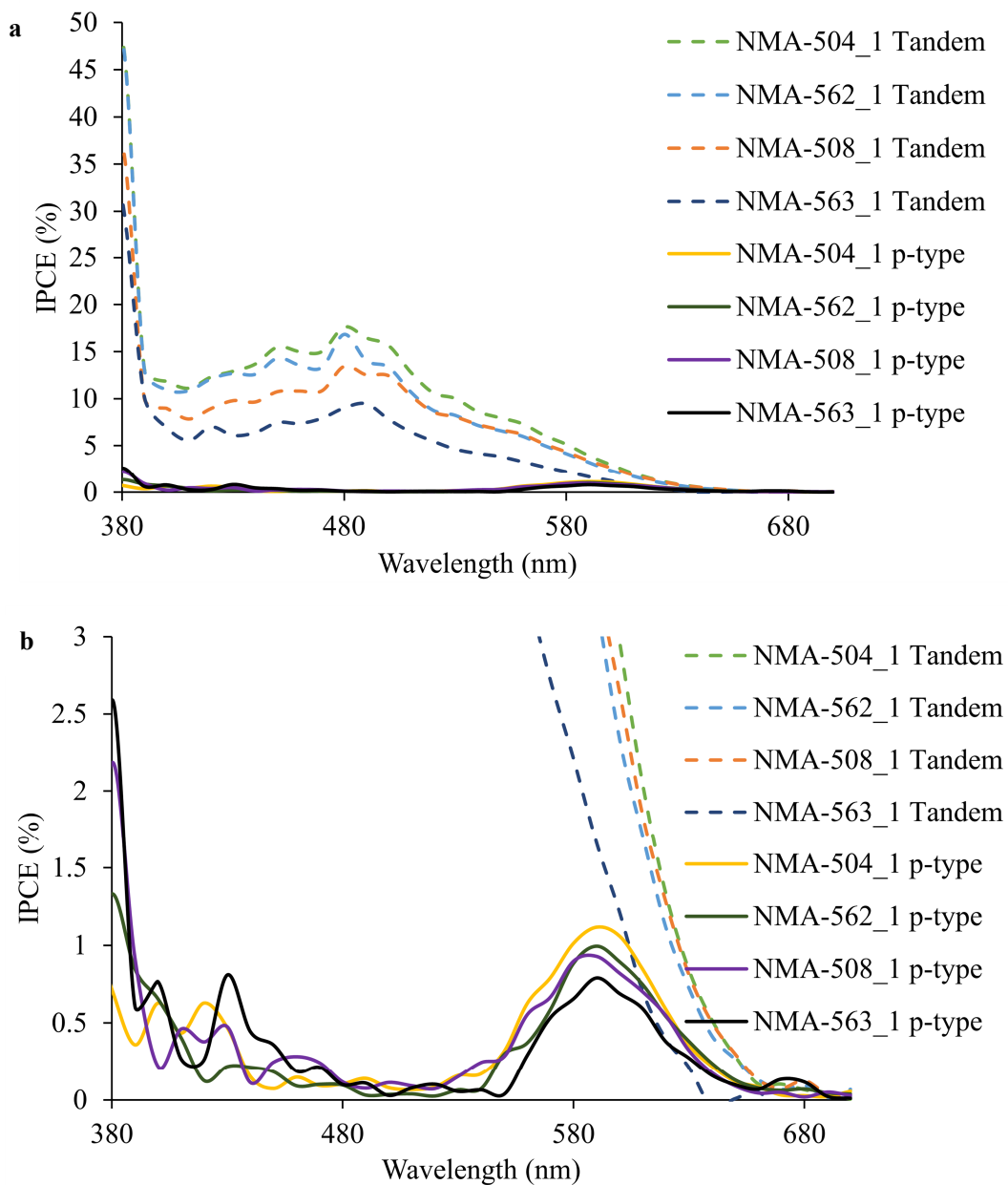


Fig. 6.18: **a:** EQE spectra for tandem DSSCs and **b:** expansion of the EQE spectrum. The composition of the cells is described in Table 6.1.

From the EQE spectra of the tandem DSSCs irradiated from the n-type side in Fig. 6.18a, it is observed that the absorption region of the all the cells agrees with the solid-state absorption ($\lambda_{max, EQE} = 480$ nm, $\lambda_{max, ssUV} = 470$ nm) for both n-type Cu(I) dyes shown in Fig. 6.16. In order to show the IPCE efficiency of both sides of the tandem cells, the EQE spectrum was taken from the p-type side as well.

In Fig. 6.18a, the EQE spectra of the tandem cells recorded from the p-type side can also be observed (solid lines), the expansion of this plot is displayed in Fig. 6.18b. The photon to current efficiencies of the tandem cells irradiated from the n-type side reflect the results seen their J_{SC} values from the sun simulation experiment. The best performing cell is NMA-504_1 with an IPCE of 18% which contains the n-type [Cu(ALP1)(dmbpy)]⁺ dye and the p-type WOC53 dye and the worst performing is the tandem cell containing the [Cu(ALP1)(dmphen)]⁺ dye and the p-type P1 dye with an IPCE of 10%. In Fig. 6.18b the EQE spectra of the tandem cells recorded from the p-type side is exhibited. It is observed that the absorption from the p-type side exhibits a small red shift compared with the solid-state absorption ($\lambda_{max, EQE, P1} = 590$ nm, $\lambda_{max, EQE, WOC53} = 580 - 590$ nm and $\lambda_{max, ssUV, P1} = 540$ nm, $\lambda_{max, ssUV, WOC53} = 530 - 620$ nm) of the p-type dyes in Fig. 6.16. The photon to current efficiency for the tandem cells measured from the NiO side is between 1.1 - 0.8%. The low efficiency may be because only a small amount of the irradiation reaches the dye because we are irradiating from the NiO side of the cell and some light is therefore absorbed by the NiO. Nevertheless, this observation is a solid argument about the contribution of the p-type side to the efficiency of the tandem cells

6.2.4 Electrochemical impedance spectroscopy (EIS) measurements

In order to investigate the processes taking place at the different interface of the tandem cells EIS measurements of the n-type, p-type and tandem DSSCs were made. The equivalent circuit used for these measurements is presented in Fig 6.19.

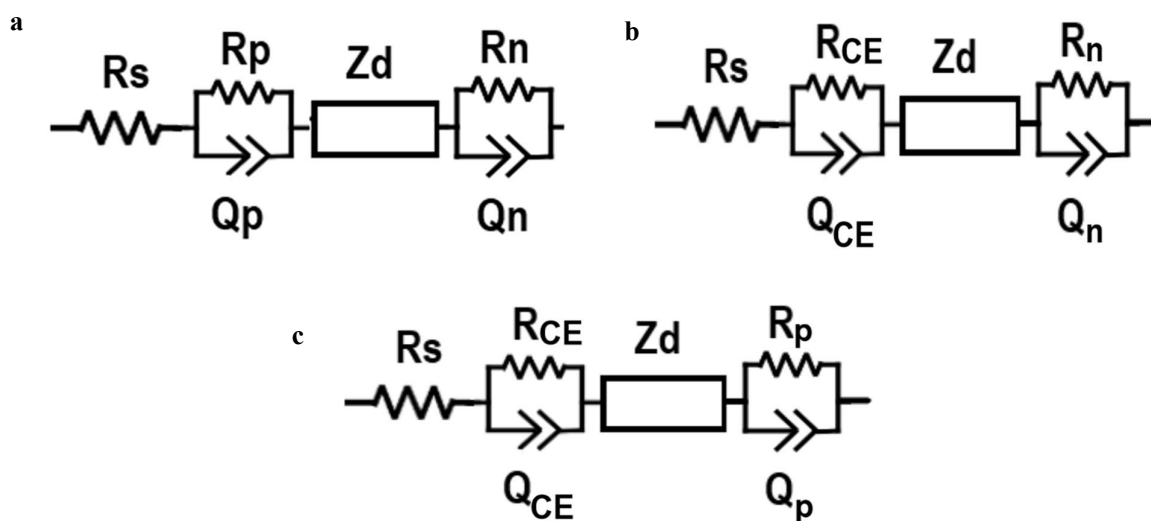


Fig. 6.19: Equivalent circuit used to fit the EIS data for **a.** Tandem DSSCs, **b.** n-type DSSCs and **c.** p-type DSSCs.

The equivalent circuit was composed of a series resistance and is seen in the Nyquist plot on the abscissa from zero to the start of the first semicircle (Fig. 6.20). An R/Q element was employed in order to calculate the resistance and capacitance of the cathode, attributed at the first semicircle on the Nyquist plot occurring in high frequency regions (Fig. 6.20b). A second R/Q element was used to fit the charge transfer process and capacitance occurring at the anode of the cell arising in intermediate frequency regions and represented as the second semicircle on the Nyquist plot (Fig. 6.20). Furthermore, the Warburg element (Z_d) was used to model the diffusion process in the high frequency region. During this study a constant phase element (CPE) was used instead of a capacitor for fitting the capacitance of the anode and cathode electrode due to the porosity of these surfaces¹³³. In Table 6.2 the parameters obtained from the EIS measurements of the tandem, n- and p-type DSSCs are summarized. The parameters obtained from the EIS reflects the results obtained from the JV curves (Fig. 6.17). As expected, the series resistance (R_s) is almost the same for all the cells examined ($13.8 \pm 3 \Omega$). The semicircles on the Nyquist plot assigned to the charge transfer processes of the anode/electrolyte interface and of the cathode/electrolyte interface for the tandem DSSC NMA-504_1 and the n-type DSSC NMA-564_1 are

Cell Name	R_s/Ω	R_{Pt}/Ω	$CPE_{Pt}/\mu F$	α_{Pt}		$CPE_p/\mu F$	α_p	R_n/Ω	$CPE_n/\mu F$	α_n	W_s
NMA-504_1	15.8	-	-	-	61.8	222.8	0.68	632.7	242.1	0.75	313.3
NMA-562_1	11.0	-	-	-	24.2	87.5	0.97	257.3	390.3	0.83	2897
NMA-508_1	11.3	-	-	-	16.8	324.2	0.97	836.6	285.5	0.96	3882
NMA-563_1	9.5	-	-	-	52.0	58.0	0.79	829.8	291.3	0.68	883.3
NMA-564_1	16.9	329.5	5.9	0.93	-	-	-	493.1	44.7	0.85	83.5
NMA-565_1	17.9	336.5	6.7	0.81	-	-	-	577.8	64.4	0.81	100.8
NMA-566_1	10.4	1634.0	516.2	0.69	865.9	10.8	0.94	-	-	-	0.94
NMA-567_1	10.0	14855	354.5	0.71	2108.0	11.1	0.94	-	-	-	137

Table 6.2: EIS data obtained from measurements at light intensity of 22mW cm^{-2} of tandem n- and p-type DSSCs (See Table 1). The electrolyte comprised of 0.2 M $[\text{Cu}(\text{dmphen})_2][\text{PF}_6]$, 0.04 M $[\text{Cu}(\text{dmphen})_2][\text{PF}_6]_2$, 0.1 M LiPF_6 , 0.5 M 4-tert-butylpyridine in acetonitrile.

overlapping each other as can be seen on the Nyquist plots in Fig. 6.20a and b and the Bode plots on Fig. 6.20c. Hence, it is not possible to entirely differentiate one charge process from the other. But the sum of both charge transfer processes can be compared, $R_p + R_n$ for the tandem cell NMA-504_1 and

the sum of $R_{CE} + R_n$ for the n-type cell NMA-564_1 (Table 6.2) ²¹². From that comparison, it can be concluded that the charge transfer resistance on the n-type cell is larger than that observed for the tandem cell (822.6 vs. 632.7 Ω for NMA-564_1 and NMA-504_1 respectively). So, the sensitized p-type side brings an improvement to the total efficiency of the tandem cell. The tandem cell NMA-562_1 sensitized with the same n-type dye as NMA-504_1 cell but with P1 as the dye on the NiO side, displays a lower R_p and R_n compared to the cell NMA-504_1 but a much higher Warburg W_s resistance (2897 vs. 313.3 Ω for NMA-562_1 and NMA-504_1 respectively). Once again, the semicircles from the Nyquist plots of the tandem cell NMA-562_1 and the n-type cell NMA-564_1, which represent the charge transfer processes for both the anode/electrolyte interface and of the cathode/electrolyte interface, are overlapping (Fig. 6.21). If we compare the sum of the charge transfer resistances for each cell, it is observed that the tandem cell has a lower overall charge transfer resistance (257.3 vs. 822.6 vs. Ω for NMA-562_1 and NMA-564_1 respectively) but a much higher Warburg resistance (83.5 vs. 2897 Ω for NMA-564_1 and NMA-562_1 respectively). For the tandem cells sensitized with $[\text{Cu}(\text{ALP1})(\text{dmphen})]^+$ on the n-type side and with WOC53 on the p-type side NMA-508_1 (Fig. 6.22) the sum of the charge transfer resistances (Table 6.2) are lower compare to the n-type DSSC sensitized with the same n-type dye NMA-565_1 (836.6 vs. 914.3 Ω for NMA-508_1 and NMA-565_1 respectively) which justifies the higher J_{sc} observed for the tandem cell (1.87 vs 1.23 mA cm^{-2} for NMA-508_1 and NMA-565_1 respectively). The tandem cell NMA-563_1 with $[\text{Cu}(\text{ALP1})(\text{dmphen})]^+$ dye (Fig. 6.23) on the n-type and P1 dye on the p-type side exhibited a higher η (Table 6.1) compared to the n-type NMA-565_1. Its higher J_{sc} (1.50 vs. 1.23 mA cm^{-2} for NMA-563_1 and NMA-565_1 respectively) is justified by the lower sum of the charge transfer resistances of the tandem cell (828.8 vs. 914.3 Ω for NMA-563_1 and NMA-565_1 respectively).

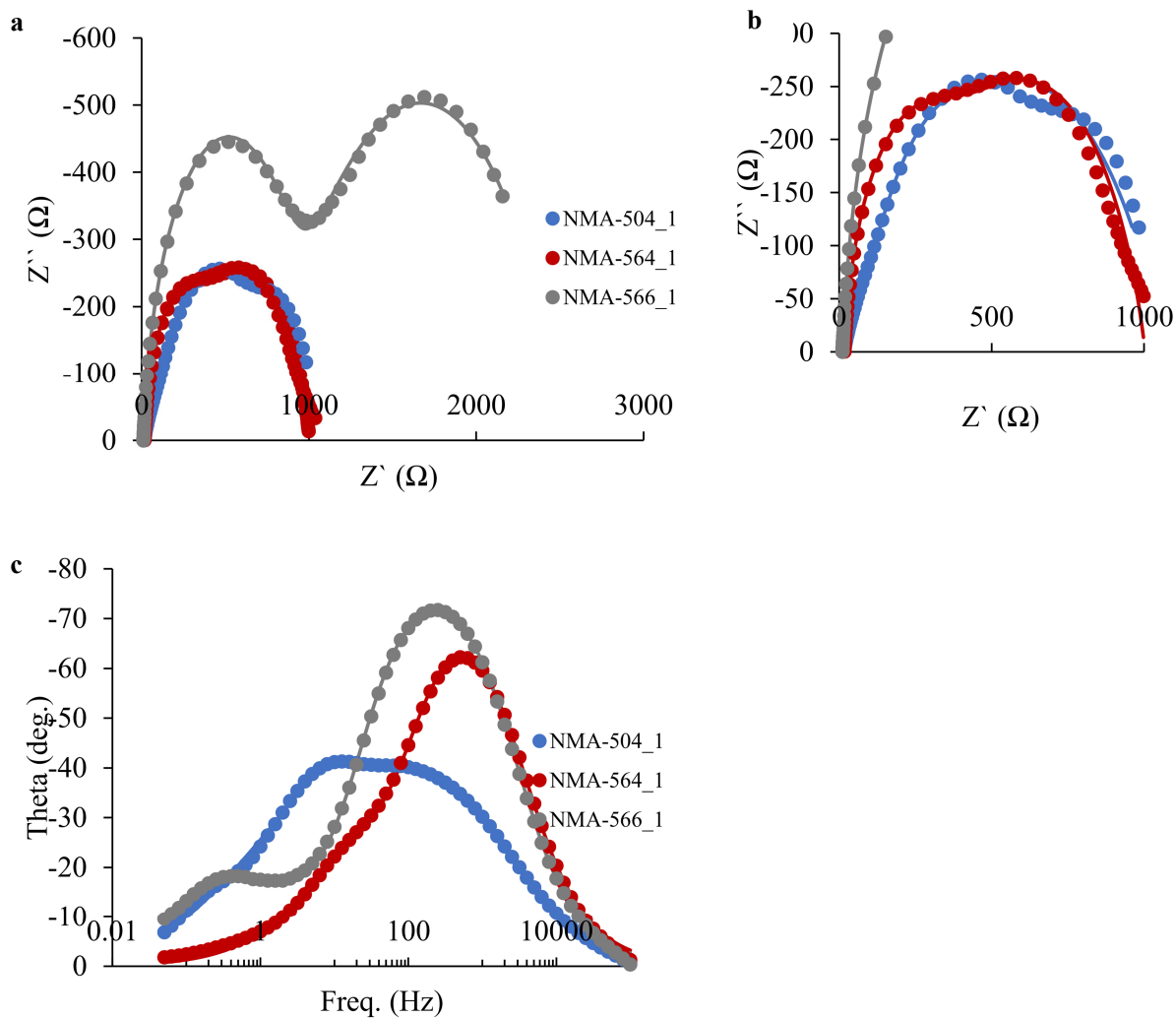


Fig. 6.20: **a.** Nyquist plot and **b.** expansion of part of the Nyquist plots **c.** Bode plots for tandem, n- and p-type DSSCs, (See Table 6.1). The electrolyte comprised of 0.2 M $[\text{Cu}(\text{dmphe})_2][\text{PF}_6]$, 0.04 M $[\text{Cu}(\text{dmphe})_2][\text{PF}_6]_2$, 0.1 M LiPF_6 , 0.5 M 4-tert-butylpyridine in acetonitrile.

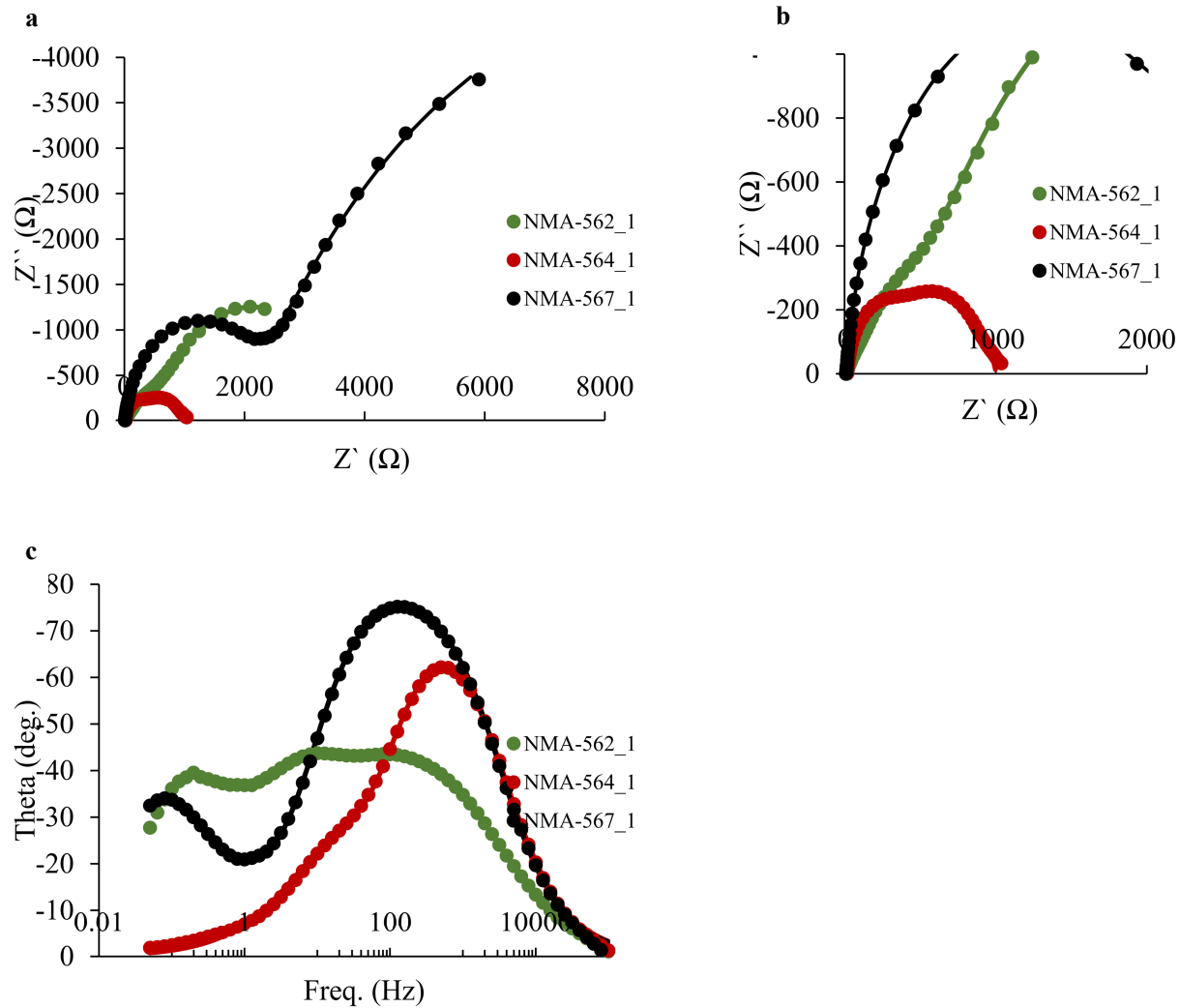


Fig. 6.21: **a.** Nyquist plot and **b.** expansion of part of the Nyquist plots **c.** Bode plots for tandem, n- and p-type DSSCs, (See Table 6.1). The electrolyte comprised of 0.2 M $[\text{Cu}(\text{dmphen})_2][\text{PF}_6]$, 0.04 M $[\text{Cu}(\text{dmphen})_2][\text{PF}_6]_2$, 0.1 M LiPF_6 , 0.5 M 4-tert-butylpyridine in acetonitrile.

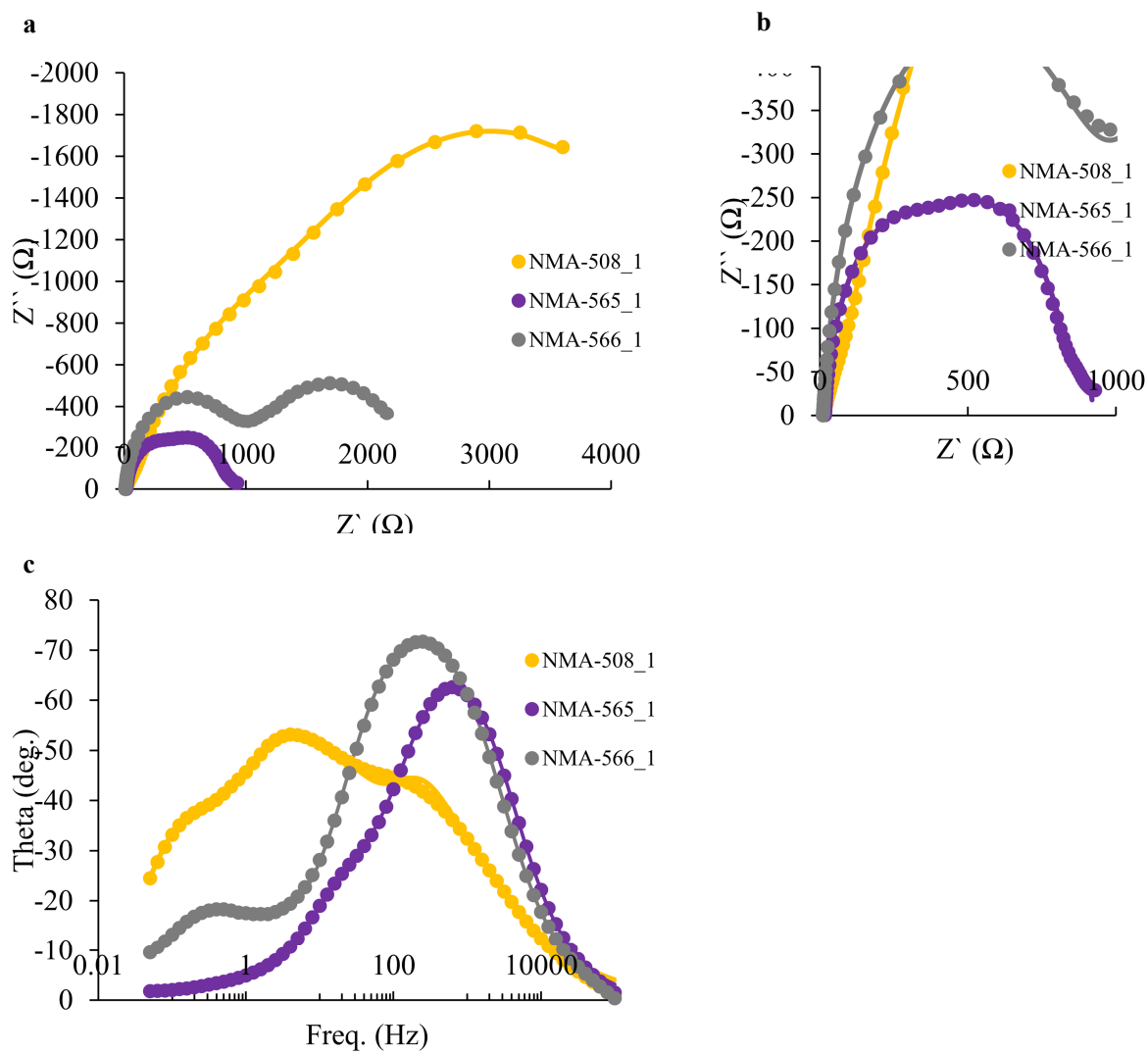


Fig. 6.22: **a.** Nyquist plot and **b.** expansion of part of the Nyquist plots **c.** Bode plots for tandem, n- and p-type DSSCs, (See Table 6.1). The electrolyte comprised of 0.2 M $[\text{Cu}(\text{dmphen})_2][\text{PF}_6]$, 0.04 M $[\text{Cu}(\text{dmphen})_2][\text{PF}_6]_2$, 0.1 M LiPF_6 , 0.5 M 4-tert-butylpyridine in acetonitrile.

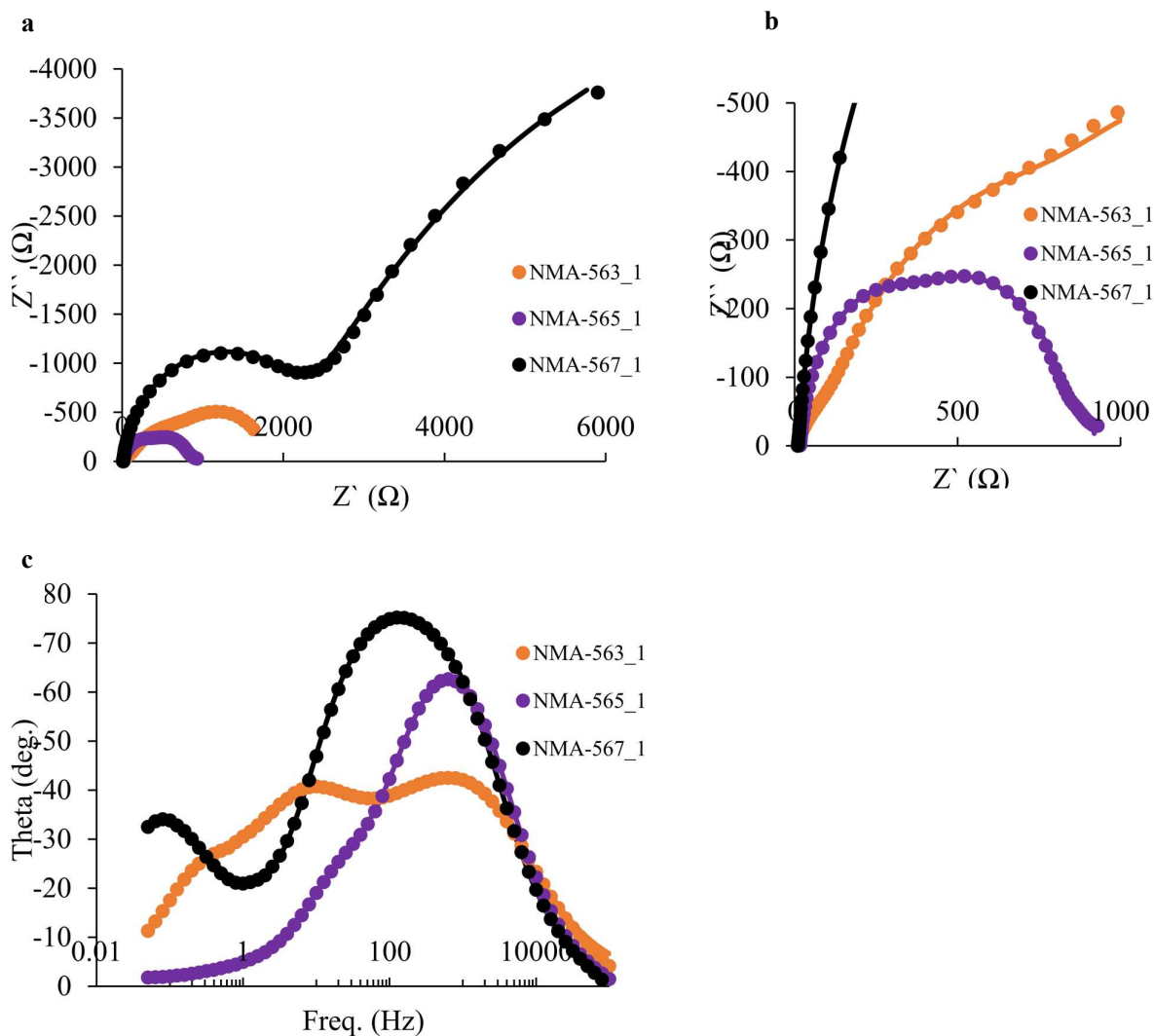


Fig. 6.23: **a.** Nyquist plot and **b.** expansion of part of the Nyquist plots **c.** Bode plots for tandem, n- and p-type DSSCs, (See Table 6.1). The electrolyte comprised of 0.2 M $[\text{Cu}(\text{dmphen})_2][\text{PF}_6]$, 0.04 M $[\text{Cu}(\text{dmphen})_2][\text{PF}_6]_2$, 0.1 M LiPF_6 , 0.5 M 4-tert-butylpyridine in acetonitrile.

6.2.5 Intensity modulated photocurrent spectroscopy measurements (IMPS)

In order to de-couple the charge transfer processes occurring in the tandem cells, different electrochemical techniques were used. This investigation was done for the three best performing tandem DSSCs (NMA-504_1, NMA-562_1 and NMA-508_1) and the n-type cells (NMA-564_1 and NMA-565_1) sensitized with the two n-type dyes of this study (Fig. 6.10).

Intensity modulated photocurrent spectroscopy measurements (IMPS) were performed on the DSSCs. During this measurement, the potential of the DSSC was potentiostatically controlled and set to short circuit conditions and the photocurrent generate was measured. At short circuit conditions, the band gap of the semiconductor is at its maximum value and as a consequence, no charges are injected and most of the reactions occur on the back layer of the electrode (FTO/semiconductor interface) where

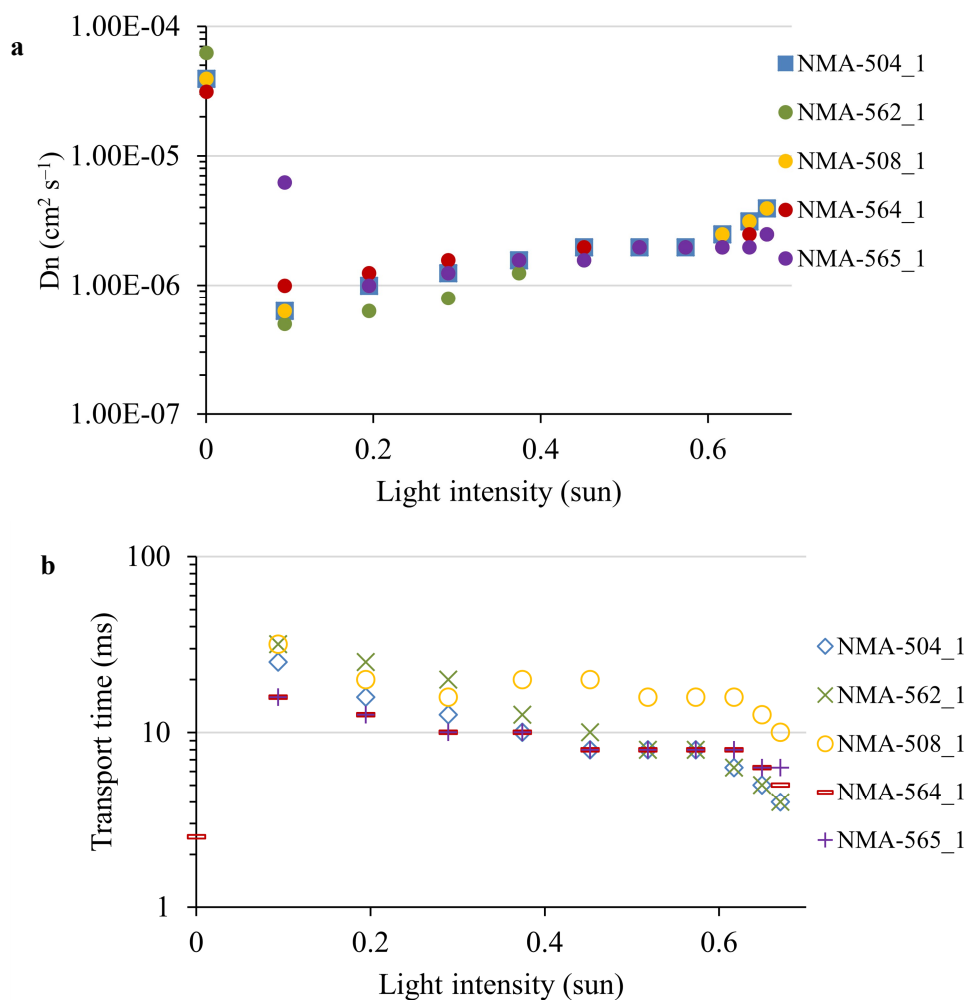


Fig. 6.24: IMPS measurements for tandem and n-type DSSCs **a.** diffusion coefficient vs. light intensities **b.** transport time (τ_{tr}) vs. light intensities (See Table 6.1). The electrolyte comprised of 0.2 M $[\text{Cu}(\text{dmphen})_2][\text{PF}_6]$, 0.04 M $[\text{Cu}(\text{dmphen})_2][\text{PF}_6]_2$, 0.1 M LiPF_6 , 0.5 M 4-tert-butylpyridine in acetonitrile.

charges are migrating. The measurements were repeated for different light intensities. Thus, the charge transport time (eq. 6.1)²²⁴ and the diffusion coefficient of the charge (eq. 6.2)²²⁴ were calculated.

$$\tau_{tr} = \frac{1}{2\pi f_{IMPS}} \quad (6.1)$$

where τ_{tr} is the electron transport time and f_{IMPS} is the minimum frequency point for each applied light intensity on the Bode plot of the IMPS spectra²²⁴.

Ideally the transport time should be low enough in order for the charge to be efficiently collected at the back layer of the anode before being lost by recombination reactions. The diffusion coefficient can be calculated from equation 6.2²²⁵

$$D_n = \frac{d^2}{4\tau_{tr}} \quad (6.2)$$

where d is the film thickness and τ_{tr} is the electron transport time. The higher the D_n the faster the photogenerated electron can be transported to the back layer of the anode electrode. From Fig. 6.24a, it is observed that values of D_n of all DSSCs increase with increase light intensities as expected. The increase rate for the tandem cells is NMA-504_1, NMA-562_1 and NMA-508_1 and the values for the n-type cells NMA-564_1 and NMA-565_1 are fairly similar with NMA-565_1 having the lowest values a higher light intensity. The tandem cell NMA-508_1 exhibited the highest values of transport time at high light intensities as seen in Fig. 6.24b which suggests a poor electron mobility and high recombination with the anchored dye and the electrolyte.

6.2.6 Short circuit charge extraction measurements

During the short circuit charge extraction experiments, the cells were illuminated at open circuit potential for a period of time, then the light was switched off and the voltage was allowed to decay for a defined time period after which the cells were short circuited and the extracted charges were measured. This process was repeated for different light intensities. From Fig. 6.25a, it is observed that the extracted charge (defined as the number of stored charges into the semiconductor at different light intensities) for the three tandem cells are varying. The tandem cell NMA-562_1 has the highest number of extracted charges followed by NMA-508_1 and NMA-504_1. For the n-type DSSCs (Fig. 6.25b), it is observed that for the cell with $[\text{Cu}(\text{ALP1})(\text{dmbpy})]^+$ sensitizer the number of collected charge are increasing rapidly at higher light intensities and exceed the number of charges collected for the cell sensitized with $[\text{Cu}(\text{ALP1})(\text{dmphen})]^+$. That result is in agreement with the results of the JV curves (Fig. 6.17 and Table 6.1) where NMA-564_1 cell has the best performance due to a higher J_{sc} (1.85 vs. 1.23 mA cm⁻² from NMA-564_1 and NMA-565_1 respectively). The low slope of collected

charges at different light intensities observed for the cell NMA.565_1 is indicating a high number of recombination reactions.

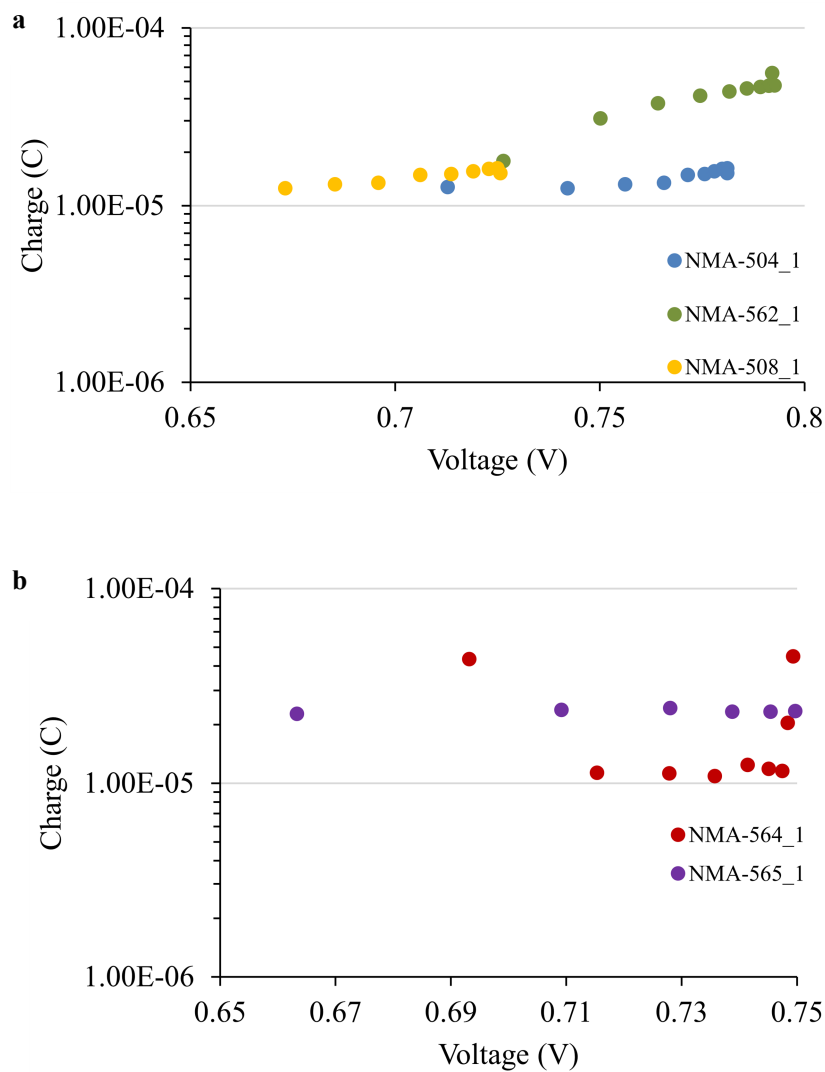


Fig. 6.25: **a.** Charge extraction under short circuit conditions vs. voltage for tandem and **b.** for n-type DSSCs (See Table 6.1). The electrolyte comprised of 0.2 M $[\text{Cu}(\text{dmphen})_2][\text{PF}_6]$, 0.04 M $[\text{Cu}(\text{dmphen})_2][\text{PF}_6]_2$, 0.1 M LiPF_6 , 0.5 M 4-tert-butylpyridine in acetonitrile.

6.2.7 Intensity modulated photovoltage measurements (IMVS)

Intensity modulated photovoltage spectroscopy measurements (IMVS) were performed on the three tandem cells. This measurement is done under open-circuit conditions and the cell is galvanostatically controlled. When the band gap is at its minimum value, and the cell reached steady state at open circuit conditions, the rate of injection of generated photoelectrons is equal with the rate of recombination. Thus, the lifetime time of the electron can be calculated from equation 6.3²²⁴.

$$\tau_n = \frac{1}{2\pi f_{IMVS}} \quad (6.3)$$

where τ_n is the electron lifetime and f_{IMVS} is the maximum frequency point for each applied light intensity on the Bode plot of the IMVS spectra.

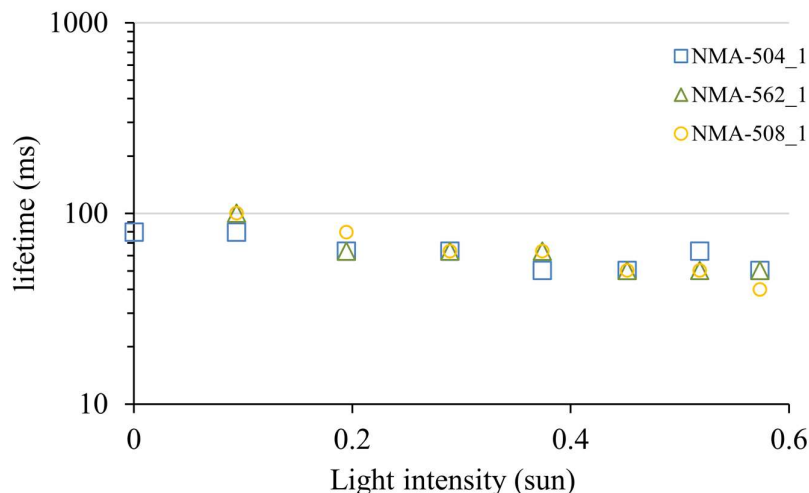


Fig. 6.26: a. IMVS measurements for tandem DSSCs vs. light intensities for tandem (See Table 6.1). The electrolyte comprised of 0.2 M $[\text{Cu}(\text{dmphen})_2][\text{PF}_6]$, 0.04 M $[\text{Cu}(\text{dmphen})_2][\text{PF}_6]_2$, 0.1 M LiPF_6 , 0.5 M 4-tert-butylpyridine in acetonitrile.

The charge lifetime is determined by the rate of recombination reaction with the electrolyte and the dye. It has been found that the lifetime depends inversely on the light intensity, which means that charges move slowly under a low light intensity, but at the same time they also react more slowly with the electrolyte and the dye²²⁶. From Fig. 6.26 it is observed that all three tandem cells have similar lifetimes with NMA-504_1 having the highest lifetime at higher light intensities and NMA-508_1 the lowest, which suggests significant recombination for the latter.

6.2.8 Open circuit voltage decay measurements (OCVD)

The open circuit photovoltage decay (OCVD) is a measurement done under dark conditions and the lifetime at open circuit voltage can be monitored. During this measurement the cell reaches open circuit voltage conditions under illumination, then the light is switched off and the cell is allowed to decay for a defined period of time. During this experiment, the lifetime was calculated using equation 6.4^{137, 138}. Since the measurement is done under dark conditions, only the recombination of the electron with the oxidized redox couple in the electrolyte is monitored and not the recombination path with the anchored dye.

$$\tau_n = -\frac{k_B T}{e} \left(\frac{dV_{OC}}{dt} \right)^{-1} \quad (6.4)$$

As can be seen from Fig. 6.27a, the cell NMA-562_1 has the slowest voltage decay among the series of the tandem cells followed by NMA-508_1 and NMA-504_1 DSSCs. That observation coupled with the higher life time of cell NMA-562_1 from Fig. 6.27b led to the conclusion that NMA-562_1 exhibits fewer recombination processes with the oxidized form of the redox couple. Cell NMA-504_1 exhibits a greater number of recombination processes. From Fig. 6.27c it is observed that the n-type cell, reaches a higher lifetime at small voltages compared with the tandem cell which drops rapidly when the voltage increases. This suggests a high rate of recombination process with the redox couple.

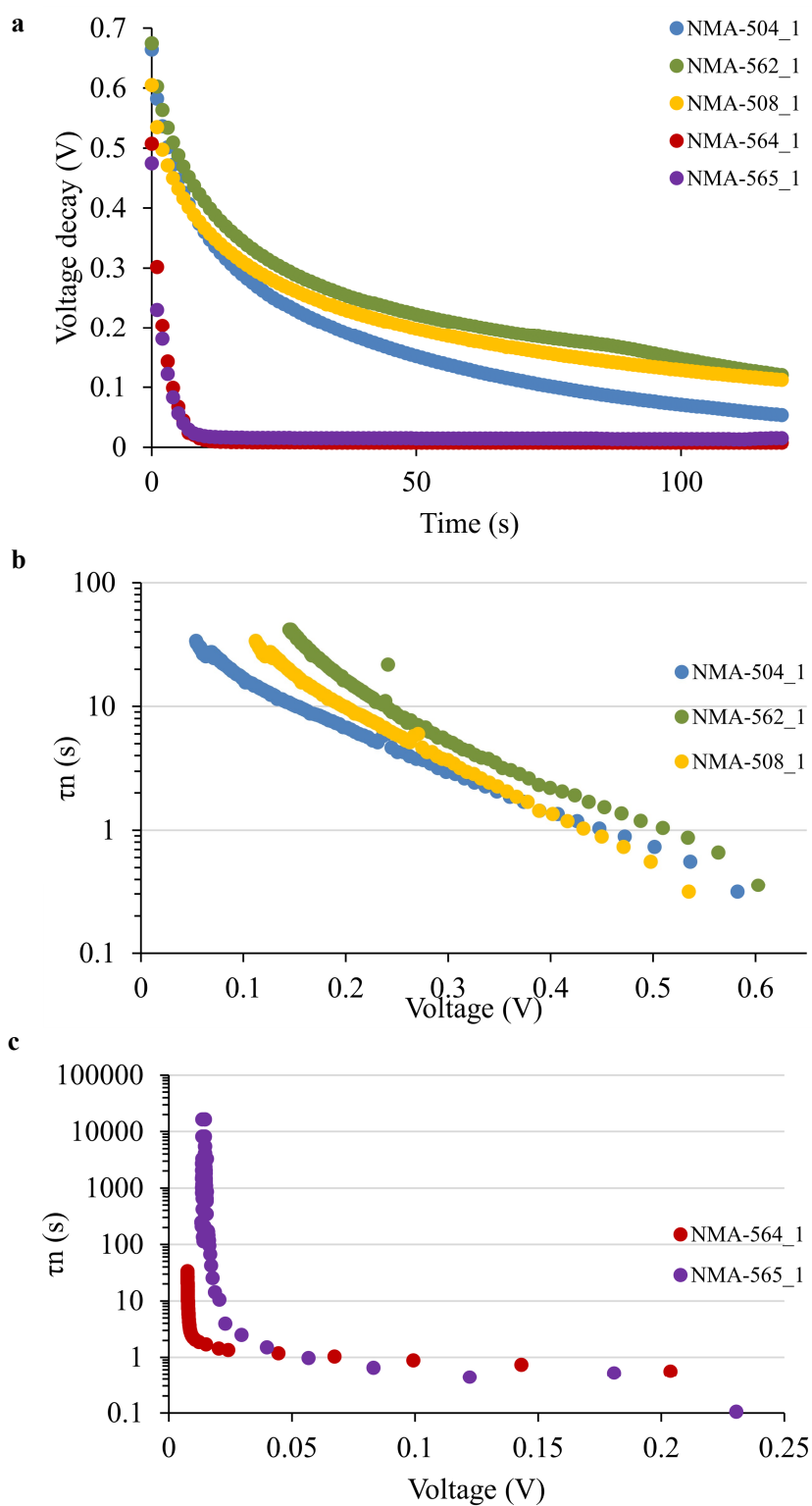


Fig. 6.27: **a.** Voltage decay measurements vs. time for tandem and n-type DSSCs **b.** Voltage decay measurements of lifetime vs. voltage for tandem DSSCs and **c.** for n-type DSSCs (See Table 6.1). The electrolyte comprised of 0.2 M $[\text{Cu}(\text{dmphen})_2][\text{PF}_6]$, 0.04 M $[\text{Cu}(\text{dmphen})_2][\text{PF}_6]_2$, 0.1 M LiPF_6 , 0.5 M 4-tert-butylpyridine in acetonitrile.

6.2.9 Conclusion

It was concluded that the tandem cell NMA-504_1 with WOC53 on the NiO and [Cu(ALP1)(dmbpy)]⁺ on the TiO₂ side outperformed the n-type dye with [Cu(ALP1)(dmbpy)]⁺ with the same electrolyte. The tandem DSSC NMA-504_1 for which the NiO side was sensitized with WOC53 dye had a better performance compared with the tandem DSSC (NMA-562_1) with P1 dye on its NiO side (Fig. 6.17, Table 6.1). From the EQE data presented in Fig. 6.18, it is suggested that the p-type side of the tandem DSSCs contributes to the improvement of the performance of the tandem cells. The EIS data showed that the tandem cell NMA.504_1 had the lowest overall resistance and low Warburg resistance compared to the other DSSCs studied here (Table 6.2). From further electrochemical analysis, it was shown that the tandem NMA-504_1 exhibits a small transport time (Fig. 6.24) and a higher lifetime compared with the other tandem cells (Fig. 6.26). Finally, the recombination process which are occurring on the cell NMA-504_1 and responsible for the electron loss are mainly recombination process with the redox couple.

6.3 Materials and Methods

6.3.1 Fabrication of TiO₂ electrodes

Working TiO₂ electrodes were made from an FTO glass plate (Solaronix TCO22-7, 2.2mm thickness, sheet resistance $\approx 7 \Omega \text{ square}^{-1}$) which was cleaned by sonicating in a 2% surfactant solution in milliQ water (Sonoswiss cleaner, SW-C L2), and rinsed with milliQ water and EtOH. After surface activation in a UV-O₃ system (Model 256-220, Jelight Company Inc) for 18 min, the FTO plates were immersed in aqueous TiCl₄ (40 mmol dm⁻³) at 70 °C for 30 min, and then washed with milliQ water and EtOH. The electrodes were dried in N₂ and a layer of TiO₂ paste (Dyename, DN-GPS-18TS) was screen printed (90T, Serilith AG, Switzerland). The printed plates were kept in an EtOH chamber for 3 min for all printing cycles, to reduce surface irregularities of the printed layer and dried for 6 min at 125 °C on a heating plate. The screen-printing process was repeated 4 times and then a final scattering layer was printed on top (Dyename, DN-GPS-22OS). The electrodes were gradually heated at 75 °C for 30 min, at 135 °C for 15 min, at 325 °C for 5 min, at 375 °C for 5 min, at 450 °C for 15 min and at 500 °C for 15 min. The annealed TiO₂ film was post-treated with 40 mmol dm⁻³ aqueous TiCl₄ solution, rinsed with milliQ water and EtOH and sintered at 500 °C for 30 min. ca. 80 °C and immersed in a 1mM DMSO solution of the anchoring ligand (ALP1) for ca. 20 h. The colourless electrodes were removed from the solution, washed with DMSO and EtOH and dried in a stream of N₂. The electrodes with adsorbed anchoring ligand were immersed in a 0.1 mM CH₂Cl₂ solution of [Cu(dmphen)₂][PF₆] or [Cu(dmbpy)₂][PF₆] for 72 h to give red-orange coloured electrodes. The electrodes were removed from the solution and were washed with CH₂Cl₂ and dried under a stream of N₂.

6.3.2 Synthesis of dyes and electrolyte

The synthesis for the n-type dyes was done by Dr. Annika Büttner and is reported in ref 14. The preparation of the electrolyte was done by Cedric Wobill and is reported in ref. 15. The synthesis of the p-type dye WOC53 was done by Cedric Wobill and has been reported in section 4.3.1.

6.3.3 Fabrication of NiO electrodes

The NiO electrodes were prepared by screen printing as described in section 3.3.8. The NiO electrodes were immersed in the dye bath (0.3 mM for the P1 dye bath in acetonitrile and 0.1 mM for the WOC53 dye bath in ethanol). The electrodes were removed from the dye bath after 16 h. and washed with acetonitrile or ethanol accordingly.

6.3.4 DSSCs assembly

For the n-type and p-type DSSCs a commercial platinum counter electrode was used (Solaronix Test Cell Platinum Electrodes) which was washed with ethanol and heated at 450 °C for 30 min. The DSSCs were assembled by combining working and counter electrode using thermoplast hot-melt sealing foil (Solaronix, Meltonix 1170-25 Series, 60 mm thick) by heating while pressing them together. The electrolyte was introduced by vacuum backfilling and the hole in the counter electrode was sealed by using a hot-melt sealing foil and cover glass.

6.3.5 Sun simulation measurements

The DSSCs were sun-soaked from the cathode side from n-type and tandem DSSCs or the anode side for p-type DSSCs for 20 min at 1 sun irradiation. The cell was then put as such for the n-type and tandem DSSCs or inverted for the p-type DSSCs and measured immediately with a LOT Quantum Design LS811 instrument ($100\text{mW cm}^{-2} = 1$ sun at AM 1.5 and 23 °C) to obtain the current density-voltage (J-V) curves. The instrument software was set to a n-type measurement mode for the n-type DSSCs and the tandem DSSCs or to p-type measurement mode (inverted configuration) for the p-type DSSCs, with 360 ms settling time, and voltage step of 5.2 mV for the n-type and the tandem DSSCs or 1.5mV for the p-type DSSCs. The voltage was scanned from the positive to the negative values for the n-type and tandem DSSCs or from the negative to positive values for the p-type DSSCs.

6.3.6 Electrochemical impedance spectroscopy (EIS)

EIS measurements were carried out on a ModuLab[®] XM PhotoEchem photoelectrochemical measurement system from Solartron Analytical. The impedance was measured around the open-circuit potential of the cell at different light intensities (590 nm) in the frequency range 0.05 Hz to 400 kHz using an amplitude of 10 mV. The impedance data were analysed using ZView[®] software from Scribner Associates Inc. Voltage decay was measured on a Modulab XM electrochemical system.

6.3.7 Intensity modulated photocurrent spectroscopy measurements (IMPS) / Intensity modulated photovoltage measurements (IMVS), Open circuit voltage decay measurements (OCVD) and charge extraction measurements

The IMPS, IMVS and charge extraction measurements were performed using a small perturbation (> 5%) of the steady state illumination. IMPS, IMVS and charge extraction and voltage decay were measured on a Modulab XM electrochemical system.

Chapter 7 Conclusion and Outlook

In conclusion, during this thesis p-type DSSCs were developed and fabricated. A method for the fabrication of the NiO photocathode was established for future generations in our lab. The good performance of the NiO was confirmed after comparing the efficiency of a p-type DSSC fabricated in our lab to the efficiency of a p-type DSSC reported in the bench marking paper of *Gibson and co-workers*⁷⁵. The NiO electrodes were fabricated using the same techniques (screen printing 2 layers of NiO onto an FTO substrate) and sintered at the same temperature (450 °C). The DSSCs fabricated were sensitized with the same commercially available dye (P1) and were back filled with the same composition of electrolyte. Moreover, the valence band of the NiO electrode was calculated using APS and Mott-Schottky equation and compared to the literature values. Furthermore, commercially available NiO electrodes were purchase and used for the fabrication of DSSCs and compared with the home-made NiO electrodes. Multiple tests were performed for the assessment of the photoelectrode such as microscopic techniques (e.g. FIB), spectroscopic techniques (e.g. APS, EDX), electrochemical techniques (e.g. CV) and JV curves in order to assess the efficiency of the fabricated cells.

A cyclometallated Ru(II) dye was synthesised in our group by Cedric Wobill¹⁵² and Felix Brunner¹⁵¹, for the sensitization of the NiO electrode. The fabricated p-type DSSCs exceeded in efficiency of the best performing DSSC previously reported, sensitized with the same type of dye synthesized by *Wu and co-workers*¹⁴⁶ (dye O18) and filled with the same composition of electrolyte. Furthermore, an organic dye (PP1) analogous with the commercially available benchmarking P1 dye was synthesized by Dr. Maximilian Klein¹²⁶. p-Type DSSCs were fabricated with both P1 and PP1 dyes and compared. The results obtained by the JV curves showed in a very similar performances of the DSSCs tested with the DSSC bearing the PP1 having a slightly lower efficiency ($\eta = 0.079\%$ vs 0.069% for DSSCs sensitized with P1 and PP1 respectively). For the assessments of the cells, EIS measurements were performed. For this lattes measurement, valuable information concerning the transport resistances and capacitances of the cells were obtained. Moreover, different electrochemical measurements including open circuit voltage decay or IMVS/IMPS measurements revealed information concerning the recombination time and the lifetime of the DSSCs.

The composition of the electrolyte contained in a p-type DSSC was investigated. The redox couple used was I^-/I_3^- . Different ionic liquids were tested and different organic solvents bearing this redox couple. Furthermore, different additives in the electrolyte composition were tested as well as different dyes as additives in the electrolyte. The performance of the DSSCs were assessed by JV curves and EIS measurements.

A tandem DSSC was for the first time fabricated into our group. This work was the result of a collaboration with Dr. Annika Büttner and Cedric Wobill. For the fabrication of the tandem DSSCs

two different n-type Cu(I) dyes and two different p-type dyes (WOC53 and P1) were used as sensitizers and all the possible combinations of these dyes were used to produce tandem DSSCs. The electrolyte comprising a $\text{Cu}^{+/2+}$ redox couple was inspired from a recent publication of our group ²¹⁸. All the tandem cells outperformed the n-type DSSCs fabricated with the respective n-type dye and same electrolyte that were used as comparison. And after taking into account the results of the EQE, EIS measurements, it was concluded that the p-type side of the tandem cells has a beneficial impact on the performance of the cell.

Future work would include investigating a different p-type semiconductor with more favourable valence band energy in order to increase the V_{OC} of the cell. Screening over different redox couple for the electrolyte will also enable to increase the V_{OC} of the cell. Moreover, more work should be done on the fabrication of tandem DSSCs. Different combination of dyes (n- and p-type dyes) with matching J_{SC} should be tested and different electrolytes should be used in order to optimize the charge transfer process through the electrolyte.

Chapter 8 References

- ¹ All fossil fuel reserve and consumption data from CIA World Factbook, 2018.
- ² World population prospects, Key findings and advance table, United Nations, New York, 2017.
- ³ NASA's Goddard institute for space Studies (GISS).
- ⁴ Intergovernmental panel on Climate Change (IPCC) of global warming of 1.5 °C.
- ⁵ C.-F. Schleussner, T. K. Lissner, E. M. Fischer, J. Wohland, M. Perrette, A. Golly, J. Rogelj, K. Childers, J. Schewe, K. Frieler, M. Mengel, W. Hare, M. Schaeffer, *Earth Syst. Dynam.*, 2016, **7**, 327.
- ⁶ L. Zhao, *Nature climate change*, 2018, **8**, 1034.
- ⁷ R. Perez, M. Perez, *The International Energy Agency SHC Programme Solar Update*, 2009, **50**, 2 and references therein.
- ⁸ A. Carella, F. Borbone, R. Centore, *Frontiers in Chem.*, 2018, **6**, 481.
- ⁹ R. R. King, D C. Law, K. M. Edmondson, C. M. Fetzer, G. S. Kinsey, H. Yoon, D. D. Krut, J. H. Ermer, R. A. Sherif, N. H. Karam, *Adv.in Optoelectr.*, 2007, **8**, 1.
- ¹⁰ B. O'Regan, M. Grätzel, *Nature*, 1991, **353**, 737.
- ¹¹ M. Grätzel, *Acc. Chem. Res.*, 2009, **11**, 1788.
- ¹² M. Ye, X. Wen, M. Wang, J. Iocozzia, N. Zhang, C. Lin, Z. Lin, *Mater. Today*, 2014, **3**, 155.
- ¹³ S. Hwangbo, J.-T. Kim. K.-S. Hwang, *Materials Science-Poland*, 2015, **33**, 237.
- ¹⁴ S. G. Hashmi, M. Ozkan, J. Halme, K. D. Misic, S. M. Zakeeruddin, J. Paltakari, J. Paltakari, M. Grätzel, P. D. Lund, *Nano Energy*, 2015, **17**, 206.
- ¹⁵ P. Mariani, L. Vesce, A. Di Carlo, *Semicond. Sci. Technol.*, 2015, **30**, 104003.
- ¹⁶ G. G. Sonai, A. Tiihonen, K. Miettunen, P. D. Lund, A. F. Nogueira, *J. Phys. Chem. C*, 2017, **121**, 17577.
- ¹⁷ Gcell, <https://gcell.com/gcell-products/custom-solar-cell>
- ¹⁸ H. Yang, C. Yu, Q. Song, Y. Xia, F. Li, Z. Chen, X. Li, T. Yi, C. Huang, *C. Chem. Mater.*, 2006, **18**, 5173
- ¹⁹ M. Berginc, U. Opara Krašovec, M. Jankovec, M. Topič, *Sol. Energy Mater. Sol. Cells*, 2007, **91**, 821.
- ²⁰ D. Zhang, T. Yoshida, T. Oekermann, K. Furuta, H. Minoura, H. *Adv. Funct. Mater.*, 2006, **16**, 1228.
- ²¹ M. J. Yun, S. I. Cha, S. H. Seo, D. Y. Lee, *Sci. Rap.*, 2015, **4**, 5322.
- ²² B. Wang, L. L. Kerr, *Sol. Energy Mater. Sol. Cells*, 2011, **95**, 2531.
- ²³ Gran View Research, Report ID:978-1-68038-644-8, "Dye Sensitized Solar Cell Market Analysis by Application (Portable Charging, BIPV/BAPV, Embedded Electronics, Outdoor Advertising, Automotive (AIPV)) And Segment Forecasts To 2022"
- ²⁴ J. He, H. Lindström, A. Hagfeldt, S.-E. Lindquist, *J. Phys. Chem. B*, 1999, **103**, 8940.

-
- ²⁵ F. Odobel, Y. Pellegrin, *J. Phys. Chem. Lett.*, 2013, **4**, 2551.
- ²⁶ F. Odobel, L. Le Pleux, Y. Pellegrin, E. Blart, *Acc. Chem. Res.*, 2010, **8**, 1063.
- ²⁷ M. Pazoki, U. B. Cappel, E. M. J. Johansson, A. Hagfeldt, G. Boschloo, *Energy Environ. Sci.*, 2017, **10**, 672.
- ²⁸ Z. Huang, G. Natu, Z. Ji, M. He, M. Yu, Y. Wu, *J. Phys. Chem. C*, 2012, **116**, 26239.
- ²⁹ C. Ye, X. Zhou, Dennis Pu, J. Stutz, James Festa, M. Spolaor, C. Tsai, C. Cantrell, R. L. Mauldin, T. Campos, A. Weinheimer, R. S. Hornbrook, E. C. Apel, A. Guenther, L. Kaser, B. Yuan, T. Karl, J. Haggerty, S. Hall, K. Ullmann, J. N. Smith, J. Ortega, C. Knote, *Nature*, 2016, **532**, 489
- ³⁰ N.J. Cherepy, G. P. Smestad, M. Grätzel, J. Z. Zhang, *J. Phys. Chem. B*, 1997, **101**, 9342.
- ³¹ M. Grätzel, *Pure Appl. Chem.*, 2001, **73**, 459.
- ³² K. Hara, H Arakawa, *Dye-sensitized Solar Cells*, In: *Handbook of Photovoltaic Science and Engineering*, A. Luque and S. Hegedus, (Ed.), Chapter 15, pp. 663-700, John Wiley & Sons, Ltd, ISBN: 0-471-49196-9. 2003.
- ³³ H. Tian, L. Liu, B. Liu, S. Yuan, X. Wang, Y. Wang, T. Yu, Z. Zou, *J. Phys. D: Appl. Phys.*, 2009, **42**, 45109.
- ³⁴ J. Halme, P. Vahermaa, K. Miettunen, P. Lund, *Adv. Mater.*, 2010, **22**, E210.
- ³⁵ M. H. Li, J. H. Yum, S. J. Moon, P. Chen, *Energies*, 2016, **9**, 331.
- ³⁶ H. Kawazoe, M. Yasukawa, H. Hyodo, M. Kurita, H. Yanagi, H. Hosono, *Nature*, 1997, **389**, 939.
- ³⁷ A. Kudo, H. Yanagi, H. Hosono, H. Kawazoe, *Appl. Phys. Lett.*, 1998, **73**, 220.
- ³⁸ M. Yu, G. Natu, Z. Ji, Y. Wu, *J. Phys. Chem. Lett.*, 2012, **3**, 1074.
- ³⁹ S. Powar, Q. Wu, M. Weidener, A. Nattestad, Z. Hu, A. Mishra, P. Bäuerle, L. Spiccia, Y. B. Cheng, U. Bach, *Energy Environ. Sci.*, 2012, **5**, 8896.
- ⁴⁰ S. Sumikura, S. Mori, S. Shimizu, H. Usami, E. Suzuki, *J. of Photochem. and Photobio. A: Chem.*, 2008, **199**, 7.
- ⁴¹ K. Ohno, M. Tanaka, J. Takeda, Y. Kawazoe, *Nano- and Micromaterials*, Springer Berlin Heidelberg, 2008.
- ⁴² L. D'Amario, G. Boschloo, A. Hagfeldt, L. Hammarström, *J. Phys. Chem. C*, 2014, **118**, 19556.
- ⁴³ L. Wei, L. Jiang, S. Yuan, X. Ren, Y. Zhao, Z. Wang, M. Zhang, L. Shi, D. Li, *Electrochimica Acta*, 2016, **188**, 309.
- ⁴⁴ G. Natu, P. Hasin, Z. Huang, Z. Ji, M. He, Y. Wu, *ACS Appl. Mater. Interfaces*, 2012, **4**, 5922.
- ⁴⁵ J. Deng, M. Mortazavi, N. V. Medhekar, J. Z. Liu, *J. of Applied Physics*, 2012, **112**, 123703.
- ⁴⁶ M. Zannotti, C. J. Wood, G. H. Summers, L. A. Stevens, M. R. Hall, C. E. Snape, R. Giovanetti, E. A. Gibson, *ACS Appl. Mater. Interfaces*, 2015, **7**, 24556.
- ⁴⁷ H. Zhu, A. Hagfeldt, G. Boschloo, *J. Phys. Chem. C*, 2007, **111**, 17455.
- ⁴⁸ L. Peter, *J. of Electroanalytical Chem.*, 2007, **599**, 233.

-
- ⁴⁹ S. Mori, S. Fukuda, S. Sumikura, Y. Takeda, Y. Tamaki, E. Suzuki, T. Abe, *J. Phys. Chem. C*, 2008, **112**, 16134.
- ⁵⁰ D. Adler, J.J. Feinleib, *J. Physical Review B*, 1970, **2**, 3112.
- ⁵¹ N. C. S. Selvam, J. J. Vijaya, L. J. Kennedy, *J. of Colloid and Interface Science*, 2013, **407**, 215.
- ⁵² M. Utriainen, M. Kröger-Laukkanen, L.-S. Johansson, L. Niinistö, *Applied Surface Science*, 2000, **157**, 151.
- ⁵³ P. Ho, L. Q. Bao, K. S. Ahn, R. Cheruku, J. H. Kim, *Synthetic Metals*, 2016, **217**, 314.
- ⁵⁴ Y. Farré, M. Raissi, A. Fihey, Y. Pellegrin, E. Blart, D. Jacquemin, F. Odobel, *ChemSusChem*, 2017, **10**, 2618.
- ⁵⁵ J. He, H. Lindström, A. Hagfeldt, S. E. Lindquist, *J. Phys. Chem. B*, 1999, **103**, 8940.
- ⁵⁶ P. Qin, H. Zhu, T. Edvinsson, G. Boschloo, A. Hagfeldt, L. Sun, *J. Am. Chem. Soc.*, 2008, **130**, 8570.
- ⁵⁷ P. Qin, M. Linder, T. Brinck, G. Boschloo, A. Hagfeldt, L. Sun, *Adv. Mater.*, 2009, **21**, 2993.
- ⁵⁸ C. J. Flynn, E. E. Oh, S. M. McCullough, R. W. Call, C. L. Donley, R. Lopez, J. F. Cahoon, *J. Phys. Chem. C*, 2014, **118**, 14177.
- ⁵⁹ L. Lepleux, B. Chavillon, Y. Pellegrin, E. Blart, L. Cario, S. Jobic, F. Odobel, *Inorg. Chem.*, 2009, **48**, 8245.
- ⁶⁰ Y. Qu, W. Zhou, X. Miao, Y. Li, L. Jiang, K. Pan, G. Tian, Z. Ren, G. Wang, H. Fu, *Chem. Asian J.*, 2013, **8**, 3085.
- ⁶¹ A. Nakasa, H. Usami, S. Sumikura, S. Hasegawa, T. Koyama, E. Suzuki, *Chem. Lett.*, 2005, **34**, 500.
- ⁶² M. Awais, D. D. Dowling, M. Rahman, J. G. Vos, F. Decker, D. Dini, *J. Appl. Electrochem.*, 2013, **43**
- ⁶³ S. Sheehan, G. Naponiello, F. Odobel, D. P. Dowling, A. Di Carlo, D. Dini, *J. Solid State Electrochem.*, 2015, **19**, 975.
- ⁶⁴ P. S. Kumar, J. Sundaramurthy, S. Sundarajan, V. J. Babu, G. Singh, S. I. Allakhverdiev, S. Ramakrishna, *Energy Environ. Sci.*, 2014, **7**, 3192.
- ⁶⁵ L. Berkat, L. Cattin, A. Reguig, M. Regragui, J.C. Bernède, *Mater. Chem. and Phys.*, 2005, **89**, 11.
- ⁶⁶ M. S. Wu, M. J. Wang, *Chem. Commun.*, 2010, **46**, 6968.
- ⁶⁷ M. Tachiki, T. Hosomi, T. Kobayashi, *Jpn. J. Appl. Phys.*, 2000, **39**, 1817.
- ⁶⁸ E. Fujii, A. Tomozawa, S. Fujii, H. Torii, M. Hattori, R. Takayama, *Jpn. J. Appl. Phys.*, 1993, **32**, 1448.
- ⁶⁹ S. Ito, P. Chen, P. Comte, M. K. Nazeeruddin, P. Liska, P. Péchy, M. Grätzel, *Prog. Photovolt: Res. Appl.*, 2007, **15**, 603
- ⁷⁰ X. L. Zhang, Z. Zhang, D. Chen, P. Bäuerle, U. Bach, Y. B. Cheng, *Chem. Commun.*, 2012, **48**, 9885.

-
- ⁷¹ D. Dini, Y. Halpin, J. G. Vos, E. A. Gibson, *Coordination Chemistry Reviews*, 2015, **304**, 179
- ⁷² B. L. Li, E. A. Gibson, P. Qin, G. Boschloo, M. Gorlov, A. Hagfeldt, L. Sun, *Adv. Mater.*, 2010, **22**, 1759.
- ⁷³ M. Bonomo, G. Naponiello, A. Di Carlo, D. Dini, *J. of Mater. Sci. & Nanotech.*, 2016, **4**, 201.
- ⁷⁴ B. Bozic-Weber, S. Y. Brauchli, E. C. Constable, S. O. Furer, C. E. Housecroft, F. J. Malzner, I. A. Wright, J. A. Zampese, *Dalton Trans.*, 2013, **42**, 12293.
- ⁷⁵ C. J. Wood, G. H. Summers, C. A. Clark, N. Kaeffer, M. Braeutigam, L. R. Carbone, L. D'Amario, K. Fan, Y. Farré, S. Narbey, F. Oswald, L. A. Stevens, C. D. J. Parmenter, M. W. Fay, A. La Torre, C. E. Snape, B. Dietzek, D. Dini, L. Hammarström, Y. Pellegrin, F. Odobel, L. Sun, V. Artero, E. A. Gibson, *Phys.Chem.Chem.Phys.*, 2016, **18**, 10727.
- ⁷⁶ F. Odobel, Y. Pellegrin, E. A. Gibson, A. Hagfeldt, A. L. Smeigh, L. Hammarström, *Coordination Chemistry Reviews*, 2012, **256**, 2414.
- ⁷⁷ E. A. Gibson, M Awais, D. Dini, D. P. Dowling, M. T. Pryce, J. G. Vos, G. Boschloo, A. Hagfeldt, *Phys. Chem. Chem. Phys.*, 2013, **15**, 2411.
- ⁷⁸ K. Darowicki, K. Andrearczyk, P.Slepski, A. Sierczynska, *G. Lota, K. Fic, K. Lota, Int. J. Electrochem. Sci.*, 2014, **9**,1702
- ⁷⁹ G. Boschloo, A. Hagfeldt, *J. Phys. Chem. B*, 2001, **105**, 3039.
- ⁸⁰ C. E. Housecroft, A. G. Sharpe, *Inorganic Chemistry*, 5th edn, Pearson, Harlow, 2018.
- ⁸¹ H. A. Becerril, J. Mao, Z. Liu, R. M. Stoltenberg, Z. Bao, Y. Chen, *ACS Nano*, 2008, **2**, 463.
- ⁸² X. Li, Y. Zhu, W. Cai, M. Borysiak, B. Han, D. Chen, R. D. Piner, L. Colombo, R. S. Ruoff, *Nano Lett.*, 2009, **9**, 4359.
- ⁸³ A. K. Geim, K. S. Novoselov, *Nature Mater.*, 2007, **6**, 183.
- ⁸⁴ H. Yang, G. H. Guai, C. Guo, Q. Song, S. P. Jiang, Y. Wang, W. Zhang, C. M. Li, *J. Phys. Chem. C*, 2011, **115**, 12209.
- ⁸⁵ H. Ding, S. Zhang, J. T. Chen, X. P. Hu, Z. F. Du, Y. X. Qiu, D. L. Zhao, *Thin Solid Films*, 2015, **584**, 29.
- ⁸⁶ A. Kahn, *Mater. Horiz.*, 2016, **3**, 7.
- ⁸⁷ I. D. Baikie, A. C. Grain, J. Sutherland, J. Law, *Applied surface science*, 2014, **323**, 45.
- ⁸⁸ I. D. Baikie, P. J. Estrup, *Review of Scientific Instruments*, 1998, **69**, 3902.
- ⁸⁹ E. Thimsen, A. B. F. Martinson, J. W. Elam, M. J. Pellin, *J. Phys. Chem. C*, 2012, **116**, 16830.
- ⁹⁰ K. Rajeshwar, *Fundamental of Semiconductors Electrochemistry and Photoelectrochemistry*, The University of Texas at Arlington, 2007
- ⁹¹ S. M. Sze, K. K. Ng, *Physics of Semiconductor Devices*, 3rd edition Wiley-Interscience, Hoboken, New Jersey, 2007.
- ⁹² S. C. Choi, K. Koumoto, H. J. Yanagida, *Mater. Sci.*, 1986, **21**, 1947.
- ⁹³ R.H. Fowler, *Phys. Rev.*, 1931, **38**, 45.

-
- ⁹⁴ J. R. Harwell, T. K. Baikie, I. D. Baikie, J. L. Payne, C. Ni J. T. S. Irvine, G. A. Turnbull, I. D. W. Samuel, *Phys.Chem.Chem.Phys.*, 2016, **18**, 19738.
- ⁹⁵ T. Daeneke, Z. Yu, G. P. Lee, D. Fu, N. W. Duffy, S. Makuta, Y. Tachibana, L. Spiccia, A. Mishra, P. Bäuerle, U. Bach, *Adv. Energy Mater.*, 2015, **5**, 1401387.
- ⁹⁶ J. Tauc, R. Grigorovici, and A. Vancu, *Phys. Status Solid*, **15**, 1966, 627.
- ⁹⁷ E. A. Davis and N. F. Mott, *Philos. Mag.*, 1970, **22**, 903.
- ⁹⁸ N. F. Mott and E. A. Davis, *Electronic Processes in Non-Crystalline Materials*, 2nd edn, Clarendon Press, Oxford, New York, 1979.
- ⁹⁹ B. D. Vriezicke, S. Patel, B. E. Davis, D. P. Birnie, *Phys. Status Solidi B*, 2015, **252**, No. 8, 1700.
- ¹⁰⁰ A. Venter, J. R. Botha, *S Afr J Sci*, 2011, **107**, 1.
- ¹⁰¹ P. Kubelka, F. Munk, *Z. Tech. Phys.*, 1931, **12**, 593.
- ¹⁰² K. Gelderman, L. Lee, S. W. Donne, *Journal of Chemical Education*, 2007 **84**, 4.
- ¹⁰³ C. Xin, Y. Wang, S. Zhang, L. Xu, Y. Yu, H. Xiang, W. Wu, J. Hua, *Phys. Status Solidi RRL*, 2017, **11**, 1700258.
- ¹⁰⁴ Q. Liu, L. Wei, S. Yuan, X. Ren, Y. Zhao, Z. Wang, M. Zhang, L. Shi, D. Li, A. Li, *RSC Adv.*, 2015, **5**, 71778.
- ¹⁰⁵ K. V. Rao, A. J., Smakula, *Appl. Phys.*, 1965, **36**, 2031.
- ¹⁰⁶ A. Mani, C. Huisman, A. Goossens, J. Schoonman, *J. Phys. Chem. B*, 2008, **112**, 10086.
- ¹⁰⁷ Adrian W. Bott, *Electrochemistry of Semiconductors, Current Separations*, 1998, **17**, 3.
- ¹⁰⁸ S. Powar, T. Daeneke, M. T. Ma, D. Fu, N. W. Duffy, G. Götz, M. Weideler, A. Mishra, P. Bäuerle, L. Spiccia, U. Bach, *Angew. Chem. Int. Ed.*, 2013, **52**, 602.
- ¹⁰⁹ G. Boschloo, A. Hagfeldt, *Acc. Chem. Res.*, 2009, **42**, 1819.
- ¹¹⁰ G. Boschloo, E. A. Gibson, A. Hagfeldt, *J. Phys. Chem. Lett.*, 2011, **2**, 3016 and references therein.
- ¹¹¹ N. Marinakis, M. Willgert, E. C. Constable, C. E. Housecroft, *Sustainable Energy Fuels*, 2017, **1**, 626.
- ¹¹² J. I. Goldstein, D.E. Newbury, D.C. Joy, C.E. Lyman, P. Echlin, E. Lifshin, L. Sawyer, J.R. Michael, *Scanning Electron Microscopy and X-ray Microanalysis*, 3rd edn, Plenum Press, New York, 2003.
- ¹¹³ E. Abrahart, *Dyes and their Intermediates*, pp. 1-12, New York: Chemical Publishing, 1977.
- ¹¹⁴ P. Qin, J. Wiberg, E. A. Gibson, M. Linder, L. Li, T. Brinck, A. Hagfeldt, B. Albinsson, L. Sun, *J. Phys. Chem. C*, 2010, **114**, 4738.
- ¹¹⁵ Z. Ji, G. Natu, Z. Huang, Y. Wu, *Energy Environ. Sci.*, 2011, **4**, 2818.
- ¹¹⁶ Y.-S. Yen, W.-T. Chen, C.-Y. Hsu, H. -H. Chou, J. T. Lin, M.-C. P. Yeh, *Org. Lett.*, 2011, **13**, 4930.
- ¹¹⁷ R. Brisse, C. Praveen, V. Maffei, T. Bourgeteau, D. Tondelier, T. Berthelot, B. Geffroy, T. Gustavsson, J. M. Raimundo, B. Jusselme, *Sustainable Energy Fuels*, 2018, **2**, 648.

-
- ¹¹⁸ A. Morandeira, J. Fortage, T. Edvinsson, L. Le Pleux, E. Blart, G. Boschloo, A. Hagfeldt, L. Hammarström, F. Odobel, *J. Phys. Chem. C*, 2008, **112**, 1721.
- ¹¹⁹ L. Le Pleux, A. L. Smeigh, E. Gibson, Y. Pellegrin, E. Blart, G. Boschloo, A. Hagfeldt, L. Hammarström, F. Odobel, *Energy Environ. Sci.*, 2011, **4**, 2075.
- ¹²⁰ E.A. Gibson, A.L. Smeigh, L. Le Pleux, L. Hammarström, F. Odobel, G. Boschloo, A. Hagfeldt, *J. Phys. Chem. C*, 2011, **115**, 9772.
- ¹²¹ X. L. Zhang, Z. Zhang, D. Chen, P. Bäuerle, U. Bach, Y.-B. Cheng, *Chem. Commun*, 2012, **48**, 9885.
- ¹²² L. Favereau, J. Warnan, Y. Pellegrin, E. Blart, M. Boujtita, D. Jacquemin, F. Odobel, *Chem. Commun.*, 2013, **49**, 8018.
- ¹²³ L. Zhang, L. Favereau, Y. Farre, E. Mijangos, Y. Pellegrin, E. Blart, F. Odobel, L. Hammarström, *Phys. Chem. Chem. Phys.*, 2016, **18**, 18515.
- ¹²⁴ B. Bozic-Weber, E. C. Constable, C. E. Housecroft, P. Kopecky, M. Neuburger, J. A. Zampese, *Dalton Trans*, 2011, **40**, 12584.
- ¹²⁵ B. Bozic-Weber, S. Y. Brauchli, E. C. Constable, S. O. Furer, C.E. Housecroft, I. A. Wright, *Phys Chem Chem Phys*, 2013, **15**, 4500.
- ¹²⁶ Y. M. Klein, N. Marinakis, E. C. Constable, C. E. Housecroft, *Crystals*, 2018, **8**, 389.
- ¹²⁷ J. Halme, G. Boschloo, A. Hagfeldt, P. Lund, *J. Phys. Chem. C*, 2008, **112**, 5623.
- ¹²⁸ X. Xu, J. Cui, J. Han, J. Zhang, Y. Zhang, L. Luan, G. Alemu, Z. Wang, Y. Shen, D. Xiong, W. Chen, Z. Wei, S. Yang, B. Hu, Y. Cheng, M. Wang, *Scientific Reports*, 2014, **4**, 3961.
- ¹²⁹ J. Bisquert, G. Garcia-Belmonte, F. Fabregat-Santiago, A. Compte, *Electrochem. Commun.*, 1999, **1**, 429.
- ¹³⁰ J. Bisquert, *J. Electroanal. Chem.*, 2010, **646**, 43.
- ¹³¹ F. Fabregat-Santiago, G. Garcia-Belmonte, I. Mora-Seró, J. Bisquert, *Phys. Chem. Chem. Phys.*, 2011, **13**, 9083.
- ¹³² F. Fabregat-Santiago, J. Bisquert, E. Palomares, L. Otero, D. Kuang, S. M. Zakeeruddin, M. Grätzel, *J. Phys. Chem. C*, 2007, **111**, 6550.
- ¹³³ P. Córdoba-Torres, *Electrochim. Acta*, 2017, **225**, 592.
- ¹³⁴ C. Cramer, S. Brunklaus, Y. Gao, K. Funke, *J. Phys.: Condens. Matter*, 2003, **15**, S2309.
- ¹³⁵ P. Ho, L.Q. Bao, K.S. Ahn, R. Cheruku, J.H. Kim, *Synth. Met.*, 2016, **217**, 314.
- ¹³⁶ M.R. Shoar Abouzari, F. Berkemeier, G. Schmitz, D. Wilmer, *Solid State Ionics*, 2009, **180**, 922.
- ¹³⁷ J. Bisquert, A. Zaban, M. Greenshtein, I. Mora-Seró, *J. Am. Chem. Soc.*, 2004, **126**, 13550.
- ¹³⁸ A. Zaban, M. Greenshtein, J. Bisquert, *ChemPhysChem*, 2003, **4**, 859.
- ¹³⁹ H. K. Dunn, P.-O. Westin, D. R. Staff, L. M. Peter, A.B. Walker, G. Boschloo, A. Hagfeldt, *J. Phys. Chem. C*, 2011, **115**, 13932.
- ¹⁴⁰ G. Schlichthörl, S. Y. Huang, J. Sprague, A. J. Frank, *J. Phys. Chem. B*, 1997, **101**, 8141.

-
- ¹⁴¹ L. Dloczik, O. Ileperuma, I. Lauermann, L. M. Peter, E. A. Ponomarev, G. Redmond, N. J. Shaw, I. Uhlendorf, *J. Phys. Chem. B*, 1997, **101**, 10281.
- ¹⁴² H. Zhu, A. Hagfeldt, G. Boschloo, *J. Phys. Chem. C*, 2007, **111**, 17455.
- ¹⁴³ L. Peter, *J. Electroanal. Chem.*, 2007, **599**, 233.
- ¹⁴⁴ Z. Ji, G. Natu, Z. Huang, O. Kokhan, X. Zhang Y. Wu, *J. Phys. Chem. C*, 2012, **116**, 16854.
- ¹⁴⁵ Z. Ji, Y. Wu, *J. Phys. Chem. C*, 2013, **117**, 18315.
- ¹⁴⁶ M. He, Z. Ji, Z. Huang, Y. Wu, *J. Phys. Chem. C*, 2014, **118**, 16518.
- ¹⁴⁷ S. Lyu, Y. Farré, L. Ducasse, Y. Pellegrin, T. Toupance, C. Olivier, F. Odobel, *RSC Adv.*, 2016, **6**, 19928.
- ¹⁴⁸ M. Gennari, F. Légalité, L. Zhang, Y. Pellegrin, E. Blart, J. Fortage, A. M. Brown, A. Deronzier, M.-N. Collomb, M. Boujtita, D. Jacquemin, L. Hammarström, F. Odobel, *J Phys Chem Lett*, 2014, **5**, 2254.
- ¹⁴⁹ A. Sinopoli, C. J. Wood, E. A. Gibson, P. I. P. Elliott, *Dyes and Pigments*, 2017, **140**, 269.
- ¹⁵⁰ J. Lu, Z. Liu, N. Pai, L. Jiang, U. Bach, A. N. Simonov, Y.-B. Cheng, L. Spiccia, *ChemPlusChem*, 2018, **83**, 711.
- ¹⁵¹ F. Brunner, N. Marinakis, C. Wobill, M. Willgert, C. D. Ertl, T. Kosmalski, M. Neuburger, B. Bozic-Weber, T. Glatzel, E. C. Constable, C. E. Housecroft, *J. Mater. Chem. C*, 2016, **4**, 9823.
- ¹⁵² N. Marinakis, C. Wobill, E. C. Constable, C. E. Housecroft, *Polyhedron*, 2018, **140**, 122.
- ¹⁵³ Y. Pellegrin, L. Le Pleux, E. Blart, A. Renaud, B. Chavillon, N. Szuwarski, M. Boujtita, L. Cario, S. Jovic, D. Jacquemin, F. Odobel, *J. Photochem. Photobiol. A*, 2011, **219**, 235.
- ¹⁵⁴ Z. Huang, G. Natu, Z. Ji, P. Hasin, Y. Wu, *J. Phys. Chem. C*, 2011, **115**, 25109.
- ¹⁵⁵ L. D'Amario, G. Boschloo, A. Hangfeldt, L. Hammarström, *J. Phys. Chem. C*, 2014, **118**, 19556.
- ¹⁵⁶ Z. Yu, N. Vlachopoulos, M. Gorlov, L. Kloo, *Dalton Trans.*, 2011, **40**, 10289.
- ¹⁵⁷ M. Wang, C. Grätzel, S. M. Zakeeruddin, M. Grätzel, *Energy Environ. Sci.*, 2012, **5**, 9394.
- ¹⁵⁸ T. W. Hamann, J. W. Ondersma, *Energy Environ. Sci.*, 2011, **4**, 370.
- ¹⁵⁹ Y.-S. Yen, H. H. Chou, Y. C. Chen, C. Y. Hsu, J. T. Lin, *J. Mater. Chem.*, 2012, **22**, 8734.
- ¹⁶⁰ M. C. Buzzeo, C. Hardacre, R. G. Compton, *ChemPhysChem.*, 2006, **7**, 176.
- ¹⁶¹ T. Welton, *Coordin. Chem. Rev.*, 2004, **248**, 2459.
- ¹⁶² C. T. Li, L. Y. Chang, M. S. Fan, P. Y. Chen, J. J. Lin, K. C. Ho, C. P. Lee, *New Class of Ionic Liquids for Dye-Sensitized Solar Cells*, Chapter 24, pp. 655, InTech, 2015.
- ¹⁶³ N. Papageorgiou, Y. Athanassov, M. Armand, P. Bonhôte, H. Pettersson, A. Azam, M. Grätzel, *J. Electrochem. Soc.*, 1996, **43**, 3099.
- ¹⁶⁴ P. Wang, S. M. Zakeeruddin, R. Humphry-Baker, M. Grätzel, *Chem. Mater.*, 2004, **16**, 2694.
- ¹⁶⁵ J. Wu, Z. Lan, J. Lin, M. Huang, Y. Huang, L. Fan, G. Luo, *Chem. Rev.*, 2015, **115**, 2136.
- ¹⁶⁶ T. Kato, A. Okazaki, S. Hayase, *J. Photochem. Photobiol. A*, 2006, **179**, 42.

-
- ¹⁶⁷ K. Tennakone, G. Kumara, A. R. Kumarasinghe, K. G. U. Wijayantha, P. M. Sirimanne, *Semicond. Sci. Technol.*, 1995, **10**, 1689.
- ¹⁶⁸ G. Kumara, A. Konno, G. K. R. Senadeera, P. V. V. Jayaweera, D. De Silva, K. Tennakone, *Sol. Energy Mater. Sol. Cells*, 2001, **69**, 195.
- ¹⁶⁹ B. O'Regan, D.T. Schwartz, *Chem. Mater.*, 1998, **10**, 1501.
- ¹⁷⁰ K. Tennakone, G. K. R. Senadeera, D. De Silva, I.R.M. Kottegoda, *Appl. Phys. Lett.*, 2000, **77**, 2367.
- ¹⁷¹ V. Perera, K. Tennakone, K. *Sol. Energy Mater. Sol. Cells*, 2003, **79**, 249.
- ¹⁷² U. Bach, D. Lupo, P. Comte, J. E. Moser, F. Weissörtel, J. Salbeck, H. Spreitzer, M. Grätzel, *Nature*, 1998, **395**, 583.
- ¹⁷³ K. Murakoshi, R. Kogure, Y. Wada, S. Yanagida, *Chem. Lett.* 1997, **26**, 471.
- ¹⁷⁴ S. Günes, H. Neugebauer, N. S. Sariciftci, *Chem. Rev.* 2007, **107**, 1324.
- ¹⁷⁵ A. Mathew, V. Anand, G. M. Rao, N. Munichandraiah, *Electrochimica Acta*, 2013, **87**, 92.
- ¹⁷⁶ I.V. Nelson, T. Iwamoto, *J. Electroanal. Chem.*, 1964, **7**, 218.
- ¹⁷⁷ E. A. Gibson, L. Le Pleux, J. Fortage, Y. Pellegrin, E. Blart, F. Odobel, A. Hagfeldt, G. Boschloo, *Langmuir*, 2012, **28**, 6485.
- ¹⁷⁸ A. Morandeira, G. Boschloo, A. Hagfeldt, L. Hammarström, *J. Phys. Chem. B*, 2005, **109**, 19403.
- ¹⁷⁹ I. Montanari, J. Nelson, J. R. Durrant, *J. Phys. Chem. B*, 2002, **106**, 12203.
- ¹⁸⁰ C. Nasr, S. Hotchandani, P. Kamat, *J. Phys. Chem. B*, 1998, **102**, 4944.
- ¹⁸¹ V. A. Macagno, M. C. Giordano, A. J. Arvia, *Electrochim. Acta*, 196,9, **14**, 335.
- ¹⁸² I. R. Perera, T. Daeneke, S. Makuta, Z. Yu, Y. Tachibana, A. Mishra, P. Bäuerle, C. A. Ohlin, U. Bach, L. Spiccia, *Angew. Chem. Int. Ed.*, 2015, **54**, 3758.
- ¹⁸³ Z. Yu, I. R Perera, T. Daeneke, S. Makuta, Y. Tachibana, J. J Jasieniak, A. Mishra, P. Bäuerle, L. Spiccia, U. Bach, *NPG Asia Materials*, 2016, **8**, 305.
- ¹⁸⁴ A. Hagfeldt, G. Boschloo, L. Sun, L. Kloo, H. Pettersson, *Chem. Rev.*, **2010**, 110, 6595.
- ¹⁸⁵ R. K. Gupta, I. Bedja, *J. Phys. D: Appl. Phys.*, 2017, **50**, 245501.
- ¹⁸⁶ Y. Liu, A. Hagfeldt, X.R. Xiao, S. E. Lindquist, *Sol. Energy Mater. Sol. Cells*, 1998, **55**, 267.
- ¹⁸⁷ V. Gutmann, *Electrochim. Acta*, 1976, **21**, 66.
- ¹⁸⁸ A. Fukui, R. Komiya, R. Yamanaka, A. Islam, L. Han, *Sol. Energy Mater. Sol. Cells*, 2006, **90**, 649.
- ¹⁸⁹ J. Hong, M. Joo, R. Vittal, K. Kim, *J. Electrochem. Soc.*, 2002, **149**, 493.
- ¹⁹⁰ C. E. Housecroft, E. C. Constable, *Chem. Soc. Rev.*, 2015, **44**, 8386 and references therein.
- ¹⁹¹ T. Stergiopoulos, A. G. Kontos, V. Likodimos, D. Perganti, P. Falaras, *J. Phys. Chem. C*, 2011, **115**, 10236.
- ¹⁹² S. Kambe, S. Nakade, T. Kitamura, Y. Wada, S. Yanagida, *J. Phys. Chem. B*, 2002, **106**, 2967.

-
- ¹⁹³ S. Nakade, Y. Saito, W. Kubo, T. Kanzaki, T. Kitamura, Y. Wada, S. Yanagida, *Electrochem. Commun.*, 2003, **5**, 804.
- ¹⁹⁴ M. K. Nazeeruddin, A. Kay, I. Rodicio, R. Humphry-Baker, E. Mueller, P. Liska, N. Vlachopoulos and M. Grätzel, *J. Am. Chem. Soc.*, 1993, **115**, 6382.
- ¹⁹⁵ C. Shi, S. Dai, K. Wang, X. Pan, F. Kong, L. Hu, *Vib. Spectrosc.* 2005, **39**, 99.
- ¹⁹⁶ G. Boschloo, L. Haggman, A. Hagfeldt, *J. Phys. Chem. B*, 2006, **110**, 13144.
- ¹⁹⁷ N. Kopidakis, K. Benkstein, J. Lagemaat, A. Frank, *J. Phys. Chem. B*, 2003, **107**, 11307.
- ¹⁹⁸ C. J. Wood, C. A. McGregor, E. A. Gibson, *ChemElectroChem*, 2016, **3**, 1827.
- ¹⁹⁹ Y. Liu, A. Hagfeldt, X. R. Xiao and S. E. Lindquist, *Sol. Energy Mater. Sol. Cells*, 1998, **55**, 267.
- ²⁰⁰ H. Zhu, A. Hagfeldt, G. Boschloo, *J. Phys. Chem. C*, 2007, **111**, 17455.
- ²⁰¹ F. J. Malzner, M. Willgert, E. C. Constable, C.E. Housecroft, *J. Mater. Chem. A*, 2017, **5**, 13717.
- ²⁰² C. Cramer, S. Brunklaus, Y. Gao, K. Funken, *J. Phys.: Condens. Matter*, 2003, **15**, S2309.
- ²⁰³ I. Hod, Z. Tachan, M. Shalom, A. Zaban, *Phys.Chem. Chem. Phys.*, 2013, **15**, 6339.
- ²⁰⁴ M. A. Green, K. Emery, Y. Hishikawa, W. Warta, E. D., Dunlop, *Prog. Photovolt. Res. Appl.*, 2015, **23**, 805.
- ²⁰⁵ M.A. Green, *Third Generation Photovoltaics: Advanced Solar Energy Conversion*, pp.160, 1st ed., Springer, New York, 2003.
- ²⁰⁶ K. Kakiage, Y. Aoyama, T. Yano, K. Oya, J. -I., Fujisawa, M. Hanaya, *Chem. Commun.*, 2015, **51**, 15894.
- ²⁰⁷ W. Shockley, H.J. Queisser, *J. Appl. Phys.*, 1961, **32**, 10.
- ²⁰⁸ C.H. Henry, *J. Appl. Phys.*, 1980, **51**, 4494.
- ²⁰⁹ J. He, H. Lindström, A. Hagfeldt, S. -E. Lindquist, *J. Phys. Chem. B*, 1999, **103**, 8940.
- ²¹⁰ A. Nattestad, A. J. Mozer, M. K. R. Fischer, Y.-B. Cheng, A. Mishra, P. Bäuerle, U. Bach, *Nature Mater.*, 2012, **9**, 31.
- ²¹¹ C. J. Wood, G. H. Summers, E. A. Gibson, *Chem. Commun.*, 2015, **51**, 3915.
- ²¹² P. Ho, S. Thogiti, L. Q. Bao, R. Cheruku, K-S. Ahn, J. H. Kim, *Solar Energy*, 2018, **161**, 9.
- ²¹³ Y. Farré, M. Raissi, A. Fihey, Y. Pellegrin, E. Blart, D. Jacquemin, F. Odobel, *Dyes and Pigments*, 2018, **148**, 154.
- ²¹⁴ S. O. Furer, L. Y. N. Luu, B. Bozic-Weber, E. C. Constable, C. E. Housecroft, *Dyes Pigments*, 2016, **132**, 72.
- ²¹⁵ S. Hattori, Y. Wada, S. Yanagida, S. Fukuzumi, *J Am Chem Soc*, 2005, **127**, 9648.
- ²¹⁶ F. J. Malzner, A. Prescimone, E. C. Constable, C. E. Housecroft, M. Willgert, *J. Mater. Chem. A*, 2017, **5**, 4671.
- ²¹⁷ M. Freitag, F. Giordano, W. Yang, M. Pazoki, Y. Hao, B. Zietz, M. Grätzel, A. Hagfeldt, G. Boschloo, *J. Phys. Chem. C*, 2016, **120**, 9595.

-
- ²¹⁸ M. Karpacheva, F. J. Malzner, C. Wobill, A. Büttner, E. C. Constable, C. E. Housecroft, *Dyes and Pigments*, 2018, **156**, 410.
- ²¹⁹ A. Büttner, *Dye Sensitized Solar Cells-Investigation of bis(diamine)copper(I) Dyes*, 2018, (doctoral dissertation), http://edoc.unibas.ch/diss/DissB_65143, University of Basel, Basel, Switzerland.
- ²²⁰ F. Kröhnke, *Synthesis*, 1976, **1976**, 1.
- ²²¹ Y. Saygili, M. Söderberg, N. Pellet, F. Giordano, Y. Cao, A. Belen Muñoz-García, S. M. Zakeeruddin, N. Vlachopoulos, M. Pavone, G. Boschloo, L. Kavan, J.-E. Moser, M. Grätzel, A. Hagfeldt, M. Freitag, *J. Am. Chem. Soc.*, 2016, **138**, 15087.
- ²²² M. Ruthkosky, F. N. Castellano, G. J. Meyer, *Inorg. Chem.*, 1996, **35**, 6406.
- ²²³ M. K. Eggleston, D. R. McMillin, . K. S. Koenig, A. J. Pallenberg, *Inorg. Chem.*, 1997, **36**, 172.
- ²²⁴ X. Mao, R. Zhou, S. Zhang, L. Ding, L. Wan, S. Qin, Z. Chen, J. Xu, S. Miao, *Scientific Reports*, 2016, **6**, 1, and references therein.
- ²²⁵ L. Dloczik, O. Illeperuma, I. Laueremann, L. M. Peter, E. A. Ponomarev, G. Redmond, N. J. Shaw, I. Uhlendorf, *J. Phys. Chem. B*, 1997, **101**, 10281.
- ²²⁶ S. Ito, R. Humphry-Baker, P. Liska, P. Comte, P. Péchy, M. K. Nazeeruddin, M. Grätzel, *ISRN Nanotechnology*, 2011, **14**, 4351.



Rue de la Gare 18,
Marin-Epagnier 2074, NE
Nationality: Swiss, Greek,
Age 34
Tel: [+41 76 816 88 60](tel:+41768168860)
Email: nathaliemarinaki@gmail.com
LinkedIn: www.linkedin.com/in/nathaliemarinakis/

Summary: Deep knowledge in analytical and electrochemical techniques, EIS, CV, FIB, SEM, IR, MS.
Working experience in industry from which I acquired project management skills and the sense of business.

WORKING EXPERIENCE IN INDUSTRY:

- SWATCH GROUP** 2019-present
- Project manager in electrochemistry
 - Responsible of the electrochemistry team of the R&D of the Swatch group
 - Conceiving new ideas for electrochemical devices for implementation
 - Assessing and resolving electrochemical problems occurring in the Swatch group.
 - Annual turnover of the company: 8.24 billion CHF
- V-FLORES - Scientific Consulting (Greece)** 2011-2012
- Consultant for a project concerning medicinal plants transformation.
 - Participation in the creation of business plan section concerning the transformation of the plants and analysis of the secondary product (essential oils, extracts, lyophilized products).
 - Annual turnover of the company: 2.000.000-2.500.000 €.
- BIODES - Scientific Collaborator (Greece)** 2006-2010
- Co-creation of an industry producing essential oils.
 - Selection of the equipment and the different variety of medicinal plants, used in production.
 - Establishment of protocols, monitoring of the production and analysis of the final product.
 - Annual turnover of the company: 800.000-1.000.000 €.

RESEARCH EXPERIENCE:

University of Basel: Doctoral research, Inorganic Chemistry, Development of p-type Dye Sensitized Solar Cells (DSSC) in collaboration with the Physics department. 2014-Present

Responsibilities:

- Establishing protocols for production of a p-type semiconductor electrode.
- Characterisation of the p-type electrode. (CV, XPS, FIB, SEM microscopy).
- Optimisation of electrolyte and additives.
- Assembly and characterisation of solar cell (Sun Simulation, EIS, EQE).
- Preparation of scientific articles and reports for internal/external review.
- Presentation of outcomes (poster and talks) in national and international conferences.

Achievements:

- Hold the record for the p-type DSSC sensitized with an inorganic dye.
- Creating protocols for the characterisation of DSSC with electrochemical technics and ensuring effective knowledge transfer to peers.
- First or second name in 6 publications.

University of Geneva: Master in Chemistry

Master thesis: Environmental Physical-Chemistry:

- Characterisation of the surface charge of TiO₂ nanoparticles.
- Monitoring and adjusting their aggregation and disaggregation process in natural water and in the presence of alginate

Achievements:

- Learned technique: DLS, ELS, CD, NMR UV-Vis.
- Independent parallel project for the characterisation and quantification of Hg in solid with (AAS) technics.

EDUCATIONAL QUALIFICATION:

PhD in Inorganic Chemistry-University of Basel (Switzerland).	2014-Present
Master in Chemistry-University of Geneva (Switzerland).	2014
Bachelor in Chemistry- University of Aristotle Thessaloniki (Greece).	2012

LEADERSHIP and PROJECT MANAGEMENT EXPERIENCE:

Supervising postgraduates and undergraduates few months long projects. 2014-2018

- 5 short-term projects during my 4 years of PhD.
- Multidisciplinary background of the students (chemistry, nanoscience, chemical engineer).
- Planning, supervising and adjusting the student's project in parallel with research.
- Assisting and correcting reports and presentations.

Supervising undergraduate students during their practical course. 2014-2018

- 4 practical courses during 4 years of PhD (15h/week over 4 months).
- Introducing theory and experimental procedure to a class of students.
- Supervising the experiment procedures and answering questions of broad spectrum.
- Pharma and chemistry undergraduates.
- Correcting reports.

SUMMER SCHOOLS and ADDITIONAL EDUCATION:

- "Project Management" (University of Basel 2018).
- "Successful Team Leading" (University of Basel 2018).
- Scientific Writing in English (University of Basel 2018).
- FIB/SEM/TEM/EDX course (Nano Imaging Lab at Basel University's Swiss Nanoscience Institute 2018).
- Summer School in EIS (UK, Bath 2017).
- International School on Hybrid and Organic Photovoltaics (IT, Castiglione della Pescaia ISOPHOS 2015 and 2016).

LANGUAGES and SOFTWARE:

English (working language C2).
French (native).
Greek (native).

MS Office-Excel, Word, Power Point (working).
Origin (working)-Origin course University of Basel (2018).

HOBBIES:

Swimming, 10 years in total, 6 of which in a professional level, during which I won the second position in Balkan meetings and the third place in Greek national's, mountain bike, hiking and painting.